Fabrication of Carbon-based Nanomaterials for Energy Conversion

Bita Bayatsarmadi

B.Sc. (Hons), M.Sc.

Thesis submitted for the degree of

Doctor of Philosophy

School of Chemical Engineering

Faculty of Engineering, Computer & Mathematical Sciences

The University of Adelaide, Australia

April 2017

Abstract

Nowadays, energy is one of the most important challenges facing mankind due to its supply and demand issues and global warming. Replacing unsustainable energy sources such as fossil fuels is among the most critical issues in the 21st century. Among different solutions for the energy challenges, electrochemistry which studies the conversion between electricity and energy stored in chemical bonds can be used to solve these issues without any significant impact to the environment. One of the energy conversion limitations in electrochemical processes is extra energy requirements to overcome the high activation barriers. To overcome this problem, electrocatalysts are always utilized to improve electrode efficiency in order to decrease activation energy and increase energy conversion. Electrocatalysts should be low-cost, durable, efficient and sustainable. One of the main categories of electrocatalysts in energy conversion reactions is precious metal- based materials which have high performance. However, they cannot be applied at large scales due to their high cost, scarcity, limited supply and weak durability. Thus, other alternative electrocatalysts based on lower cost material such as non-precious metal or metal free catalysts have been widely developed. Carbon-based materials are one of the most important materials which have been playing a significant role in the development of energy conversion and storage devices because of their abundance, low cost, stability, easy accessibility, good recycling, and relatively environmentally friendly characteristics with high durability, especially in alkaline medium. This thesis aims to design and fabricate a series of advanced electrocatalysts for the different range of electrochemical reactions including oxygen reduction reaction (ORR), oxygen evolution reaction (OER) and hydrogen evolution reaction (HER) which are principals of various types of energy conversion devices.

The first part of the thesis focuses on the development of metal-free nitrogen-doped mesoporous carbon spheres prepared via soft-templating procedure by tuning different nitrogen precursor contents and carbonization temperature. The synthesized electrocatalyst showed a favourable catalytic activity in ORR with high kinetic current and positive onset potential due to its high surface area, high pore volume, narrow mesopore size distribution, high conductivity and high nitrogen content.

In the second part, carbon-based composites co-doped with nitrogen and trace amount of metallic cobalt have been developed as electrocatalysts for water splitting system at low overpotential and high current density. An excellent electrochemical activity of newly

developed electrocatalyst originates from its graphitic nanostructure and highly active Co-N_x sites. Based on the spectroscopic and electrochemical investigations the newly identified Co-N_x sites in the carbon framework are responsible for the high electrocatalytic activity of the Co, N-doped carbon.

The third research project is to utilize the physical synthesis technique to ensure high control and tunability of morphology, structure and composition of multi-component materials. In this context, pulsed laser deposition (PLD) is particularly versatile in the tuning of properties of deposited materials which is based on ablating a target material by laser pulses and has been applied to develop new carbon-based thin films. Thus, cobalt oxide nanoparticles deposited on porous nitrogen -doped carbon films were successfully developed via a two-step pulsed laser deposition technique. The synthesised material behaves as an efficient OER electrocatalyst with superior activity in alkaline electrolyte. The excellent catalytic activity of prepared electrodes could be attributed to the surrounding N-carbon framework, and it was found that a higher ratio of Co^{2+}/Co^{3+} yields better catalytic activity towards the OER. Transport of reactants and products involved in electrochemical reactions was also facilitated by the porous structure of material. Additionally, the carbon framework, comprising carbons adjacent to cobalt (oxide) nanoparticles, increases catalytic sites and prevents the aggregation or dissolution of nanoparticles.

The last part of the thesis aims to design an efficient and stable bifunctional electrocatalyst for both HER and OER in the same electrolyte for overall water electrolysis. Thus a novel type of robust binary Ni-Co nanoparticles coated on porous N-carbon thin film with low overpotential has been reported. The efficient OER activity might be contributed to the available metal oxide nanoparticles with effective electronic structure configuration, enhanced mass/charge transport capability. At the same time, the porous nitrogen doped carbon incorporated with cobalt and nickel species might serve as an excellent HER catalyst. As a result, the newly developed electrocatalysts manifest high current densities and strong electrochemical stability in overall water splitting, outperforming most of the previously reported non-precious metal-based counterparts.

Declaration

I certify that this work contains no material which has been accepted for the award of any other degree or diploma in my name, in any university or other tertiary institution and, to the best of my knowledge and belief, contains no material previously published or written by another person, except where due reference has been made in the text. In addition, I certify that no part of this work will, in the future, be used in a submission in my name, for any other degree or diploma in any university or other tertiary institution without the prior approval of the University of Adelaide and where applicable, any partner institution responsible for the joint-award of this degree.

I give consent to this copy of my thesis when deposited in the University Library, being made available for loan and photocopying, subject to the provisions of the Copyright Act 1968.

The author acknowledges that copyright of published works contained within this thesis resides with the copyright holder(s) of those works.

I also give permission for the digital version of my thesis to be made available on the web, via the University's digital research repository, the Library Search and also through web search engines, unless permission has been granted by the University to restrict access for a period of time.

Bita Bayatsaramadi Date: 23.04.2017

List of Publications

The doctoral thesis is prepared in “Publication” style according to the “specifications for Thesis (2016)” of the University of Adelaide. It includes publications that have been published:

1) **B. Bayatsarmadi**, Y. Zheng, A. Vasileff, S.Z. Qiao, “Recent advances in atomic metal doping of carbon-based nanomaterials for energy conversion”, ***Small***, 2017, DOI: 10.1002/smll.201700191.
2) **B. Bayatsarmadi**, Y. Zheng, M. Jaroniec and S.Z. Qiao, “Soft-Templating Synthesis of N-Doped Mesoporous Carbon Nanospheres for Enhanced Oxygen Reduction Reaction”, ***Chemistry – An Asian Journal***, 2015, 10, 1546-1553.
3) **B. Bayatsarmadi**, Y. Zheng, Y. Tang, M. Jaroniec and S.Z. Qiao, “Significant Enhancement of Water Splitting Activity of N-Carbon Electrocatalyst by Trace Level Co Doping”, ***Small***, 2016, 12, 3703-3711.
4) **B. Bayatsarmadi**, Y. Zheng, C.S. Casari, V. Russo and S.Z. Qiao, “Pulsed laser deposition of porous N-carbon supported cobalt (oxide) thin films for highly efficient oxygen evolution”, ***Chemical Communications***, 2016, 52, 11947-11950
5) **B. Bayatsarmadi**, Y. Zheng, C.S. Casari, V. Russo, L. Ge and S.Z. Qiao, “Highly Active binary Nickel-Cobalt/Nanocarbon thin films as Efficient Water Splitting electrodes”, ***Nanoscale***, 2016, 8, 18507-18515.

Acknowledgments

First of all, I would like to express my profound appreciation and thanks to my principal supervisor, Prof. Shi-Zhang Qiao for his valuable guidance, support and encouragements throughout my PhD study. I would also thank Dr. Yao Zheng, my Co-supervisor, who has always supported me with his generosity, care and deep technical knowledge. They were tremendous mentors for me and without their enthusiastic supervision, inspiration, guidance and endless supports completion of this thesis would not have been possible. Furthermore, I am grateful to A/Prof. Bo Jin who gave me useful advice during my research. Words cannot express the deepness of my gratitude to my supervisory panel.

I would like to give special thanks to all my group members and lab mates from Prof. Qiao's research group for their help, supports, technical assistance and useful discussion. Working with them was a real joy.

My grateful thanks go to the School of Chemical Engineering staff, analytical lab manager, workshop technical staff and administration team at the University of Adelaide for their individual helps.

I would like to thank Prof. Carlo Spartaco Casari, my host supervisor, Dr. Valeria Russo and Ms. Anna Facibeni from Micro and Nano-structured Lab at the Polytechnic University of Milan, for all their kind cooperation, supports and valuable discussions during my Endeavour Fellowship in Italy.

Special thanks to my fellow friends at the University of Adelaide and all around the world who supported me and incented me to strive towards my goal.

I would also like to acknowledge the Australian Government and the University of Adelaide for APA scholarship to financially support me during my PhD study and the Endeavour Fellowship to support my overseas short-term research study as a part of my PhD.

Last but not list, special thanks to my family. Words cannot express how grateful I am to my mother, my father and my brothers for all of their unconditional love and supports. In the end, I would like to express my deep appreciation to my husband Sam Saeed, who has always been my best friend. Without his encouragement, patience and unwavering love, I could not surely conduct this work.

Table of Content

Chapter 1

1. Introduction

1.1. Significance of the Project

Nowadays, energy is one of the most important challenges facing mankind due to its supply and demand issues and global warming because of the rapid increase in greenhouse emissions, long-lasting environmental consequences and global climate changes. Thus, replacing unsustainable energy sources such as fossil fuels (e.g. coal, oil, natural gas, etc.) which have finite reserves and reducing CO_2 emissions are among the most critical issues in the 21st century.[1-4]

Over the past decades, alternative technologies have been developed to harvest and use clean and sustainable energy sources including solar energy, wind power, biofuels, hydrothermal, geothermal and nuclear energies. New energy storage and conversion technologies are practical and price competitive and can be an efficient substitution in the upcoming decades.[2, 5]

Among different solutions for the energy challenges, electrochemistry which studies the conversion between electricity and energy stored in chemical bonds can be used to solve these issues. Electrochemical energy conversion is based on chemical reactions at the interface which is a direct and clean process without any major impact on the environment.[6] Also, electrochemical systems can be applied as efficient and stable platforms for energy storage and conversion.[3]

Among the alternative and sustainable energy sources and technologies as mentioned earlier, fuel cells, batteries, water splitting systems and supercapacitors are termed collectively as electrochemical energy technologies that rely on a common electrochemical principle. They convert chemical energy directly into electrical energy with little or no pollution and are environmentally friendly. These new technologies are exclusively important to mobile and automotive applications.[2, 7-10]

The most important energy-related electrochemical conversions are oxygen reduction reaction (ORR), oxygen evolution reaction (OER), hydrogen oxidation reaction (HOR) and hydrogen evolution reaction (HER). One of the energy conversion limitations in electrochemical processes is extra energy requirements to overcome the high activation barriers.[3, 11]

To overcome this problem, electrocatalysts are always utilised to improve electrode efficiency in order to decrease activation energy and increase energy conversion. Electrocatalysts should be low-cost, durable, efficient and sustainable.[3, 10, 12, 13] The state-of-the-art electrocatalysts for these electrochemical reactions are usually precious metals (Pt for ORR and HER, IrO_2 or RuO_2 for OER) which have high performance. On the other hand, they cannot be applied at large scales due to their high cost, scarcity, limited supply and weak durability.[3, 9, 14, 15] Thus, it is momentous but challenging to develop other alternative cost-effective, highly active, stable, durable and environmental friendly electrocatalysts such as non-precious metal based or metal-free materials to promote the sustainable energy technologies.

1.2. Research Objectives

The major aim of this research project is to develop novel low-cost, active and durable carbon-based electrocatalysts as a substitute for Noble metal materials in the key electrocatalytic processes (e.g. ORR, OER and HER) in the renewable fuel cells, metal-air batteries and water electrolysers.

The main objectives of this research project include:

- Studying the nitrogen doping and porous structure effect of mesoporous carbon spheres as metal-free electrocatalysts on ORR performance and developing facile and low-cost soft-templating synthesis procedure to fabricate N-doped mesoporous carbon spheres with high surface area and nitrogen content.
- Investigating the effect of trace level of Co doping into the N-carbon electrocatalyst on both OER and HER performance as two important half reaction in water splitting systems.
- Revealing the morphology dependence of OER activity on Co(Ox) nanoparticles deposited on porous N-carbon thin films and optimizing the electrocatalytic performance of resultant materials by tuning the chemical composition and nanostructure of the catalysts.
- Designing new bimetallic nanoparticles on N-carbon thin films as bifunctional catalyst electrode for HER and OER to promote the overall water splitting. The optimum water splitting activity can be obtained by adjusting the Ni/Co doping ratio on N-carbon films,

displaying low overpotential and highly stable bifunctional electrodes in Alkaline solution.

1.3. Thesis Outline

This thesis is the outcome of my research studies during my Ph.D. program which is presented in the form of journal publications. The chapters of this thesis are arranged in the following sequence;

- **Chapter 1:** This chapter introduces the significance of research project and thesis and outlines the objective and key contributions to the field of research.
- **Chapter 2:** This chapter reviews the literature covering the recent advances in atomic metal doping of carbon-based nanomaterials for energy storage and conversion systems.
- **Chapter 3:** This chapter presents the research findings for the soft-templating synthesis of N-doped mesoporous carbon nanospheres for enhanced oxygen reduction reaction.
- **Chapter 4:** This chapter investigates the significant enhancement of water splitting activity of N-carbon electrocatalyst by trace level Co doping.
- **Chapter 5:** This chapter devotes to the pulsed laser deposition of porous N-carbon supported cobalt (oxide) thin films for highly efficient oxygen evolution.
- **Chapter 6:** This chapter develops highly active binary nickel-cobalt/nanocarbon thin films as efficient water splitting electrodes.
- **Chapter 7:** This chapter presents conclusions and perspectives for future work on synthesis and development of non-precious electrocatalysts and their application with the deep understanding of the reaction mechanisms.

1.4. References

1. J. L. Fillol, Z. Codolà, I. Garcia-Bosch, L. Gómez, J. J. Pla and M. Costas, *Nat. Chem.*, 2011, **3**, 807.
2. A. Manthiram, A. Vadivel Murugan, A. Sarkar and T. Muraliganth, *Energy Environ. Sci.*, 2008, **1**, 621-638.
3. Y. Liang, Y. Li, H. Wang and H. Dai, *J. Am. Chem. Soc.* , 2013, **135**, 2013-2036.
4. R. Subbaraman, D. Tripkovic, K.-C. Chang, D. Strmcnik, A. P. Paulikas, P. Hirunsit, M. Chan, J. Greeley, V. Stamenkovic and N. M. Markovic, *Nat. Mater.*, 2012, **11**, 550-557.
5. S. L. Candelaria, Y. Shao, W. Zhou, X. Li, J. Xiao, J.-G. Zhang, Y. Wang, J. Liu, J. Li and G. Cao, *Nano Energy*, 2012, **1**, 195-220.

6. J. Kunze and U. Stimming, *Angew. Chem. Int. Ed.*, 2009, **48**, 9230-9237.

7. M. Armand and J. M. Tarascon, *Nature*, 2008, **451**, 652-657.

8. A. S. Arico, P. Bruce, B. Scrosati, J.-M. Tarascon and W. van Schalkwijk, *Nat. Mater*., 2005, **4**, 366.

9. Y. Zheng, Y. Jiao, M. Jaroniec, Y. Jin and S. Z. Qiao, *Small*, 2012, **8**, 3550-3566.

10. J. Hou, Y. Shao, M. W. Ellis, R. B. Moore and B. Yi, *Phys. Chem. Chem. Phys*., 2011, **13**, 15384-15402.

11. E. H. Yu, U. Krewer and K. Scott, *Energies*, 2010, **3**, 1499-1528.

12. Y. Yang, K. Chiang and N. Burke, *Catal. Today*, 2011, **178**, 197-205.

13. W. Xiong, F. Du, Y. Liu, A. Perez, M. Supp, T. S. Ramakrishnan, L. Dai and L. Jiang, *J. Am. Chem. Soc.,* 2010, **132**, 15839-15841.

14. J. Liang, Y. Zheng, J. Chen, J. Liu, D. Hulicova-Jurcakova, M. Jaroniec and S. Z. Qiao, *Angew. Chem. Int. Ed.*, 2012, **51**, 3892-3896.

15. Y. Zheng, Y. Jiao, J. Chen, J. Liu, J. Liang, A. Du, W. Zhang, Z. Zhu, S. C. Smith, M. Jaroniec, G. Q. Lu and S. Z. Qiao, *J. Am. Chem. Soc*., 2011, **133**, 20116-20119.

Chapter 2

2. Literature Review

2.1. Introduction

Nowadays, energy is one of the most important challenges facing mankind due to its supply and demand issues as well as global warming. Many advanced technologies for clean and sustainable energy conversion, such as water splitting and fuel cells are extensively studied. In principle, the kinetics of a series of electrochemical processes, including oxygen reduction reaction (ORR), oxygen evolution reaction (OER), and hydrogen evolution reaction (HER), significantly influences the performances of the devices as mentioned earlier. The practical large-scale application of these techniques is constrained by the lack of efficient catalysts composed of inexpensive, earth-abundant elements. In recent years, besides metal-free electrocatalysts, a wide variety of trace transition metal contained electrocatalysts have been developed, in which the active sites of these catalysts, like other solid heterogeneous catalysts, are sparsely distributed at selective sites on the surface of bulk materials. To expose more active sites, these catalysts are generally downsized into nano-particulate form and stabilized onto certain substrates (e.g. carbon-based substrates) to form advanced composite materials. Although atomic metal-doped carbon-based materials for electrocatalytic conversion are the subject of extensive studies in recent years, there is no comprehensive review on the theory and experiment toward molecular design, synthesis, characterization and performance of this type of electrocatalysts. Thus, we propose a timely review on the recent advances in highly active atomic metal doped carbon-based electrocatalysts for HER, OER and ORR as the most important energy-related electrocatalytic reactions. This Features Article could pave the way of making electrochemically active materials for high-performance batteries, supercapacitors, fuel cells, water splitting systems and other types of energy storage and conversion devices.

2.2. Recent advances in atomic metal doping of carbon-based nanomaterials for energy conversion

This section is included in the thesis as it appears as a Review paper published by **Bita Bayatsarmadi**, Yao Zheng, Anthony Vasileff, and Shi-Zhang Qiao, Recent advances in atomic metal doping of carbon-based nanomaterials for energy conversion, to ***Small***.

Statement of Authorship

Title of Paper	Recent advances in atomic metal doping of carbon-based nanomaterials for energy conversion		
Publication Status	☑ Published ☐ Submitted for Publication	☐ Accepted for Publication ☐ Unpublished and Unsubmitted work written in manuscript style	
Publication Details	B. Bayatsarmadi, Y. Zheng, A. Vasileff, S.Z. Qiao*, “Recent Advances in Atomic Metal Doping of Carbon-based Nanomaterials for Energy Conversion”, ***Small***, 2017, DOI:10.1002/smll.201700191		

Principal Author

Name of Principal Author (Candidate)	Bita Bayatsarmadi		
Contribution to the Paper	Performing the Literature Review and writing the manuscript		
Overall percentage (%)	80%		
Certification:	This paper reports on original research I conducted during the period of my Higher Degree by Research candidature and is not subject to any obligations or contractual agreements with a third party that would constrain its inclusion in this thesis. I am the primary author of this paper.		
Signature		Date	17/04/2017

Co-Author Contributions

By signing the Statement of Authorship, each author certifies that:

i. the candidate’s stated contribution to the publication is accurate (as detailed above);
ii. permission is granted for the candidate in include the publication in the thesis; and
iii. the sum of all co-author contributions is equal to 100% less the candidate’s stated contribution.

Name of Co-Author	Dr. Yao Zheng		
Contribution to the Paper	Manuscript review and assessment.		
Signature		Date	17/04/2017

Name of Co-Author	Anthony Vasileff		
Contribution to the Paper	Manuscript review.		
Signature		Date	17/04/2017

Name of Co-Author	Prof. Shi-Zhang Qiao		
Contribution to the Paper	Manuscript review and assessment.		
Signature		Date	17/04/2017

ADVANCED SCIENCE NEWS
www.advancedsciencenews.com

small

Electrocatalysis

Recent Advances in Atomic Metal Doping of Carbon-based Nanomaterials for Energy Conversion

*Bita Bayatsarmadi, Yao Zheng, Anthony Vasileff, and Shi-Zhang Qiao**

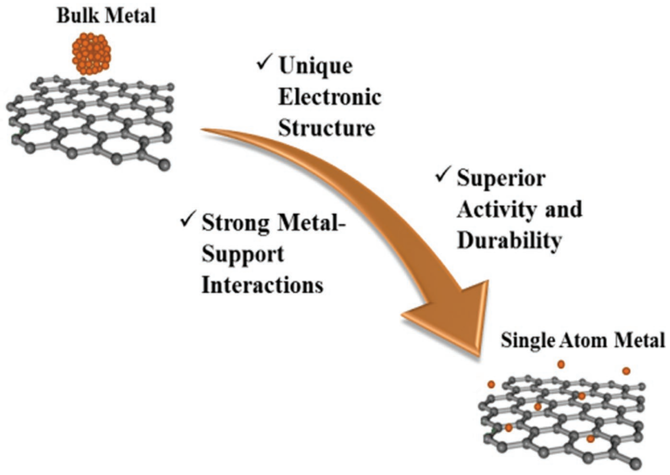

From the Contents

Nanostructured metal-contained catalysts are one of the most widely used types of catalysts applied to facilitate some of sluggish electrochemical reactions. However, the high activity of these catalysts cannot be sustained over a variety of pH ranges. In an effort to develop highly active and stable metal-contained catalysts, various approaches have been pursued with an emphasis on metal particle size reduction and doping on carbon-based supports. These techniques enhances the metal-support interactions, originating from the chemical bonding effect between the metal dopants and carbon support and the associated interface, as well as the charge transfer between the atomic metal species and carbon framework. This provides an opportunity to tune the well-defined metal active centers and optimize their activity, selectivity and stability of this type of (electro)catalyst. Herein, recent advances in synthesis strategies, characterization and catalytic performance of single atom metal dopants on carbon-based nanomaterials are highlighted with attempts to understand the electronic structure and spatial arrangement of individual atoms as well as their interaction with the supports. Applications of these new materials in a wide range of potential electrocatalytic processes in renewable energy conversion systems are also discussed with emphasis on future directions in this active field of research.

1. Introduction

Nowadays, energy security and sustainability is one of the most important challenges facing society due to issues with depleting reserves of conventional fuels, rising demand and climate change. The need for efficient, economical and environmentally benign processes is not only critical for the global economy but also to help in the mitigation of environmental hazards caused by fossil fuels.[1] To offer scientific and technological solutions for energy-related problems and diminishing sources of fossil fuels, significant efforts have been devoted to exploiting alternative sustainable and clean energy sources including solar energy, wind power, biofuels, hydrothermal, geothermal, and nuclear energies.[2]

To date, electrocatalysis which studies the conversion between electricity and energy stored in chemical bonds can be used as an alternative technology without any major impact to the environment. Thus, the development of sustainable energy storage and conversion devices such as fuel cells, metal-air batteries and supercapacitors as well as renewable energy systems, such as water splitting systems with high efficiency and low cost, have become an important research focus.[3] These electrochemical energy technologies rely on a common electrochemical principle which converts chemical energy directly into electrical energy with little or no pollution. The most important energy-related electrochemical conversions are the oxygen reduction reaction (ORR), oxygen evolution reaction (OER), hydrogen oxidation reaction (HOR) and hydrogen evolution reaction (HER). The ORR is a cathodic reaction and a key process in a range of energy applications such as fuel cells and metal-air batteries in which the strong $O{=}O$ bond is difficult to break.[4] The OER is the electrochemical oxidation of water to generate molecular oxygen. This reaction is a half-cell reaction of the water splitting process, which is involved in rechargeable metal-air batteries, and solar fuel synthesis.[5] The HER is the process of H_2 production from water which is the cathodic half-cell reaction in water splitting.[6] Conversely, the HOR is the reverse reaction to convert H_2 into electricity, which is the anodic reaction in H_2-O_2 fuel cells.[7] However, the implementation of these advanced technologies is still a big challenge due to the sluggish electrode kinetics associated with these electrochemical reactions. In practice, electrochemical energy conversion reactions suffer from high overpotential or low faradic efficiency which lead to energy underutilization. To overcome this problem, electrocatalysts are utilized to improve electrode efficiency in order to decrease activation energies and increase energy conversion. Thus, catalyst design plays an important role in enhancing the performance of energy storage and conversion devices.[8]

Utilization of an efficient, highly active, durable, low-cost, and sustainable electrocatalyst is key for the large-scale application of electrochemical energy conversion systems. However, the state-of-the-art electrocatalysts, which are mostly precious metal-based catalysts (e.g. Pt-group metals, Ir- and Ru-based compounds), fall short in one or more of these requirements, hindering their widespread use.[9] Therefore, it is important to design efficient and cost-effective materials with high activity and stability, something that has gained much research attention in recent years. For this purpose, extensive efforts have been extended to non-precious materials for electrochemical reactions including metal-free and non-noble metal materials. Recent advances in metal-free catalysts (carbon materials doped by one or multiple heteroatoms) have shown potential in energy conversion and storage systems.[10] It is reported that some carbon-based catalysts have demonstrated comparable ORR activity, enhanced stability and fuel tolerance compared to that of state-of-the-art electrocatalysts, which make them competitive alternatives to Pt. Such superior catalytic activity is attributed to the charge relocation due to the introduction of electronegative heteroatoms in the carbon framework.[11] However, it is still challenging to develop systemic molecular designed metal-free electrocatalysts to achieve high catalytic activity compared to current commercially available catalysts.[12] To address this, different metal species and derivative components have been introduced into the carbon-based materials in order to further enhance their catalytic activities. Recently, various types of non-precious metal and their derivatives have been selected as effective candidates as active additives. However, their high activity cannot be sustained over a range of pH due to inherent corrosion and oxidation susceptibility, limiting their application in catalytic processes.[13]

In an effort to develop highly active and stable supported metal catalysts, various approaches have been perused with an emphasis metal particle size reduction to the atomic scale for well-defined, homogeneously distributed active centers, which are a critical factor in determining the efficiency and reactivity of this type of catalyst.[14] Size reduction of metal particles also benefits the metal-support interactions, originating from the chemical bonding effect between the metal dopants and carbon support and the associated interface, as well as the charge transfer between metal species and carbon framework.[15] The single-atom catalysts contain isolated metal species, atomically dispersed on the support framework in order to provide an opportunity to tune the well-defined metal active centers and optimize the activity, selectivity and stability of this group of electrocatalysts.[16] There are different types of single atom catalysts which differ according to the chemical interaction between the single metal atoms and the variety of supports. These include single metal atoms doped on metal oxides, metal surfaces, carbon-based nanomaterials such as graphene, carbon nanotubes, carbon nanosheets, etc. and porous materials such as metal-organic frameworks and zeolites. Single atom catalysts exhibit superior activity in a various range of applications including

B. Bayatsarmadi, Dr. Y. Zheng, A. Vasileff,
Prof. S. Z. Qiao
School of Chemical Engineering
The University of Adelaide
Adelaide, SA 5005, Australia
E-mail: s.qiao@adelaide.edu.au

The ORCID identification number(s) for the author(s) of this article can be found under http://dx.doi.org/10.1002/smll.201700191.

DOI: 10.1002/smll.201700191

electrocatalysis,[16a,17] heterogeneous catalysis[18] and water-gas shift catalysis.[19] Herein, we highlight recent advances in synthesis strategies and structural and catalytic performance characterization techniques of single atom metal supported electrocatalysts with attempts to understand their electronic structures and the spatial arrangement of single atoms as well as their interaction with carbon-based supports. In addition, some potential applications of single metal atoms doped in carbon-based materials for electrocatalysis are summarized.

2. Single Atom Metal-doped Catalysts: Synthesis Strategies, Structure and Properties

Preparation of single metal atom supported catalysts with robust structure and high activity are still challenging due to the tendency for aggregation of single metal atoms. Recent technological advances have evolved effective strategies overcoming the difficulties associated with the preparation of single atom supported catalysts. Applications of these new materials in a wide range of potential electrocatalytic processes such as the ORR, OER and HER in renewable energy conversion systems are also discussed, highlighting the future directions of this active field of research.

2.1. Synthesis strategies

Synthesis of single atom catalysts is not trivial due to the mobility of the single atoms on the support surface and their tendency to aggregate because of their high surface energies, specifically under reaction conditions.[18b,20] To obtain single metal atom supported catalysts, preparation of a highly atomically dispersed metal species on the appropriate support is a prerequisite and is the main factor affecting catalyst properties.[21] Thus, it is necessary to devise proper synthesis routes for the preparation of highly dispersed and size-controlled single atom catalysts. This has been achieved using either improved wet chemistry methods or mass-selected soft-landing techniques (**Figure 1**a).[22]

For the wet-chemistry approach, single metal atom species need to be anchored on the support effectively to prevent the aggregation of the metal species into larger particles. Thus, utilization of surface uncapped sites or aggregation inhibitors on the supports plays an essential role in stabilizing the single metal atom species.[19c,23] This method has been recognized as a successful technique in the preparation of a site-isolated single atom supported on high surface area oxide catalysts such as atomically dispersed Pd on graphene (Pd_1/Graphene) fabricated using the atomic layer deposition technique (ALD).[24] The Pd_1/Graphene was fabricated via a three step synthesis procedure including anchor site creation on pristine graphene through oxidation in acid, anchor site selection via thermal deoxygenation and Pd ALD on the reduced graphene support (Figure 1b). Since the anchoring sites on the support are not always abundant, the concentrations of metal atoms are generally extremely low, which hinders further study of the catalyst's macroscopic properties.[23e,25] Wei et al. developed a FeO_x-supported Pt single-atom catalyst through the co-precipitation of metal precursors and precipitation agent. The resultant material was found to be an efficient catalyst for the chemoselective hydrogenation of functionalized nitroarenes.[26] The final Pt/FeO_x product was obtained after a series of post-treatments including filtration, washing, drying, calcination, and reduction with H_2/He. The Pt loading of isolated Pt atoms on the support was measured to be as small as 0.08 wt%.

The mass-selected soft-landing technique is an accurate method to prepare supported metal clusters with controlled metal species size by using high-energy atom beams and regulating the surface structure of the supports through vacuum surface procedures.[27] However, this method suffers from high cost and low-yield limiting its scope for practical applications.[28] Johnson et al. reported a controlled preparation of monodisperse ligand-capped gold clusters on surfaces

Bita Bayatsarmadi received her Bachelors and Masters in Chemical Engineering at Iran University of Science and Technology (Iran) in 2007 and 2011, respectively. Currently, she is a PhD student in the School of Chemical Engineering at the University of Adelaide (Australia) working with Prof. Shi-Zhang Qiao. Her research interests focus on the fabrication of novel carbon-based nanomaterials for variety of electrochemical reactions including oxygen reduction/evolution and hydrogen evolution reactions and implementing the newly developed electrocatalysts in energy conversion systems such as fuel cells, water splitting systems, etc.

Yao Zheng received his Bachelor and PhD degrees from Nanjing Tech University (China) and University of Queensland (Australia) in 2006 and 2014, respectively. Currently he is a DECRA research fellow at the University of Adelaide (Australia) working with Prof. Shi-Zhang Qiao. His research focuses on developing efficient catalysts for some key electrocatalysis processes like oxygen reduction, hydrogen evolution, and CO_2 reduction reactions. He is trying to develop a design procedure for electrocatalysts by combining DFT computation, nanotechnology, materials characterization, and electrochemical measurement.

Shi-Zhang Qiao received his PhD degree in chemical engineering from Hong Kong University of Science and Technology, and is currently a Chair Professor at School of Chemical Engineering of the University of Adelaide. His research expertise is in nanomaterials for new energy technologies (electrocatalysis, photocatalysis, batteries, fuel cell, supercapacitors). He has co-authored more than 280 papers in refereed journals (over 20,000 citations, h-index: 74), and is a Thomson Reuters Highly Cited researcher.

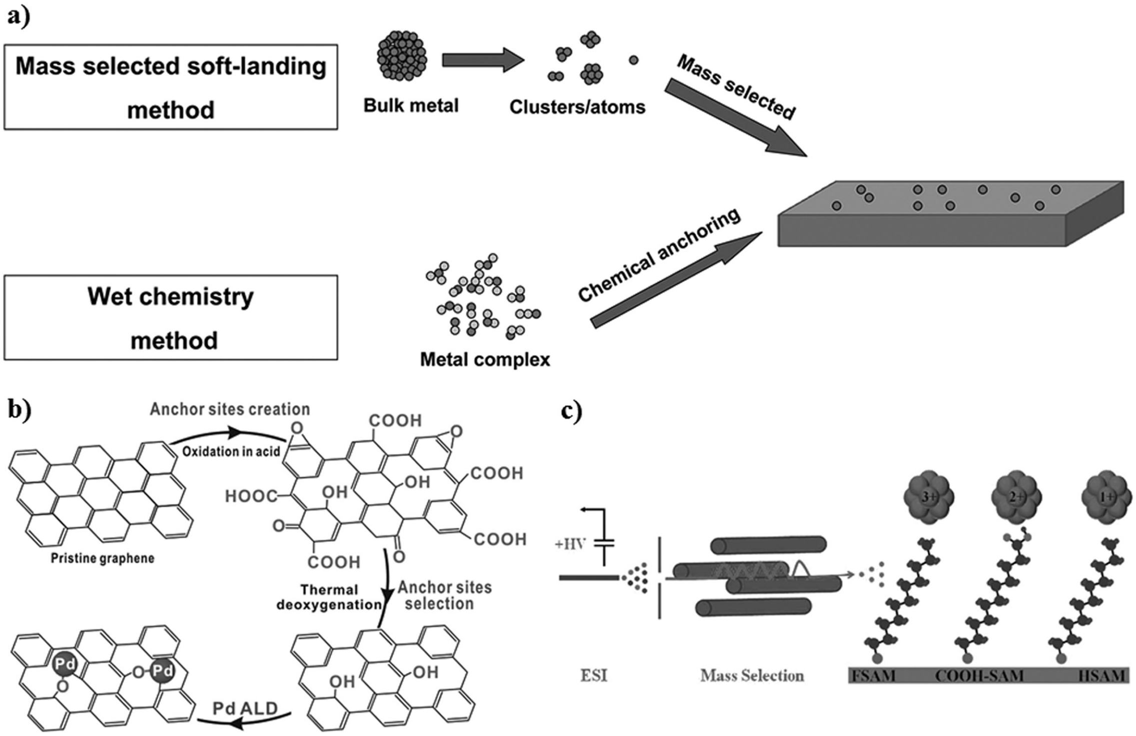

Figure 1. a) Methods for preparing single atom catalysts: (top) mass-selected soft-landing and (bottom) wet chemistry. Reprinted with permission from Ref. [22a]. Copyright 2013, American Chemical Society. b) Schematic illustration of single-atom Pd$_1$/graphene catalyst synthesis via a process of anchor site creation and selection and Pd ALD on pristine graphene, Reprinted with permission from Ref. [24]. Copyright 2015, American Chemical Society. c) Schematic illustration explaining the soft landing of mass-selected gold clusters onto surfaces. The clusters are introduced into the gas phase from solution using electrospray ionization, filtered according to mass-to-charge ratio using a quadrupole mass filter, and delivered to SAM surfaces at controlled energies. Reprinted with permission from Ref. [29]. Copyright 2012, American Chemical Society.

in different charge states using soft-landing of mass-selected ions.[29] As shown in Figure 1c, the ligand stabilized gold clusters are introduced into the gas phase through electrospray ionization followed by employment of mass selection to isolate a single ionic cluster species which was delivered to the surface at controlled energies. Although electrospray ionization is a relatively inexpensive technique, finding suitable precursors that are stable in solution which can be electrosprayed is a limitation.[30]

2.2. Geometric Structure and Location of Atomic Metal Dopants on the Support

The locations of metal dopants correspond with anchoring sites and available vacancies on the support, which facilitate the interaction of the metal atoms with the supports.[31] He et al., created spatially pre-defined vacancy sites in graphene in order to form and anchor iron dimer dopants through the introduction of additional iron precursors. The graphene vacancies were relatively stable with the Fe-dimers, however, there may exist a bonding configuration conversion which results in single Fe atoms residing in graphene divacancies.[32]

Wang et al. reported an efficient way to dope single metal atoms through the creation of vacancies (i.e., single vacancy to holes of a few nanometers) by high energy atom/ion bombardment via a Pulsed Laser Deposition (PLD) process and filling the vacancies with desired dopants (Co, Pt and In).[31c] The aberration-corrected transmission electron microscopy (TEM) images (**Figure 2**a-c) confirm the formation of monovacancy (V_1), bivacancy (V_2) and trivacancy (V_3) in the first step. The monovacancies are ideal for trapping heteroatoms with similar atomic radii as carbon while Nobel and transition metals are trapped in larger vacancies (e.g., V_2 and V_3). Next, the dopants were deposited by a less energetic atom/ion source into the created vacancies. For instance, Pt atoms were deposited in a bivacancy and a trivacancy with atomic configurations derived from the TEM images (Figure 2d-i).

The anchoring sites used for trapping the atomic transition metal dopants, such as iron or cobalt, may be in the form of M-N$_x$/C with strong covalent transition metal-nitrogen bonds which enhance the stability and activity of these materials.[33] According to the theory of coordination chemistry, nitrogen with a lone pair (i.e., the pyridinic nitrogen atom and the pyrrolic cation with the lost proton) is able to coordinate transition metals with empty orbitals.[34] Depending on the synthesis method and precursor choice, the structure of the resulting material could be varied, such as M-N$_2$/C, M-N$_4$/C, M-N$_2$+$_2$/C, etc. (**Figure 3**) in which M-N$_4$/C is usually formed due to its lowest formation energy requirement and is the most likely and stable structure of the M-N$_x$/C group. Moreover, metal (hydro)oxide nanoparticles (Fe_3O_4, Co_3O_4, etc.) can be grown and attached to the functional N-rich graphene on its out-of-plane surface with a strong coupling effect arising from an M-N-C bond. This coupling can lead to

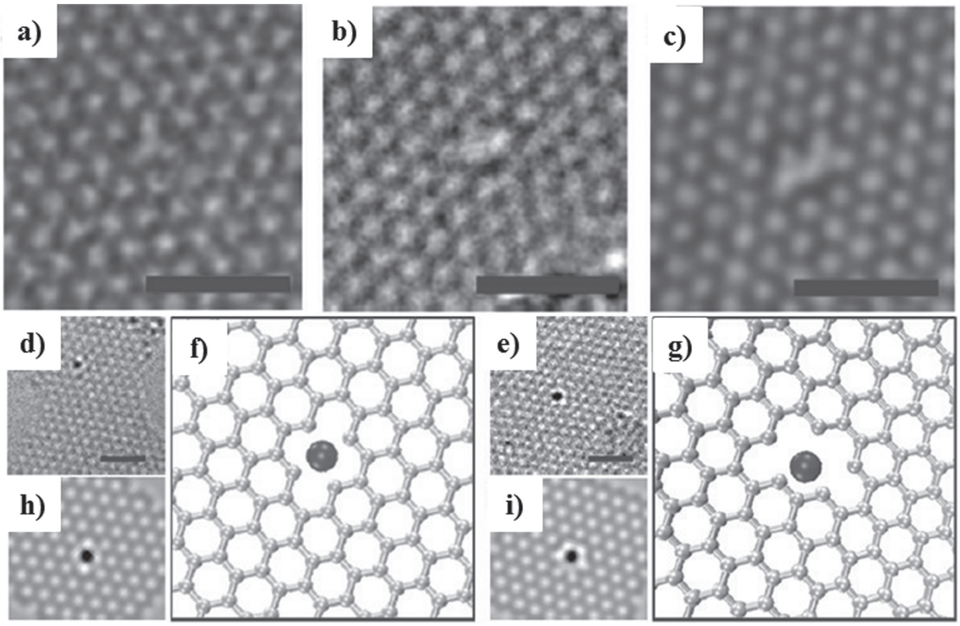

Figure 2. HRTEM image of a) a monovacancy, b) a bivacancy and c) a trivacancy. Scale bar: 1 nm, HRTEM images of a Pt atom trapped in d) a bivacancy and e) a trivacancy. f,g) Atomic models and h,i) simulated HRTEM images for the Pt-vacancy complexes in d,e). Reproduced with permission from Ref. [31c]. Copyright 2012, American Chemical Society.

enhanced activity towards electrochemical processes such as the ORR.[9,35]

2.3. Unique Electronic Structure

The geometric structure and chemical bonding of a single metal atom dopant on the support results in unique electronic structures which leads to charge transfer between metal atoms and the support due to differences in chemical potentials.[36] As a result, the anchored metal atom dopants carry some charge and contribute in the electron donation to the support, verified by various spectral characterizations and computational modelling.[37] Notably, the local density of states at the Fermi level might be attributed to the localized states around the metallic atoms. Therefore, the charge density difference between the metal and carbon in the support versus the carbon-carbon in the support might lead to the anchoring of the metal atom dopant in any of the unoccupied states.[38] For example, graphene can be either p-doped with Pt and Co atoms or n-doped with In dopants due to the charge differences between the carbon and metal dopants compared to the charge density between neighbor carbon atoms based on a Löwdin charge analysis.[31c,39] Qiu et al. have also investigated the electronic structure of monatomic nickel dopants in graphene frameworks by density functional theory (DFT) calculations, (**Figure 4**) suggesting that the substitutional Ni atom lies out of the graphene plane and that strong and stable Ni-C bindings were formed. Notably, sp-d orbital-charge transfer between Ni and surrounding C atoms results in an empty C-Ni hybrid orbital close to the Fermi energy level, which turns the local structural unit into a catalytically active site for electrochemical reactions.[40]

2.4. Substrate Coupling Effect on the Electrocatalytic Active Catalysts

The single metal atom active sites can be supported on metal/metal oxides, graphene and other carbon-based materials using different synthesis techniques in order to form unique assemblies that lead to excellent catalytic performance.

There are many reports which confirm that atomically dispersed noble metals such as Pt, Pd, Au, etc. can be predominantly synthesized at very low loadings only due to the small surface area of the support materials (metal and/or metal oxides), as well as the lack of strong interactions between the single atoms and the supports, which hinders the stability and durability of the catalysts in reaction environments.[41] Carbon-based materials have been used as supports in many reactions due to their high surface areas, thermal and

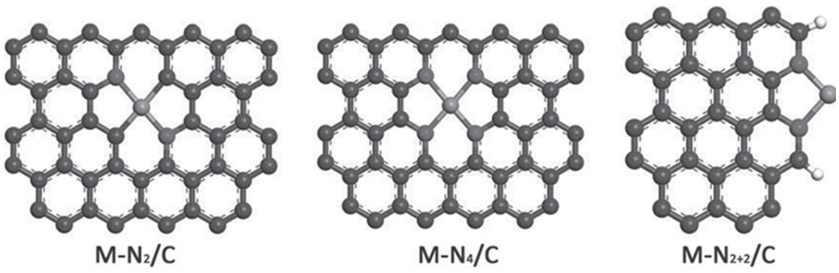

Figure 3. Representative molecular structures of $M-N_2/C$, $M-N_4/C$, $M-N_{2+2}/C$ respectively. Green: carbon; blue: nitrogen; yellow: transition metals (e.g., iron or cobalt). Reproduced from Ref. [33a] with permission. Copyright 2015, The Royal Society of Chemistry.

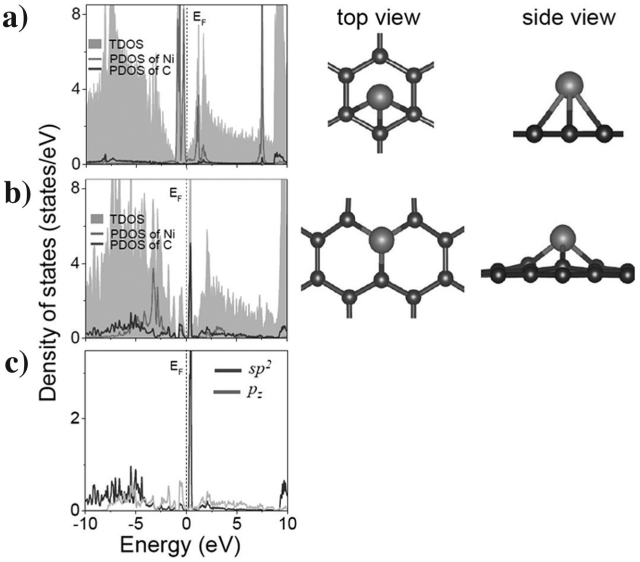

Figure 4. Left panel: DFT calculations of the total density of states (TDOS) and partial density of states (PDOS) projected onto the Ni atom (red lines) and the nearest neighboring C atoms (green lines) with optimized structures of Ni-doped graphene. a) Ni-absorbed at the hollow sites of graphene lattices, b) substitutional Ni at a carbon site in the graphene lattice and c) the orbital-dependent PDOS of the nearest neighboring C atoms in the Ni-doped graphene of b). Right panel: The local atomic structures of the Ni-absorbed (upper) and Ni-doped (lower) graphene. Blue and green balls denote the Ni and C atoms respectively. Reproduce from Ref. [40] with permission. Copyright 2015, Wiley–VCH.

mechanical stability, electronic behavior, low density, inertness and ability to tailor their structures.[42] The interplay between carbon-based supports and single metal atom dopants are known to be strong metal–support interactions (SMSIs).[43] This can modify the overall physicochemical and electronic structures of the resultant material as efficient catalysts with specific catalytic properties.[44] For example, N-doped carbon-based supports (e.g., N-graphene) are able to behave as an efficient macro-ligand. In this case, the individual metal atoms are anchored firmly by the surface species of the support such as pyridinic-type nitrogen atoms, which are sparsely distributed at selective sites (e.g., the open graphene edges).[45] This sparse distribution and SMSI prevents the single metal atom dopants from aggregation and forms stable catalysts at elevated temperatures. Therefore, the structure of the active site formed by intimate bonding and synergistic coupling effects between the single metal atom dopant and the carbon-based support is ideal for electrochemical reactions to proceed at high rates and with excellent durability.

As shown in **Figure 5**, Deng et al. suggested that the interaction between metal atom dopants with carbon-based supports may change their local work function. This was confirmed by UV laser enhanced photoemission electron microscopy (PEEM). Bright spots in the PEEM image corresponded to the metal dopants interacting with the support. This suggests a decreased work function at that region, which is in agreement with theoretical calculations. Therefore, the reduced local work function at the carbon surface at metal atom dopant sites is expected to enhance its chemical activity.[46]

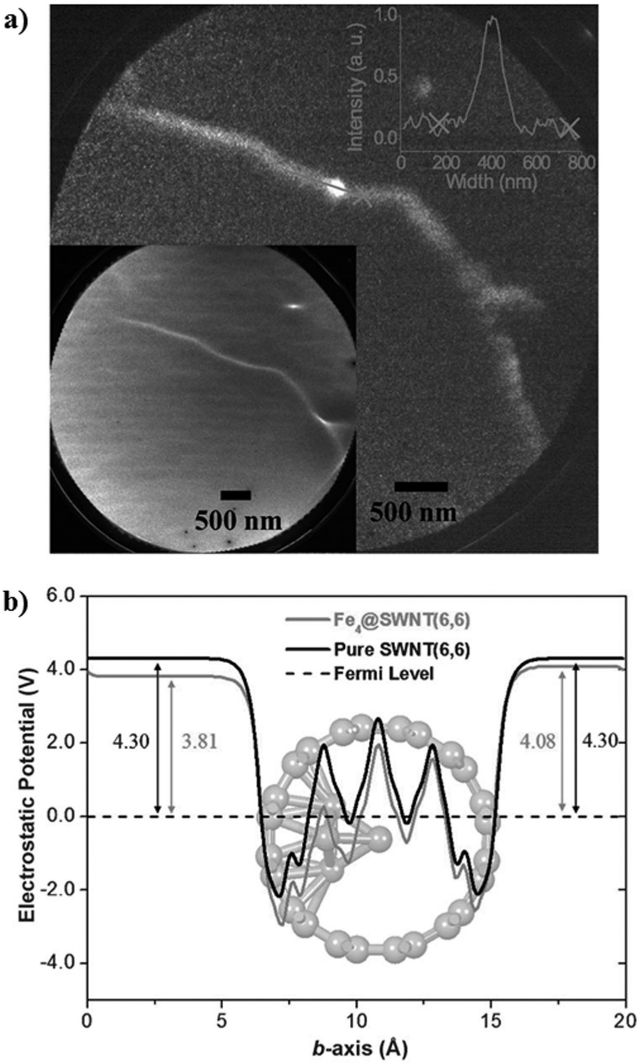

Figure 5. a) PEEM image of Pod-Fe with a laser start voltage of 1.7 V. The top inset showing the brightness profile along the green line. The bottom inset showing the corresponding LEEM image of the same region. b) The electrostatic potential profiles averaged on the plane perpendicular to the b-axis as a function of the b-axis of the supercell of Fe4@SWNT and pure SWNT respectively. The structure of Fe$_4$@SWNT is shown in the background. Reproduce from Ref. [46] with permission. Copyright 2013, Wiley–VCH.

It should also be noted that due to the chemical bonding of the single metal atoms on the supports and the properties of charged single atoms on supports, atomic active centers exhibit satisfactory stability under different (electro) chemical processes. For instance, there are a few reports which present that the stability of metal atom dopants on carbon-based supports is mostly due to the presence of nitrogen-containing chelating ligands which form stable metal-nitrogen-carbon (M-N-C) bonds.[38b,44b,47] Liu et al. reported the successful synthesis of a self-supporting Co–N–C catalyst with single-atom dispersion. A variety of analytical techniques provided compelling evidence that the cobalt atoms were coordinated with four pyridinic nitrogen atoms in the graphitic layer (Co-N$_4$), which formed the catalytic active structure for chemical transformation processes.[48]

Recently, Choi et al. developed single Pt atoms (with a relatively high concentration of 5 wt%) supported on zeolite-templated carbon (ZTC), containing a large amount (up to 17 wt%) of sulfur, for the production of H_2O_2 by electrochemical means in fuel cells.[49] Notably, the abundant S-functionalities and unique carbon structure lead to stabilization of the relatively high Pt loading in the form of atomically dispersed Pt. Interestingly, there are some reports claiming the unique triple-interaction of metal-oxide-metal-carbon based supports which exhibit higher stability and durability compared to the dual-interaction catalysts such as metal on carbon-based support and/or metal on metal oxide supports.[50]

3. Physicochemical Characterization of Single Atom Metal-doped Catalysts

The characterization of single metal atoms on carbon-based supports is an important factor which currently hinders the development of such catalysts. Various types of atomic resolution characterization techniques, which can precisely provide information regarding the location of the individual metal atoms on the support, are required.[23c,51] The vacancy of support and atomic structures of metal dopants can be characterized using aberration-corrected high angle annular dark field scanning transmission electron microscopy (HAADF-STEM). In addition, with the combination of state-of-the-art chemical characterization techniques and advanced modelling and simulation methods such as density functional theory (DFT), more in-depth information regarding the structure and properties of single metal atom supported on carbon-based materials can be investigated. The chemical characterization methods include X-ray spectroscopy techniques such as X-ray absorption near-edge structure (XANES), extended X-ray absorption fine structure (EXAFS) and X-ray photoelectron spectroscopy (XPS).

3.1. Electron Microscopy Imaging

The morphology of prepared metal atom doped catalysts is usually first examined by scanning electron microscopy (SEM) and transmission electron microscopy (TEM). SEM and TEM images reveal the morphological features of the resultant catalysts on the support, underscoring the atomic size of the metallic dopant. Therefore, to investigate the atomic structure of the single metal atoms on carbon-based supports, other high-resolution and precise imaging techniques need to be applied. For instance, Fei et al. conducted SEM and HAADF-STEM to find out structural information of the atomic cobalt on nitrogen doped graphene nanosheets (Co-NG). SEM and TEM images (**Figure 6**a,b) show the nanosheet structure of Co-NG without any bulk and aggregated cobalt-derived particles. The presence and the close proximity distributions of Co and N elements were further confirmed by the energy-dispersive X-ray spectroscopy (EDS) spectrum taken in the area shown in Figure 6c of the scanning transmission electron microscopy (STEM) image. In addition, the bright-field STEM image (Figure 6d)

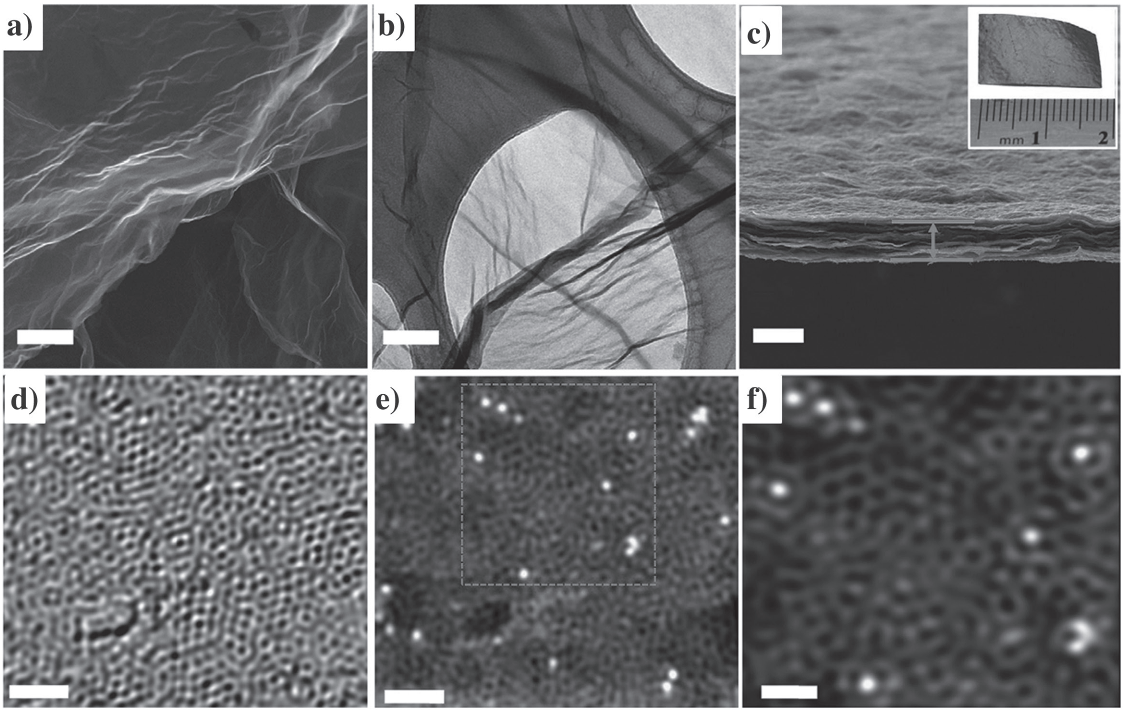

Figure 6. a) SEM image of the Co-NG nanosheets. Scale bar: 2 µm. b) TEM image of the Co-NG nanosheets. Scale bar: 50 nm. c) STEM image of the Co-NG nanosheet. Scale bar: 20 nm. Inset is the EDS elemental line scan from A to B showing the presence of C, N and Co elements. d) Bright-field aberration-corrected STEM image of the Co-NG showing the defective and disordered graphitic carbon structures. Scale bar: 1 nm. e) HAADF-STEM image of the Co-NG, showing many Co atoms well-dispersed in the carbon matrix. Scale bar: 1 nm. f) The enlarged view of the selected area in b. Scale bar: 0.5 nm. Reproduced with permissions from Ref. [45a]. Copyright 2015, Nature Publishing Group (NPG).

demonstrates the defective structure of graphitic carbon in Co-NG nanosheets. The corresponding HAADF image and enlarged view of selected sites (Figure 6e,f) confirm the presence of cobalt atoms well dispersed on the support framework in which each of the Co atoms is centered by the light elements such as carbon, nitrogen and/or oxygen.[45a]

The precise structural analysis of metal atom doped carbon-based materials can be obtained using aberration-corrected HRTEM as reported by Deng et al. High-resolution TEM, aberration-corrected HRTEM and HAADF-HRTEM images confirmed the homogenous dispersion of metal atoms (Fe atoms in this case) in the graphene matrix support, which is in good agreement with the selected area electron diffraction (SAED) pattern (**Figure 7**a-f). The electron energy loss spectroscopy (EELS) atomic spectra of the bright dots affirm the formation of Fe-N_x bonding in the graphene framework (Figure 7g). A low-temperature STM image of a single FeN_4 center in the graphene matrix suggests that the iron center modifies the density of state of adjacent atoms and that the FeN_4 center is in the graphitic plane and forms stable bonds with neighboring carbon atoms (Figure 7h,i).[52]

3.2. X-ray Spectroscopy

Theoretically, the atoms in different chemical environments have different characteristic energies which can be observed by some accurate energy spectroscopies. Therefore, the

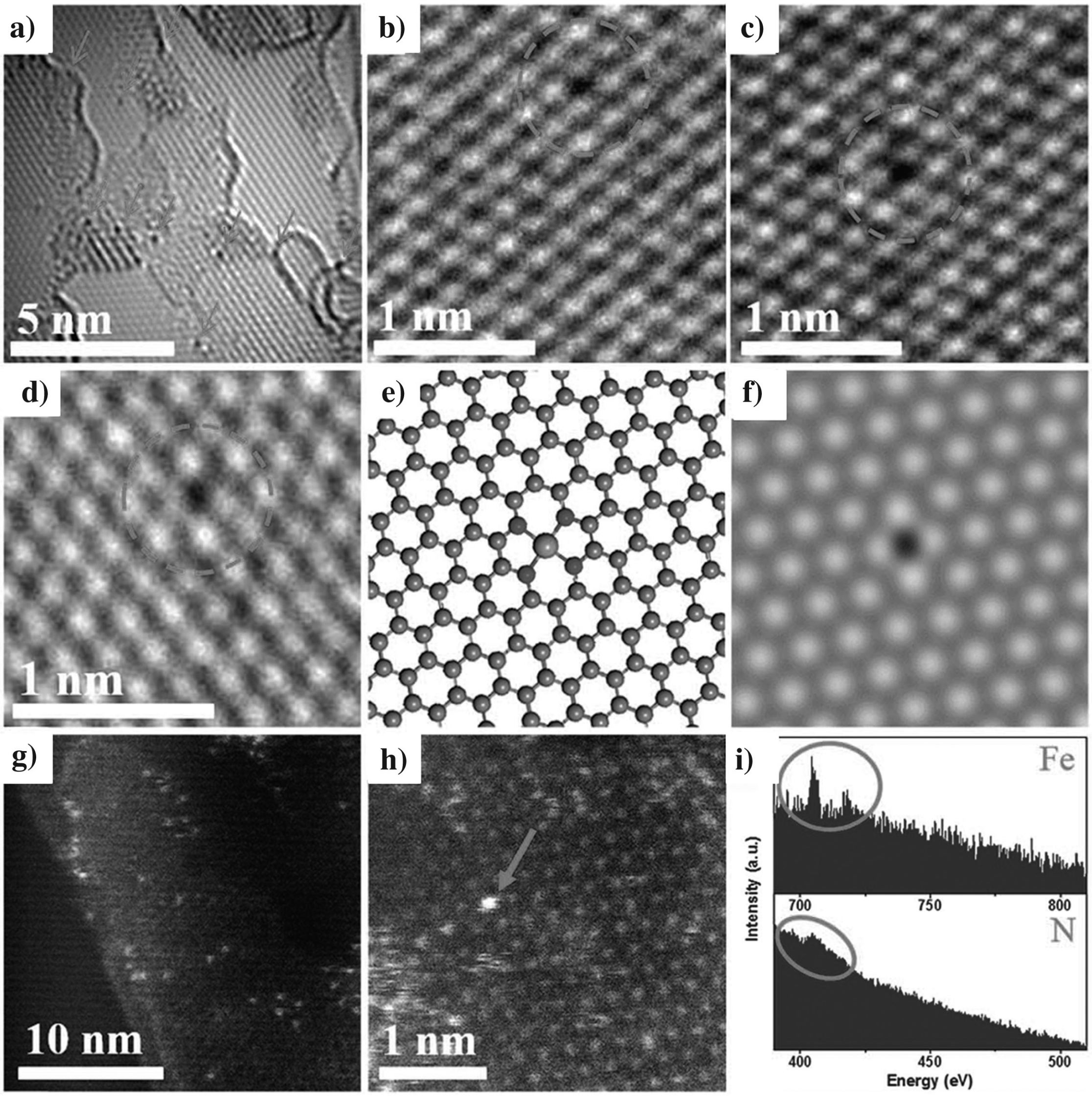

Figure 7. a–c) High-resolution transmission electron microscopy (HRTEM) images and (inset of c) corresponding selected area electron diffraction (SAED) pattern of FeN_4/GN. The area with arrows and the dashed circles shows some typical single Fe atoms in the nanosheets. d–f) High-angle annular dark-field scanning transmission electron microscopy (HAADF-STEM) images of FeN_4/GN. g) The electron energy loss spectroscopy (EELS) atomic spectra of Fe and N elements from the bright dots as shown by the red arrow in (f), h) Low-temperature scanning tunneling microscopy (LS-STM) image of FeN4/GN, measured at a bias of 1.0 V and a current of 0.3 nA (2 nm × 2 nm). i) Simulated STM image for (h). The inserted schematic structures represent the structure of the graphene-embedded FeN_4. The grey, blue, and light blue spheres represent C, N, and Fe atoms respectively. Reproduced with permissions from Ref. [52]. Copyright 2015, American Association for the Advancement of Science (AAAS).

chemical composition and coordination of elements in single metal atom doped carbon-based materials can be revealed by these precise analytical techniques. One of the common techniques used is X-ray photoelectron spectroscopy (XPS), by which, the valence state of the support and dopants are usually determined. However, the energy resolution of the XPS is not high enough to deconvolute every single chemical state, especially, in the case of low concentration elements/dopants in the catalyst materials. Thus, inductively coupled plasma (ICP) might be required in order to confirm XPS results.[44b] For instance, the composition of atomic cobalt doped N-graphene has been examined by XPS which showed the presence of C, N and O peaks in the Co-NG sample but no significant signal was found in the Co region due to the small amount of the cobalt species (**Figure 8**a). Thus, inductively coupled plasma optical emission spectroscopy (ICP-OES) was performed to quantify the elements present and confirmed the low content of the Co species (less than 1 at%) in Co-NG sample.[45a] High-resolution Co 2p and N 1s XPS spectra affirmed the formation of Co-N as a form of Pyridinic/N-Co species which could play an important role in the catalytic activity of the synthesized materials.

To achieve a higher energy resolution to further probe the chemical state and coordination structure of the confined single metal atoms, Synchrotron-radiated X-ray adsorption fine structure (XAFS) measurements, including XANES and EXAFS, have been performed. XANES is sensitive to charge transfer and orbital occupancy of the metal atoms; EXAFS could provide information on the distance between the central and neighboring atoms and the coordination number of the central atoms.[53] Deng et al. claimed that the valence state of atomic iron in N-doped graphene (FeN_4/GN) remained the same with the iron precursor resource as shown in the Fe K-edge of the XANES spectra (**Figure 9**a). The EXAFS of the Fe K-edge (Figure 9b) exhibited that the magnitude of the Fourier Transform (FT) spectra also closely resembles the reference curve of the iron precursor resource. Moreover, both the C K-edge and N K-edge XANES spectra further revealed that the Fe-N_4 centers were embedded into the graphene matrix as active centers for electrocatalysis.[52]

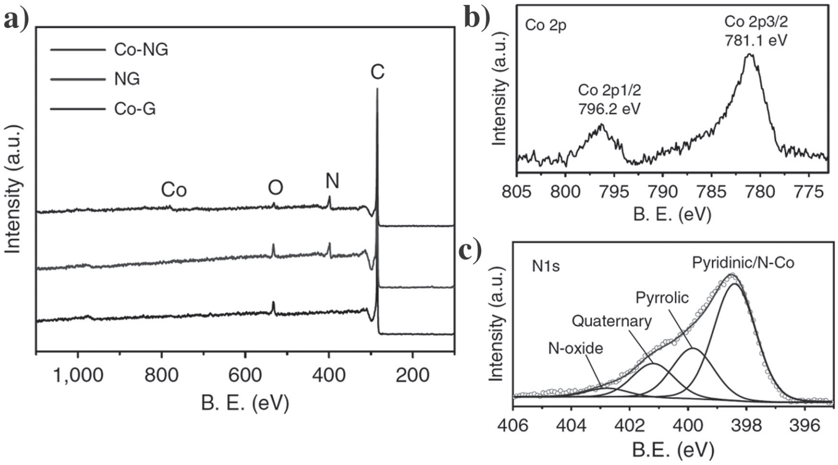

Figure 8. a) XPS survey spectra of the Co-NG, NG and Co-G. b,c) High-resolution XPS Co2p and N1s spectra respectively. Reproduced with permissions from Ref. [45a]. Copyright 2015, Nature Publishing Group (NPG).

Yin et al. also conducted XAFS measurements which revealed information regarding the atomic Co dopants in the support. The XANES spectra (**Figure 10**a) determined the valence state of the atomic Co to be between Co^0 and Co^{2+}, suggesting that the single Co sites possess a porphyrinic planner structure.[54] The FT spectra of EXAFS (Figure 10b-d) demonstrated that the Co atoms are atomically dispersed with a coordination number of Co-N_x ($x = 2$ or 4), varied by the pyrolysis temperature of the final product. The results also explain that the distance of adjacent Co atoms was varied and provided more free N sites facilitated by pre-mediated mixing of Zn. This prevented the formation of Co-Co and anchored the Co atoms to the N-doped carbon support after the evaporation of the Zn atoms.[55]

3.3. DFT Calculations and Modelling

Besides the physicochemical characterization of catalysts to investigate their physical structures and chemical compositions, some powerful computational methods such as density functional theory (DFT) are being developed to investigate catalyst properties at the atomic level. DFT is a powerful tool in revealing the catalytically active centers in order to help with the design of better electrocatalysts and discovering the electrochemical reaction mechanism.[56] In the case of single metal atom doped carbon-based materials, catalytic activity arises from the unique electronic structures that are attributed to the chemical interaction and location of the single metal dopants with the support,[57] as explained previously (Section 2.2 and 2.3). DFT calculations also help to study the electronic structure and electron transfer properties of the hybrid systems for a variety of applications. For instance, an atomic Fe dopant can be replaced with a carbon atom to have a better electron transport properties compared to the metal atom adsorbed at a vacant site on the surface of the carbon substrate. Such studies reveal information regarding the effect of heteroatom doping and their location dependency on the structural and electronic properties of (electro) catalysts. These originate from the nanoscale charge localizations in the hybrid system.[58]

Zhao et al. investigated different configuration of Fe atoms doped in graphene using first principal DFT calculations. In this study, the most stable configurations for single Fe atoms investigated were found to be at armchair or zigzag edges of the graphene framework, including an arrangement in which iron atoms replace the first two rows of carbon atoms at an open edge.[59] Qiu et al. also studied the electronic structure of single atom Ni-doped graphene sheets using DFT. The Ni dopants were presented in different positions and forms with different bonding energies. DFT calculations confirmed substitutional and anchored Ni atoms are energetically favorable for electrochemical reactions. Results also exhibited that the

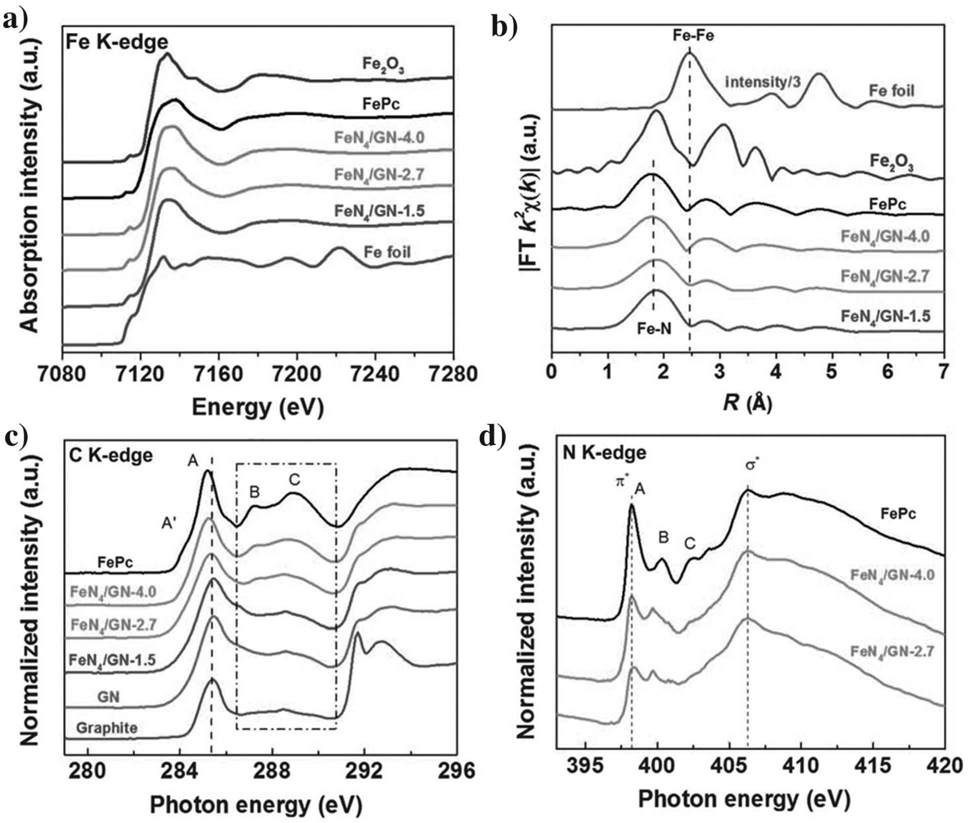

Figure 9. a) Fe K-edge X-ray absorption near-edge structure (XANES) and b) Fourier transform (FT) extended X-ray absorption fine structure (EXAFS) signals of FeN4/GN samples with various Fe content in comparison to FePc, Fe foil, and Fe2O3. c) C K-edge and d) N K-edge X-ray absorption spectroscopy (XAS) spectra of FeN4/GN samples with various Fe content in comparison to that of FePc. Reproduced with permission from Ref. [52]. Copyright 2015, American Association for the Advancement of Science (AAAS).

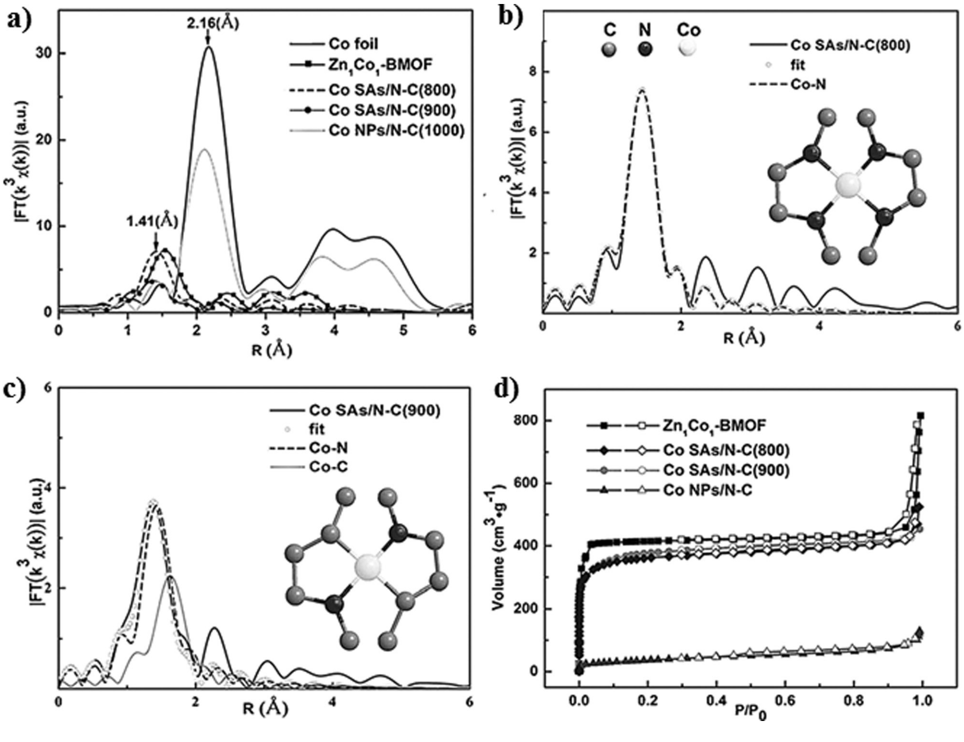

Figure 10. a) Co K-edge XANES spectra and b) the k3-weighted c(k)-function of the EXAFS spectra. The corresponding EXAFS fitting curves for the samples c) Co SAs/N-C(800) and d) Co SAs/N-C(900). Insets are the proposed Co-N$_x$ architectures. Reproduced from Ref. [55] with permission. Copyright 2016, Wiley–VCH.

optimized structure of substituted atomic Ni dopants lied out of graphene plane and that strong and stable Ni-C binding was formed (**Figure 11**a,b). Particularly, sp-d orbital-charge transfer between Ni and the surrounding C atoms results in an empty C-Ni hybrid orbital close to the Fermi level energy which makes Ni-C a catalytic active site (Figure 11c,d).[40]

Moreover, Deng et al. investigated the formation energy of FeN_4 centers in graphene matrices and found that it is significantly lower compared to doping single Fe atoms in pristine graphene. This confirms the important anchoring role of N atoms in order to stabilize Fe into graphene (**Figure 12**a). The combination of experimental results (e,g. XANES and EXAFS) and DFT calculations indicated that the FeN_4 centers play an important role as catalytic active sites towards Benzene oxidation (Figure 12b).[52] Recently, Yan et al. studied the ORR catalytic activity of carbon nanofibers doped with transition metals (TM = Fe or Co) and nitrogen (N) in both Acidic and Alkaline electrolyte. The advanced electron microscopy images at the atomic scale and DFT calculations revealed that the ORR active sites in these catalysts were the TM–N_4 clusters embedded between two graphene edges and the pyridinic nitrogen derived carbon atoms, which supports previous studies on the unique electronic structures of such hybrid systems.[60]

Until now, only a few reports exist about theoretical studies on atomic metal-doped carbons for (electro)catalysis. However, accurate assessment of the catalytic sites resulting from single metal atoms in doped carbon electrocatalysts requires further in-depth study.

4. Various Active Atomic Metal-doped (Electro)-Catalysts for Energy Storage and Conversion

Individual and isolated metal atoms anchored to the support are known as active centers in single atom (electro)-catalysts. These types of catalysts have high activities and enable the utmost utilization of the supported metals (noble

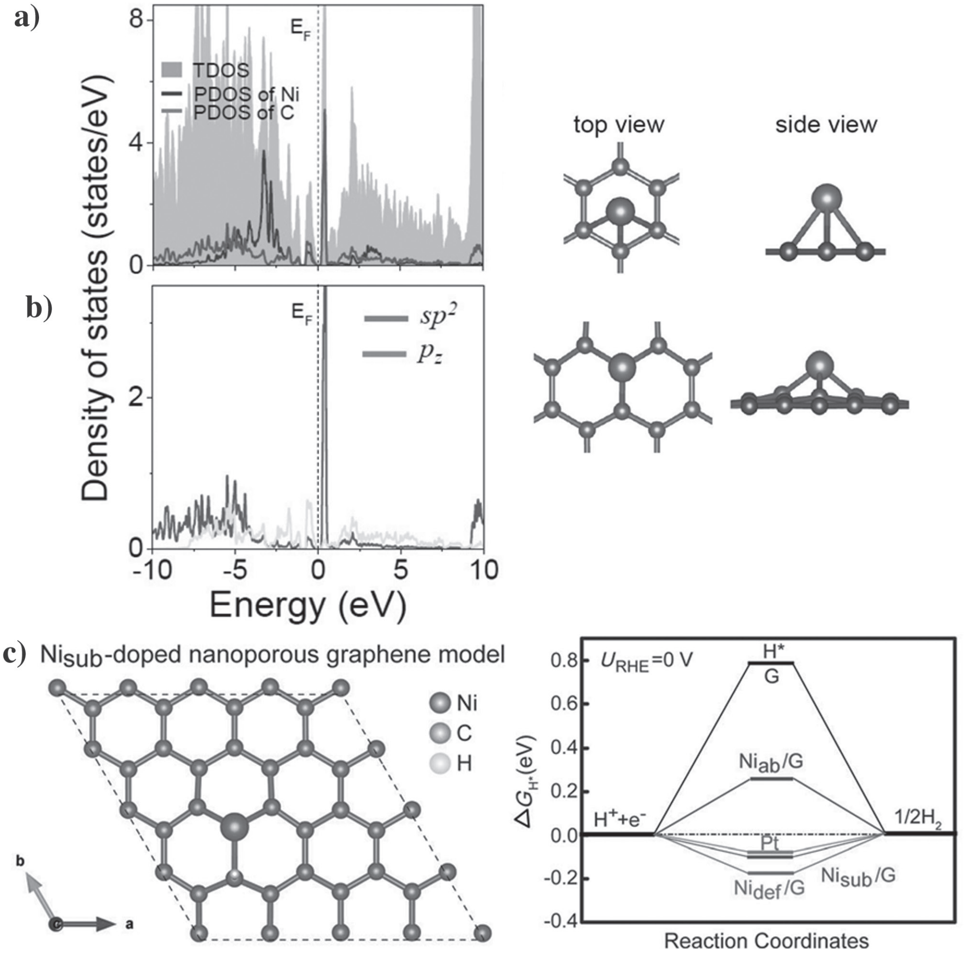

Figure 11. Left panel: DFT calculations of total density of states (TDOS) and partial density of states (PDOS) projected onto the Ni atom (red lines) and the nearest neighboring C atoms (green lines) with optimized structures of Ni-doped graphene; a) Substitutional Ni at a carbon site in the graphene lattice and b) the orbital-dependent PDOS of the nearest neighboring C atoms in the Ni-doped graphene of (a). Right panel: the local atomic structures of the Ni-absorbed (upper) and Ni-doped (lower) graphene. The blue and green spheres represent the Ni and C atoms respectively. c) Hydrogen adsorption sites and configuration of the Nisub/G model with ΔGH* = 0.10 eV (left) and calculated Gibbs free energy diagram (right) of the HER at equilibrium potential for a Pt catalyst and Ni-doped graphene (Niab/G, Nisub/G, and Nidef/G) samples. The free energies for hydrogen adsorption on pristine graphene and Pt metal are plotted for comparison, with ΔGH* = 0.79 and 0.09 eV respectively. Reproduced from Ref. [40] with permission. Copyright 2015, Wiley–VCH.

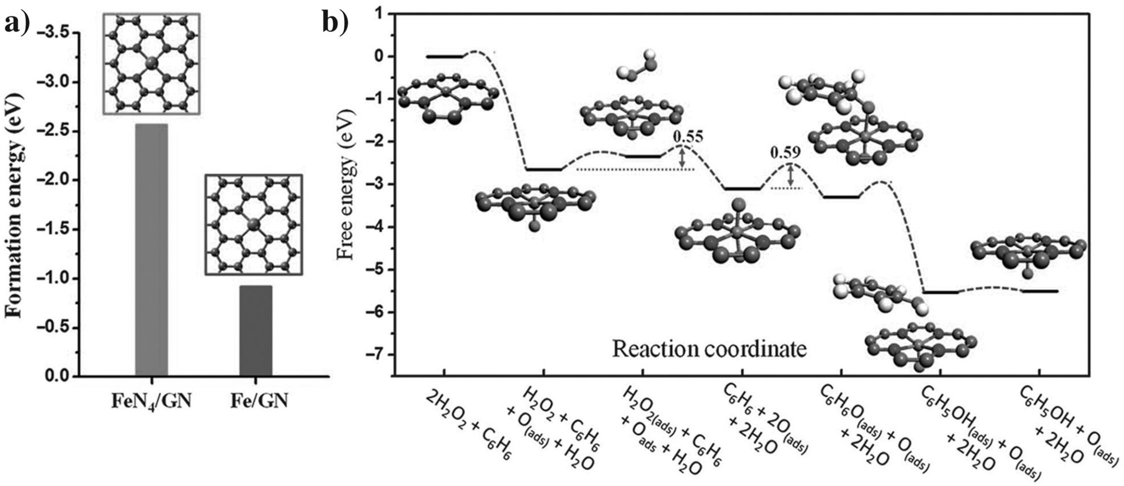

Figure 12. a) The formation energies of FeN$_4$/GN and Fe/GN structures. The formation energy is calculated as follows: $E_{\text{Fe-embedded}} - E_{\text{Fe-bulk}} - E_{\text{(N)GN}}$, where $E_{\text{Fe-embedded}}$ and $E_{\text{Fe-bulk}}$ are the total energies of FeN$_4$/GN and the Fe/GN structure and a Fe atom in Fe bulk respectively, and $E_{\text{(N)GN}}$ is the total energy of the optimized structure of FeN$_4$/GN or Fe/GN with the Fe atom removed from the system. b) Free energy diagram of the oxidation of benzene to phenol on FeN$_4$/NG. The grey, blue, light blue, red, and white spheres represent C, N, Fe, O, and H atoms respectively. Reproduced with permission from Ref. [52]. Copyright 2015, American Association for the Advancement of Science (AAAS).

or non-precious metals) with superior selectivity towards a range of reactions (**Table 1**). Below, we briefly discuss some results from various active single metal atoms doped on carbon-based materials for (electro)catalysis. These examples open a new area of investigation for the precise design of efficient (electro)catalysts in the future.

4.1. Co-doped Carbon Materials

Cobalt doped carbon-based catalysts have been long studied for electrocatalysis. The reason for this is due to the low cost of cobalt species as well as their ability to perform well in both alkaline and acidic electrolytes.[61] Notably, the electrocatalytic performance of metal free carbon-based materials has been improved significantly by cobalt doping. Specifically, Co-N-C composites have been extensively studied as efficient electrocatalysts for the ORR, OER and HER. In these types of materials, the synergistic effect between the incorporated cobalt and nitrogen dopants results in enhanced electrocatalytic activity.[62] Moreover, the cobalt nanoparticles can be protected by the carbon layers in these materials which enable them to remain active over a wide range of pH.[63] Liang et al. developed molecular Co-N$_x$ centers in porous carbon for the HER in both acidic and alkaline electrolytes. It was claimed that the simultaneous incorporation of nitrogen and cobalt into carbon, forming CoN$_x$/C, led to improved HER performance as reflected by a large shift in the polarization curve to a lower overpotential compared with cobalt free (N/C) and nitrogen-free (Co/C) catalysts (**Figure 13**).[64] In addition, Giri et al. reported an improved capacitive behavior and lower electrical resistance compared to HCl doped PANI (DPANI)/MWCNT in supercapacitor applications. Such high performance and exceptional power were attributed to the redox reaction in cobalt-doped polyaniline in the presence of MWCNT, which lead to the

Table 1. Summary of atomic metal-doped carbon based materials for (electro)catalysis.

Materials	Synthesis Method/Metal precursor	Application	Active center	Activity	Refs.
CoN$_x$/C	Wet chemistry/Co-oPD & CoTMP	HER	Co-N$_x$	Comparable	[64]
Co-NG	Wet chemistry/CoCl$_2$.6H$_2$O	HER	Co-N$_x$	Comparable	[45a]
Co SAs/N-C	Wet chemistry/(Zn/Co)MOF	ORR	Co-N$_x$	Better	[55]
FeN$_x$/C	Wet chemistry/FeTPPC1	ORR	Fe–N$_x$	Better	[68]
FeN$_4$/GN	Wet chemistry/FePC	Oxidation of Benzene	Fe–N$_4$	Better than Fe/NG	[52]
Ni-doped graphene	CVD/Ni-substrate	HER	Ni-C	Comparable	[40]
M-g-C$_3$N$_4$	Wet chemistry/MCl$_2$.xH$_2$O	ORR/OER	M-N$_2$	Comparable	[69]
Nb-C	Arc-discharge approach	ORR	Nb-C	Better	[70]
Pt/N-CNFs		Formic acid decomposition	Pt-N$_2$	Better	[38b]
Pt-GNS	ALD/MeCpPtMe$_3$	Methanol oxidation	Pt-O	Better	[17b]
[Ir(C$_2$H$_4$)$_2$]/zeolite Y	Wet chemistry/Ir(C$_2$H$_4$)$_2$	Cyclohexene hydrogenation	Ir$_4$	Comparable	[51c]
Au/ZnO	Wet chemistry/HAuCl$_4$	Hydrogenation of Butadine	Au	Comparable	[71b]

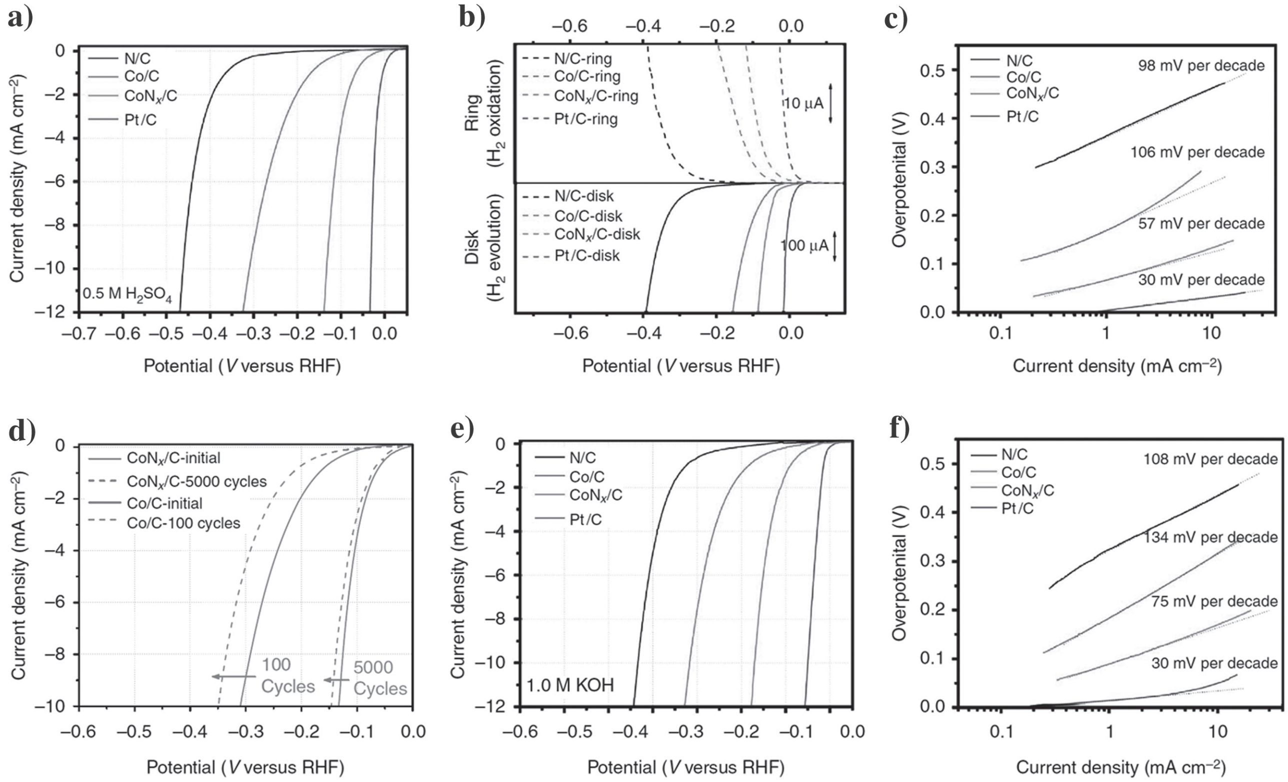

Figure 13. a) HER polarization plots of the CoN$_x$/C, N/C, Co/N, and Pt/C catalysts in 0.5 M H$_2$SO$_4$. b) RRDE measurements of hydrogen evolution from a 0.5 M H$_2$SO$_4$ solution on different catalyst-modified electrodes. The Pt-ring electrode was maintained at 0.7 V for the oxidation of the H$_2$ that was evolved on the disk electrode. c) Tafel plots obtained from the polarization curves in (a). d) Initial and post-potential cyclic voltammograms of CoN$_x$/C (5000 cycles) and Co/N (100 cycles) in 0.5 M H$_2$SO$_4$. Potential sweeps were cycled between 0.2 and 0.25 V versus RHE (not iR-corrected). e) HER polarization plots of CoN$_x$/C, N/C, Co/N, and Pt/C catalysts in 1.0 M KOH. f) Tafel plots obtained from the polarization curves in (c). For all RDE and RRDE measurements, the catalyst loading was 2.0 mg cm^{-2} for non-Pt materials and 0.2 mg cm^{-2} (40 μgPt cm^{-2}) for the Pt/C catalyst. For CoN$_x$/C catalysts, the cobalt loading is only 2.8 μgCo cm^{-2}, based on the ICP-AES measurements. Electrode rotational speed: 1600 rpm; scan rate: 5 mVs^{-1}. Reproduced with permission from Ref. [64]. Copyright 2015, Nature Publishing Group (NPG).

greater accumulation of charge with an increment in doping level.[65]

Fei et al. reported an electrocatalyst for hydrogen evolution based on small amounts of cobalt dispersed as individual atoms on N-doped graphene. Thus, N-C species coupling with a single cobalt atom exhibited high catalytic activity towards the HER in acidic media with very low overpotential (**Figure 14**a,b). The single cobalt atoms enhanced the HER activity in pure graphene and further improved the catalytic activity of N-doped graphene, which is attributed to the active centers associated with the metal centers coordinated to nitrogen.[45a] Furthermore, single cobalt atoms anchored on N-doped carbon-based materials, as reported by Yin et al., demonstrated outstanding ORR activity in alkaline media which outperformed commercial Pt/C (Figure 14c,d).[55] Therefore, this unusual atomic composition of supported cobalt is suggestive of a new approach to preparing highly efficient single atom catalysts for a variety of electrochemical reactions.

4.2. Fe-doped Carbon Materials

Iron is another popular transition metal species with low cost and good catalytic performance. Fe metal-ion centers have been found to display optimal electrocatalytic properties, attributed to its distinct redox properties, and have been proposed as the active sites for a variety of electrochemical reactions, specifically the ORR.[66] This has been adequately studied and explained; the efficient ORR catalytic activity of such Fe-doped catalysts is mostly attributed to the presence of Fe ions coordinated by four nitrogen atoms.[67] It should be noted that while a focus should be maintained on the development of Fe-N$_x$/C catalysts being the active centers, it is possible to tune the electronic and structural properties of these active sites in order to enhance the electrochemical reaction kinetics.[33b,42b] Ramaswamy et al. stated that it is energetically necessary to form Fe-N$_x$ centers in carbon-supported materials, which have been proven to be highly active and stable for ORR electrocatalytic performance.[68]

Li et al. developed an ORR electrocatalyst based on carbon nanotube–graphene complexes with a very small amount of iron and nitrogen impurities. The resultant material exhibited a high activity, excellent tolerance to methanol and superior stability in comparison to other non-precious metal catalysts in both acidic and alkaline solutions which might be attributed to the iron-containing catalytic sites (**Figure 15**). The distribution of iron and nitrogen atoms on the atomic scale has also been investigated.[11d] From this, it has been frequently observed that iron atoms exist on

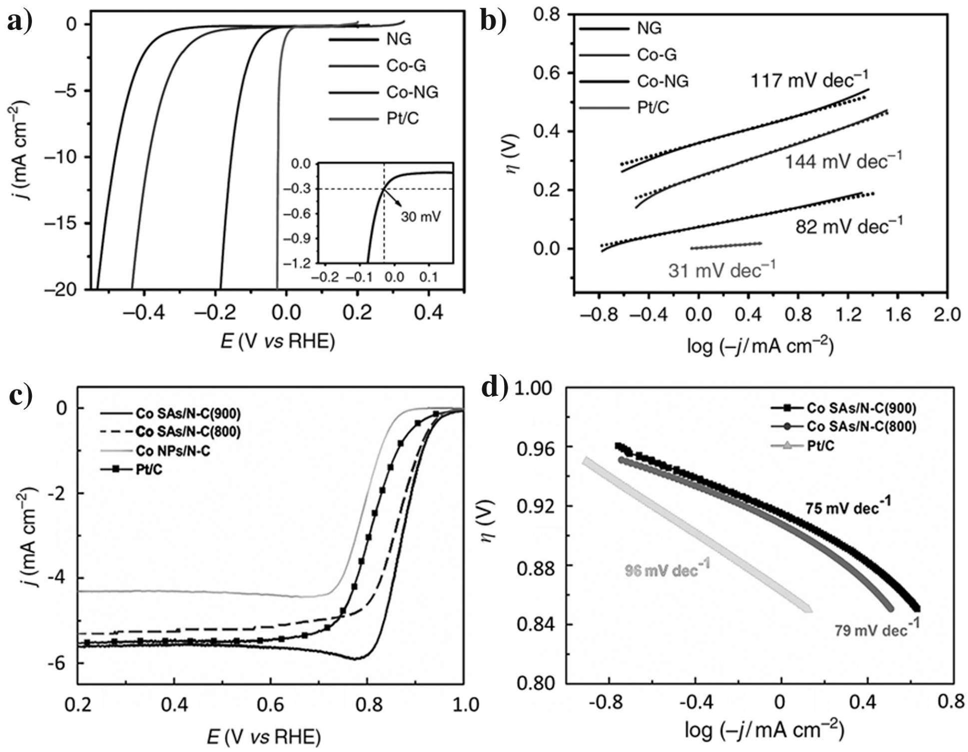

Figure 14. a) LSV of NG, Co-G, Co-NG and Pt/C in 0.5 M H_2SO_4 at a scan rate of 2 mV s^{-1}. The inset shows the enlarged view of the LSV for the Co-NG near the onset region. b) Tafel plots of the polarization curves. Reproduced with permissions from Ref. [45a] Copyright 2015 Nature Publishing Group (NPG). c) RDE polarization curves of Co SAs/N-C, Co NPs-N/C, and Pt/C in O_2-saturated 0.1 M KOH with a sweep rate of 10 mV s^{-1} and 1600 rpm. d) Corresponding Tafel plots obtained from the RDE polarization curves. Reproduced from Ref. [55] with permission. Copyright 2016, Wiley–VCH.

the edges of graphene sheets in close proximity to nitrogen species.

Moreover, Deng et al. fabricated a new single iron site confined in an N-graphene matrix which exhibited high activity and selectivity for the catalytic oxidation of Benzene at room temperature. This could also be explained by the availability of a moderate amount and homogenous dispersion of FeN_4 centers in graphene and their bonding with the graphene.[52]

4.3. Other Transition Metal-doped Carbon Materials

Besides cobalt and iron, other transition metal atom doped catalysts, such as nickel and niobium supported by carbon-based materials, have been studied for catalysis. Zheng et al. developed a range of molecule-level graphitic carbon nitride coordinated transition metals ($M–C_3N_4$; M = Cr, Mn, Fe, Co, Ni, Cu, Zn) as a new generation of M–N/C catalysts for the oxygen electrode reactions. Experimental studies combined with DFT computation demonstrated that Co, Fe and Ni with g-C_3N_4 ligand exhibited the strongest binding energies and highest structural stability compared to other fabricated transition metal based catalysts. Moreover, Co–C_3N_4/CNT possesses comparable activities with precious metal benchmarks for the ORR and OER in alkaline media in which the active sites are identified as Co–N_2 coordination moiety in the g-C_3N_4 matrix.[69] Qiu et al. claimed that, compared to commercial Pt/C and other reported catalysts, atomic nickel doped graphene has good HER activity with small overpotential and Tafel slope in acidic electrolyte. The origin of this performance was found to originate from the strong interaction of the Ni substitutes in the carbon framework (**Figure 16**).[40] Zhang et al. reported the formation of abundant single niobium atoms incorporated into onion-like carbon shells which exhibited high electrocatalytic activity and selectivity towards the ORR. It was deduced that the superior 4e$^-$ ORR catalytic characteristics of niobium atoms in carbon was mainly due to the presence and stability of a large number of single niobium atoms.[70]

4.4. Noble Metal-doped Carbon Materials

Atomically dispersed noble metal catalysts have attracted research attention due to their excellent catalytic performance and high atom efficiency at relatively low cost.[17a,71] There are some reports available on single noble metal atoms doped on carbon-based supports for catalysis. Single noble metal atom doped catalysts are considered “atom-efficient” because they allow the use of all active atoms in the catalytic reaction, in contrast to catalysts with metallic nanoparticles where a significant proportion of the expensive metal is inaccessible for catalysis.[31a,71c,72] Bulushev et al. claimed that the homogeneous precipitation of single Pt, Pd or Ru atoms onto N-doped carbon nanofibers (NCNFs) greatly improves the catalytic performance of the resultant material towards the selective production of H_2 from formic acid, in comparison to

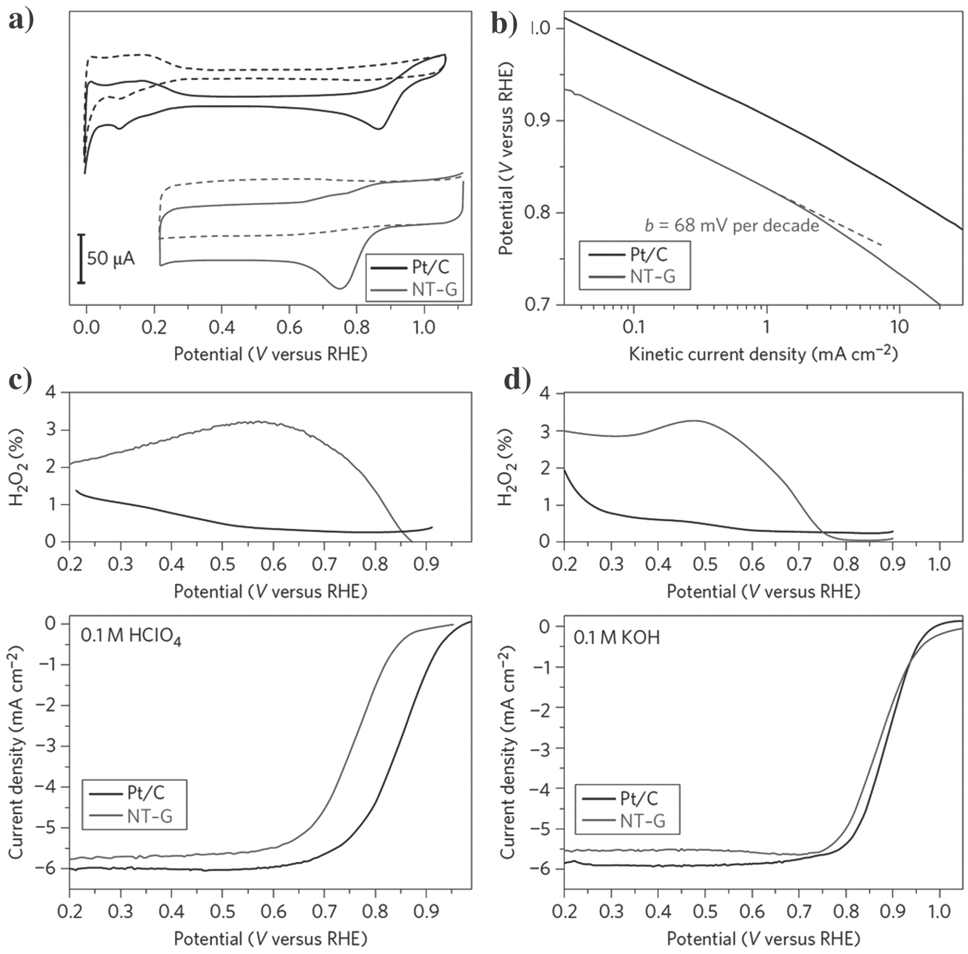

Figure 15. a) CVs of commercial 20% Pt/C (black) and NT–G (red) catalysts in O_2-saturated (solid) or argon-saturated (dotted) 0.1 M $HClO_4$. b) RRDE polarization curves and peroxide yield of Pt/C (black) and NT–G (red) in O_2-saturated 0.1 M $HClO_4$. c) Kinetic current densities versus potential derived from the mass transport correction of the corresponding RRDE disk currents in (b). d) RRDE polarization curves and peroxide yield of Pt/C (black) and NT–G (red) in O_2-saturated 0.1 M KOH. NT–G exhibits high ORR electrocatalytic activity in both acidic and alkaline electrolytes. For all the RRDE measurements, the loading of catalysts is 16 mgPt cm^{-2} for Pt/C and 0.485 mg cm^{-2} for NT–G. Electrode rotational speed: 1600 rpm; scan rate: 5 mV s^{-1}. Platinum data were collected from anodic sweeps. Reproduced with permissions from Ref. [11d]. Copyright 2012, Nature Publishing Group (NPG).

the properties of the same noble metals on N-free CNFs.[38b] This could be due to the fact that the N-doped CNFs are able to behave as an efficient macro-ligand, which strongly anchors the individual metal atoms via pyridinic nitrogen atoms located at the open edges leading to catalyst stability, whereas the structure of the active site formed proves ideal for catalysis applications.

Sun et al. also reported a practical synthesis method for isolated single Pt atoms anchored to graphene nanosheets via the ALD technique. The resultant catalyst exhibited significantly improved catalytic activity towards methanol oxidation and superior CO tolerance compared to conventional Pt/C catalysts. The lower coordinated and unsaturated 5d orbitals of the single Pt atoms were found to be responsible for this excellent electrochemical performance, as revealed by XAFS analyses.[17b] Another successful example at the lab scale includes the well-defined monatomic iridium complex supported within the supercages of a zeolite (Ir_1/zeolite Y) which is reported by Bayram et al. as the catalytically active species for hydrogenation of cyclohexene.[51c] Zhang et al. claimed that isolated Au^{3+} on zirconia supports are obtained by loading a small amount of gold which is highly active for the selective hydrogenation of butadine to buthane.[71b]

5. Summary and Future Challenges

We have summarized the unique structural features, synthesis approaches, state-of-the-art characterization techniques, and potential applications of single metal atoms doped in carbon-based materials for electrocatalysis. In these types of materials, the size of the metal dopants is reduced to single atoms which leads to enhanced catalytic performance due to the low-coordination environment, single atomic and quantum size effect and improved metal-support interactions. Notably, single metal atoms doped in carbon-based materials with well-defined and atomically dispersed metal atoms on these supports can maximize the metal utilization efficiency, when acting as the active centers. Moreover, single

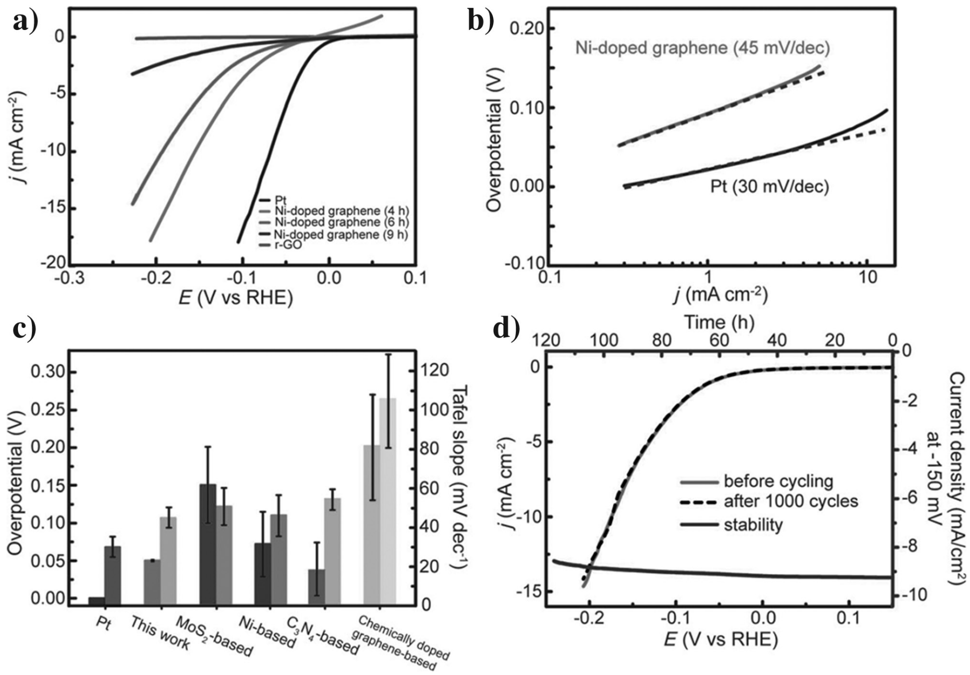

Figure 16. a) Polarization curves of Ni-doped graphene samples with different Ni dissolution periods (4, 6 and 9 h) along with those of Pt and reduced graphene oxide (r-GO) electrodes for comparison. b) Tafel plots of Ni-doped graphene (6 h dissolution) and Pt. c) Overpotential (left) and Tafel slope (right) analysis of different HER catalysts in acid solutions. d) Durability of Ni-doped graphene at a constant overpotential of 150 mV for 120 h (green line) and cycling stability tests (red line: polarization curve of pristine Ni-doped graphene (6 h dissolution); black dashed line: after 1000 cycles). Reproduce from Ref. [40] with permission. Copyright 2015, Wily–VCH.

metal atom doped carbon-based materials can act as a simple model system for comparison of theoretical calculations with experimental results. In these types of catalysts, carbon-based supports act in a similar way as ligands for metal active sites and serve as the active centers for electrocatalysis. The utilization of single metal atom doping on carbon-based supports provides vast opportunities for catalytic applications. Thus, the future direction of the development of these catalysts should focus on the fundamental studies of electrocatalysis at the molecular scale by the combination of theoretical and experimental methods. In addition, emphasis should be placed on the utilization of various characterization techniques to confirm the active sites and to observe the reaction processes. With a deep understanding of the nature of single atom catalysis, we believe that this new series of nanostructured materials could shed new light on the molecular design of the next generation of electrocatalysts for high-performance energy storage and conversion devices.

Many exciting research contributions are highlighted in this Review paper to illustrate the important applications of single metal atoms supported on carbon-based nanomaterials. Specifically, different aspects in this field have been discussed, which include the synthesis strategies and analytical techniques in order to develop new single metal-doped carbon-based nanoelectrode materials for energy storage and conversion devices. With all the successes in this field, many new synthesis routes and applications are emerging. It is clear from the many examples discussed in this Review paper that the synthesis of single metal atoms doped on carbon-based supports still presents significant conceptual challenges, where most methods used involve multi-step approaches and work successfully only for specific conditions. For instance, these types of materials must not be considered to be superior to conventional nanostructured catalysts since the single atom metal sites may limit their application in catalytic processes requiring multi-metal active sites. In addition, the control over functionality, size, shape, and structure is worth further exploration. From this, new or enhanced properties and the prevention of aggregation (due to the large surface energy of single metal atoms) of small clusters and atomic dopants in the case of high metal loadings may be achieved. Furthermore, it is very important to develop new techniques for robust stabilization of the single atoms on the support, especially when confronting liquid reactants, as well a profound ability to tune the strong metal–support interactions involved in this group of the electrocatalyst. Although recent works have provided significant insight into the physiochemical behavior and interactions of single metals and supports, however, the electrochemical reaction mechanisms and the electrocatalytic behavior of these materials are still unknown. Consequently, this requires an in-depth study into these novel electrocatalysts by means of both theoretical and experimental studies in order to facilitate their large scale application in the near future.

Acknowledgements

B.B. and Y.Z. contribute equally to this work. We gratefully acknowledge the financial support by the Australian Research Council

(ARC) through the Discovery Project programs (DP140104062, DP160104866, DP170104464, and DE160101163).

Conflict of Interest

The authors declare no conflict of interest.

---

[1] a) W. Tong, A. West, K. Cheung, K.-M. Yu, S. C. E. Tsang, *ACS Catal.* **2013**, *3*, 1231; b) J. L. Fillol, Z. Codolà, I. Garcia-Bosch, L. Gómez, J. J. Pla, M. Costas, *Nat. Chem.* **2011**, *3*, 807; c) S. Chu, A. Majumdar, *Nature* **2012**, *488*, 294.

[2] a) I. Dincer, *Renew. Sustainable Energy Rev.* **2000**, *4*, 157; b) A. Sharma, V. V. Tyagi, C. R. Chen, D. Buddhi, *Renew. Sustainable Energy Rev.* **2009**, *13*, 318; c) J. Ben-Iwo, V. Manovic, P. Longhurst, *Renew. Sustainable Energy Rev.* **2016**, *63*, 172; d) R. Baños, F. Manzano-Agugliaro, F. G. Montoya, C. Gil, A. Alcayde, J. Gómez, *Renew. Sustainable Energy Rev.* **2011**, *15*, 1753; e) N. Kannan, D. Vakeesan, *Renew. Sustainable Energy Rev.* **2016**, *62*, 1092; f) A. Cherubini, A. Papini, R. Vertechy, M. Fontana, *Renew. Sustainable Energy Rev.* **2015**, *51*, 1461; g) A. Ambrosi, C. K. Chua, A. Bonanni, M. Pumera, *Chem. Rev.* **2014**, *114*, 7150.

[3] a) G.-F. Chen, T. Y. Ma, Z.-Q. Liu, N. Li, Y.-Z. Su, K. Davey, S.-Z. Qiao, *Adv. Funct. Mater.* **2016**, *26*, 3314; b) B. Dunn, H. Kamath, J.-M. Tarascon, *Science* **2011**, *334*, 928.

[4] a) M. Armand, J. M. Tarascon, *Nature* **2008**, *451*, 652; b) B. Bayatsarmadi, Y. Zheng, M. Jaroniec, S. Z. Qiao, *Chem. Asian J.* **2015**, *10*, 1546.

[5] a) M. G. Walter, E. L. Warren, J. R. McKone, S. W. Boettcher, Q. Mi, E. A. Santori, N. S. Lewis, *Chem. Rev.* **2010**, *110*, 6446; b) A. Kudo, Y. Miseki, *Chem. Soc. Rev.* **2009**, *38*, 253.

[6] N. M. Marković T. J. Schmidt, V. Stamenković P. N. Ross, *Fuel Cells* **2001**, *1*, 105.

[7] M. Cifrain, K. Kordesch, in *Handbook of Fuel Cells*, John Wiley & Sons, Ltd, Chichester, UK **2010**.

[8] a) W. Sheng, A. P. Bivens, M. Myint, Z. Zhuang, R. V. Forest, Q. Fang, J. G. Chen, Y. Yan, *Energy Environ. Sci.* **2014**, *7*, 1719; b) J. Zhang, Z. Xia, L. Dai, *Sci. Adv.* **2015**, *1*, 1500564; c) M. S. Faber, S. Jin, *Energy Environ. Sci.* **2014**, *7*, 3519.

[9] Y. Liang, Y. Li, H. Wang, H. Dai, *J. Am. Chem. Soc.* **2013**, *135*, 2013.

[10] a) K. Gong, F. Du, Z. Xia, M. Durstock, L. Dai, *Science* **2009**, *323*, 760; b) K. Ai, Y. Liu, C. Ruan, L. Lu, G. Lu, *Adv. Mater.* **2013**, *25*, 998; c) S. Wang, L. Zhang, Z. Xia, A. Roy, D. W. Chang, J.-B. Baek, L. Dai, *Angew. Chem. Int. Ed.* **2012**, *51*, 4209; d) I.-Y. Jeon, S. Zhang, L. Zhang, H.-J. Choi, J.-M. Seo, Z. Xia, L. Dai, J.-B. Baek, *Adv. Mater.* **2013**, *25*, 6138; e) W. Wei, Y. Tao, W. Lv, F.-Y. Su, L. Ke, J. Li, D.-W. Wang, B. Li, F. Kang, Q.-H. Yang, *Sci. Rep.* **2014**, *4*, 6289.

[11] a) Y. Jiao, Y. Zheng, M. Jaroniec, S. Z. Qiao, *J. Am. Chem. Soc.* **2014**, *136*, 4394; b) R. Liu, D. Wu, X. Feng, K. Müllen, *Angew. Chem. Int. Ed.* **2010**, *122*, 2619; c) W. Qi, W. Liu, B. Zhang, X. Gu, X. Guo, D. Su, *Angew. Chem. Int. Ed.* **2013**, *52*, 14224; d) Y. Li, W. Zhou, H. Wang, L. Xie, Y. Liang, F. Wei, J.-C. Idrobo, S. J. Pennycook, H. Dai, *Nat. Nanotechnol.* **2012**, *7*, 394.

[12] a) K. Qu, Y. Zheng, S. Dai, S. Z. Qiao, *Nano Energy* **2016**, *19*, 373; b) J. Duan, S. Chen, M. Jaroniec, S. Z. Qiao, *ACS Nano* **2015**, *9*, 931; c) Y. Zheng, Y. Jiao, L. H. Li, T. Xing, Y. Chen, M. Jaroniec, S. Z. Qiao, *ACS Nano* **2014**, *8*, 5290; d) J. Zhang, Z. Zhao, Z. Xia, L. Dai, *Nat. Nanotechnol.* **2015**, *10*, 444; e) J. Zhang, L. Qu, G. Shi, J. Liu, J. Chen, L. Dai, *Angew. Chem. Int. Ed.* **2016**, *55*, 2230.

[13] a) T. R. Cook, D. K. Dogutan, S. Y. Reece, Y. Surendranath, T. S. Teets, D. G. Nocera, *Chem. Rev.* **2010**, *110*, 6474; b) J. Zhuo, T. Wang, G. Zhang, L. Liu, L. Gan, M. Li, *Angew. Chem. Int. Ed.* **2013**, *52*, 10867; c) M. A. Lukowski, A. S. Daniel, F. Meng, A. Forticaux, L. Li, S. Jin, *J. Am. Chem. Soc.* **2013**, *135*, 10274; d) B. E. Conway, B. V. Tilak, *Electrochim. Acta* **2002**, *47*, 3571; e) D. Hou, W. Zhou, K. Zhou, Y. Zhou, J. Zhong, L. Yang, J. Lu, G. Li, S. Chen, *J. Mater. Chem. A.* **2015**, *3*, 15962; f) K. Elumeeva, J. Ren, M. Antonietti, T.-P. Fellinger, *ChemElectroChem* **2015**, *2*, 584; g) J. Wang, W. Cui, Q. Liu, Z. Xing, A. M. Asiri, X. Sun, *Adv. Mater.* **2016**, *28*, 215.

[14] a) B. Qiao, A. Wang, X. Yang, L. F. Allard, Z. Jiang, Y. Cui, J. Liu, J. Li, T. Zhang, *Nat. Chem.* **2011**, *3*, 634; b) M. Ranocchiari, C. Lothschütz, D. Grolimund, J. A. van Bokhoven, *Proc. R. Soc. A.* **2012**, *468*1985; c) M. Flytzani-Stephanopoulos, B. C. Gates, *Annu. Rev. Chem. Biomol. Eng.* **2012**, *3*, 545; d) M. Tavakkoli, T. Kallio, O. Reynaud, A. G. Nasibulin, C. Johans, J. Sainio, H. Jiang, E. I. Kauppinen, K. Laasonen, *Angew. Chem. Int. Ed.* **2015**, *54*, 4535; e) J. M. Thomas, R. Raja, D. W. Lewis, *Angew. Chem. Int. Ed.* **2005**, *44*, 6456.

[15] a) C. T. Campbell, *Nat. Chem.* **2012**, *4*, 597; b) B. Zhang, D. S. Su, *ChemCatChem* **2015**, *7*, 3639; c) R. L. Vander Wal, T. M. Ticich, V. E. Curtis, *Carbon* **2001**, *39*, 2277; d) M. Bayati, K. Scott, *Electrochim. Acta* **2016**, *213*, 927.

[16] a) J. Deng, H. Li, J. Xiao, Y. Tu, D. Deng, H. Yang, H. Tian, J. Li, P. Ren, X. Bao, *Energy Environ. Sci.* **2015**, *8*, 1594; b) G. Kyriakou, M. B. Boucher, A. D. Jewell, E. A. Lewis, T. J. Lawton, A. E. Baber, H. L. Tierney, M. Flytzani-Stephanopoulos, E. C. H. Sykes, *Science* **2012**, *335*, 1209.

[17] a) N. Cheng, S. Stambula, D. Wang, M. N. Banis, J. Liu, A. Riese, B. Xiao, R. Li, T.-K. Sham, L.-M. Liu, G. A. Botton, X. Sun, *Nat. Commun.* **2016**, *7*, 13638; b) S. Sun, G. Zhang, N. Gauquelin, N. Chen, J. Zhou, S. Yang, W. Chen, X. Meng, D. Geng, M. N. Banis, R. Li, S. Ye, S. Knights, G. A. Botton, T.-K. Sham, X. Sun, *Sci. Rep.* **2013**, *3*, 1775; c) J. S. Jirkovský, I. Panas, E. Ahlberg, M. Halasa, S. Romani, D. J. Schiffrin, *J. Am. Chem. Soc.* **2011**, *133*, 19432.

[18] a) J. H. Kwak, L. Kovarik, J. Szanyi, *ACS Catal.* **2013**, *3*, 2094; b) M. Moses-DeBusk, M. Yoon, L. F. Allard, D. R. Mullins, Z. Wu, X. Yang, G. Veith, G. M. Stocks, C. K. Narula, *J. Am. Chem. Soc.* **2013**, *135*, 12634; c) L. Zhang, A. Wang, J. T. Miller, X. Liu, X. Yang, W. Wang, L. Li, Y. Huang, C.-Y. Mou, T. Zhang, *ACS Catal.* **2014**, *4*, 1546; d) Q. Fu, Y. Luo, *J. Phys. Chem. C.* **2013**, *117*, 14618; e) F. R. Lucci, M. T. Darby, M. F. G. Mattera, C. J. Ivimey, A. J. Therrien, A. Michaelides, M. Stamatakis, E. C. H. Sykes, *J. Phys. Chem. Lett.* **2016**, *7*, 480; f) X. Guo, G. Fang, G. Li, H. Ma, H. Fan, L. Yu, C. Ma, X. Wu, D. Deng, M. Wei, D. Tan, R. Si, S. Zhang, J. Li, L. Sun, Z. Tang, X. Pan, X. Bao, *Science* **2014**, *344*, 616.

[19] a) Q. Fu, H. Saltsburg, M. Flytzani-Stephanopoulos, *Science* **2003**, *301*, 935; b) J. Lin, A. Wang, B. Qiao, X. Liu, X. Yang, X. Wang, J. Liang, J. Li, J. Liu, T. Zhang, *J. Am. Chem. Soc.* **2013**, *135*, 15314; c) M. Yang, L. F. Allard, M. Flytzani-Stephanopoulos, *J. Am. Chem. Soc.* **2013**, *135*, 3768.

[20] A. Corma, P. Concepción, M. Boronat, M. J. Sabater, J. Navas, M. J. Yacaman, E. Larios, A. Posadas, M. A. López-Quintela, D. Buceta, E. Mendoza, G. Guilera, A. Mayoral, *Nat. Chem.* **2013**, *5*, 775.

[21] a) A. Wieckowski, E. R. Savinova, C. G. Vayenas, *Catalysis and Electrocatalysis at Nanoparticle Surface*, Marcel Dekker, Inc., New York, **2003**; b) W. Vielstich, A. Lamm, H. A. Gasteiger, *Handbook of Fuel Cells: Fundamentals, Technology, Applications*, John Wiley and Sons, Ltd., New Jersey, **2003**.

[22] a) X.-F. Yang, A. Wang, B. Qiao, J. Li, J. Liu, T. Zhang, *Acc. Chem. Res.* **2013**, *46*, 1740; b) K. Mao, L. Li, W. Zhang, Y. Pei, X. C. Zeng, X. Wu, J. Yang, *Sci. Rep.* **2014**, *4*, 5441.

[23] a) S. F. J. Hackett, R. M. Brydson, M. H. Gass, I. Harvey, A. D. Newman, K. Wilson, A. F. Lee, *Angew. Chem. Int. Ed.* **2007**, *46*, 8593; b) C. Zhang, F. Liu, Y. Zhai, H. Ariga, N. Yi, Y. Liu, K. Asakura, M. Flytzani-Stephanopoulos, H. He, *Angew. Chem. Int. Ed.* **2012**, *51*, 9628; c) J. Lu, C. Aydin, N. D. Browning, B. C. Gates,

Angew. Chem. Int. Ed. **2012**, *51*, 5842; d) M. Piernavieja-Hermida, Z. Lu, A. White, K.-B. Low, T. Wu, J. W. Elam, Z. Wu, Y. Lei, *Nanoscale* **2016**, *8*, 15348; e) S. Zhang, L. Nguyen, J.-X. Liang, J. Shan, J. Liu, A. I. Frenkel, A. Patlolla, W. Huang, J. Li, F. Tao, *Nat. Commun.* **2015**, *6*, 7938.

[24] H. Yan, H. Cheng, H. Yi, Y. Lin, T. Yao, C. Wang, J. Li, S. Wei, J. Lu, *J. Am. Chem. Soc.* **2015**, *137*, 10484.

[25] a) K. Ding, A. Gulec, A. M. Johnson, N. M. Schweitzer, G. D. Stucky, L. D. Marks, P. C. Stair, *Science* **2015**, *350*, 189; b) H. Zhang, T. Watanabe, M. Okumura, M. Haruta, N. Toshima, *Nat. Mater.* **2012**, *11*, 49.

[26] H. Wei, X. Liu, A. Wang, L. Zhang, B. Qiao, X. Yang, Y. Huang, S. Miao, J. Liu, T. Zhang, *Nat. Commun.* **2014**, *5*, 5634.

[27] a) W. E. Kaden, T. Wu, W. A. Kunkel, S. L. Anderson, *Science* **2009**, *326*, 826; b) S. Abbet, A. Sanchez, U. Heiz, W. D. Schneider, A. M. Ferrari, G. Pacchioni, N. Rösch, *J. Am. Chem. Soc.* **2000**, *122*, 3453; c) Y. Lei, F. Mehmood, S. Lee, J. Greeley, B. Lee, S. Seifert, R. E. Winans, J. W. Elam, R. J. Meyer, P. C. Redfern, D. Teschner, R. Schlögl, M. J. Pellin, L. A. Curtiss, S. Vajda, *Science* **2010**, *328*, 224; d) G. E. Johnson, M. Lysonski, J. Laskin, *Anal. Chem.* **2010**, *82*, 5718; e) S. Abbet, K. Judai, L. Klinger, U. Heiz, *Pure Appl. Chem.* **2002**, *74*, 1527.

[28] a) U. Heiz, A. Sanchez, S. Abbet, W. D. Schneider, *J. Am. Chem. Soc.* **1999**, *121*, 3214; b) B. Yoon, H. Häkkinen, U. Landman, A. S. Wörz, J.-M. Antonietti, S. Abbet, K. Judai, U. Heiz, *Science* **2005**, *307*, 403; c) U. Heiz, *Appl. Phys. A* **1998**, *67*, 621.

[29] G. E. Johnson, T. Priest, J. Laskin, *ACS Nano* **2012**, *6*, 573.

[30] E. C. Tyo, S. Vajda, *Nat. Nanotechnol.* **2015**, *10*, 577.

[31] a) C. I. Contescu, K. van Benthem, S. Li, C. S. Bonifacio, S. J. Pennycook, P. Jena, N. C. Gallego, *Carbon* **2011**, *49*, 4050; b) J. M. Thomas, Z. Saghi, P. L. Gai, *Top. Catal.* **2011**, *54*, 588; c) H. Wang, Q. Wang, Y. Cheng, K. Li, Y. Yao, Q. Zhang, C. Dong, P. Wang, U. Schwingenschlögl, W. Yang, X. X. Zhang, *Nano Lett.* **2012**, *12*, 141; d) O. Cretu, A. V. Krasheninnikov, J. A. Rodríguez-Manzo, L. Sun, R. M. Nieminen, F. Banhart, *Phys. Rev. Lett.* **2010**, *105*, 196102; e) J. M. Thomas, *Phys. Chem. Chem. Phys.* **2014**, *16*, 7647; f) C. G. Claessens, U. Hahn, T. Torres, *Chem. Rec.* **2008**, *8*, 75; g) O. Lehtinen, J. Kotakoski, A. V. Krasheninnikov, A. Tolvanen, K. Nordlund, J. Keinonen, *Phys. Rev. B.* **2010**, *81*, 153401; h) S. R. Stoyanov, P. Král, *J. Chem. Phys.* **2008**, *129*, 234702.

[32] Z. He, K. He, A. W. Robertson, A. I. Kirkland, D. Kim, J. Ihm, E. Yoon, G.-D. Lee, J. H. Warner, *Nano Lett.* **2014**, *14*, 3766.

[33] a) Y. Jiao, Y. Zheng, M. Jaroniec, S. Z. Qiao, *Chem. Soc. Rev.* **2015**, *44*, 2060; b) Z. Chen, D. Higgins, A. Yu, L. Zhang, J. Zhang, *Energy Environ. Sci.* **2011**, *4*, 3167.

[34] R. Zhou, M. Jaroniec, S.-Z. Qiao, *ChemCatChem* **2015**, *7*, 3808.

[35] Z.-S. Wu, S. Yang, Y. Sun, K. Parvez, X. Feng, K. Müllen, *J. Am. Chem. Soc.* **2012**, *134*, 9082.

[36] a) N. Ohta, R. Arafune, N. Tsukahara, M. Kawai, N. Takagi, *J. Phys. Chem. C.* **2013**, *117*, 21832; b) Y. Wang, S. Li, J. Yi, *Sci. Rep.* **2016**, *6*, 24153; c) G.-X. Chen, D.-D. Wang, J.-Q. Wen, A. P. Yang, J.-M. Zhang, *Int. J. Quantum Chem.* **2016**, *116*, 1000.

[37] a) J. L. Shi, J. Wu, X. Zhao, X. Xue, Y. Gao, Z. Guo, S. Li, *Nanoscale* **2016**, *8*, 19256; b) V. V. Ivanovskaya, A. Zobelli, A. Gloter, N. Brun, V. Serin, C. Colliex, *Phys. Rev. B.* **2008**, *78*, 134104.

[38] a) D. Kepaptsoglou, T. P. Hardcastle, C. R. Seabourne, U. Bangert, R. Zan, J. A. Amani, H. Hofsäss, R. J. Nicholls, R. M. D. Brydson, A. J. Scott, Q. M. Ramasse, *ACS Nano* **2015**, *9*, 11398; b) D. A. Bulushev, M. Zacharska, A. S. Lisitsyn, O. Y. Podyacheva, F. S. Hage, Q. M. Ramasse, U. Bangert, L. G. Bulusheva, *ACS Catal.* **2016**, *6*, 3442.

[39] I. Mayer, *Chem. Phys. Lett.* **2004**, *393*, 209.

[40] H. J. Qiu, Y. Ito, W. Cong, Y. Tan, P. Liu, A. Hirata, T. Fujita, Z. Tang, M. Chen, *Angew. Chem. Int. Ed.* **2015**, *54*, 14031.

[41] a) N. Yi, H. Saltsburg, M. Flytzani-Stephanopoulos, *ChemSusChem* **2013**, *6*, 816; b) B. Qiao, J. Liu, Y.-G. Wang, Q. Lin, X. Liu, A. Wang, J. Li, T. Zhang, J. Liu, *ACS Catal.* **2015**, *5*, 6249; c) Y. Shi, C. Zhao, H. Wei, J. Guo, S. Liang, A. Wang, T. Zhang, J. Liu, T. Ma, *Adv. Mater.* **2014**, *26*, 8147; d) J. C. Matsubu, V. N. Yang, P. Christopher, *J. Am. Chem. Soc.* **2015**, *137*, 3076; e) C. K. Narula, L. F. Allard, G. M. Stocks, M. Moses-DeBusk, *Sci. Rep.* **2014**, *4*, 7238; f) M. Yang, J. Liu, S. Lee, B. Zugic, J. Huang, L. F. Allard, M. Flytzani-Stephanopoulos, *J. Am. Chem. Soc.* **2015**, *137*, 3470; g) J.-X. Liang, X.-F. Yang, A. Wang, T. Zhang, J. Li, *Catal. Sci. Tech.* **2016**, *6*, 6886.

[42] a) C. Moreno-Castilla, F. J. Maldonado-Hódar, *Carbon* **2005**, *43*, 455; b) J. Wang, G. Wang, S. Miao, J. Li, X. Bao, *Farad. Discuss.* **2014**, *176*, 135.

[43] S. Liang, C. Hao, Y. Shi, *ChemCatChem* **2015**, *7*, 2559.

[44] a) B. Bayatsarmadi, Y. Zheng, V. Russo, L. Ge, C. S. S. Casari, S. Qiao, *Nanoscale* **2016**, *8*, 18507; b) B. Bayatsarmadi, Y. Zheng, Y. Tang, M. Jaroniec, S.-Z. Qiao, *Small* **2016**, *12*, 3703; c) W. Zhou, J. Jia, J. Lu, L. Yang, D. Hou, G. Li, S. Chen, *Nano Energy* **2016**, *28*, 29; d) M. M. Giangregorio, W. Jiao, G. V. Bianco, P. Capezzuto, A. S. Brown, G. Bruno, M. Losurdo, *Nanoscale* **2015**, *7*, 12868.

[45] a) H. Fei, J. Dong, M. J. Arellano-Jimenez, G. Ye, N. Dong Kim, E. L. G. Samuel, Z. Peng, Z. Zhu, F. Qin, J. Bao, M. J. Yacaman, P. M. Ajayan, D. Chen, J. M. Tour, *Nat. Commun.* **2015**, *6*, 8668; b) Ç. Ö. Girit, J. C. Meyer, R. Erni, M. D. Rossell, C. Kisielowski, L. Yang, C.-H. Park, M. F. Crommie, M. L. Cohen, S. G. Louie, A. Zettl, *Science* **2009**, *323*, 1705.

[46] D. Deng, L. Yu, X. Chen, G. Wang, L. Jin, X. Pan, J. Deng, G. Sun, X. Bao, *Angew. Chem. Int. Ed.* **2013**, *52*, 371.

[47] a) S. Azevedo, C. Chesman, J. R. Kaschny, *Eur Phys J. B.* **2010**, *74*, 123; b) A. Morozan, V. Goellner, Y. Nedellec, J. Hannauer, F. Jaouen, *J. Electrochem. Soc.* **2015**, *162*, 719.

[48] W. Liu, L. Zhang, W. Yan, X. Liu, X. Yang, S. Miao, W. Wang, A. Wang, T. Zhang, *Chem. Sci.* **2016**, *7*, 5758.

[49] C. H. Choi, M. Kim, H. C. Kwon, S. J. Cho, S. Yun, H.-T. Kim, K. J. J. Mayrhofer, H. Kim, M. Choi, *Nat. Commun.* **2016**, *7*, 10922.

[50] a) N. Cheng, J. Liu, M. N. Banis, D. Geng, R. Li, S. Ye, S. Knights, X. Sun, *Int. J. Hydrogen Energy* **2014**, *39*, 15967; b) Y. Chen, J. Wang, X. Meng, Y. Zhong, R. Li, X. Sun, S. Ye, S. Knights, *Int. J. Hydrogen Energy* **2011**, *36*, 11085; c) H. Lv, N. Cheng, T. Peng, M. Pan, S. Mu, *J. Mater. Chem.* **2012**, *22*, 1135; d) R. Kou, Y. Shao, D. Mei, Z. Nie, D. Wang, C. Wang, V. V. Viswanathan, S. Park, I. A. Aksay, Y. Lin, Y. Wang, J. Liu, *J. Am. Chem. Soc.* **2011**, *133*, 2541; e) H. Xie, J. Lu, M. Shekhar, J. W. Elam, W. N. Delgass, F. H. Ribeiro, E. Weitz, K. R. Poeppelmeier, *ACS Catal.* **2013**, *3*, 61.

[51] a) S. Wang, A. Y. Borisevich, S. N. Rashkeev, M. V. Glazoff, K. Sohlberg, S. J. Pennycook, S. T. Pantelides, *Nat. Mater.* **2004**, *3*, 143; b) P. E. Batson, *Microsc. Microanal.* **2008**, *14*, 89; c) E. Bayram, J. Lu, C. Aydin, A. Uzun, N. D. Browning, B. C. Gates, R. G. Finke, *ACS Catal.* **2012**, *2*, 1947; d) Y.-C. Lin, D. O. Dumcenco, H.-P. Komsa, Y. Niimi, A. V. Krasheninnikov, Y.-S. Huang, K. Suenaga, *Adv. Mater.* **2014**, *26*, 2857; e) T. Ling, D.-Y. Yan, Y. Jiao, H. Wang, Y. Zheng, X. Zheng, J. Mao, X.-W. Du, Z. Hu, M. Jaroniec, S.-Z. Qiao, *Nat. Commun.* **2016**, *7*, 12876; f) P. M. Koenraad, M. E. Flatte, *Nat. Mater.* **2011**, *10*, 91; g) M. Zhou, H. Qian, M. Y. Sfeir, K. Nobusada, R. Jin, *Nanoscale* **2016**, *8*, 7163.

[52] D. Deng, X. Chen, L. Yu, X. Wu, Q. Liu, Y. Liu, H. Yang, H. Tian, Y. Hu, P. Du, R. Si, J. Wang, X. Cui, H. Li, J. Xiao, T. Xu, J. Deng, F. Yang, P. N. Duchesne, P. Zhang, J. Zhou, L. Sun, J. Li, X. Pan, X. Bao, *Sci Adv.* **2015**, *1*, 1500462.

[53] a) Y. Liang, H. Wang, J. Zhou, Y. Li, J. Wang, T. Regier, H. Dai, *J. Am. Chem. Soc.* **2012**, *134*, 3517; b) Y. Liang, H. Wang, P. Diao, W. Chang, G. Hong, Y. Li, M. Gong, L. Xie, J. Zhou, J. Wang, T. Z. Regier, F. Wei, H. Dai, *J. Am. Chem. Soc.* **2012**, *134*, 15849; c) H. R. Byon, J. Suntivich, E. J. Crumlin, Y. Shao-Horn, *Phys. Chem. Chem. Phys.* **2011**, *13*, 21437; d) H. Funke, A. C. Scheinost, M. Chukalina, *Phys. Rev. B.* **2005**, *71*, 094110; e) U. I. Kramm, J. Herranz, N. Larouche, T. M. Arruda, M. Lefevre, F. Jaouen,

P. Bogdanoff, S. Fiechter, I. Abs-Wurmbach, S. Mukerjee, J.-P. Dodelet, *Phys. Chem. Chem. Phys.* **2012**, *14*, 11673.

[54] a) A. Zitolo, V. Goellner, V. Armel, M.-T. Sougrati, T. Mineva, L. Stievano, E. Fonda, F. Jaouen, *Nat. Mater.* **2015**, *14*, 937; b) S. Kattel, P. Atanassov, B. Kiefer, *J. Mater. Chem. A.* **2014**, *2*, 10273.

[55] P. Yin, T. Yao, Y. Wu, L. Zheng, Y. Lin, W. Liu, H. Ju, J. Zhu, X. Hong, Z. Deng, G. Zhou, S. Wei, Y. Li, *Angew. Chem. Int. Ed.* **2016**, *55*, 10800.

[56] a) J. K. Nørskov, J. Rossmeisl, A. Logadottir, L. Lindqvist, J. R. Kitchin, T. Bligaard, H. Jónsson, *J. Phys. Chem. B.* **2004**, *108*, 17886; b) L. Zhang, Z. Xia, *J. Phys. Chem. C.* **2011**, *115*, 11170; c) L. Yu, X. Pan, X. Cao, P. Hu, X. Bao, *J. Catal.* **2011**, *282*, 183; d) L. Zhang, J. Niu, L. Dai, Z. Xia, *Langmuir* **2012**, *28*, 7542; e) T. G. Gopakumar, T. Brumme, J. Kröger, C. Toher, G. Cuniberti, R. Berndt, *J. Phys. Chem. C.* **2011**, *115*, 12173; f) A. V. Krasheninnikov, P. O. Lehtinen, A. S. Foster, P. Pyykkö, R. M. Nieminen, *Phys. Rev. Lett.* **2009**, *102*, 126807; g) M. Sargolzaei, N. Lotfizadeh, *Phys. Rev. B.* **2011**, *83*, 7.

[57] a) X. Sun, J. Du, G. Jiang, *J. Struct. Chem.* **2013**, *24*, 1289; b) C. Chen, J. Zhang, G. Dong, H. Shao, B.-y. Ning, L. Zhao, X.-j. Ning, J. Zhuang, *Nanoscale Res. Lett.* **2014**, *9*, 235.

[58] a) G. R. Berdiyorov, H. Abdullah, M. A. Ezzi, G. V. Rakhmatullaeva, H. Bahlouli, N. Tit, *AIP Advances* **2016**, *6*, 125102; b) S. Aslanzadeh, *Journal of Molecular Modeling* **2016**, *22*, 160.

[59] a) J. Zhao, Q. Deng, A. Bachmatiuk, G. Sandeep, A. Popov, J. Eckert, M. H. Rümmeli, *Science* **2014**, *343*, 1228; b) X. Jia, M. Hofmann, V. Meunier, B. G. Sumpter, J. Campos-Delgado, J. M. Romo-Herrera, H. Son, Y.-P. Hsieh, A. Reina, J. Kong, M. Terrones, M. S. Dresselhaus, *Science* **2009**, *323*, 1701.

[60] X. Yan, K. Liu, T. Wang, Y. You, J. Liu, P. Wang, X. Pan, G. Wang, J. Luo, J. Zhu, *Journal of Materials Chemistry A* **2017**, *5*, 3336.

[61] a) J. L. Dempsey, B. S. Brunschwig, J. R. Winkler, H. B. Gray, *Acc. Chem. Res.* **2009**, *42*, 1995; b) V. Artero, M. Chavarot-Kerlidou, M. Fontecave, *Angew. Chem. Int. Ed.* **2011**, *50*, 7238; c) B. Bayatsarmadi, Y. Zheng, C. S. Casari, V. Russo, S. Z. Qiao, *Chem. Commun.* **2016**, *52*, 11947.

[62] a) S. Chao, Z. Bai, Q. Cui, H. Yan, K. Wang, L. Yang, *Carbon* **2015**, *82*, 77; b) C. Han, X. Bo, Y. Zhang, M. Li, A. Nsabimana, L. Guo, *Nanoscale* **2015**, *7*, 5607.

[63] a) X. Zou, X. Huang, A. Goswami, R. Silva, B. R. Sathe, E. Mikmeková, T. Asefa, *Angew. Chem. Int. Ed.* **2014**, *53*, 4372; b) J. Wang, D. Gao, G. Wang, S. Miao, H. Wu, J. Li, X. Bao, *J. Mater. Chem. A.* **2014**, *2*, 20067.

[64] H.-W. Liang, S. Bruller, R. Dong, J. Zhang, X. Feng, K. Mullen, *Nat. Commun.* **2015**, *6*, 7992.

[65] S. Giri, C. K. Das, S. S. Kalra, *J. Mater. Sci. Res.* **2012**, *1*, 10.

[66] a) F. Jaouen, S. Marcotte, J.-P. Dodelet, G. Lindbergh, *J. Phys. Chem. B.* **2003**, *107*, 1376; b) M. Lefèvre, J. P. Dodelet, P. Bertrand, *J. Phys. Chem. B.* **2002**, *106*, 8705.

[67] a) U. I. Koslowski, I. Abs-Wurmbach, S. Fiechter, P. Bogdanoff, *J. Phys. Chem. C.* **2008**, *112*, 15356; b) A. L. Bouwkamp-Wijnoltz, W. Visscher, J. A. R. van Veen, E. Boellaard, A. M. van der Kraan, S. C. Tang, *J. Phys. Chem. B.* **2002**, *106*, 12993; c) H. Schulenburg, S. Stankov, V. Schünemann, J. Radnik, I. Dorbandt, S. Fiechter, P. Bogdanoff, H. Tributsch, *J. Phys. Chem. B.* **2003**, *107*, 9034.

[68] N. Ramaswamy, U. Tylus, Q. Jia, S. Mukerjee, *J. Am. Chem. Soc.* **2013**, *135*, 15443.

[69] Y. Zheng, Y. Jiao, Y. Zhu, Q. Cai, A. Vasileff, L. H. Li, Y. Han, Y. Chen, S.-Z. Qiao, *J. Am. Chem. Soc* **2017**, *139*, 3336.

[70] X. Zhang, J. Guo, P. Guan, C. Liu, H. Huang, F. Xue, X. Dong, S. J. Pennycook, M. F. Chisholm, *Nat. Commun.* **2013**, *4*, 1924.

[71] a) M. Yang, S. Li, Y. Wang, J. A. Herron, Y. Xu, L. F. Allard, S. Lee, J. Huang, M. Mavrikakis, M. Flytzani-Stephanopoulos, *Science* **2014**, *346*, 1498; b) X. Zhang, H. Shi, B.-Q. Xu, *Angew. Chem. Int. Ed.* **2005**, *117*, 7294; c) D. I. Kochubey, V. V. Chesnokov, S. E. Malykhin, *Carbon* **2012**, *50*, 2782; d) E. J. Peterson, A. T. DeLaRiva, S. Lin, R. S. Johnson, H. Guo, J. T. Miller, J. Hun Kwak, C. H. F. Peden, B. Kiefer, L. F. Allard, F. H. Ribeiro, A. K. Datye, *Nat. Commun.* **2014**, *5*, 4885.

[72] a) J. Pérez-Ramírez, *Angew. Chem. Int. Ed.* **2013**, *52*, 9892; b) A. Bruix, Y. Lykhach, I. Matolínová, A. Neitzel, T. Skála, N. Tsud, M. Vorokhta, V. Stetsovych, K. Ševčíková, J. Mysliveček, R. Fiala, M. Václavç K. C. Prince, S. Bruyère, V. Potin, F. Illas, V. Matolín, J. Libuda, K. M. Neyman, *Angew. Chem. Int. Ed.* **2014**, *53*, 10525; c) Y.-T. Kim, K. Ohshima, K. Higashimine, T. Uruga, M. Takata, H. Suematsu, T. Mitani, *Angew. Chem. Int. Ed.* **2006**, *45*, 407.

Received: January 16, 2017
Revised: March 15, 2017

Chapter 3

3. Soft-templating synthesis of N-doped mesoporous carbon nanospheres for enhanced oxygen reduction reaction

3.1. Introduction

Carbon nanoparticles with ordered mesostructures and controlled morphologies have great advantages because of their remarkable properties including high surface area, high pore volume, tunable pore size and the diffusion channels for fast mass transfer. These outstanding features make them great candidates for catalysis applications such as electrocatalysts for oxygen reduction reaction (ORR). Doping mesoporous carbon spheres with guest atoms can improve their catalytic activity for ORR and thus can be considered as a potential substitute for the expensive Pt/C catalyst in fuel cells or metal-air batteries. In this work, N-doped mesoporous carbon spheres are prepared via a facile and low-cost dual soft-templating procedure. The effect of nitrogen doping functions and different pyrolysis temperatures on conductivity and catalytic activity of synthesized electrocatalysts have been comprehensively investigated. The preeminent sample is applied in complementary ORR tests to underline the stability and durability of synthesized metal-free electrocatalysts in alkaline solution.

The highlights of this work include:

1. Nitrogen doped mesoporous carbon spheres were fabricated via a facile and low-cost synthesis procedure due to the use of cheap precursors (melamine and resorcinol-formaldehyde resin) and soft template techniques (F127 and FC4), which makes the method feasible for large scale production.

2. By controlling nitrogen precursor contents and pyrolysis temperature, the effects of surface area, pore volume, conductivity, and nitrogen doping configuration toward catalytic activity of synthesized spheres have been comprehensively investigated for the first time which may pave the way of feasibly designing nitrogen-containing carbon materials for highly efficient oxygen reduction electrocatalysis.

3. The well-structured mesoporosity and abundant surface defect sites of the synthesized materials assure an efficient ORR catalytic performance of theses metal-free electrocatalysts, showing a high activity, better durability and methanol tolerance ability as compared to the Pt/C catalyst.

4. By applying ORR as a probing reaction, which is also considered as a cornerstone to explore the mechanism of other multi-electron transfer processes, we expect the study will largely expand the spectrum of catalysts for more energy-related electrocatalytic reactions.

3.2. Research outcome

This section is included in the thesis as it appears as a journal paper published by **Bita Bayatsarmadi**, Yao Zheng, Mietek Jaroniec, and Shi-Zhang Qiao, "Soft-templating synthesis of N-doped mesoporous carbon nanospheres for enhanced oxygen reduction reaction", ***Chemistry-An Asian Journal***, 2015, 10, 1546-1553.

Statement of Authorship

Title of Paper	Soft-Templating Synthesis of N-Doped Mesoporous Carbon Nanospheres for Enhanced Oxygen Reduction Reaction.
Publication Status	☑ Published ☐ Accepted for Publication ☐ Submitted for Publication ☐ Unpublished and Unsubmitted work written in manuscript style
Publication Details	B. Bayatsarmadi, Y. Zheng, M. Jaroniec and S.Z. Qiao*, “Soft-Templating Synthesis of N-Doped Mesoporous Carbon Nanospheres for Enhanced Oxygen Reduction Reaction”, ***Chemistry – An Asian Journal***, 2015, 10, 1546-1553, [IF: 4.59].

Principal Author

Name of Principal Author (Candidate)	Bita Bayatsarmadi		
Contribution to the Paper	Research plan, material synthesis, most of the material characterisations, performance assessments and manuscript drafting.		
Overall percentage (%)	85 %		
Certification:	This paper reports on original research I conducted during the period of my Higher Degree by Research candidature and is not subject to any obligations or contractual agreements with a third party that would constrain its inclusion in this thesis. I am the primary author of this paper.		
Signature		Date	18/11/2016

Co-Author Contributions

By signing the Statement of Authorship, each author certifies that:

i. the candidate’s stated contribution to the publication is accurate (as detailed above);
ii. permission is granted for the candidate in include the publication in the thesis; and
iii. the sum of all co-author contributions is equal to 100% less the candidate’s stated contribution.

Name of Co-Author	Dr. Yao Zheng		
Contribution to the Paper	Discussion of research plan, manuscript review and assessment.		
Signature		Date	21/11/2016

Name of Co-Author	Prof. Mietek Jaroniec		
Contribution to the Paper	Manuscript review		
Signature		Date	Nov 21, 2016

Name of Co-Author	Prof. Shi-Zhang Qiao		
Contribution to the Paper	Supervised development of the work, organisation of the research, manuscript review and assessmen		
Signature		Date	18/11/2016

ACES
DOI: 10.1002/asia.201500287
CHEMISTRY
AN ASIAN JOURNAL
Full Paper

Mesoporous Materials

Soft-Templating Synthesis of *N*-Doped Mesoporous Carbon Nanospheres for Enhanced Oxygen Reduction Reaction

Bita Bayatsarmadi,[a] Yao Zheng,[a] Mietek Jaroniec,[b] and Shi Zhang Qiao*[a]

Abstract: The development of ordered mesoporous carbon materials with controllable structures and improved physicochemical properties by doping heteroatoms such as nitrogen into the carbon framework has attracted a lot of attention, especially in relation to energy storage and conversion. Herein, a series of nitrogen-doped mesoporous carbon spheres (NMCs) was synthesized via a facile dual soft-templating procedure by tuning the nitrogen content and carbonization temperature. Various physical and (electro)chemical properties of the NMCs have been comprehensively investigated to pave the way for a feasible design of nitrogen-containing porous carbon materials. The optimized sample showed a favorable electrocatalytic activity as evidenced by a high kinetic current and positive onset potential for oxygen reduction reaction (ORR) due to its large surface area, high pore volume, good conductivity, and high nitrogen content, which make it a highly efficient ORR metal-free catalyst in alkaline solutions.

Introduction

Porous carbon materials with ordered nanostructures are advantageous because of their remarkable properties including high surface areas, tunable pore structures, and uniform and adjustable pore sizes, assuring fast diffusion and mass transfer. These outstanding features make these carbon materials great candidates for energy storage and conversion applications such as supercapacitors, fuel cells, and lithium-ion batteries[1] Carbon materials with high specific surface areas, large pore volumes, and well-developed mesoporosity not only assure facile access of reactants to the active sites and favor mass transport of the intermediate species but also facilitate electron delivery through the continuous framework structure.[2] However, electrocatalysts need to possess good electrical conductivity for electron transfer, excellent activity, and high chemical stability besides high surface area and controlled nanostructure. Thus, heteroatoms such as nitrogen are usually doped into the carbon matrix to improve the overall conductivity of catalysts, provide more active sites, and enhance interactions between carbon and other molecules by tuning electron donor/acceptor properties.[3] Mesoporous carbon nanoparticles can be prepared either through a hard-templating method by filling the mesopores of silica templates with an organic precursor or by an organic–organic assembly (soft-templating) method. The hard-templating method is a costly, multistep, and time-consuming procedure as compared to soft-templating, which requires fewer synthesis steps, is less expensive, and well suited for preparation of particles with well-defined pore structures and narrow pore size distributions.[3a,4] Various synthetic strategies have been reported so far to prepare heteroatom-doped mesoporous carbons including post-treatment of mesoporous carbons with reactive heteroatom sources,[5] or a one-step pyrolysis of heteroatom-containing precursor with the carbon precursor.[6] The first route leads to carbons with an insufficient heteroatom fraction and a small amount of catalytic active sites due to the resistance of the pre-existing graphitic structure to the heteroatom doping, while the second approach can result in higher heteroatom content.[7]

N-Doped mesoporous carbon nanospheres can act as an electrode for oxygen reduction reaction (ORR) because of their unique physical and chemical properties. Specifically, their spherical morphology, high surface area, and large pore volume can enhance the activity of electrocatalysts by assuring an easy access of reactants to catalytically active sites and fast mass transfer, which can dramatically affect the electrocatalytic performance of the electrode.[8] Conductivity or graphitic nature of a carbon material, which can be enhanced by high-temperature carbonization, is also a crucial factor affecting the catalyst's activity.[9] Moreover, from the theoretical calculation perspective, the nitrogen content and bonding configuration of nitrogen atoms in a carbon matrix are considered as the key factors influencing the electrocatalytic activity.[9,10] However, the design of inexpensive and efficient catalysts followed by

---

[a] *B. Bayatsarmadi, Dr. Y. Zheng, Prof. S. Z. Qiao*
School of Chemical Engineering
the University of Adelaide
Adelaide, SA 5005 (Australia)
E-mail: s.qiao@adelaide.edu.au

[b] *Prof. M. Jaroniec*
Department of Chemistry and Biochemistry
Kent State University
Kent, Ohio 44240 (USA)

Supporting information for this article is available on the WWW under http://dx.doi.org/10.1002/asia.201500287.

a comprehensive study considering all above factors is still not fully available, and their effect on the ORR activity is still inconclusive.

Herein, we report the preparation of *N*-doped mesoporous carbon spheres (NMCs) via a facile and low-cost dual soft-templating procedure using a resorcinol-formaldehyde resin and melamine as carbon and nitrogen precursors, respectively. The surface area, pore volume, conductivity, and nitrogen-doping configuration of the synthesized NMC were tuned by adjusting the nitrogen content and pyrolysis temperature, and their effect on the catalytic activity was comprehensively investigated for the first time. A complete testing of one preeminent sample was performed for ORR to demonstrate the stability and durability of this type of electrocatalysts in alkaline solutions. The well-structured mesoporosity and abundant surface defect sites assured an efficient ORR catalytic performance of this material with a better durability and methanol tolerance ability as compared to the Pt/C catalyst. This study may pave the way for a feasible design of nitrogen-containing porous carbon materials for different applications such as fuel cells and lithium oxygen batteries.

Results and Discussion

The *N*-doped mesoporous carbon nanospheres were synthesized via a dual soft-templating method as shown in Scheme 1. The first synthesis step involved combining two surfactants (F127 and FC4) in ethanol/HCl solution and adding mesitylene (TMB) as a swelling agent for the formation of micelles.[1b,11] Next, resorcinol and formaldehyde (RF) precursors were polymerized in the hydrophilic domains of micelles at 30 °C under acidic conditions. Following the cross-linking of RF and self-assembly with micelles under hydrothermal conditions at 100 °C, the as-synthesized mesoporous polymer spheres were obtained. In the second step, the dried solid products were finely ground with a specified amount of melamine as nitrogen-rich doping source, and the templates were removed by heating at 350 °C. Finally, nitrogen-doped mesoporous carbon spheres were produced by direct carbonization of the as-made mesoporous RF resin spheres at high temperature (e.g., 900 °C) under N_2 flow. In the meantime, melamine was subjected to thermal polymerization at a temperature of about 500 °C to form g-C_3N_4 by releasing gaseous NH_3, which served as a nitrogen dopant and substituted some of the oxygen-containing functional groups in the carbon framework, resulting in doping nitrogen species into the carbon matrix of NMCs. Moreover, the as-formed g-C_3N_4 was decomposed by increasing the temperature to >800 °C, which played the role of a sacrificial nitrogen precursor to further dope the NMC materials and also minimized nitrogen leaching from it at high temperatures.[11a,12] The synthesized *N*-doped mesoporous carbon spheres are designated as NMCR-T, where R and T represent the ratio of N/C precursors and carbonization temperature, respectively. For the purpose of comparison, mesoporous carbon spheres without nitrogen doping (denoted as MC-900) were synthesized by pyrolysis of the RF resin at 350 °C to remove surfactant templates and carbonized at 900 °C under N_2 flow.

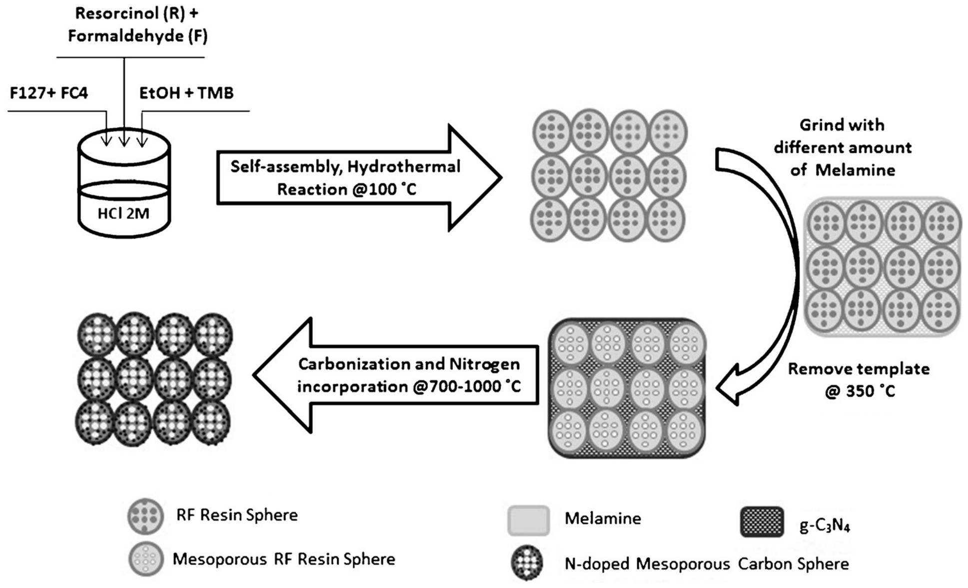

Scheme 1. Fabrication of *N*-doped mesoporous carbon spheres through a soft-templating process.

The morphology and mesostructure of NMCs were first investigated by scanning electron microscopy (SEM) and high-resolution transmission electron microscopy (HRTEM). The SEM image of a typical NMC5-900 sample clearly displays the spherical morphology with an approximately uniform diameter of about 260 nm (Figure 1 a). The SEM image also shows that spheres are randomly stacked together, which might be attributed to the defective structure of synthesized spheres due to the presence of doped nitrogen atoms.[12b] The HRTEM image further confirms the spherical morphology of NMC5-900 with an ordered mesostructure and uniform pore diameter of about

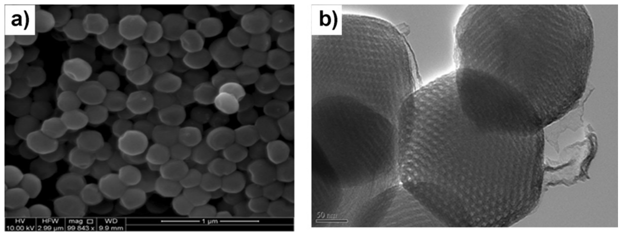

Figure 1. Electron microscopy images of *N*-doped mesoporous carbon spheres with an N/C ratio of 5 obtained by carbonization at 900 °C (NMC5-900): SEM image (a) and HRTEM image (b).

4 nm (Figure 1 b). The energy-dispersive spectrum (EDS) of NMC5-900 exhibits the presence of nitrogen dopant as well as oxygen and carbon in the structure of the synthesized spheres (Figure S1, Supporting Information). It should be noted that all the products prepared under different pyrolysis conditions maintain similar morphologies and mesostructures except some shrinkage at higher pyrolysis temperature (Figures S2 and S3, Supporting Information).[13]

The surface area and porosity of the synthesized samples were characterized using nitrogen adsorption–desorption data. Adsorption isotherms measured for NMC5-900 and MC-900 (Figure 2 a) exhibit a similar type-IV shape with a visible hysteresis loop, indicative of the presence of mesopores.[14] A sharp increase in the adsorption relative pressures close to unity indicates capillary condensation of nitrogen inside the extra-large mesopores and small macropores possibly created due to agglomeration of carbon spheres. This may be due to the fact that NMC5-900 spheres have more structural defects caused by incorporation of nitrogen into the carbon framework.[15] A rapid rise in adsorption at low relative pressures (below 0.05) for both samples suggests the presence of micropores in carbon spheres. The microporous structure of mesoporous carbons obtained via soft-templating synthesis is mainly caused by thermal degradation of oxygen-containing bridges during carbonization of the RF resin.[4a]

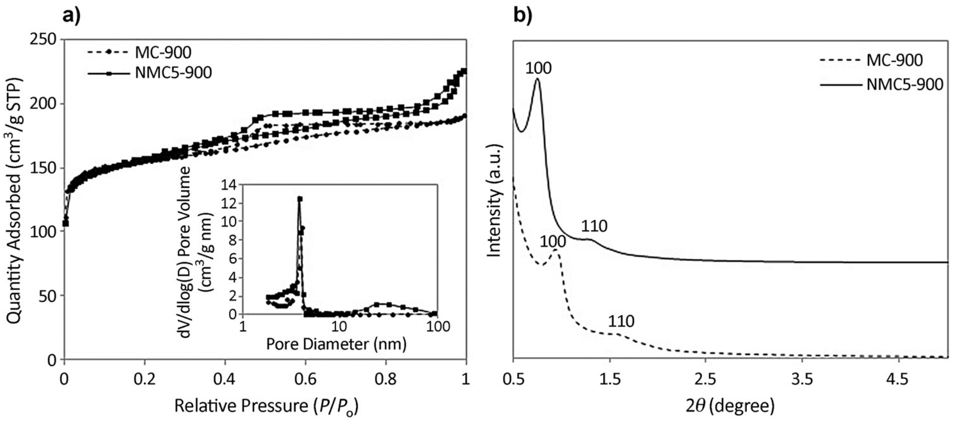

Figure 2. (a) Nitrogen adsorption isotherms (inset in panel a: pore size distribution) and (b) low-angle XRD patterns of synthesized mesoporous carbon spheres with and without nitrogen doping at a pyrolysis temperature of 900 °C.

The pore size distributions of both MC-900 and NMC5-900 (inset in Figure 2 a) show sharp peaks, thus confirming the uniform pore structures of the synthesized spheres. The pore diameter of NMC5-900 is slightly lower than that of MC-900, which is probably because of the incorporation of nitrogen atoms into carbon. Moreover, the pore size distribution curves show that NMC5-900 exhibits another wide peak at about 25 nm, which is due to extra-large mesopores formed by stacking carbon spheres together.[1c] It is anticipated that mesoporous structures of carbon spheres with narrow pore size distributions are favorable for penetration of ions into pores, which should result in higher activity toward oxygen reduction.[13] Figure S4 in the Supporting Information shows that the nitrogen content in the carbon spheres has no significant effect on the nitrogen adsorption–desorption isotherms and the corresponding pore size distributions. The pore size distributions (Figure S4 b) exhibit sharp peaks centered at about 4 nm. Again, a higher amount of nitrogen doping leads to significant agglomeration of particles.

The BET surface areas of MC-900 and NMC5-900 are 431 and 484 $m^2 g^{-1}$ and the total pore volumes are 0.35 and 0.41 $m^3 g^{-1}$, respectively. The BET surface area and pore volume show a tendency to increase with increasing carbonization temperature (Table 1), which is due to the complete decomposition of degradable species and nitrogen precursor resulting in the formation of additional microporosity at 900 °C.[17] A further increase in the carbonization temperature to 1000 °C led to a small decrease of the BET surface and pore volume due to some shrinkage of the framework.[4a, 14]

Small-angle XRD patterns (Figure 2 b) of MC-900 and NMC5-900 show two resolved peaks, which are indexed as the 10 and 11 reflections of 2D hexagonal mesostructure (p6mm). These data clearly demonstrate that a surfactant-assisted self-assembly occurs.[1c, 11c, 15] The lattice constants (*a*) calculated from the XRD patterns are 9.5 and 11.7 nm for MC-900 and NMC5-900, respectively, indicating the expansion in the catalyst structure by doping nitrogen atoms into the carbon lattice.

Table 1. Summary of physicochemical and electrochemical properties of the electrocatalysts studied.

Sample	NMC5-700	NMC5-800	NMC5-900	NMC5-1000
S_{BET} [$m^2 g^{-1}$]	307	469	484	483
V_t [$cm^3 g^{-1}$]	0.30	0.38	0.41	0.38
N content [%]	25.7	12.7	7.9	5.5
I_G/I_D	0.88	0.91	0.97	0.96
J_k@−0.5 V [$mA\,cm^{-2}{}_{geometric}$]	1.10	3.50	11.30	6.30
n@−0.5 V	2.50	2.60	3.50	2.80
Onset potential [V]	−0.31	−0.19	−0.11	−0.14

The chemical structure of the synthesized spheres was first characterized by Fourier transform IR (FTIR) spectroscopy as shown in Figure 3 a. The FTIR spectrum of mesoporous carbon spheres shows some bands for carbon-based functional groups such as C–O (1050 cm^{-1}), C–H (1135 cm^{-1}), and C=C (1630 cm^{-1}).[16]

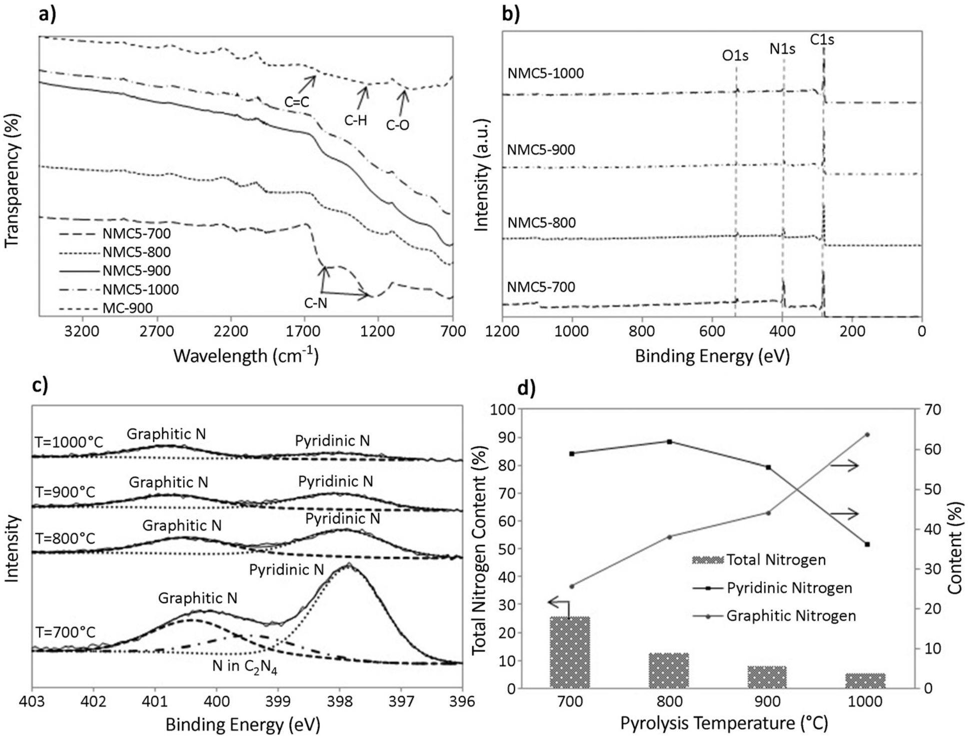

Figure 3. (a) FTIR spectra, (b) XPS survey spectra, (c) high-resolution N1s spectra, and (d) nitrogen content plots against pyrolysis temperature for *N*-doped mesoporous carbon spheres with an N/C ratio of 5 at different pyrolysis temperatures (700–1000 °C).

Additionally, the FTIR spectra of nitrogen-doped mesoporous carbons prepared at different pyrolysis temperatures confirm the presence of C–N (1230, 1560 cm^{-1}).[17] As can be clearly seen from this figure, the peak related to the C–N binding in the structure of g-C_3N_4 (1230 cm^{-1}) disappears with increasing the pyrolysis temperature to 900 °C, which confirms the complete decomposition of g-C_3N_4 and nitrogen doping at such a high temperature.

The nitrogen-bonding configuration of fresh NMCs were further investigated by X-ray photoelectron spectroscopy (XPS). The XPS survey spectra of NMCs synthesized at different pyrolysis temperatures (Figure 3 b) exhibit similar elemental compositions as those obtained from EDS and reported previously for *N*-doped carbons including a dominant C1s peak, N1s peak, and O1s peak.[4a,18] The incorporation of nitrogen heteroatoms into the carbon framework of the carbon spheres could be also confirmed by high-resolution N1s spectra (Figure 3 c). The calculated total nitrogen content (Figure 3 d) exhibits decreased from 25.7 % to 5.5 % when the pyrolysis temperature was increased from 700 to 1000 °C (the high nitrogen content at 700 °C is attributed to the nitrogen species present in the structure of remaining g-C_3N_4, which did not completely decompose), thus indicating decomposition of C–N bonds and nitrogen leaching at higher pyrolysis temperature, which is consistent with the FTIR results and other reported data.[7,15,18] Specifically, as shown in Figure 3 c, the N1s spectra have two peaks at 398–399 eV and 400–401 eV, which are assigned to pyridinic-like and graphitic-like (quaternary-N) nitrogen species, respectively. For NMC5-700, a peak at 399.4 eV is observed, which can be assigned to the pyrrolic-like nitrogen species as suggested in other reports.[4b,15,19] The relative content of the graphitic-like nitrogen species increases from 25.6 to 63.6 % with increasing pyrolysis temperature from 700 to 1000 °C, while that of the pyridine-like nitrogen species is correspondingly reduced from 59.1 to 36.3 %. This may be due to the fact that graphitic-like nitrogen species have a higher binding energy and higher thermal stability than pyridinic-like nitrogen species.[15]

Raman spectra further demonstrate the effect of pyrolysis temperatures on the chemical structure of mesoporous carbon spheres (Figure 4 a). Two remarkable peaks are visible, with the typical G band representing sp^2-hybridized graphitic carbon atoms (~1580 cm^{-1}) and the D band resulting from the disordered carbon framework at defect sites (~1350 cm^{-1}). For mesoporous carbon spheres without any nitrogen dopant (Figure S5a, Supporting Information), the D and G bands are weaker than those for the samples with nitrogen dopant, and the intensity ratio of the G and D bands (I_G/I_D) decreases with increasing nitrogen content, indicating that the degree of

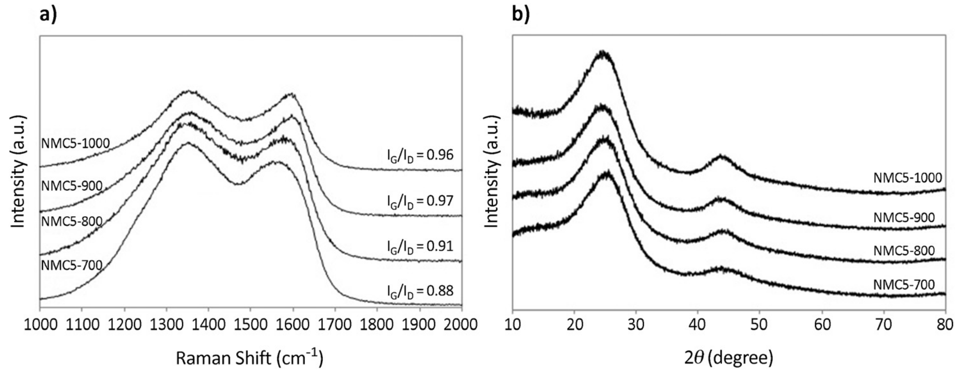

Figure 4. (a) Raman spectra and (b) wide-angle XRD patterns of *N*-doped mesoporous carbon spheres with an N/C ratio of 5 at different pyrolysis temperatures (700–1000 °C).

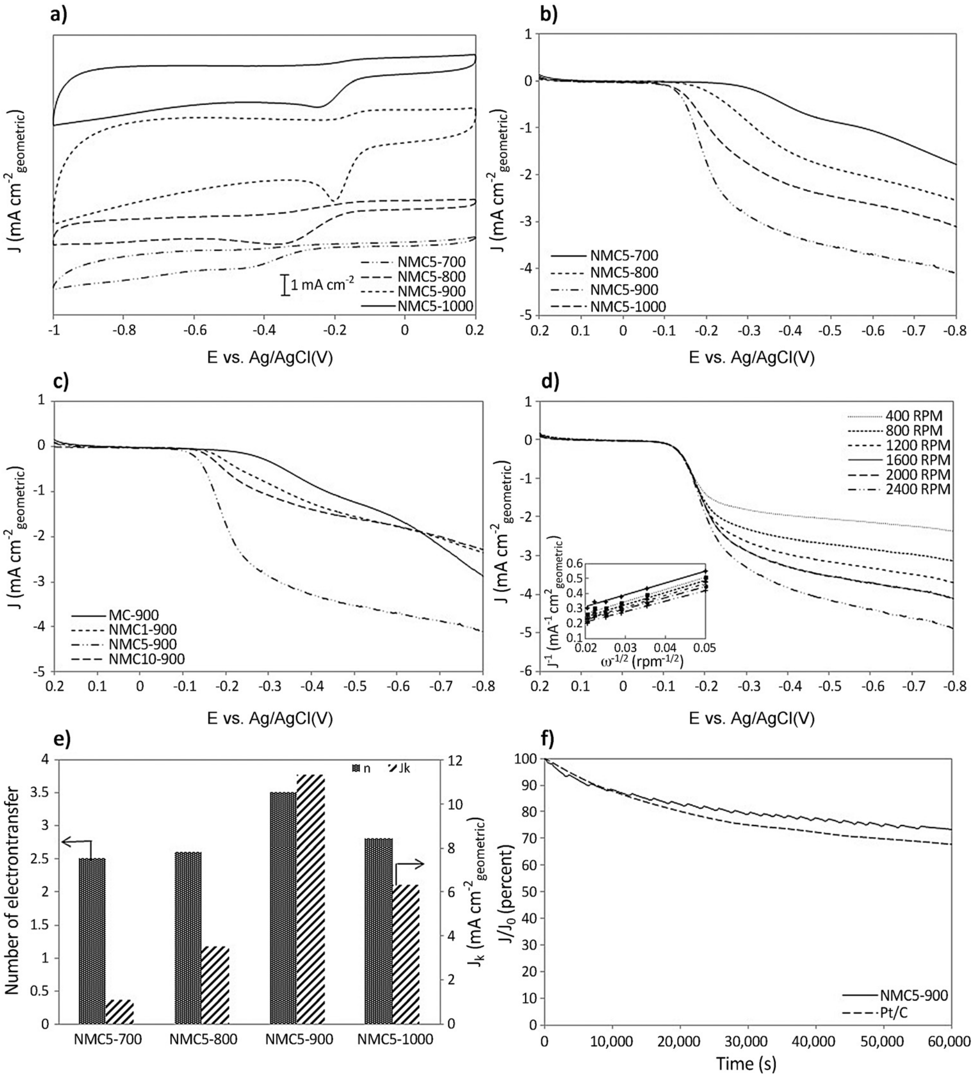

Figure 5. (a) CVs of ORR on the synthesized electrocatalysts at different pyrolysis temperatures in an O_2-saturated 0.1 M KOH solution (scan rate: 100 mV s^{-1}). (b) LSVs of the synthesized electrocatalysts at different pyrolysis temperatures on an RDE (1600 rpm, scan rate: 5 mV s^{-1}), (c) LSVs of the synthesized electrocatalysts with different N/C ratios on a RDE (1600 rpm, scan rate: 5 mV s^{-1}), (d) LSVs and (inset of d) K–L plots) of NMC5-900 on a RDE at different rotating speeds from 400 rpm to 2400 rpm, (e) summary of the kinetic current (J_k) and the electron transfer number (*n*) on the basis of RDE data at −0.5 V, (f) the chronoamperometric response of NMC5-900 and commercial Pt/C at −0.3 V after 60 000 s.

graphitic structure is reduced by nitrogen doping. As shown in Figure 4a, both D and G bands get narrower as the calcination temperature increases, which is attributed to the formation of graphitic domains due to "self-repairing" of the spheres at higher temperature.[12b] Specifically, the highest I_G/I_D ratio among all synthesized samples was obtained for NMC5-900, indicating its highest graphitization degree and best electrical conductivity.

Wide-angle XRD patterns (Figure 4b, S5b) show two broad XRD diffraction peaks at $2\theta=$ 23–24° and $2\theta=43$–44°, which are usually attributed to the (002) plane of the graphitic structure and the (100) plane of the disordered amorphous carbon, respectively.[15,19a] As the pyrolysis temperature increases, the peak positions slightly shift to a smaller angle and peaks are further intensified since the degree of graphitization is improved at higher pyrolysis temperature.[4a]

The ORR catalytic performance of synthesized materials was first evaluated by cyclic voltammetry (CV) in an O_2-saturated electrolyte (0.1 M KOH) at a scan rate of 100 mV s^{-1}. As shown in Figure 5a, NMC5-900 showed a distinct ORR peak centered at −0.2 V (vs. Ag/AgCl) and obviously the biggest double-layer capacitance derived from the highest specific surface area as compared to other electrocatalysts prepared at different pyrolysis temperatures or with different nitrogen precursor amount (Figure S6, Supporting Information). Linear sweep voltammetrograms (LSVs) of all samples were then monitored using a rotating disk electrode (RDE) in O_2-saturated electrolyte to further investigate the ORR activity of electrocatalysts. The onset potential and reaction current density of NMCs were acquired from LSVs at 1600 rpm (Figure 5b, c). Remarkably, NMC5-900 showed the most positive onset potential (−0.11 V) and highest reaction current density at a certain overpotential, suggesting the fastest reaction kinetics among the samples synthesized under different conditions (calcination temperature and/or N/C precursor ratio). This may be due to its high graphitic nitrogen content enhanced by transformation of pyridinic nitrogen to graphitic nitrogen during thermal annealing at temperatures higher than 800 °C. It is believed that graphitic-like nitrogen species have a higher activity toward ORR than pyridinic-like nitrogen species.[20] Moreover, as the nitrogen atom in the graphitic-like nitrogen species is inserted into the carbon matrix and bonded to three carbon atoms, such a configuration can improve the conductivity of carbon materials due to the presence of five valence electrons including three valence electrons from σ bonds, the fourth electron from the *p*-state, and the fifth electron from the π*-state, giving a *p*-doping effect.[14] The different doping positions of pyridinic-like nitrogen species make them more complicated in terms of their influence on the electrochemical performance of *N*-doped carbon materials. Although there is an additional electron in the delocalized π-system on pyridinic-like nitrogen at the edge of the carbon matrix, which can improve the conductivity of carbon materials,[21] the pyridinic-like nitrogen at the basal planes causes many surface defects and increases the localized electronic states in the carbon matrix, which weakens the electrochemical performance of *N*-doped carbon materials.[4c] Therefore, graphitic-like nitrogen is favorable for an improved electrochemical performance of synthesized NMC spheres.

A series of LSVs were also recorded at rotating rates from 400 to 2400 rpm for NMC5-900 (Figure 5 d and Figures S7 and S8), which show reaction current growth at increasing rotation speed. The inset in Figure 5 d presents the Koutecky–Levich plots of NMC5-900 at different potentials obtained from RDE at several rotation rates. Accurate electron transfer numbers (*n*) and limiting current density (J_K) of all synthesized materials were calculated through K–L plots (Figures S7 and S8, Supporting Information). Figure 5 e shows the n and J_K values at -0.5 V of NMCs synthesized at different pyrolysis temperatures; these data clearly indicate that oxygen is reduced on the NMC5-900 catalyst via a more efficient reaction pathway (close to four electron ($4e^-$) reaction) with higher limiting current density, while this reaction occurs via a combined $2e^-$ and $4e^-$ reaction pathway on other catalysts (Figure S9, Supporting Information).

The durability of the NMC5-900 catalyst was evaluated by the chronoamperometric response under a constant voltage of -0.3 V (Figure 4 f). This catalyst exhibits a reliable stability, retaining 73 % of the initial current after 60 000 seconds, while the Pt/C catalyst loses 35 % of its initial current after the same period of time. The current loss of the catalysts can be possibly related to desorption of OH^- (product) from the catalyst's surface, peeling off the catalyst from the glassy carbon electrode, and to the instability of the Nafion polymer binder. Therefore, other polymeric binders or supports can be applied to form strong interactions such hydrogen bonding and covalent bonding with the catalyst to assure strong electrode durability during the ORR process.[19a, 22] The methanol tolerance ability of the selected catalyst was tested by monitoring the ORR current after the addition of methanol into the electrolyte solution (with the resulting methanol concentration of 3 M). As shown in Figure S10 in the Supporting Information, there is no significant change in the ORR performance of the NMC5-900 catalyst under -0.3 V after the addition of methanol into electrolyte, suggesting the high selectivity of the catalyst towards ORR.

Conclusions

In summary, we have developed a simple and low-cost method to synthesize a series of *N*-doped mesoporous carbon spheres via a dual soft-templating procedure using a resorcinol-formaldehyde resin and melamine as inexpensive carbon precursor and nitrogen source, respectively. The synthesized NMCs exhibit a high surface area, large pore volume, narrow mesopore size distribution, high conductivity, high nitrogen content, and excellent catalytic activity toward ORR. The superior electrocatalytic activity of NMCs as compared to MCs without nitrogen doping could be attributed to the enhanced graphitization degree and the incorporation of nitrogen atoms into the carbon lattice, which favor the reactivity of the neighboring carbon atoms via alteration of the electronic structure, as in the case of *N*-doped carbon nanotubes[23] and *N*-doped graphene.[12b] Moreover, the best performance of NMC5-900 for catalyzing ORR would be the result of a balanced graphitization degree and active species retained at moderate heating temperature, the presence of highly active C–N species, good conductivity, well-structured mesoporosity, large pore size, sufficient surface area, and high pore volume, which make NMC5-900 a promising catalyst for ORR in alkaline solutions. This comprehensive study can also provide some information regarding the effect of different parameters on the catalytic performance of the synthesized NMC samples, which is beneficial for the development of analogous electrocatalysts.

Experimental Section

Chemicals

Pluronic (F127), potassium chloride (KCl, $\geq$99 %), mesitylene (1,3,5-trimethylbenzene, 98 %), resorcinol ($C_6H_6O_2$, 99 %) and melamine ($C_3H_6N_6$,%99) were purchased from Sigma–Aldrich. Hydrochloric acid (HCl, 37 %), ethanol (EtOH, absolute) and formaldehyde solution (HCHO, 37/10) were purchased from Chem-Supply. Fluorocarbon surfactant (FC4) was purchased from Yick-Vic chemicals & pharmaceuticals (H.K) Ltd., China. All chemicals were directly used without any further treatment and purification.

Synthesis of *N*-doped mesoporous carbon spheres

In a typical synthesis, 1.0 g of well-dissolved Pluronic in 25 mL of ethanol, 0.2 g of fluorocarbon surfactant, and 1.0 g of potassium chloride were added to 60 mL of 2 M hydrochloric acid at 30 °C under vigorous stirring (1000 rpm) followed by introduction of 1 mL of mesitylene. When the copolymer was fully dissolved, 0.56 mL of formaldehyde solution and 0.4 g of resorcinol were added to the reaction solution and stirred for 24 h at 30 °C. Afterwards, the solution was heated for 24 h at 100 °C under static conditions in a Teflon-lined autoclave and the solid product was collected by centrifugation and washed with ethanol and deionized water followed by air-drying at 100 °C for 48 h. The obtained polymers were finely ground with a proper amount of melamine (melamine/carbon precursors ratio, denoted as N/C ratio = 1, 5, 10) and the mixtures were heated at 350 °C for 3 h at a heating rate of 1.5 $^{\circ}C\,min^{-1}$ in a nitrogen flow to remove the template. Then, *N*-doped mesoporous carbon spheres were produced by direct carbonization of the as-made polymer at different temperatures (700, 800, 900 and 1000 °C) for 4 h in a nitrogen flow at a heating rate of 2.3 $^{\circ}C\,min^{-1}$. After the pyrolysis step, the final products were left to cool down to room temperature under the same atmosphere and collected for physical and (electro)chemical characterization. The resulting *N*-doped mesoporous carbon spheres designated as NMCR-T, where R and T represent the N/C-precursors ratio and carbonization temperature, respectively. Pure mesoporous carbon spheres without nitrogen doping were synthesized at 900 °C (denoted as MC-900) for the purpose of comparison.

Characterization of materials

The morphology of the synthesized samples was characterized by using a high-resolution transmission electron microscope (TEM, CM 200 TEM/STEM, Philips) operating at 120 kV and a scanning electron microscope (SEM, Quanta 450 ESEM, FEI) operating at 10 kV. Nitrogen adsorption–desorption isotherms were measured on Tristar II instrument (Micrometrics) at −196 °C. Pore size distributions were calculated by using the Barrett–Joyner–Halenda (BJH) model using the data of adsorption branch of the isotherm. The specific surface areas were calculated using adsorption data at the relative pressure range of $P/P_0 = 0.05$–0.3 by the Brunauer–Emmett–Teller (BET) model. The total pore volumes were estimated from the adsorbed amounts at a relative pressure (P/P_0) of 0.994. All the samples were degassed at 150 °C for more than 6 h prior to the nitrogen adsorption–desorption tests. Fourier transform infrared (FTIR) spectra were obtained using a Nicolet 6700 spectrometer (Thermo Fisher). Raman spectra were collected on a LabRAM instrument (Horiba Ltd) with a 532 nm laser. X-ray diffraction (XRD) patterns (10–80° in 2θ) were collected on a powder X-ray diffractometer at 40 kV and 15 mA using $\mathrm{Co}_{K\alpha}$ radiation (Miniflx-600, Rigaku). X-ray diffraction patterns at low angle (0.5–5° in 2θ) were collected on a D8 X-ray diffractometer (Bruker) equipped with a LynxEye detector operating at 40 kV and 40 mA using $\mathrm{Cu}_{K\alpha}$ radiation.

Electrode preparation and electrochemical measurements

All electrochemical measurements were performed under identical conditions (the same catalyst mass loading). In a typical electrode preparation, 2.0 mg of synthesized catalyst were ultrasonically dispersed in 0.5 mL of 0.5 % Nafion aqueous solution. Subsequently, 20 μL of the catalyst dispersion (4.0 mg mL^{-1}) were transferred onto the glassy carbon rotating disk electrode (RDE, 0.196 cm^2, Pine Research Instrumentation, USA) via a controlled drop-casting approach and dried in an ambient environment for 1 h, serving as a working electrode. KOH aqueous solution (0.1 M) was used as the electrolyte, which was purged with O_2 for at least 30 min to achieve O_2-saturated solution. The reference electrode was an Ag/AgCl in 4 M KCl solution and the counter electrode was a platinum wire.

Cyclic voltammograms (CVs) and linear sweep voltammograms (LSVs) tests were carried out using a glassy carbon rotating disk electrode. The scan rate of CVs was kept as 100 mV s^{-1}, while it was 5 mV s^{-1} for LSVs and RDE tests. The data were recorded using a CHI 760D bipotentiostat (CH Instruments, Inc., USA).

The overall electron transfer numbers per oxygen molecule involved in a typical ORR process can be calculated from the slopes of Koutecky–Levich plots using the following equation:

$$1/j_D = 1/j_K + 1/(B\omega^{1/2}) \qquad (1)$$

where j_K is the kinetic current density in mA cm^{-2} at a constant potential, j_D is the measured current density on RDE, ω is the electrode rotating speed in rpm, and B is the reciprocal of the slope, which could be determined from the slope of Koutecky–Levich plot using Levich equation:

$$B = 0.2nF(\nu)\text{-}1/6C_{O2}(D_{O2})^{2/3} \qquad (2)$$

where n is the number of electrons transferred per oxygen molecule, F is the Faraday constant, ν is the kinetic viscosity, C_{O2} is the bulk concentration of O_2, and D_{O2} is the diffusion coefficient of O_2 in 0.1 M KOH. The constant 0.2 is adopted when the rotating speed is expressed in rpm.

The stability tests were performed at a static potential of −0.3 V vs. Ag/AgCl at room temperature in the O_2-saturated 0.1 M KOH aqueous electrolyte. The methanol tolerance of materials was tested under the same conditions before and after adding methanol to the electrolyte.

Acknowledgements

This research is financially supported by Australian Research Council (ARC) through the Discovery Project program (DP1095861, DP130104459).

Keywords: electrocatalyst · mesoporous carbon · nitrogen-doping · oxygen reduction reaction · soft-templating

[1] a) J. Liang, X. Du, C. Gibson, X. W. Du, S. Z. Qiao, *Adv. Mater.* **2013**, *25*, 6226–6231; b) D. Zhao, Y. Wan, W. Zhou, *Ordered Mesoporous Materials, Vol. 1, 1st ed.*, Wiley-VCH, Weinheim, **2013**; c) J. Wei, D. Zhou, Z. Sun, Y. Deng, Y. Xia, D. Zhao, *Adv. Funct. Mater.* **2013**, *23*, 2322–2328; d) T. Yang, J. Liu, R. Zhou, Z. Chen, H. Xu, S. Z. Qiao, M. J. Monteiro, *J. Mater. Chem. A* **2014**, *2*, 18139–18146; e) M. Armand, J. M. Tarascon, *Nature* **2008**, *451*, 652–657; f) B. C. H. Steele, A. Heinzel, *Nature* **2001**, *414*, 345–352.

[2] S. H. Oh, R. Black, E. Pomerantseva, J.-H. Lee, L. F. Nazar, *Nat. Chem.* **2012**, *4*, 1004–1010.

[3] a) S. Ratso, I. Kruusenberg, M. Vikkisk, U. Joost, E. Shulga, I. Kink, T. Kallio, K. Tammeveski, *Carbon* **2014**, *73*, 361–370; b) Y. Hu, H. Liu, Q. Ke, J. Wang, *J. Mater. Chem. A* **2014**, *2*, 11753–11758; c) H. Chen, F. Sun, J. Wang, W. Li, W. Qiao, L. Ling, D. Long, *J. Phys. Chem. C* **2013**, *117*, 8318–8328.

[4] a) J. Yu, M. Guo, F. Muhammad, A. Wang, G. Yu, H. Ma, G. Zhu, *Microporous Mesoporous Mater.* **2014**, *190*, 117–127; b) Y. Okamoto, *Appl. Surf. Sci.* **2009**, *256*, 335–341; c) Y. Wang, Y. Shao, D. W. Matson, J. Li, Y. Lin, *ACS Nano* **2010**, *4*, 1790–1798.

[5] J. Yang, Y. Zhai, Y. Deng, D. Gu, Q. Li, Q. Wu, Y. Huang, B. Tu, D. Zhao, *J. Colloid Interface Sci.* **2010**, *342*, 579–585.

[6] S. Feng, W. Li, Q. Shi, Y. Li, J. Chen, Y. Ling, A. M. Asiri, D. Zhao, *Chem. Commun.* **2014**, *50*, 329–331.

[7] W.-J. Jiang, J.-S. Hu, X. Zhang, Y. Jiang, B.-B. Yu, Z.-D. Wei, L.-J. Wan, *J. Mater. Chem. A* **2014**, *2*, 10154–10160.

[8] W. Li, Q. Yue, Y. Deng, D. Zhao, *Adv. Mater.* **2013**, *25*, 5129–5152.

[9] K. K. R. Datta, V. V. Balasubramanian, K. Ariga, T. Mori, A. Vinu, *Chem. Eur. J.* **2011**, *17*, 3390–3397.

[10] a) D. Wei, Y. Liu, Y. Wang, H. Zhang, L. Huang, G. Yu, *Nano Lett.* **2009**, *9*, 1752–1758; b) J. Park, Y. Nabae, T. Hayakawa, M.-a. Kakimoto, *ACS Catal.* **2014**, *4*, 3749–3754; c) W. Xia, J. Masa, M. Bron, W. Schuhmann, M. Muhler, *Electrochem. Commun.* **2011**, *13*, 593–596; d) W. Yang, T.-P. Fellinger, M. Antonietti, *J. Am. Chem. Soc.* **2011**, *133*, 206–209; e) L. Lai, J. R. Potts, D. Zhan, L. Wang, C. K. Poh, C. Tang, H. Gong, Z. Shen, J. Lin, R. S. Ruoff, *Energy Environ. Sci.* **2012**, *5*, 7936–7942.

[11] a) B. Jürgens, E. Irran, J. Senker, P. Kroll, H. Müller, W. Schnick, *J. Am. Chem. Soc.* **2003**, *125*, 10288–10300; b) Y. Li, B. P. Bastakoti, M. Imura, J. Tang, A. Aldalbahi, N. L. Torad, Y. Yamauchi, *Chem. Eur. J.* **2015**, *21*, 6375–6380; c) J. Liu, T. Yang, D.-W. Wang, G. Q. Lu, D. Zhao, S. Z. Qiao, *Nat. Commun.* **2013**, *4*, 2798.

[12] a) Y. Zhang, Q. Pan, G. Chai, M. Liang, G. Dong, Q. Zhang, J. Qiu, *Sci. Rep.* **2013**, *3*, 1943; b) Z.-H. Sheng, L. Shao, J.-J. Chen, W.-J. Bao, F.-B. Wang, X.-H. Xia, *ACS Nano* **2011**, *5*, 4350–4358.

[13] N. D. Kim, W. Kim, J. B. Joo, S. Oh, P. Kim, Y. Kim, J. Yi, *J. Power Sources* **2008**, *180*, 671–675.

[14] H. M. Jeong, J. W. Lee, W. H. Shin, Y. J. Choi, H. J. Shin, J. K. Kang, J. W. Choi, *Nano Lett.* **2011**, *11*, 2472–2477.

[15] D. Zhang, Y. Hao, L. Zheng, Y. Ma, H. Feng, H. Luo, *J. Mater. Chem. A* **2013**, *1*, 7584–7591.

[16] J. Duan, Y. Zheng, S. Chen, Y. Tang, M. Jaroniec, S. Z. Qiao, *Chem. Commun.* **2013**, *49*, 7705–7707.

[17] H. Peng, Z. Mo, S. Liao, H. Liang, L. Yang, F. Luo, H. Song, Y. Zhong, B. Zhang, *Sci. Rep.* **2013**, *3*, 1765.

[18] Z. Liu, H. Nie, Z. Yang, J. Zhang, Z. Jin, Y. Lu, Z. Xiao, S. Huang, *Nanoscale* **2013**, *5*, 3283–3288.

[19] a) Y. Zhao, R. Nakamura, K. Kamiya, S. Nakanishi, K. Hashimoto, *Nat. Commun.* **2013**, *4*, 2390; b) T.-P. Fellinger, F. Hasché, P. Strasser, M. Antonietti, *J. Am. Chem. Soc.* **2012**, *134*, 4072–4075; c) Y. Zheng, Y. Jiao, L. Ge, M. Jaroniec, S. Z. Qiao, *Angew. Chem. Int. Ed.* **2013**, *52*, 3110–3116; *Angew. Chem.* **2013**, *125*, 3192–3198.

[20] a) K. Parvez, S. Yang, Y. Hernandez, A. Winter, A. Turchanin, X. Feng, K. Müllen, *ACS Nano* **2012**, *6*, 9541–9550; b) Y. Zheng, Y. Jiao, M. Jaroniec, Y. Jin, S. Z. Qiao, *Small* **2012**, *8*, 3550–3566; c) J. Zhang, Z. Zhao, Z. Xia, L. Dai, *Nat. Nano* **2015**, *48*, 1038.

[21] Z. R. Ismagilov, A. E. Shalagina, O. Y. Podyacheva, A. V. Ischenko, L. S. Kibis, A. I. Boronin, Y. A. Chesalov, D. I. Kochubey, A. I. Romanenko, O. B. Anikeeva, T. I. Buryakov, E. N. Tkachev, *Carbon* **2009**, *47*, 1922–1929.

[22] S. Chen, J. Duan, J. Ran, S. Z. Qiao, *Adv. Sci.* **2015**, *2*, 140015–140020.

[23] L. Mabena, S. Sinha Ray, S. Mhlanga, N. Coville, *Appl. Nanosci.* **2011**, *1*, 67–77.

Manuscript received: March 24, 2015
Accepted article published: April 16, 2015
Final article published: May 12, 2015

3.3. Supporting Information

This section is included in the thesis as supplementary information to section 3.2. It includes additional information which is not put in the main text of the published paper; however, it is freely accessible online as an electronic supplementary information.

CHEMISTRY
AN ASIAN JOURNAL

Supporting Information

Soft-Templating Synthesis of *N*-Doped Mesoporous Carbon Nanospheres for Enhanced Oxygen Reduction Reaction

Bita Bayatsarmadi,[a] Yao Zheng,[a] Mietek Jaroniec,[b] and Shi Zhang Qiao*[a]

asia_201500287_sm_miscellaneous_information.pdf

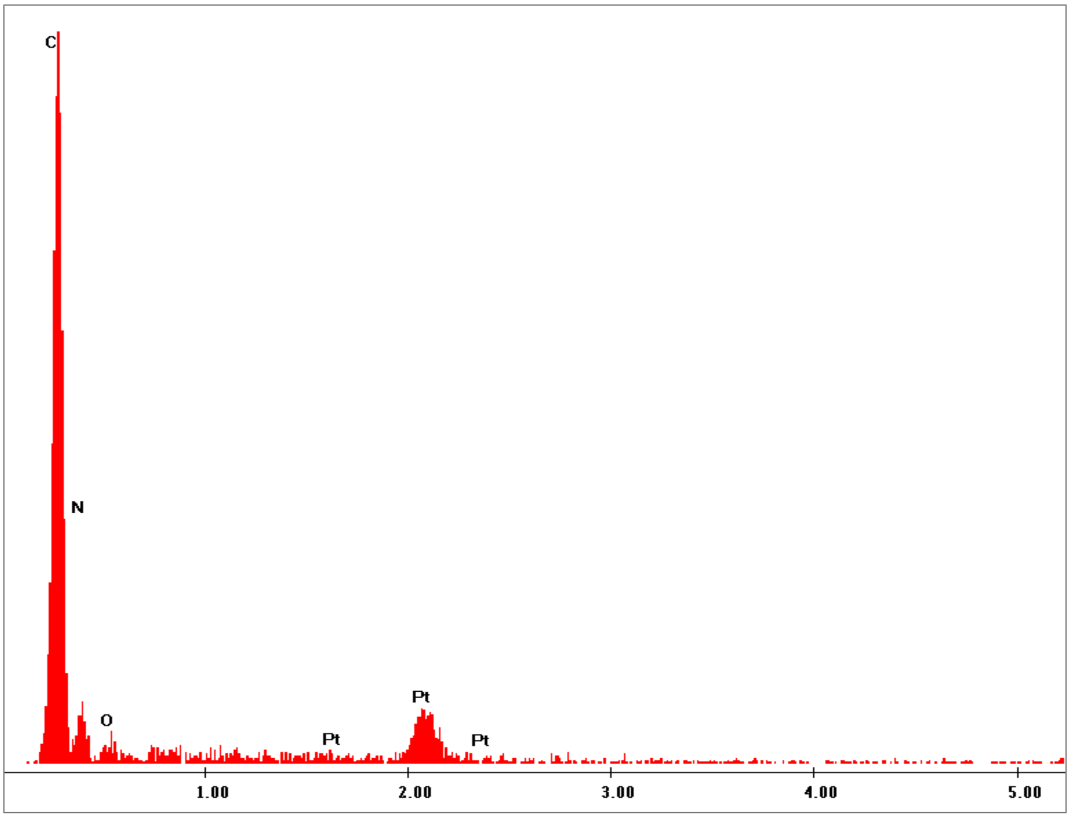

Figure S1. EDS spectra of N-doped mesoporous carbon spheres prepared by using the melamine/carbon precursors ratio = 5 and carbonization temperature of 900°C (NMC5-900).

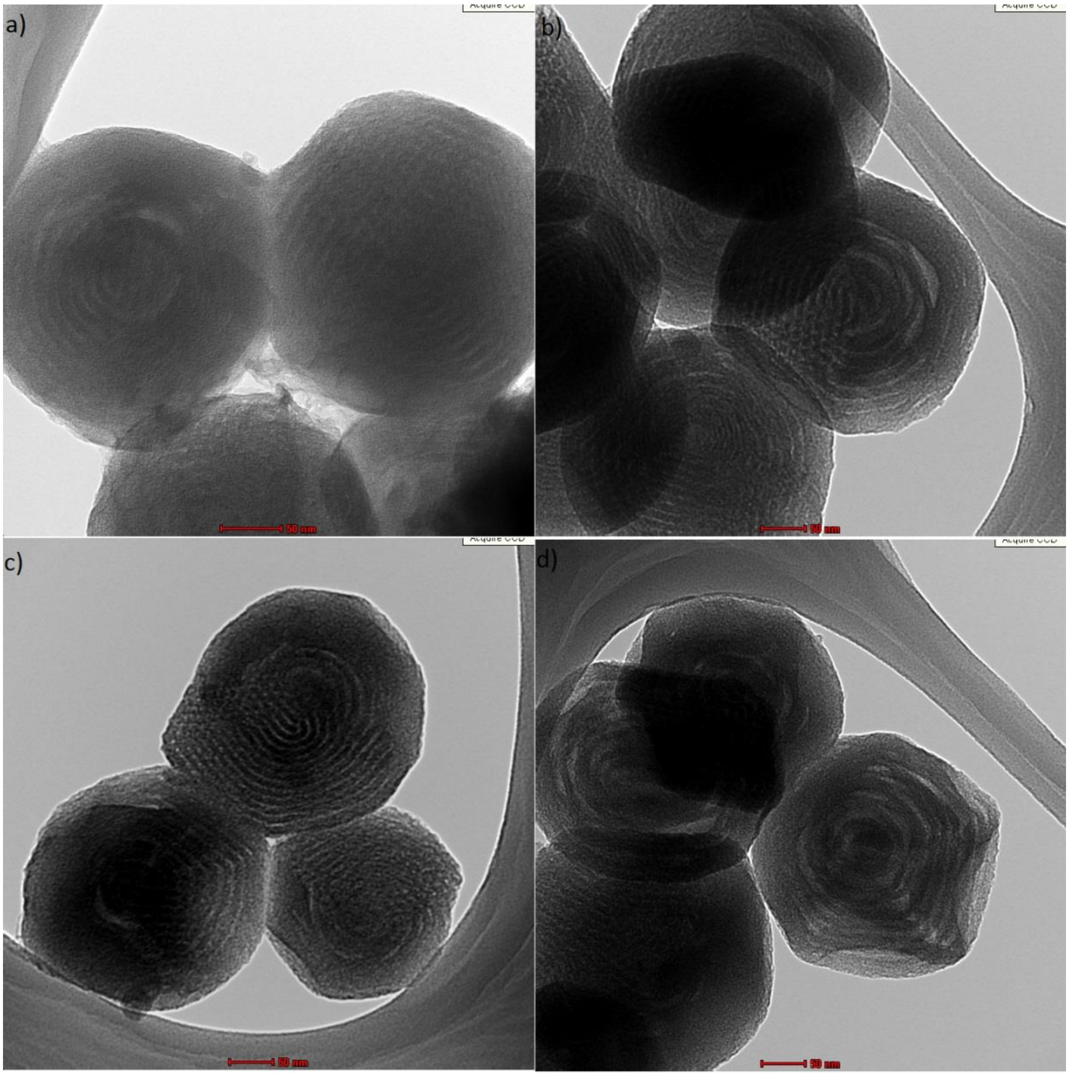

Figure S2. TEM images of N-doped mesoporous spheres prepared at different carbonization temperatures of (a) 700˚C, (b) 800˚C, (c) 900˚C and (d) 1000˚C.

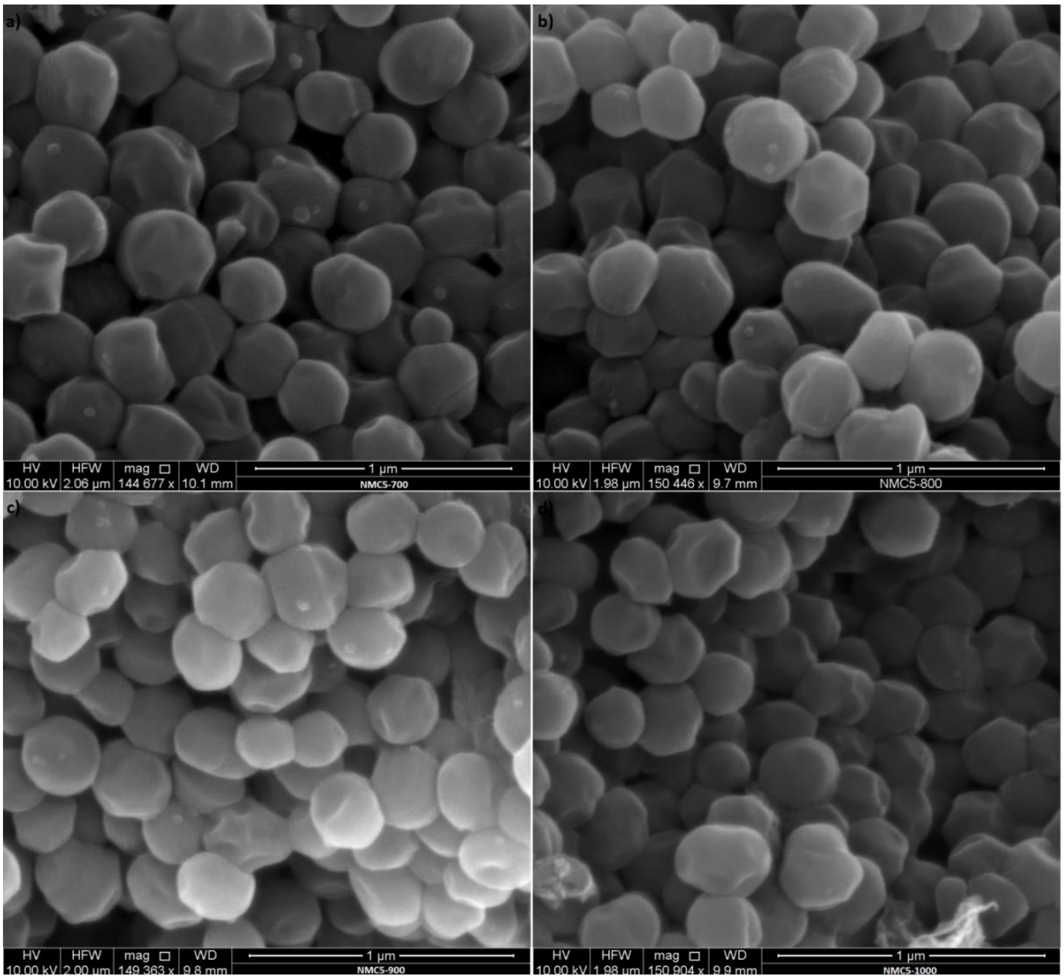

Figure S3. SEM images of N-doped mesoporous spheres prepared at different carbonization temperatures of (a) 700˚C, (b) 800˚C, (c) 900˚C and (d) 1000˚C.

a)

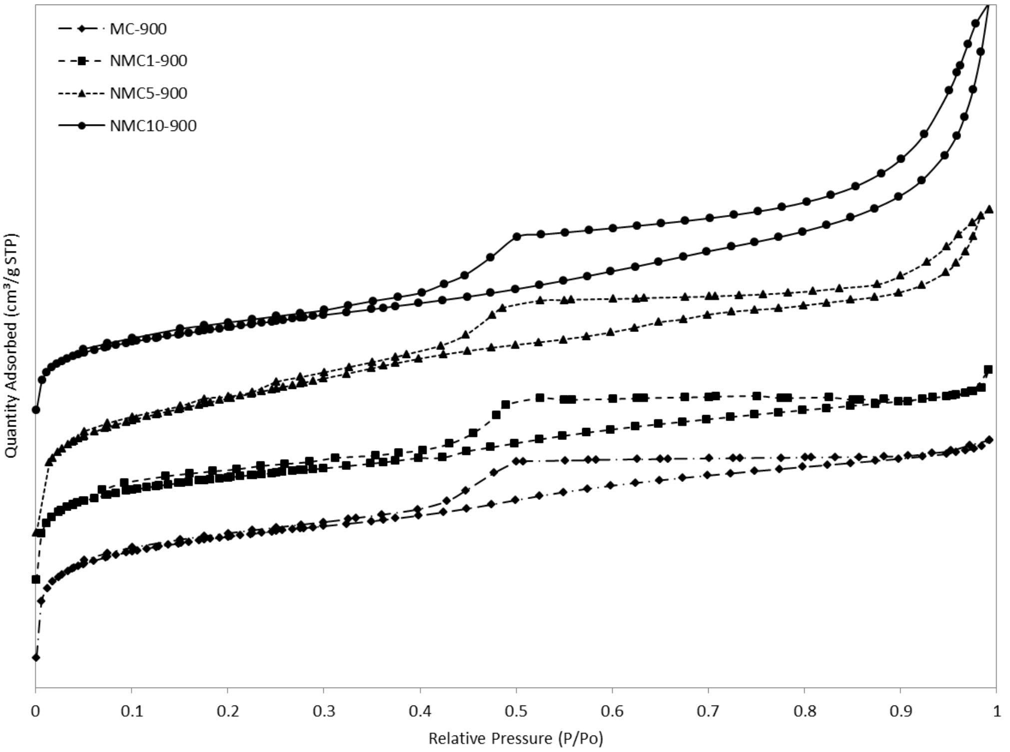

b)

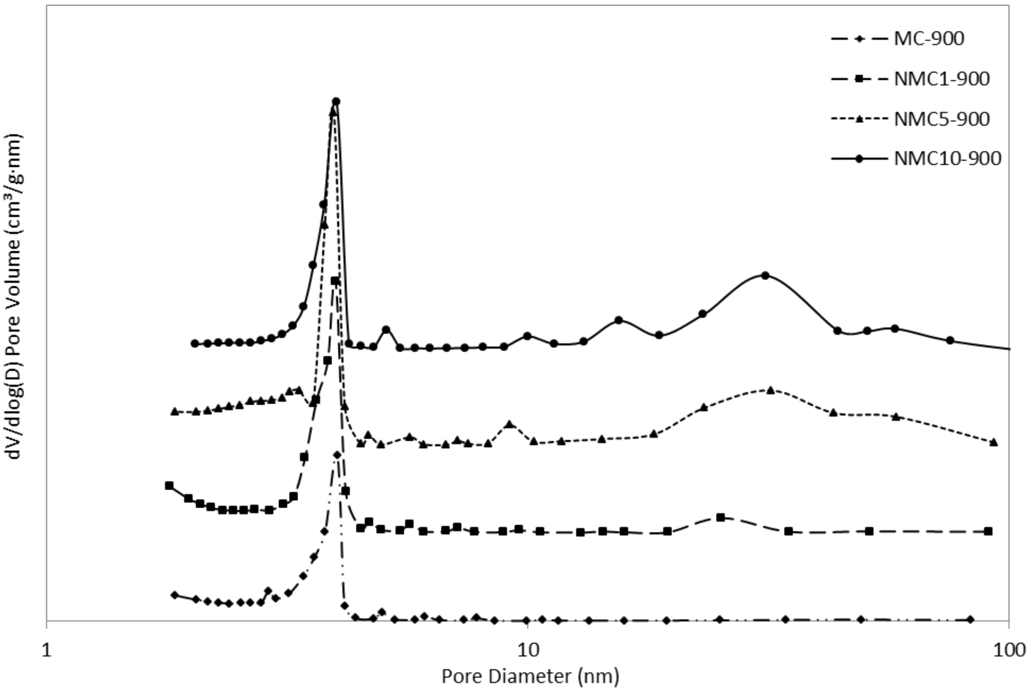

Figure S4. Effect of the N/C precursor ratio on (a) nitrogen sorption isotherm and (b) the corresponding pore size distributions.

a)

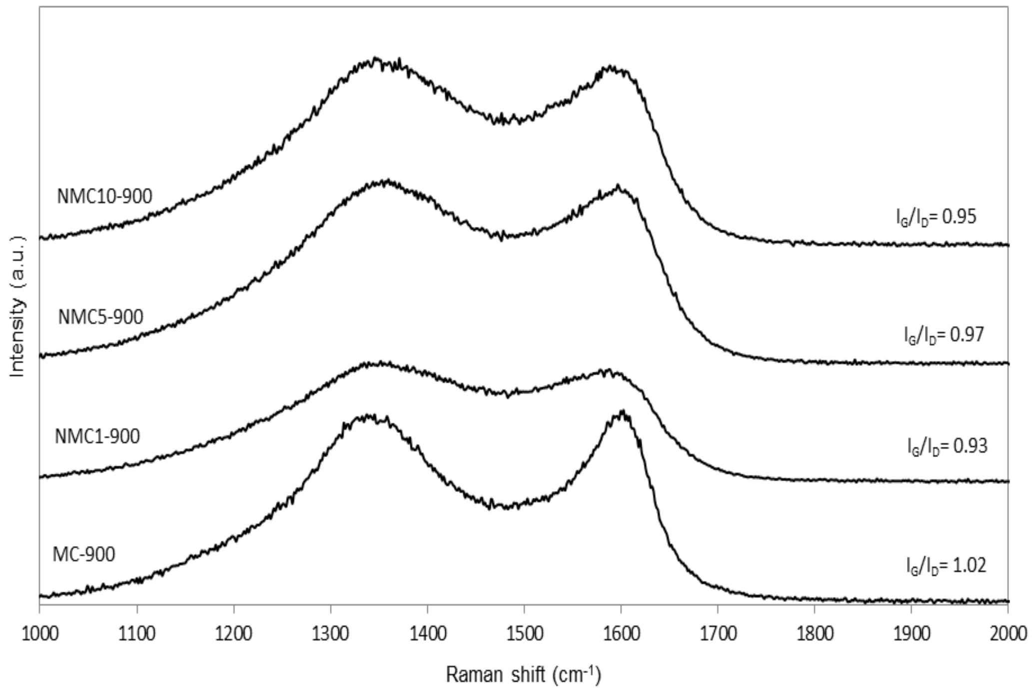

b)

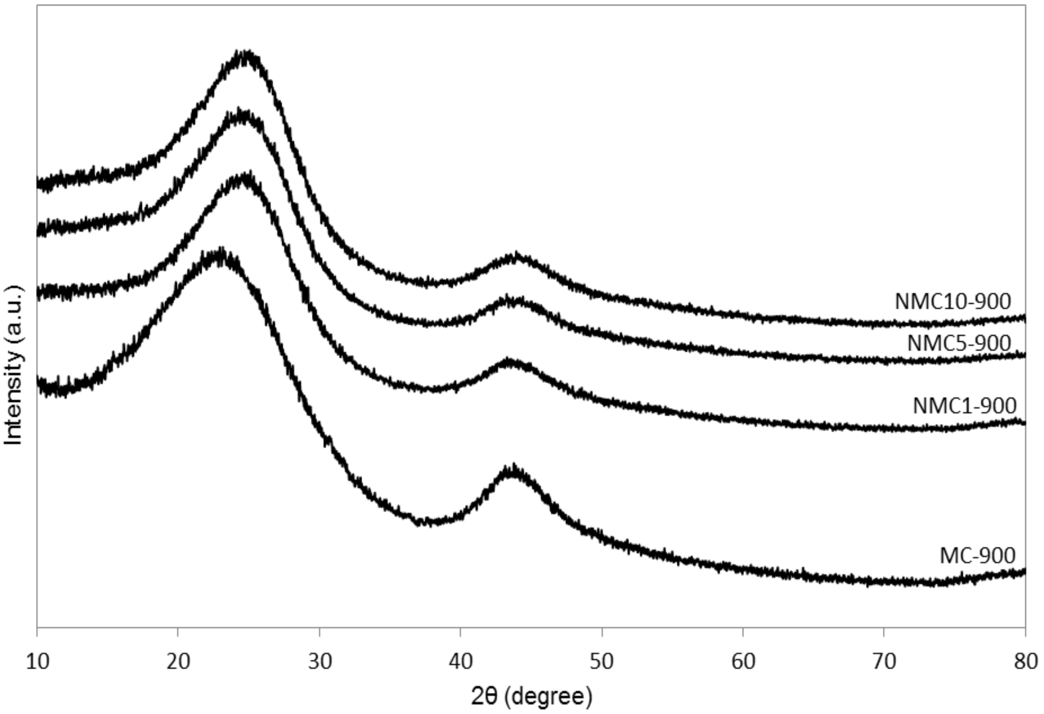

Figure S5. (a) Raman spectra and (b) wide-angle XRD patterns of mesoporous carbon spheres prepared by using different N/C precursor ratio.

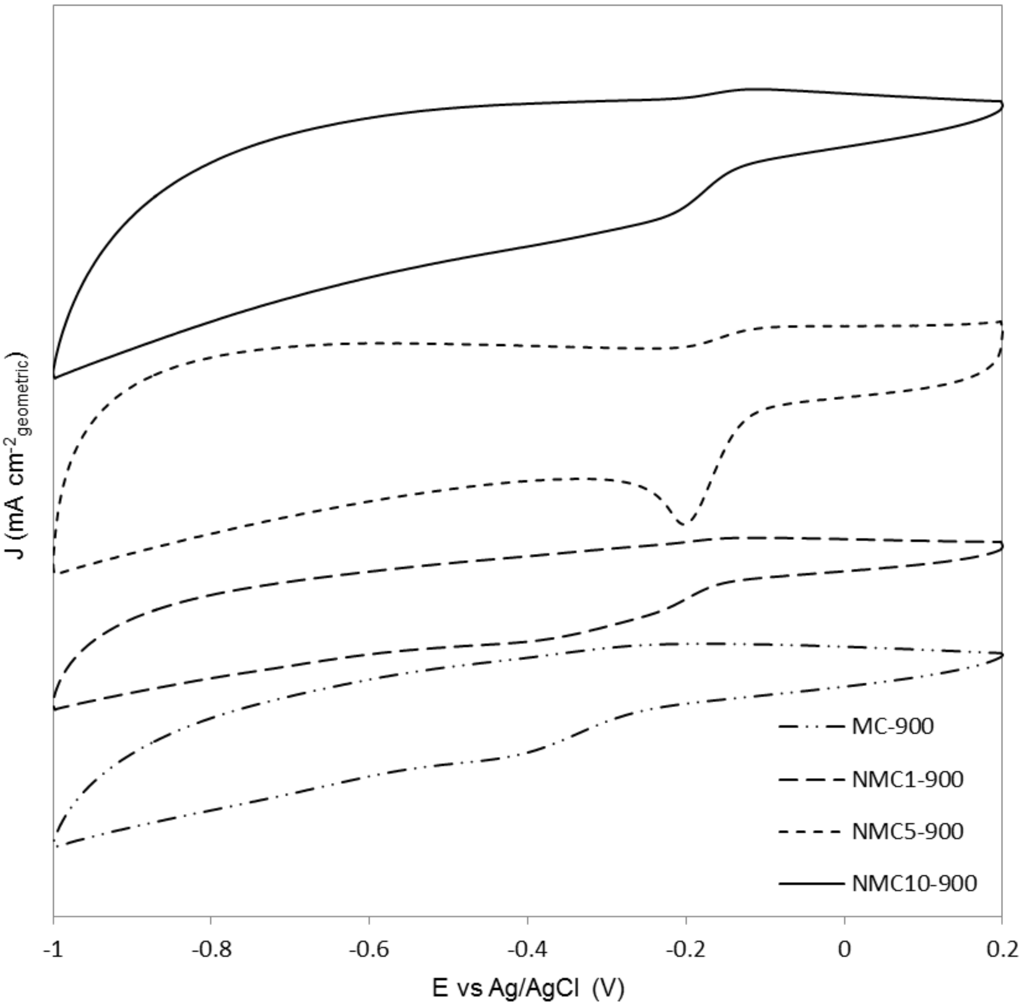

Figure S6. CV curves of mesoporous carbon spheres obtained by using different the N/C precursor ratio.

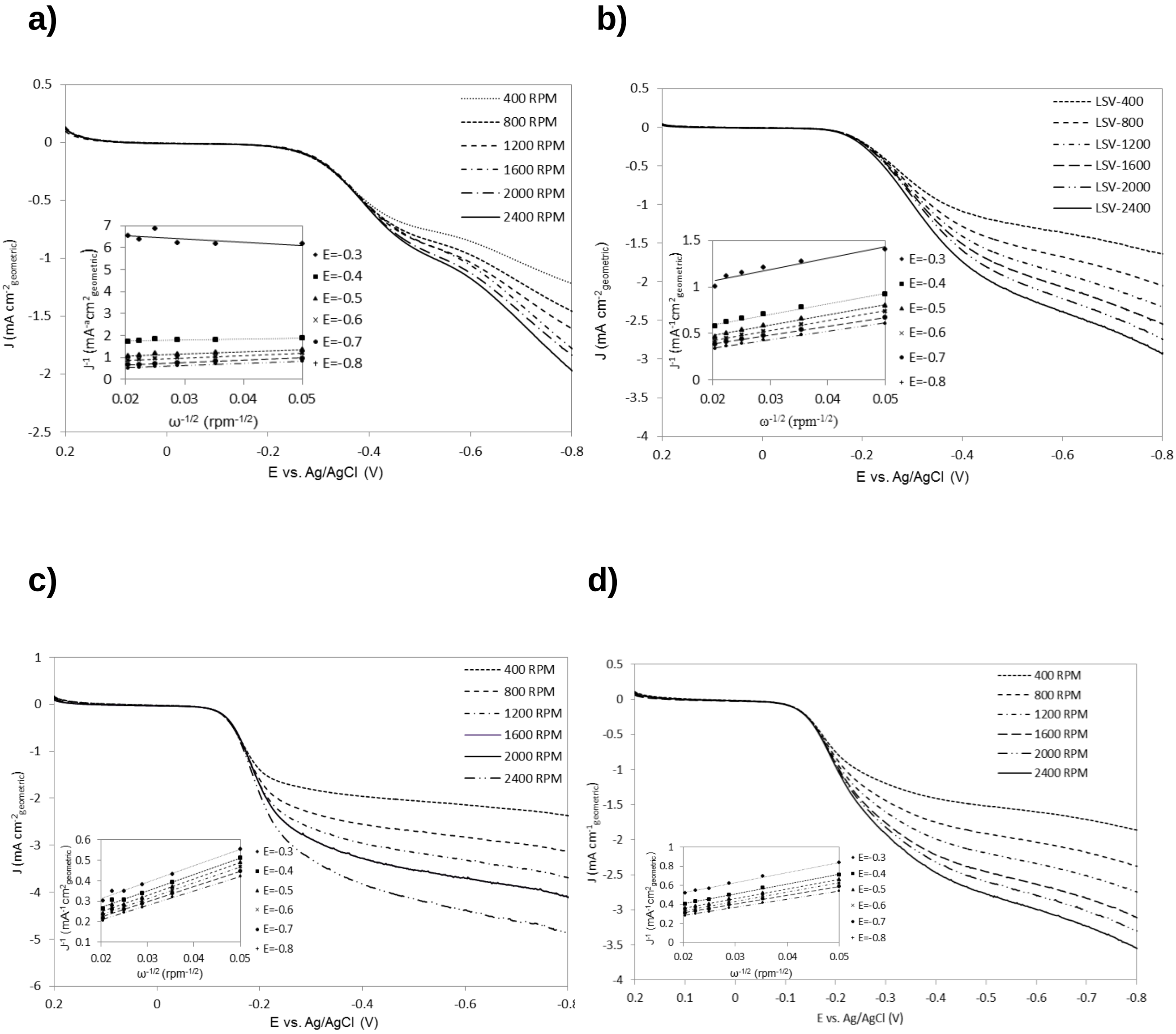

Figure S7. LSVs and K-L plots (insets in all panels) of (a) NMC5-700, (b) NMC5-800, (c) NMC5-900 and (d) NMC5-1000 on a RDE at different rotating speeds from 400prm to 2400 rpm.

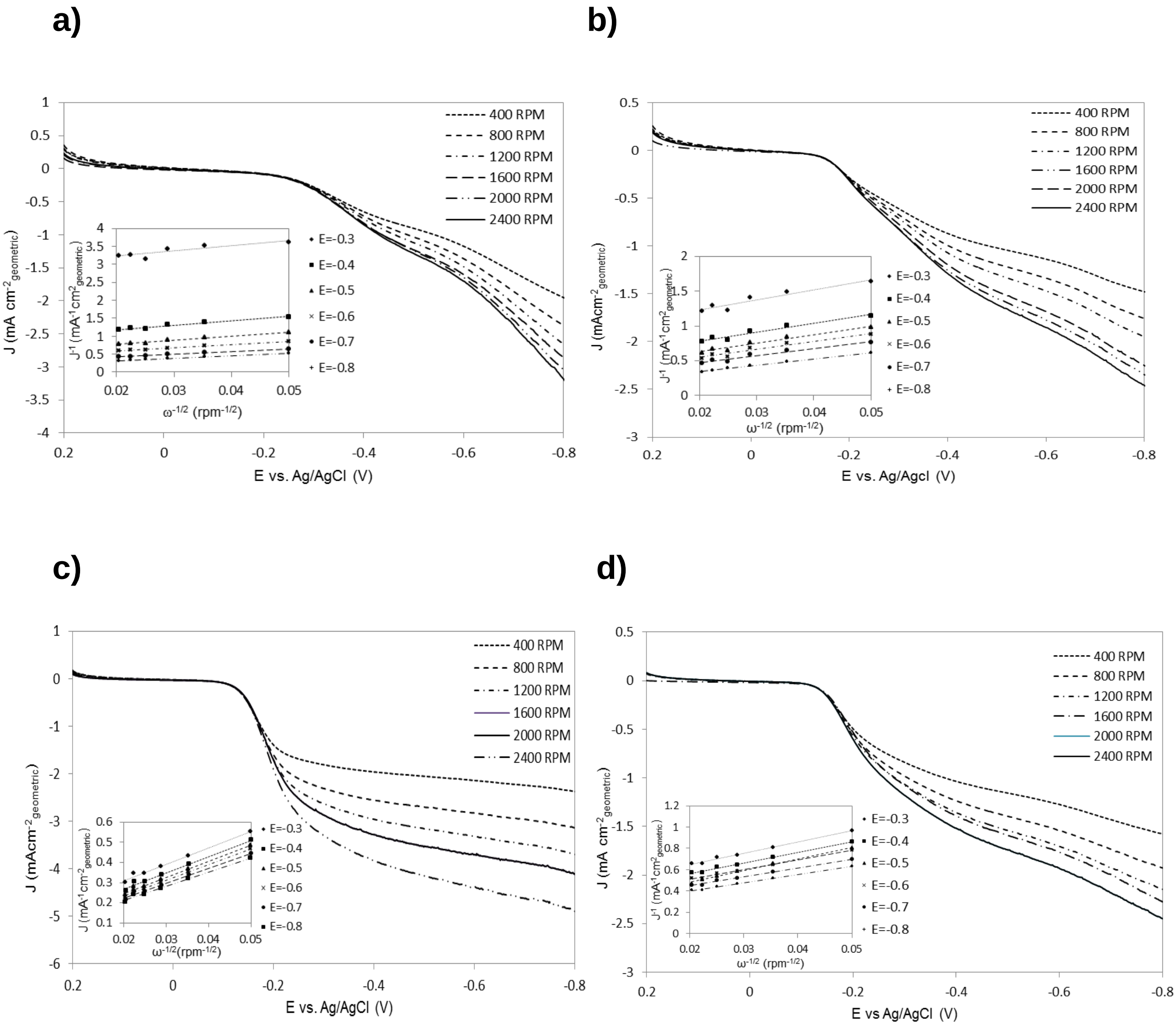

Figure S8. LSVs and K-L plots (insets in all panels) of (a) MC-900, (b) NMC1-900, (c) NMC5-900 and (d) NMC10-900 on a RDE at different rotating speeds from 400prm to 2400 rpm.

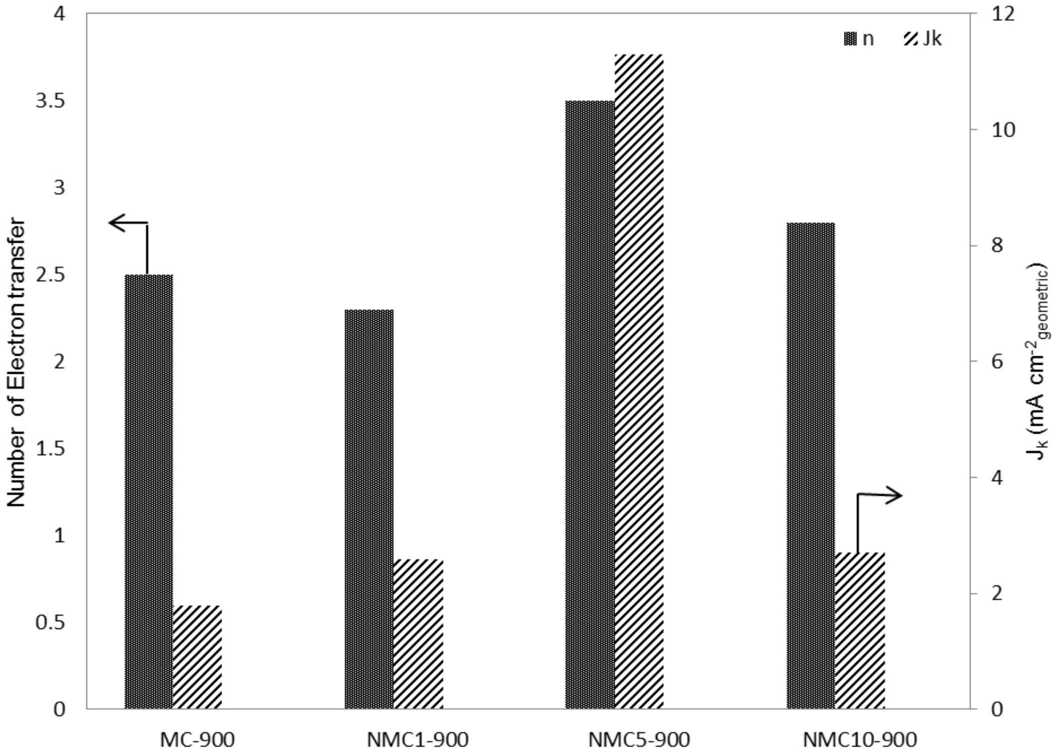

Figure S9. Electron transfer number and the limiting kinetic current density at -0.5 V of mesoporous carbon spheres prepared by using different N/C precursor ratios.

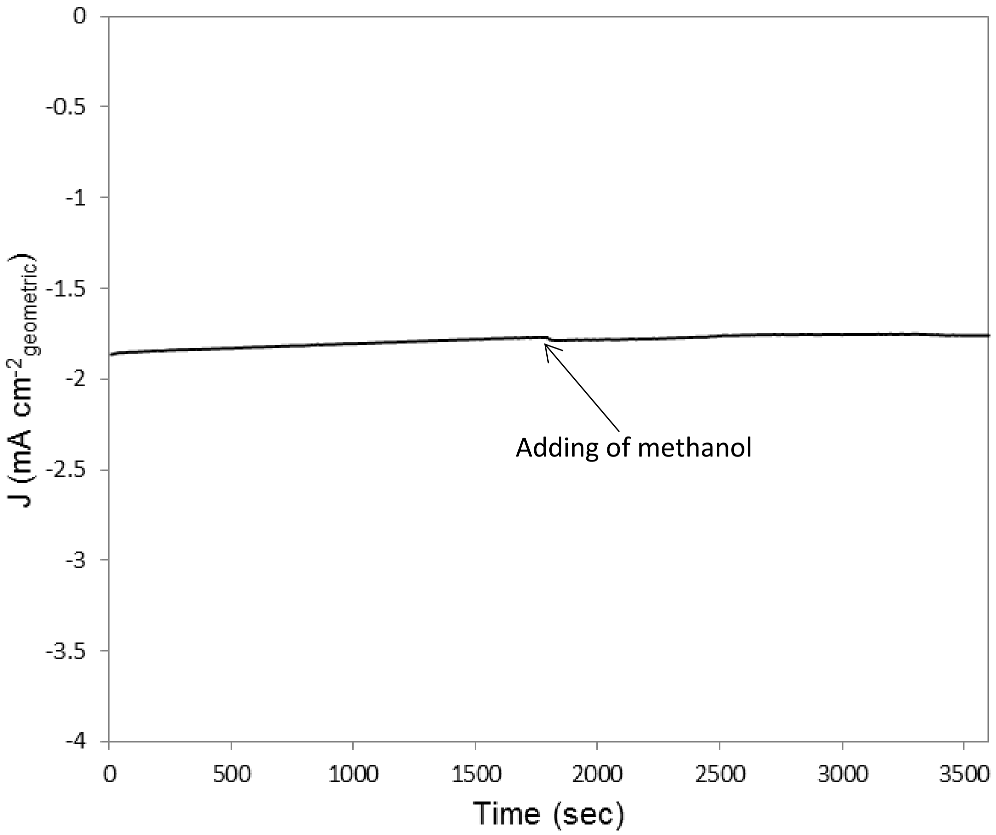

Figure S10. The chronoamperometric response of NMC5-900 at -0.3 V after methanol addition.

Chapter 4

4. Significant Enhancement of Water Splitting Activity of N-Carbon Electrocatalyst by Trace Level Co Doping

4.1. Introduction

Replacement of high cost and scarce precious metal catalysts with cost-effective alternatives for completely splitting water at low voltage has attracted wide attention in both industrial and scientific catalysis research. In recent years, a wide variety of transition metals and their derivatives have been selected as effective components for either HER or OER. However, these classes of materials always suffer from (electro) chemical corrosion issues under reaction conditions. Currently, one of the popular strategies for further optimizing their catalytic performances is coupling with nanocarbons to form advanced composite materials. Although considerable catalysts can be applied in water splitting systems, it is highly challenging to control the surface structure and expose a greater amount of active sites by incorporating a few metal atoms in the catalysts framework for splitting water. Herein, we present for the first time a carefully-designed method for synthesis of a series of nanostructured carbon spheres co-doped with nitrogen and a trace amount of cobalt (i.e. %1 atm) as a co-electrocatalyst for water splitting in alkaline solutions.

The highlights of this work include:

1. Cobalt and nitrogen co-doped porous carbon sphere with in-situ grown N-carbon nanosheets ((Co-NMC)/NC) has been developed via a dual soft-templating technique, with the trace amount of non-precious metal and low-cost procedure which makes the method feasible for large scale production.

2. This work shows that the Co-N_x molecules located in carbon framework were responsible for the excellent HER and OER performances in ((Co-NMC)/NC), and free-standing Co particles contribute little activity. Moreover, the nanostructured catalysts exhibited a high specific surface area, high pore volume, and a certain graphitic structure, which also contributed to the high electrocatalytic activity on resultant composites.

3. The HER and OER catalytic activity and efficiency of the optimized sample ((Co-NMC)$_1$/NC) are comparable with those obtained on that of previously reported non-precious metal doped and metal-free counterparts under the same condition.

4. These findings provide evidence that the incorporation of the trace amount of cobalt into specific nitrogen-containing carbon framework can significantly enhance hybrids' electrocatalytic activity, therefore shedding new light on the molecular design of next generation electrocatalysts for water splitting.

4.2. Research Outcome

This section is included in the thesis as it appears as a journal paper published by **Bita Bayatsarmadi**, Yao Zheng, Youhong Tang, Mietek Jaroniec, and Shi-Zhang Qiao, “Significant Enhancement of Water Splitting Activity of N-Carbon Electrocatalyst by Trace Level Co Doping”, ***Small***, 2016, 12, 3703-3711.

Statement of Authorship

Title of Paper	Significant Enhancement of Water Splitting Activity of N-Carbon Electrocatalyst by Trace Level Co Doping
Publication Status	☑ Published ☐ Accepted for Publication ☐ Submitted for Publication ☐ Unpublished and Unsubmitted work written in manuscript style
Publication Details	B. Bayatsarmadi, Y. Zheng*, Y. Tang, M. Jaroniec and S.Z. Qiao*, "Significant Enhancement of Water Splitting Activity of N-Carbon Electrocatalyst by Trace Level Co Doping", ***Small***, 2016, 12, 3703-3711, [IF=8.32].

Principal Author

Name of Principal Author (Candidate)	Bita Bayatsarmadi		
Contribution to the Paper	Research plan, material synthesis, most of the material characterisations, performance assessments and manuscript drafting.		
Overall percentage (%)	80 %		
Certification:	This paper reports on original research I conducted during the period of my Higher Degree by Research candidature and is not subject to any obligations or contractual agreements with a third party that would constrain its inclusion in this thesis. I am the primary author of this paper.		
Signature		Date	18/11/2016

Co-Author Contributions

By signing the Statement of Authorship, each author certifies that:

i. the candidate's stated contribution to the publication is accurate (as detailed above);
ii. permission is granted for the candidate in include the publication in the thesis; and
iii. the sum of all co-author contributions is equal to 100% less the candidate's stated contribution.

Name of Co-Author	Dr. Yao Zheng		
Contribution to the Paper	Discussion of research plan, manuscript review and assessment.		
Signature		Date	21/11/2016

Name of Co-Author	Dr. Youhong Tang		
Contribution to the Paper	Assistance with part of material characterisations.		
Signature		Date	22-Nov-2016

Name of Co-Author	Prof. Mietek Jaroniec		
Contribution to the Paper	Manuscript review.		
Signature		Date	Nov 21, 2016

Name of Co-Author	Prof. Shi-Zhang Qiao		
Contribution to the Paper	Supervised development of the work, organisation of the research, manuscript review and assessment.		
Signature		Date	18/11/2016

Significant Enhancement of Water Splitting Activity of N-Carbon Electrocatalyst by Trace Level Co Doping

Bita Bayatsarmadi, Yao Zheng, Youhong Tang, Mietek Jaroniec, and Shi-Zhang Qiao**

Replacement of precious metal electrocatalysts with highly active and cost efficient alternatives for complete water splitting at low voltage has attracted a growing attention in recent years. Here, this study reports a carbon-based composite co-doped with nitrogen and trace amount of metallic cobalt (1 at%) as a bifunctional electrocatalyst for water splitting at low overpotential and high current density. An excellent electrochemical activity of the newly developed electrocatalyst originates from its graphitic nanostructure and highly active Co-N$_x$ sites. In the case of carefully optimized sample of this electrocatalyst, 10 mA cm^{-2} current density can be achieved for two half reactions in alkaline solutions—hydrogen evolution reaction and oxygen evolution reaction—at low overpotentials of 220 and 350 mV, respectively, which are smaller than those previously reported for nonprecious metal and metal-free counterparts. Based on the spectroscopic and electrochemical investigations, the newly identified Co-N$_x$ sites in the carbon framework are responsible for high electrocatalytic activity of the Co,N-doped carbon. This study indicates that a trace level of the introduced Co into N-doped carbon can significantly enhance its electrocatalytic activity toward water splitting.

1. Introduction

Nowadays, energy is one of the key challenges facing mankind due to the limited supplies and population growth. Among different solutions the use of highly efficient electrochemical devices is considered as a viable way for energy conversion and storage. Electrolysis of water is of particular interest because it utilizes only an abundant resource, water, as the feedstock and a renewable energy (wind or solar-derived electricity) for hydrogen fuel production.[1] Therefore, a complete electrochemical water splitting via electrocatalytic hydrogen evolution reaction (HER) and oxygen evolution reaction (OER) in alkaline or neutral solutions is the key process presenting a great potential for the fabrication of alternative renewable energy devices.[2] However, a large-scale use of this process is constrained by the lack of efficient catalysts composed of inexpensive and earth-abundant elements.[3]

Up to now, platinum is the best catalyst for HER, showing high cathodic current densities at negligible overpotential. Contrarily, OER is more complicated and involves several electron transfer steps, for which the best catalysts contain also less abundant and expensive materials such as RuO_2 or IrO_2.[4] Therefore, it is highly desirable to develop alternative electrocatalyts based on earth abundant elements with high catalytic activity and stability for large scale energy production. In recent years, a wide variety of transition metals

---

B. Bayatsarmadi, Dr. Y. Zheng, Prof. S. Z. Qiao
School of Chemical Engineering
the University of Adelaide
Adelaide, SA 5005, Australia
E-mail: yao.zheng01@adelaide.edu.au;
s.qiao@adelaide.edu.au

Dr. Y. Tang
School of Computer Science, Engineering & Mathematics
Flinders University
Adelaide, SA 5001, Australia

Prof. M. Jaroniec
Department of Chemistry and Biochemistry
Kent State University
Kent, OH 44240, USA

DOI: 10.1002/smll.201601131

including cobalt, nickel, iron, molybdenum and their compounds have been explored as effective catalysts for either HER or OER, respectively.[5] However, these materials always suffer from (electro) chemical corrosion under HER/OER conditions. On the other hand, a highly promising family of electrocatalysts and various carbon-based materials feature unique advantages due to their tunable molecular structures, abundance, strong tolerance to acid/alkaline environments, and high surface areas.[6] Currently, one of the popular strategies for the design of highly active and stable advanced composite catalysts is coupling of transition metal species with nanocarbons. The latter represent favorable supports with unique properties such as large surface area, high electrical conductivity, and enhanced electron transfer, which make the resultant composites highly competitive to traditional metallic electrocatalysts.[7]

Although numerous HER or OER catalysts can be applied in water splitting systems, it is highly challenging to control their surface structure and the amount of exposed active sites by incorporating a small amount of metal atoms in the catalyst for splitting water. Herein, we present for the first time a carefully designed method for the synthesis of a series of nanostructured carbon spheres co-doped with nitrogen and a trace amount of cobalt (1 at%) as a co-electrocatalyst for water splitting in alkaline solutions. Among catalysts studied the best one, Co and N co-doped mesoporous carbon interrelated with N-doped carbon sheets (Co-NMC)$_1$/NC, showed overpotentials of 220 and 350 mV to achieve the current density of 10 mA cm^{-2} for HER and OER, respectively, which are smaller than the previously reported values for nonprecious metal doped and metal-free counterparts under the same conditions. It was shown by X-ray adsorption spectroscopy analysis that the Co-N$_x$ species located in the carbon framework are responsible for the excellent HER and OER performance. Moreover, the resulting nanostructured catalysts were to some degree graphitized and featured a high specific surface area (540 m^2 g^{-1}) and high pore volume (0.58 m^3 g^{-1}), which also contributed to their high electrocatalytic activity. These findings provide evidence that the incorporation of a trace amount of cobalt into N-doped carbon frameworks can significantly enhance the electrocatalytic activity of these hybrid materials, shedding a new light on the molecular design of next generation electrocatalysts for water splitting.

2. Results and Discussion

A multistep preparation process of the Co,N co-doped mesoporous carbon spheres and in situ grown N-doped carbon nanosheet hybrids (Co-NMC/NC) is displayed in Figure S1 (Supporting Information). The resulting electrocatalysts were synthesized via a dual soft-templating procedure using the cetyltrimethylammonium bromide (CTAB) and Pluronic (F127) to form micelles with the help of L-cysteine to create dual mesoporous structure with higher surface area followed by introduction of cobalt precursor (CoCl$_2$·6H$_2$O). After crosslinking of micelles, aminophenol and formaldehyde in the presence of CoCl$_2$ under hydrothermal conditions, aminophenol-formaldehyde resin nanospheres doped with cobalt species were produced. Then any accessible cobalt species outside the polymer framework were completely washed out from the solid product. The soft template was removed through pyrolysis and the resulting brownish product after grounding with melamine and g-C$_3$N$_4$ was carbonized under protection of N$_2$ flow.[8] In this step, carbonaceous gases released during pyrolysis of resin and g-C$_3$N$_4$ served as a precursor for the formation of carbon nanosheets in the presence of Co species.[9] The released nitrogenous gases from thermal polymerization of melamine and decomposed g-C$_3$N$_4$ served as nitrogen dopant for both porous carbon spheres and in situ grown carbon nanosheets.[10] During high temperature pyrolysis, CoCl$_2$ was reduced to metallic cobalt nanoparticles by highly reductive nitrogen-rich carbon species to form active Co-N$_x$ moieties.[11]

To obtain some insight into the electrocatalytic activity of the synthesized Co-NMC/NC composites, a series of control samples was prepared by using higher amount of the cobalt precursor only (Co$_{10}$-NMC/NC) and higher amounts of both N and Co precursors ((Co-NMC)$_{10}$/NC) as well as the (Co-NMC)$_1$ sample without carbon nanosheets and a metal-free NMC sample; all these samples were prepared by keeping the remaining synthesis conditions the same (see the Experimental Section).

The morphology and microstructure of the hybrid materials were investigated by scanning electron microscopy (SEM) and transmission electron microscopy (TEM) imaging. The SEM image of (Co-NMC)$_1$/NC in **Figure 1**a (bottom panel) shows the presence of entangled foam-like carbon nanosheets between the porous carbon spheres, which interconnect them to form a porous network. Moreover, energy dispersive X-ray spectra (EDS) (top panel in Figure 1a) collected from porous carbon spheres zone or carbon nanosheets zone indicate that the former may serve as active sites for HER/OER due to the presence of Co and N, while the latter are mainly N-doped carbon enhancing conductivity of the final product. The scanning transmission electron microscope (STEM) dark field image and the corresponding elemental mappings (Figure 1b) further reveal that cobalt and nitrogen atoms are homogeneously distributed in the carbon spheres. The magnified TEM image (Figure 1c) shows the morphology of carbon nanospheres with diameter of 70 nm, which are interconnected because of the available structural defects and nitrogen species.[12] As shown in Figure S2 (Supporting Information), an increase in the amounts of carbon, nitrogen and cobalt precursors causes a more severe aggregation of synthesized spheres due to the weak interactions between agglomerated cobalt species and resin, and results in the interconnected spheres with numerous surface active sites.[13] Note that there is no sign for the presence of bulk cobalt/cobalt oxide in the carbon framework, which affirms the removal of free-standing metallic cobalt during the washing step. The high-resolution TEM image (Figure 1d) clearly shows the presence and distribution of Co crystals (with sizes of 4–5 nm) on the carbon spheres surface, which might be cobalt crystals bonded with acid tolerable species (i.e., nitrogen) to form Co-N$_x$ moieties.[14]

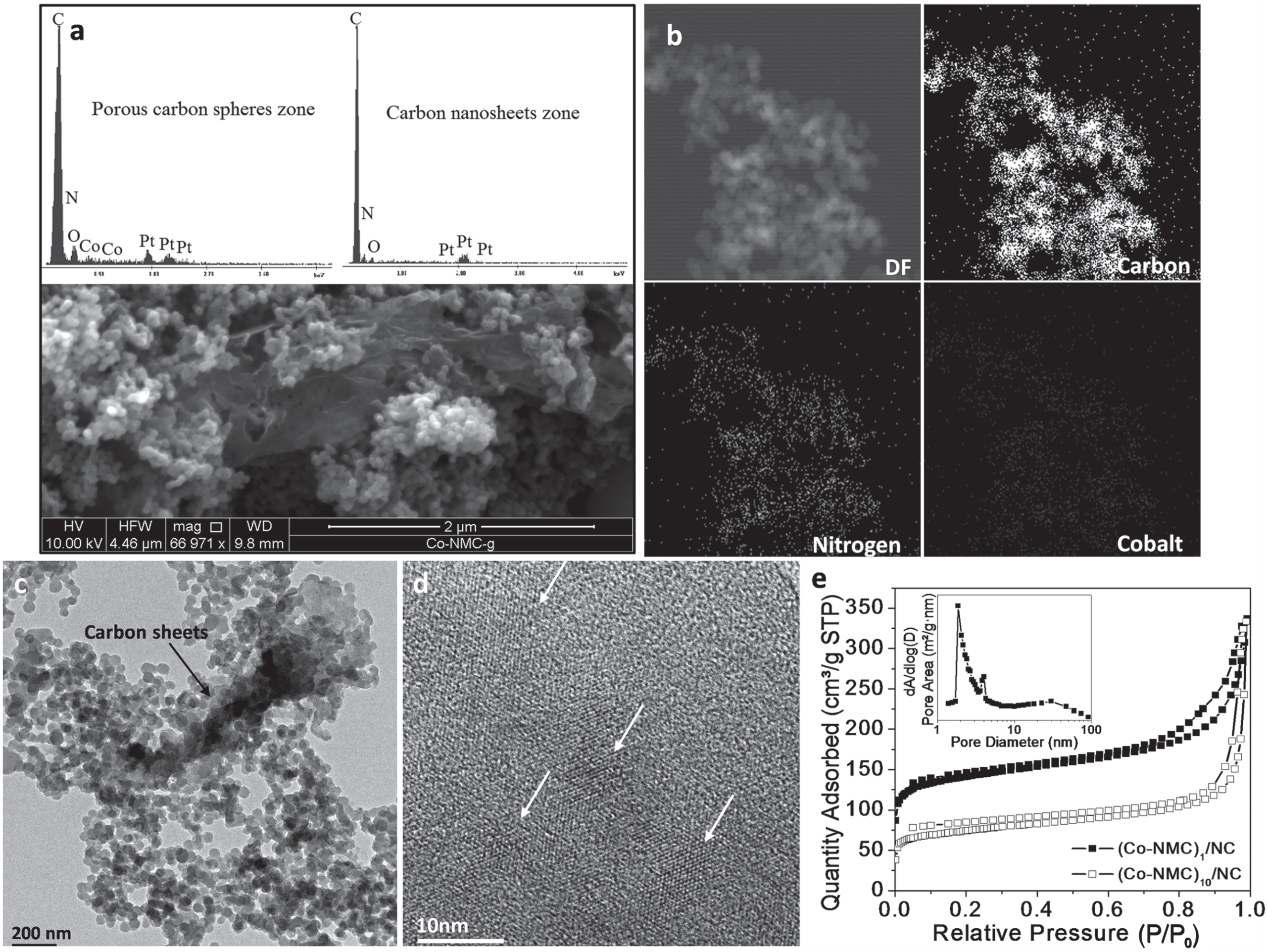

Figure 1. a) SEM image of $(\text{Co-NMC})_1/\text{NC}$ and the corresponding EDS spectra; b) STEM and the corresponding elemental mapping analysis; c) TEM image of $(\text{Co-NMC})_1/\text{NC}$ connected to entangle-like carbon nanosheets; d) HRTEM image of crystalline Co species in the carbon framework, where the white arrows indicate highly dispersed Co NPs; e) Nitrogen adsorption-desorption isotherms and (inset) the corresponding pore size distribution.

Nitrogen adsorption-desorption isotherms were measured to further analyze the porosity of the hybrid materials (Figure 1e). The adsorption isotherm obtained for $(\text{Co-NMC})_1/\text{NC}$ exhibits type IV with visible H4 hysteresis loop, which is an indicative of complex porosity as evidenced by high Brunauer–Emmett–Teller (BET) surface area of 540 $\text{m}^2\ \text{g}^{-1}$ and pore volume of 0.58 $\text{cm}^3\ \text{g}^{-1}$.[15] However, in the case of $(\text{Co-NMC})_{10}/\text{NC}$, a sharp increase in the adsorption curve is observed at relative pressures close to unity. This indicates the capillary condensation of nitrogen inside extra-large mesopores created due to agglomeration of carbon spheres, which is in a good agreement with the corresponding TEM image of $(\text{Co-NMC})_{10}/\text{NC}$ (Figure S2a, Supporting Information). For $(\text{Co-NMC})_1/\text{NC}$, a rapid increase in the volume adsorbed at low relative pressures ($P/P_0 < 0.05$) suggests the presence of micropores in the carbon spheres that are formed by thermal degradation of oxygen-containing bridges during carbonization of the resin.[16] The pore size distribution curve (inset in Figure 1e) shows one sharp peak centered at about 2 nm confirming the presence of small mesopores. It is anticipated that the highly porous structure of the synthesized electrocatalysts is favorable for penetration of ions into pores, which should result in high electrochemical activity. The high surface area and nitrogen doping are able to attach cobalt species and create a large amount of active sites.[17]

To further probe the chemical composition and nature of doping, synchrotron-based X-ray photoelectron spectroscopy (XPS) and near-edge X-ray absorption fine structure (NEXAFS) measurements have been performed for $(\text{Co-NMC})_1/\text{NC}$ and $(\text{Co-NMC})_{10}/\text{NC}$. The survey XPS spectra of the composites reveal sharp peaks assigned to C1s, O1s, and N1s and a weak peak related to Co2/3p (Figure S3, Supporting Information). Considering that XPS is a good technique to study the solid surfaces, a quantitative analysis of the obtained results shows that metallic Co is almost embedded into the carbon framework and the detected cobalt content by this method is smaller than the value determined by Inductively coupled plasma mass spectrometry (ICP-MS) (Table S1, Supporting Information).

The nitrogen K-edge NEXAFS spectra (**Figure 2**a) of both samples show two π^* resonances representing sp^2 hybridized pyridine-like nitrogen (≈398.5 eV) and graphite-like nitrogen (≈401.5 eV), which is also consistent with

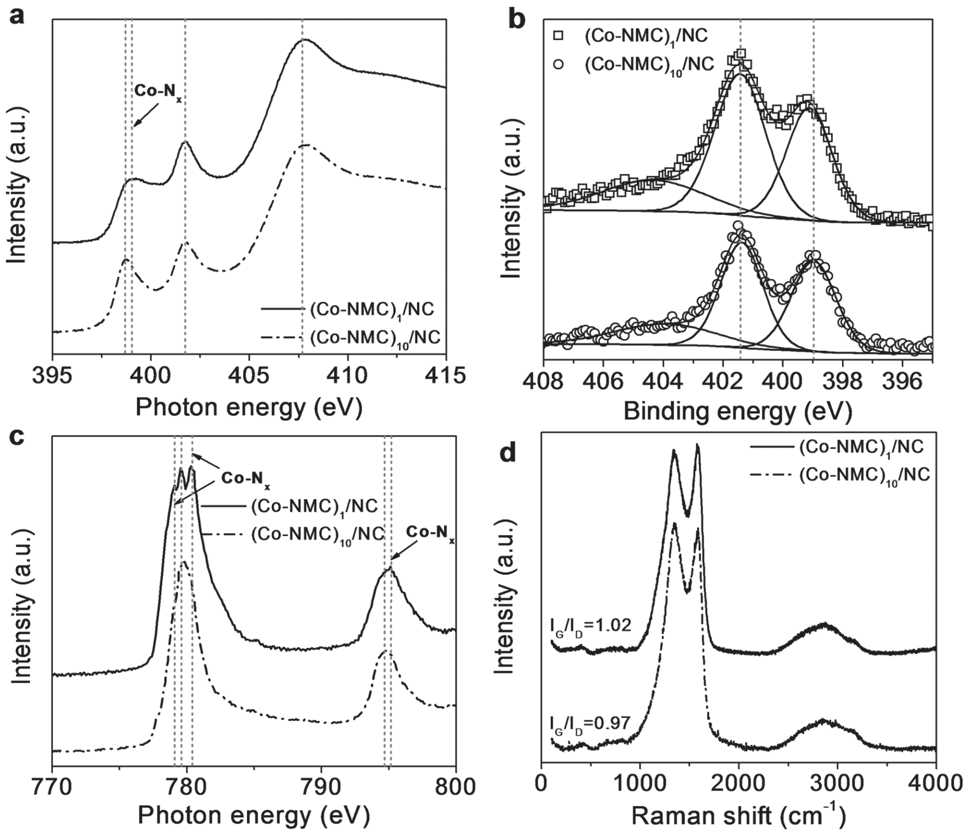

Figure 2. Chemical structures of (Co-NMC)$_1$/NC and (Co-NMC)$_{10}$/NC hybrids. a) Nitrogen K-edge NEXAFS spectra; b) high-resolution N1s XPS spectra; c) Cobalt L-edge NEXAFS spectra; d) Raman spectra.

high-resolution N1s XPS results (Figure 2b).[4b,6,18] Moreover, N1s XPS spectra exhibit a wide peak (≈404.0 eV), which is assigned to oxidized-nitrogen species.[4b,18a,19] As compared with the data obtained for (Co-NMC)$_{10}$/NC, there is an obvious shoulder (around 399.0 eV) overlapping with pyridine nitrogen's resonance on the spectrum of (Co-NMC)$_1$/NC. These new species located at the higher energy position of pyridine nitrogen can be identified as Co-N$_x$ due to the electron donor properties of pyridine-like nitrogen species bonded with available ionic cobalt atoms.

A successful incorporation of Co into nitrogen-containing carbon framework was further revealed by the cobalt L-edge NEXAFS spectra of (Co-NMC)$_1$/NC (Figure 2c), which show three separated peaks in L$_3$-edge at 779.0, 779.9, and 780.5 eV and an overlapping peak position of Co L$_2$-edge at ≈794.0 eV with a weak shoulder at 795.5 eV. Specifically, the peaks at 779.9 and 794.0 eV can be assigned to metallic cobalt. Two extra peaks and shoulder can be assigned to the newly formed Co-N$_x$ species due to the chemical interactions between Co and pyridinic-type nitrogen species, consistent with nitrogen K-edge spectra.[20] Additionally, one can see that the cobalt L$_3$-edge spectrum of (Co-NMC)$_{10}$/NC exhibits an overlapping peak at 779.9 eV and a weak shoulder at 780.5 eV representing the presence of both metallic cobalt/cobalt oxide and a smaller amount of Co-N$_x$ as compared to that of (Co-NMC)$_1$/NC, which also agrees with the evidence provided by the L$_2$-edge peaks. This might be attributed to the limited amount of active ionic cobalt and available nitrogen defect structures to form Co-N$_x$ species in the (Co-NMC)$_{10}$/NC framework due to a significant agglomeration of nanospheres resulting in a less-developed mesostructure. Thus, a combination of polarization-dependent NEXAFS and XPS measurements provides a crucial evidence for interactions between cobalt and the available pyridine-like nitrogen species to create highly active Co-N$_x$ sites in the catalyst's structure.

The Raman spectrum of (Co-NMC)$_1$/NC (Figure 2d) presents two peaks assigned to D and G bands as well as a weak 2D band. The D and 2D bands indicate the presence of substantial defects or disordered sites in the composite studied and the G band refers to the graphitic structure. The structural defects might be mainly caused by the presence of N dopants and concomitant absence of C atoms. By analyzing the intensity of the G band with respect to that of the D band, the graphitization degree of the synthesized materials can be determined qualitatively (I_G/I_D). The I_G/I_D ratio increases from (Co-NMC)$_1$/NC (1.02) to (Co-NMC)$_{10}$/NC (0.97), which can be attributed to the introduction of cobalt atoms bonded with pyridine-like nitrogen in the carbon framework resulting in higher graphitization degree. This fact is favored by the improvement of the stacking of graphitic layers by the catalytic effect of cobalt and by smaller shrinkage of microporous structure of these samples.[21] The I_G/I_D ratio obtained for NMC, (Co-NMC)$_1$ and (Co-NMC)$_1$/NC materials (Figure S4, Supporting Information) increases with graphitization degree by incorporating cobalt into the

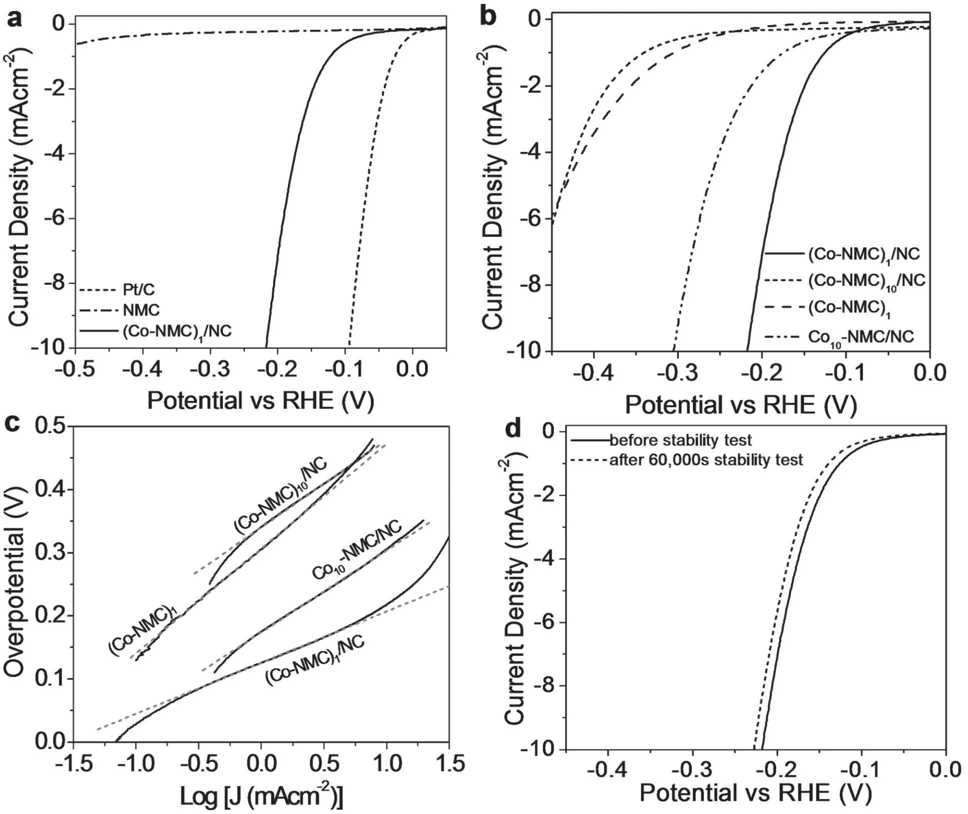

Figure 3. a) HER polarization curves measured for nonmetallic NMC, hybrid (Co-NMC)$_1$/NC, and benchmarked Pt/C samples in 0.1 M KOH solution; b,c) HER polarization curves and the corresponding HER Tafel plots for different samples containing trace amounts of Co in 0.1 M KOH solution; and d) HER polarization curves of (Co-NMC)$_1$/NC before and after stability test.

carbon framework and further increases by in situ growth of carbon nanosheets interconnecting the overall structure of composites.

The electrochemical function of trace metallic species and the electrocatalytic activity of various electrocatalysts for both HER and OER were first evaluated using the rotating disk electrode (RDE) technique in a N_2-saturated 0.1 M KOH solution. **Figure 3**a shows the HER polarization curves recorded for (Co-NMC)$_1$/NC as compared to those measured for the metal-free NMC and commercial Pt/C. The curve obtained for NMC (without cobalt doping) shows a negligible electrocatalytic activity for HER, while the activity of (Co-NMC)$_1$/NC is significantly enhanced by the presence of additional active sites generated by simultaneous incorporation of nitrogen and cobalt into carbon framework and by formation of carbon nanosheets, as reflected by the large shift of the polarization curve to a lower overpotential.

As shown in Figure 3b, a superior HER activity of (Co-NMC)$_1$/NC in comparison with the samples possessing higher amounts of nitrogen and cobalt, i.e., (Co-NMC)$_{10}$/NC, (Co$_{10}$-NMC)/NC, and also the sample without carbon nanosheets (Co-NMC)$_1$, clearly confirms that the origin of HER activity of the synthesized electrocatalysts is not only related to the available cobalt active sites but first of all to the synergetic coupling between cobalt and nitrogen resulting in the formation of Co-N$_x$ species.[1,22] For example, in the case of (Co-NMC)$_{10}$/NC some surface active sites were not accessible to the excessive agglomeration of spheres (as proved by XPS, NEXAFS, and TEM data) as compared to (Co-NMC)$_1$/NC. Moreover, an increase in the cobalt loading in the synthesis gel did not increase the catalytic activity due to the removal of excessive cobalt species during washing step (Figure S5 and Table S1, Supporting Information) and somewhat limited accessibility of nitrogen active sites on the surface of aggregated spheres. The in situ formed carbon nanosheets can also significantly facilitate the HER process as reflected by comparison of the polarization curves obtained for the catalysts with ((Co-NMC)$_1$/NC) and without (Co-NMC)$_1$ nanosheets, while their chemical composition and porous structures are similar. The effect of porosity of the electrocatalysts studied on the performance of HER is illustrated in Figure S6a (Supporting Information), showing the linear sweep voltammogram (LSV) data confirming higher activity of porous materials as compared to amorphous carbon spheres, which could be attributed to easier mass transport and higher surface area.[23]

To achieve a current density of 10 mA cm^{-2}, which is the value expected for a 10% efficient solar water-splitting device, (Co-NMC)$_1$/NC requires an overpotential of 220 mV, lower than those of the control samples. Figure 3c displays the Tafel plots to provide some insight into the HER pathways on various catalysts. Specifically, the Tafel slope obtained for (Co-NMC)$_1$/NC is equal to 81.0 mV decade^{-1}, which is much lower than that of C$_{10}$-NMC/NC (136.2 mV decade^{-1}), (Co-NMC)$_{10}$/NC (146.9 mV decade^{-1}), and (Co-NMC)$_1$ (159.9 mV decade^{-1}), suggesting its favorable HER kinetics.

The mechanism of hydrogen evolution is not fully clear but the Tafel slope reveals that HER may be controlled by a Volmer-Heyrovsky mechanism because the Tafel slope is similar to that of a smooth Ni surface and because the electrochemical desorption is a rate limiting step.[24] The exchange current density (i_0) values derived from the Tafel plots for different electrocatalysts (Figure S6b, Supporting Information) further confirm the superior HER performance of (Co-NMC)$_1$/NC that is most likely due to higher conductivity, availability of numerous Co-N$_x$ active sites and higher surface area boosting the capacity of proton adsorption and reduction. It should be noted that the HER catalytic activity of (Co-NMC)$_1$/NC is much higher than the reported activities of the metal-free counterparts (e.g., N-graphene, P-graphene, N-P graphene and N,S-graphene, etc.),[4b,22a] and some nonprecious metal-based catalysts (e.g., cobalt-based and nickel-based catalysts).[23] Moreover, it is comparable to the activities of traditional metallic catalysts (e.g., bulk Au, Mo and Ni/Mo alloys, etc.),[25] while it is not as good as that of the state-of-the-art nanostructures MoS$_2$, WS$_2$, and commercial Pt/C.[26] This might be due to an insufficient amount of Co-N$_x$ active sites (only ≈1 at%) in (Co-NMC)$_1$/NC.

Electrochemical stability is an important requirement for an HER catalyst. Therefore, the chronoamperometric test was carried out under a constant voltage of –1.4 V (vs Ag/AgCl) in 0.1 M KOH (Figure S7, Supporting Information). The current density shows a negligible degradation even after a long period of 60 000 s. The retained activity of (Co-NMC)$_1$/NC is ascribed to the protected Co species in the carbon structure and newly formed Co-N$_x$ moieties,[27] while a slight degradation in the activity may be caused by consumption of OH$^-$ or variation of the valence state of Co-N$_x$.[28] Moreover, a superior durability of the catalyst for HER was confirmed by the LSV test before and after stability test, which shows only a slight negative shift of the HER polarization curve (10 mV shift of the overpotential at 10 mA cm^{-2}) (Figure 3d), suggesting a good prognosis for these hybrid materials as efficient HER electrocatalysts.

The electrocatalytic OER activity of the synthesized catalysts was also evaluated by linear sweep voltammograms. As shown in **Figure 4**a, the metal-free NMC exhibits a negligible OER activity, while the current density of (Co-NMC)$_1$/NC reaches 5 mA cm^{-2} at the potential of 1.5 V (vs reversible hydrogen electrode (RHE)), which is better than 1.54 V for IrO$_2$/CNT. The (Co-NMC)$_1$/NC catalyst requires an overpotential of 360 mV to achieve the current density of 10 mA cm^{-2} (Figure 4b), which is superior to the overpotential values of the remaining (Co-NMC)$_1$, (Co-NMC)$_{10}$/NC, (Co$_{10}$-NMC)/NC, and metal-free NMC electrocatalysts in this study and the most of the metal-free carbon-based materials and earth-abundant inorganic catalysts reported so far.[29]

The catalytic kinetics of OER was examined on the basis of the Tafel plots (Figure 4c). The Tafel slope value for (Co-NMC)$_1$/NC (83.3 mV decade^{-1}) indicates a more favorable kinetics for this sample as compared to that of (Co-NMC)$_{10}$/NC (89.9 mV decade^{-1}), (Co$_{10}$-NMC)/NC (114.3 mV decade^{-1}), and (Co-NMC)$_1$ (92.4 mV decade^{-1}). This result agrees with the higher catalytic current density

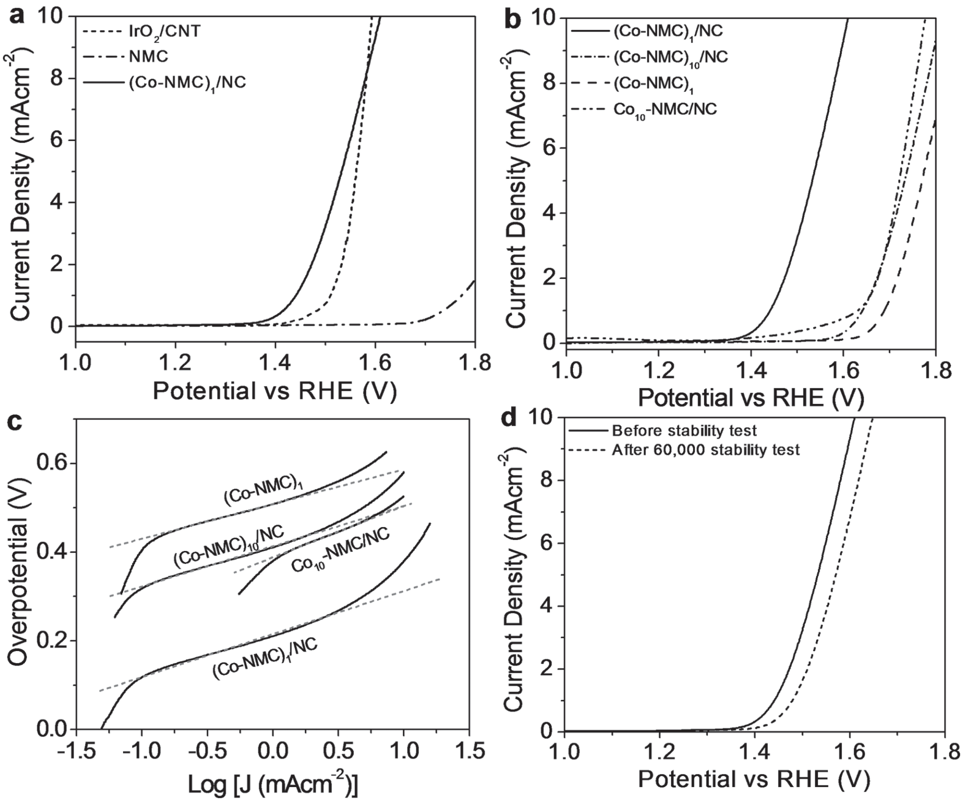

Figure 4. a) OER polarization curves measured for nonmetallic NMC, hybrid (Co-NMC)$_1$/NC and benchmarked IrO$_2$ samples in 0.1 M KOH solution, b,c) OER polarization curves and the corresponding OER Tafel plots for different catalysts containing trace amounts of cobalt in 0.1 M KOH solution, and d) OER polarization curves obtained for (Co-NMC)$_1$/NC before and after stability test.

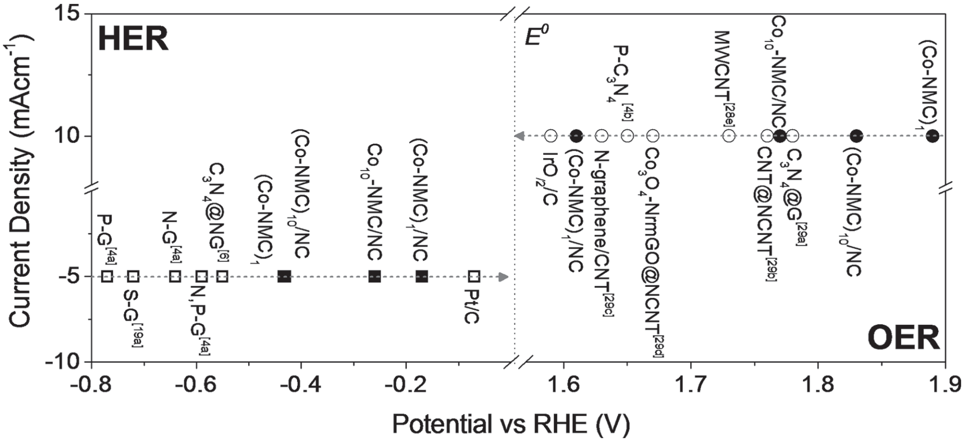

Figure 5. Comparison of the synthesized electrocatalysts and reported bifunctional electrocatalysts for both HER and OER reactions.

of (Co-NMC)$_1$/NC than the values achieved for other synthesized electrocatalysts in this study in the range of high potentials (>1.62 V; Figure 4b), suggesting its better catalytic activity and efficient electron/mass transfer.

A strong coupling between (Co-NMC)$_1$ and N-carbon nanosheets facilitates the electron transfer between two components,[30] and the mesoporous structure assures a good transport of reactants and products and enlarges the reactive interface between the catalyst and electrolyte.[29h] More importantly, (Co-NMC)$_1$/NC has a large catalytically active surface area, which can be estimated on the basis of the electrochemical double-layer capacitance (C_{dl}, Figure S8, Supporting Information). The value of C_{dl} measured for (Co-NMC)$_1$/NC is 12.47 mF cm^{-2}, which is higher than that of (Co-NMC)$_1$ (C_{dl} = 11.64 mF cm^{-2}). Since C_{dl} is proportional to the active surface area of electrocatalysts,[7a,31] this comparison demonstrates that the formation of N-doped carbon nanosheets associated with the (Co-NMC)$_1$ framework is more effective in enlarging the active surface area than (Co-NMC)$_1$ nanoparticles alone. The effect of porosity on OER was also investigated; the LSV data suggest that the well-developed porosity in (Co-NMC)$_1$ can assure a good transport of reactants and products involved in electrochemical reactions (Figures S9, Supporting Information).

Electrochemical stability of the newly developed catalysts for OER was tested by the chronoamperometric measurements under a constant voltage of +0.8 V (vs Ag/AgCl) in 0.1 M KOH. As shown in Figure S10 (Supporting Information), (Co-NMC)$_1$/NC exhibited high stability with a very slow attenuation after 1000 min, and a high relative current of 93% was still retained. The LSV data collected before and after durability tests show a slight negative shift of the OER polarization curve (18 mV shift of the overpotential at 10 mA cm^{-2}), which might be due to both activation and phase conversion of the catalyst surface during long time of electrochemical testing (Figure 4d).[32] These results demonstrate the excellent potential of (Co-NMC)$_1$/NC as an effective and stable OER catalyst.

The overall water splitting electrode activity has been evaluated by the difference of HER and OER metrics (relative potential at $E = -5$ mA cm^{-2} from HER polarization curve and potential at $E = 10$ mA cm^{-2} from OER polarization curve; $\Delta E = E_{j=-5} - E_{j=10}$). The smaller the ΔE is, the catalyst is closer to an ideal bifunctional water splitting electrode. Remarkably, (Co-NMC)$_1$/NC exhibits a ΔE value of 1.78 V, which is much lower than that of the recently reported nonmetallic materials and also other electrocatalysts tested in this work (**Figure 5**). Although remarkable HER or OER catalysts (Pt/C and IrO_2-based catalysts, respectively) can be applied in water splitting systems, however the use of a bifunctional electrocatalyst for both HER and OER is still challenging. Taking into account this fact, we can conclude that the (Co-NMC)$_1$/NC hybrid is shown to be highly efficient, nonnoble metal-based bi-functional electrocatalyst for HER and OER in alkaline media with lower overpotential (at constant current) for water splitting as compared to other synthesized electrocatalysts in this work.

3. Conclusions

A unique coupling of Co,N co-doped porous carbon spheres with in situ grown N-carbon nanosheets results in a highly active bifunctional electrocatalyst, which successfully combines the desired merits such as highly active Co-N$_x$ species, good conductivity, porous structure very good mass transport, and sufficiently large surface area with accessible catalytically active sites. This excellent characteristics assure its excellent HER and OER catalytic activity as judged on the basis of the favorable onset potentials, small Tafel slopes and good stability, which make it a promising bifunctional electrocatalyst for both HER and OER.

4. Experimental Section

Chemicals: Pluronic (F127), hexadecyltrimethylammonium bromide (CTAB, ≥98%), L-cysteine ((R)-2-amino-3-mercaptopropionic acid, ≥97%), 3-aminophenol (C_6H_7NO, 98%), formaldehyde (37 wt%), cobalt (II) chloride hexahydrate ($CoCl_2 \cdot 6H_2O$), and melamine ($C_3H_6N_6$, %99) were purchased from Sigma-Aldrich. Formaldehyde solution (HCHO, 37/10) and ethanol (EtOH, absolute) were purchased from Chem-Supply. All chemicals were directly used without any further treatment and purification.

Material Synthesis: In a typical synthesis, 0.25 g of fully dissolved Pluronic F127 in 20 mL of EtOH was added to 50 mL of DI-water at 25 °C. Then 0.325 g of hexadecyltrimethylammonium bromide and 0.5 g of L-cysteine were added to the solution and kept stirred for 30 min. Next, 0.50 g of 3-aminophenol were added followed by introduction of 0.70 mL of formaldehyde and stirred for another 30 min. Afterward, a given amount of $CoCl_2 \cdot 6H_2O$ was added to the mixture and kept stirring at 25 °C for 24 h. Finally, the mixture was transferred to a Teflon-lined autoclave for hydrothermal reaction at 100 °C for 24 h. The resulting Co-doped aminophenol-formaldehyde nanospheres (Co-APFNS) were collected by vacuum filtration and dried followed by washing with DI-water, ethanol, and 0.50 M H_2SO_4 for three times and drying at 100 °C for 24 h. This washing step led to the removal of free cobalt species, which were outside of the carbon framework. Co,N co-doped mesoporous carbon spheres (Co-NMC) were obtained by calcination of Co-APFNS under N_2 flow in a tubular furnace at 350 °C using heating rate of 1 °C min^{-1} for 3 h to remove the template followed by carbonization at 900 °C with heating rate of 2.3 °C min^{-1} for 4 h. To prepare (Co-NMC/NC), dried Co-APFNS were heated up to 350 °C for 3 h with heating rate of 1 °C min^{-1} under N_2 flow to remove the template. The obtained solid products were finely ground with melamine and g-C_3N_4 (prepared by heating melamine in air at 550 °C for 4 h) with the mass ratio 1:5:5 in an agate mortar and the mixture was heated to 900 °C with heating rate of 2.3 °C min^{-1} for 4 h.

Chemical Characterization: The morphology of synthesized samples was characterized by high-resolution transmission electron microscope (HRTEM, JEM-2100) operating at 200 kV and scanning electron microscope (SEM, Quanta 450 ESEM, FEI) operating at 10 kV. Elemental mapping was conducted using EDAX detector attached on JEM-2100. Nitrogen adsorption–desorption isotherms were measured on Tristar II (Micrometrics) at −196 °C. Pore size distributions were calculated by Barrett–Joyner–Halenda model using the data of adsorption branch of the isotherm. The specific surface areas were calculated using adsorption data at the relative pressure range of $P/P_0 = 0.05–0.30$ by BET equation. The total pore volumes were estimated from the adsorbed amounts at a relative pressure (P/P_0) of 0.994. All the samples were degassed at 150 °C for more than 6 h prior to the nitrogen sorption tests. Raman spectra were collected on LabRAM (Horiba Ltd) with 532 nm laser. The NEXAFS measurements were carried out on the soft X-ray spectroscopy beamline at the Australian Synchrotron, which is equipped with a hemispherical electron analyzer and a micro channel plate detector that enables a simulation recording of the total electron yield and partial electron photon beam, measured on an Au grid. The synchrotron based XPS were collected by a high-resolution and high-sensitivity hemispherical electron analyzer with nine channel electron multiplier (SPECS Phoibos 150).

Electrode Preparation and Electrochemical Characterization: All the electrochemical measurements were performed in a three-electrode glass cell and under identical conditions. The data were recorded using a CHI 760 D bipotentiostst (CH Instruments, Inc., USA). In a typical electrode preparation, 2.0 mg of synthesized catalyst were ultrasonically dispersed in 0.5 mL of 0.1 wt% Nafion aqueous solution. Next, 20 µL of catalyst dispersion (4.0 mg mL^{-1}) were then transferred onto the glassy carbon RDE (0.196 cm^2, Pine Research Instrumentation, USA) via a controlled drop casting approach, dried in ambient environment for 1 h, and served as a working electrode. The reference electrode was an Ag/AgCl in 4 M KCl solution and the counter electrode was platinum wire. A flow of N_2 was maintained over the electrolyte (0.1 M KOH) during the OER and HER electrochemical measurements to eliminate dissolved oxygen. All potentials were referenced to an RHE.[33]

In addition, all polarization curves were recorded with the slow scan rate of 0.5 mV s^{-1} to minimize the capacitive current and corrected for the iR contribution within the cell. The working electrode was rotated at 1600 rpm to remove hydrogen or oxygen gas bubbles formed at the catalyst surface.

Supporting Information

Supporting Information is available from the Wiley Online Library or from the author.

Acknowledgements

This research was financially supported by Australian Research Council (ARC) through the Discovery Project program (DP160104866, DP140104062, and DP130104459).

[1] S. Gao, G.-D. Li, Y. Liu, H. Chen, L.-L. Feng, Y. Wang, M. Yang, D. Wang, S. Wang, X. Zou, *Nanoscale* **2015**, *7*, 2306.
[2] J. A. Turner, *Science* **1999**, *285*, 687.
[3] a) M. Ledendecker, G. Clavel, M. Antonietti, M. Shalom, *Adv. Funct. Mater.* **2015**, *25*, 393; b) M. G. Walter, E. L. Warren, J. R. McKone, S. W. Boettcher, Q. Mi, E. A. Santori, N. S. Lewis, *Chem. Rev.* **2010**, *110*, 6446.
[4] a) T. Y. Ma, J. Ran, S. Dai, M. Jaroniec, S. Z. Qiao, *Angew. Chem., Int. Ed.* **2015**, *54*, 4646; b) Y. Zheng, Y. Jiao, L. H. Li, T. Xing, Y. Chen, M. Jaroniec, S. Z. Qiao, *ACS Nano* **2014**, *8*, 5290.
[5] Y. Jiao, Y. Zheng, M. Jaroniec, S. Z. Qiao, *Chem. Soc. Rev.* **2015**, *44*, 2060.
[6] Y. Zheng, Y. Jiao, Y. Zhu, L. H. Li, Y. Han, Y. Chen, A. Du, M. Jaroniec, S. Z. Qiao, *Nat. Commun.* **2014**, *5*, 3783.
[7] a) D. Kong, H. Wang, Z. Lu, Y. Cui, *J. Am. Chem. Soc.* **2014**, *136*, 4897; b) M. Shen, C. Ruan, Y. Chen, C. Jiang, K. Ai, L. Lu, *ACS Appl. Mater. Interfaces* **2015**, *7*, 1207; c) J. Liang, R. F. Zhou, X. M. Chen, Y. H. Tang, S. Z. Qiao, *Adv. Mater.* **2014**, *26*, 6074; d) H. Lei, A. Han, F. Li, M. Zhang, Y. Han, P. Du, W. Lai, R. Cao, *Phys. Chem. Chem. Phys.* **2014**, *16*, 1883; e) Y. Wu, M. Chen, Y. Han, H. Luo, X. Su, M.-T. Zhang, X. Lin, J. Sun, L. Wang, L. Deng, W. Zhang, R. Cao, *Angew. Chem., Int. Ed.* **2015**, *54*, 4870.
[8] B. Bayatsarmadi, Y. Zheng, M. Jaroniec, S. Z. Qiao, *Chem. – Asian J.* **2015**, *10*, 1546.
[9] Z.-W. Liu, F. Peng, H.-J. Wang, H. Yu, W.-X. Zheng, J. Yang, *Angew. Chem., Int. Ed.* **2011**, *50*, 3257.
[10] a) Y. Zhang, Q. Pan, G. Chai, M. Liang, G. Dong, Q. Zhang, J. Qiu, *Sci. Rep.* **2013**, *3*, 1943; b) J. Liang, X. Du, C. Gibson, X. W. Du, S. Z. Qiao, *Adv. Mater.* **2013**, *25*, 6226.
[11] a) Y. Zhu, B. Zhang, X. Liu, D.-W. Wang, D. S. Su, *Angew. Chem., Int. Ed.* **2014**, *53*, 10673; b) M. Li, X. Bo, Y. Zhang, C. Han, A. Nsabimana, L. Guo, *J. Mater. Chem. A* **2014**, *2*, 11672.
[12] Z.-H. Sheng, L. Shao, J.-J. Chen, W.-J. Bao, F.-B. Wang, X.-H. Xia, *ACS Nano* **2011**, *5*, 4350.
[13] M. K. Khan, M. J. MacLachlan, *ACS Macro Lett.* **2015**, *4*, 1351.

[14] J. Deng, P. Ren, D. Deng, L. Yu, F. Yang, X. Bao, *Energy Environ. Sci.* **2014**, *7*, 1919.

[15] M. Thommes, *Chem. Ing. Tech.* **2010**, *82*, 1059.

[16] J. Yu, M. Guo, F. Muhammad, A. Wang, G. Yu, H. Ma, G. Zhu, *Microporous Mesoporous Mater.* **2014**, *190*, 117.

[17] N. D. Kim, W. Kim, J. B. Joo, S. Oh, P. Kim, Y. Kim, J. Yi, *J. Power Sources* **2008**, *180*, 671.

[18] a) E. Raymundo-Piñero, D. Cazorla-Amorós, A. Linares-Solano, J. Find, U. Wild, R. Schlögl, *Carbon* **2002**, *40*, 597; b) N. Daems, X. Sheng, I. F. J. Vankelecom, P. P. Pescarmona, *J. Mater. Chem. A* **2014**, *2*, 4085; c) H. Peng, Z. Mo, S. Liao, H. Liang, L. Yang, F. Luo, H. Song, Y. Zhong, B. Zhang, *Sci. Rep.* **2013**, *3*, 1765; d) Z. Wang, S. Xiao, Z. Zhu, X. Long, X. Zheng, X. Lu, S. Yang, *ACS Appl. Mater. Interfaces* **2015**, *7*, 4048.

[19] T. Xing, Y. Zheng, L. H. Li, B. C. C. Cowie, D. Gunzelmann, S. Z. Qiao, S. Huang, Y. Chen, *ACS Nano* **2014**, *8*, 6856.

[20] a) F. Vollnhals, D. Drost, F. Tu, E. Carrasco, A. Späth, R. H. Fink, H. P. Steinrück, H. Marbach, *Beilstein J. Nanotechnol.* **2014**, *5*, 1175; b) F. Zheng, S. Alayoglu, J. Guo, V. Pushkarev, Y. Li, P.-A. Glans, J.-L. Chen, G. Somorjai, *Nano Lett.* **2011**, *11*, 847.

[21] a) F. J. Maldonado-Hódar, C. Moreno-Castilla, J. Rivera-Utrilla, Y. Hanzawa, Y. Yamada, *Langmuir* **2000**, *16*, 4367; b) L. C. Cotet, M. Baia, L. Baia, I. C. Popescu, V. Cosoveanu, E. Indrea, J. Popp, V. Danciu, *J. Alloys Compd.* **2007**, *434–435*, 854.

[22] a) Y. Ito, W. Cong, T. Fujita, Z. Tang, M. Chen, *Angew. Chem., Int. Ed.* **2015**, *54*, 2131; b) H.-W. Liang, S. Bruller, R. Dong, J. Zhang, X. Feng, K. Mullen, *Nat. Commun.* **2015**, *6*, 7992.

[23] a) S. Cobo, J. Heidkamp, P.-A. Jacques, J. Fize, V. Fourmond, L. Guetaz, B. Jousselme, V. Ivanova, H. Dau, S. Palacin, M. Fontecave, V. Artero, *Nat. Mater.* **2012**, *11*, 802; b) A. Le Goff, V. Artero, B. Jousselme, P. D. Tran, N. Guillet, R. Métayé, A. Fihri, S. Palacin, M. Fontecave, *Science* **2009**, *326*, 1384; c) E. S. Andreiadis, P.-A. Jacques, P. D. Tran, A. Leyris, M. Chavarot-Kerlidou, B. Jousselme, M. Matheron, J. Pécaut, S. Palacin, M. Fontecave, V. Artero, *Nat. Chem.* **2013**, *5*, 48.

[24] a) B. E. Conway, B. V. Tilak, *Electrochim. Acta* **2002**, *47*, 3571; b) M. P. Marceta Kaninski, V. M. Nikolic, G. S. Tasic, Z. L. Rakocevic, *Int. J. Hydrogen Energy* **2009**, *34*, 703.

[25] a) W.-F. Chen, K. Sasaki, C. Ma, A. I. Frenkel, N. Marinkovic, J. T. Muckerman, Y. Zhu, R. R. Adzic, *Angew. Chem., Int. Ed.* **2012**, *51*, 6131; b) W. F. Chen, C. H. Wang, K. Sasaki, N. Marinkovic, W. Xu, J. T. Muckerman, Y. Zhu, R. R. Adzic, *Energy Environ. Sci.* **2013**, *6*, 943.

[26] X. Zou, Y. Zhang, *Chem. Soc. Rev.* **2015**, *44*, 5148.

[27] J. Xie, J. Zhang, S. Li, F. Grote, X. Zhang, H. Zhang, R. Wang, Y. Lei, B. Pan, Y. Xie, *J. Am. Chem. Soc.* **2013**, *135*, 17881.

[28] Y.-F. Xu, M.-R. Gao, Y.-R. Zheng, J. Jiang, S.-H. Yu, *Angew. Chem., Int. Ed.* **2013**, *52*, 8546.

[29] a) J. Tian, Q. Liu, A. M. Asiri, K. A. Alamry, X. Sun, *ChemSusChem* **2014**, *7*, 2125; b) G.-L. Tian, Q. Zhang, B. Zhang, Y.-G. Jin, J.-Q. Huang, D. S. Su, F. Wei, *Adv. Funct. Mater.* **2014**, *24*, 5956; c) G.-L. Tian, M.-Q. Zhao, D. Yu, X.-Y. Kong, J.-Q. Huang, Q. Zhang, F. Wei, *Small* **2014**, *10*, 2251; d) Y. Liang, Y. Li, H. Wang, J. Zhou, J. Wang, T. Regier, H. Dai, *Nat. Mater.* **2011**, *10*, 780; e) X. Lu, W.-L. Yim, B. H. R. Suryanto, C. Zhao, *J. Am. Chem. Soc.* **2015**, *137*, 2901; f) M.-R. Gao, Y.-F. Xu, J. Jiang, Y.-R. Zheng, S.-H. Yu, *J. Am. Chem. Soc.* **2012**, *134*, 2930; g) J. Masa, W. Xia, I. Sinev, A. Zhao, Z. Sun, S. Grützke, P. Weide, M. Muhler, W. Schuhmann, *Angew. Chem., Int. Ed.* **2014**, *53*, 8508; h) J. Nai, H. Yin, T. You, L. Zheng, J. Zhang, P. Wang, Z. Jin, Y. Tian, J. Liu, Z. Tang, L. Guo, *Adv. Energy Mater.* **2015**, *5*, 7; i) G.-L. Tian, M.-Q. Zhao, D. Yu, X.-Y. Kong, J.-Q. Huang, Q. Zhang, F. Wei, *Small* **2014**, *10*, 2251; j) Y. Cheng, Y. Tian, X. Fan, J. Liu, C. Yan, *Electrochim. Acta* **2014**, *143*, 291; k) Y. Wu, J. Zang, L. Dong, Y. Zhang, Y. Wang, *J. Power Sources* **2016**, *305*, 64.

[30] a) J. Liang, Y. Jiao, M. Jaroniec, S. Z. Qiao, *Angew. Chem., Int. Ed.* **2012**, *51*, 11496; b) T. Y. Ma, S. Dai, M. Jaroniec, S. Z. Qiao, *Angew. Chem., Int. Ed.* **2014**, *53*, 7281.

[31] J. Tian, Q. Liu, A. M. Asiri, X. Sun, *J. Am. Chem. Soc.* **2014**, *136*, 7587.

[32] a) F. Song, X. Hu, *J. Am. Chem. Soc.* **2014**, *136*, 16481; b) M. Gao, W. Sheng, Z. Zhuang, Q. Fang, S. Gu, J. Jiang, Y. Yan, *J. Am. Chem. Soc.* **2014**, *136*, 7077.

[33] a) L. Wang, C.-Y. Lee, P. Schmuki, *J. Mater. Chem. A* **2013**, *1*, 212; b) R. Saito, Y. Miseki, K. Sayama, *Chem. Commun.* **2012**, *48*, 3833; c) S. Hoang, S. Guo, N. T. Hahn, A. J. Bard, C. B. Mullins, *Nano Lett.* **2012**, *12*, 26.

Received: April 3, 2016
Revised: May 7, 2016

4.3. Supporting Information

This section is included in the thesis as supplementary information to section 4.2. It includes additional information which is not put in the main text of the published paper; however, it is freely accessible online as an electronic supplementary information.

NANO small MICRO

Supporting Information

for *Small.*, DOI: 10.1002/smll.201601131

Significant Enhancement of Water Splitting Activity of N-Carbon Electrocatalyst by Trace Level Co Doping

Bita Bayatsarmadi, Yao Zheng, Youhong Tang, Mietek Jaroniec, and Shi-Zhang Qiao**

Supporting Information

Significant enhancement of water splitting activity of N-carbon electrocatalyst by trace level Co doping

*Bita Bayatsarmadi, Yao Zheng**, *Youhong Tang, Mietek Jaroniec and Shi-Zhang Qiao**

B. Bayatsarmadi, Dr. Y. Zheng, Prof. S.Z. Qiao
School of Chemical Engineering, the University of Adelaide, Adelaide, South Australia 5005, Australia
E-mail: s.qiao@adelaide.edu.au; yao.zheng01@adelaide.edu.au

Dr Y. Tang
School of Computer Sc, Engineering & Mathematics, Flinders University, Adelaide, South Australia 5001, Australia

Prof. M. Jaroniec
Department of Chemistry and Biochemistry, Kent State University, Kent, Ohio 44240, USA

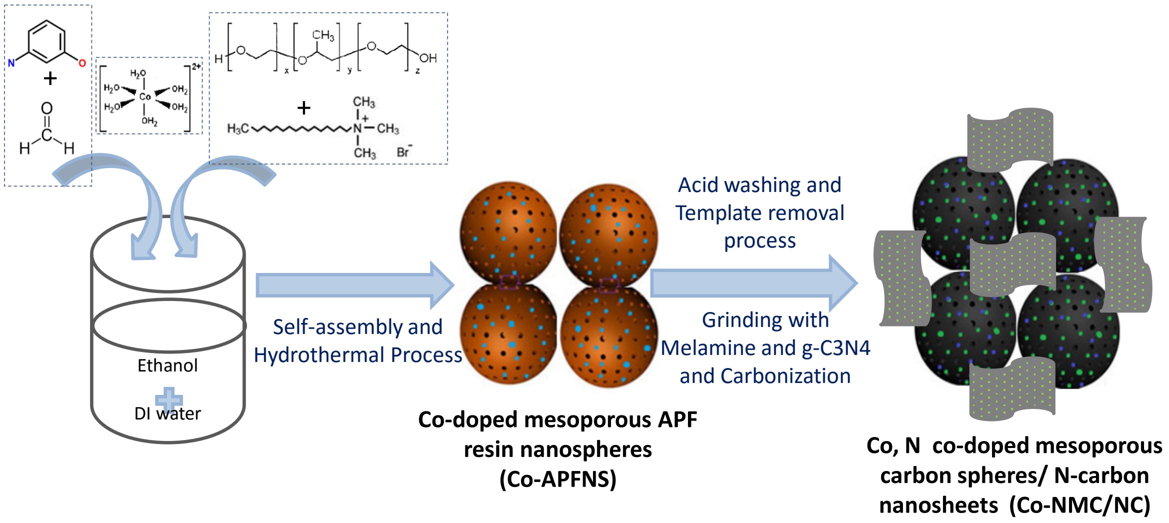

Figure S1. Schematic illustration of the synthesis of in situ grown N-carbon nanosheets at Co,N co-doped mesoporous carbon spheres (Co-NMC/NC).

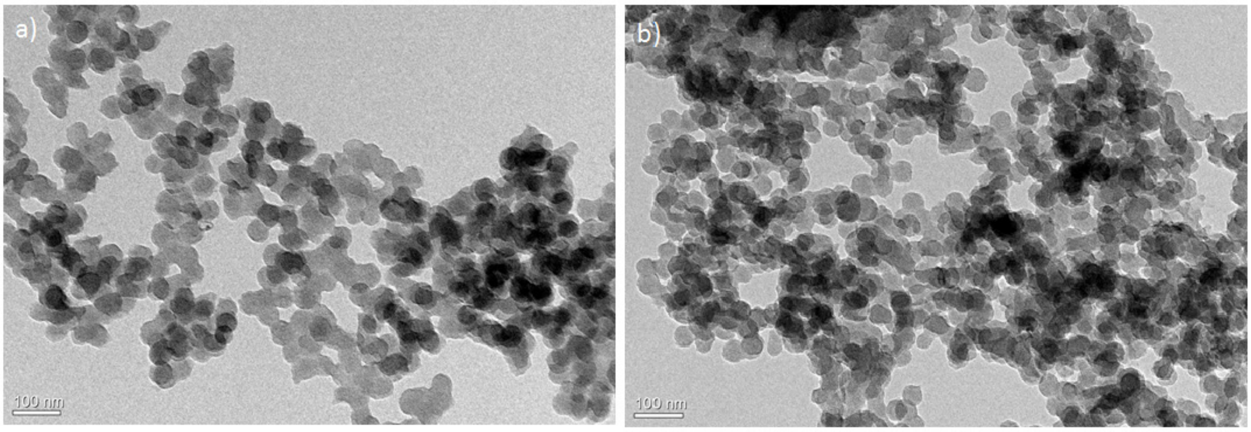

Figure S2. Magnified TEM images of the synthesized electrocatalysts (a) $(\text{Co-NMC})_{10}$/NC and (b) Co_{10}-NMC/NC.

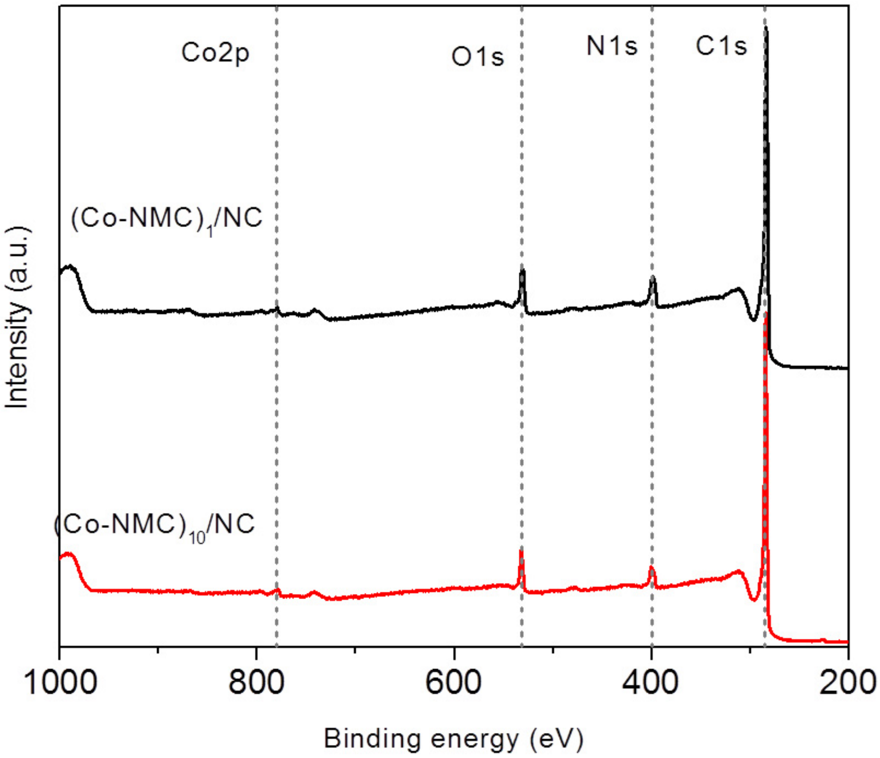

Figure S3. (a) XPS survey spectra of (Co-NMC)$_1$/NC and (Co-NMC)$_{10}$/NC.

Table S1. Cobalt concentration values obtained by different methods and the BET surface areas of (Co-NMC)$_y$/NC and Co$_x$-NMC/NC hybrids.

Sample	Cobalt concentration (at. %)			BET surface area (m^{2}g^{-1})
	ICP-MS	XPS	Elemental mapping	
(Co-NMC)$_1$/NC	1.48	0.30	1.38	540
(Co-NMC)$_{10}$/NC	2.12	0.33	2.08	239
Co$_{10}$-NMC/NC	1.89	0.31	1.72	257

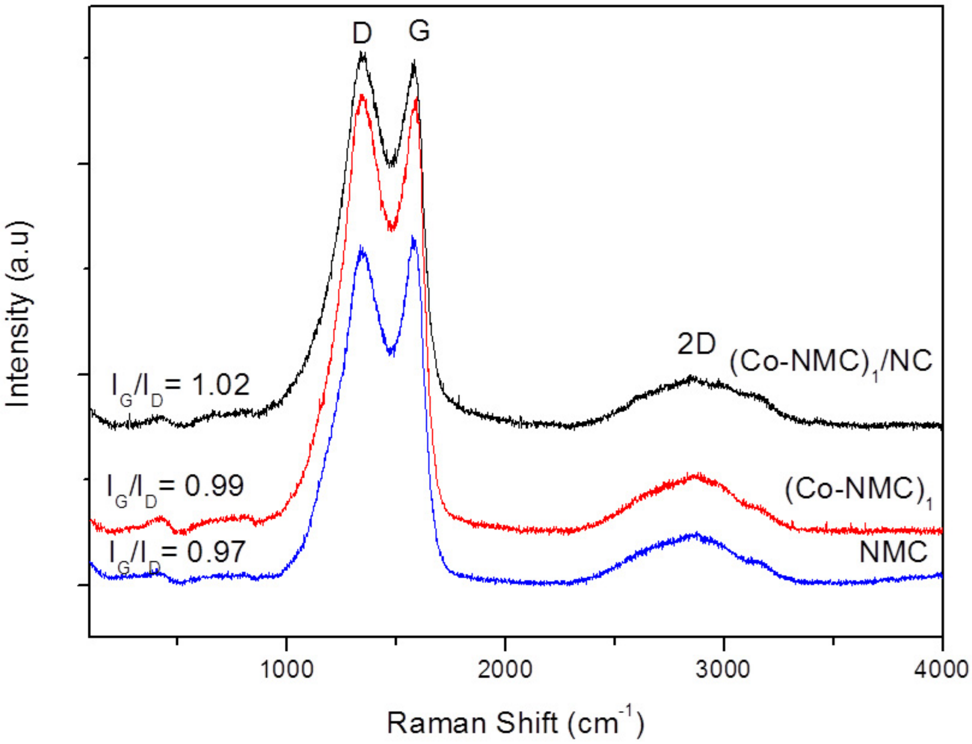

Figure S4. Raman spectra of NMC, (Co-NMC)$_1$ and (Co-NMC)$_1$/NC.

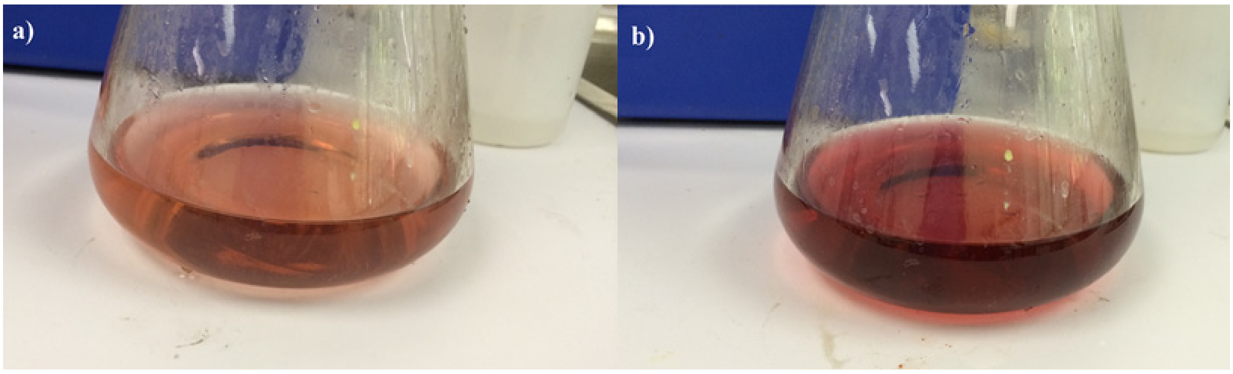

Figure S5. Washing residue from washing step of cobalt-doped mesoporous APF resin nanospheres performed to remove the free standing and unreacted cobalt species from (a) Co$_1$-APFNS and (b) Co$_{10}$-APFNS.

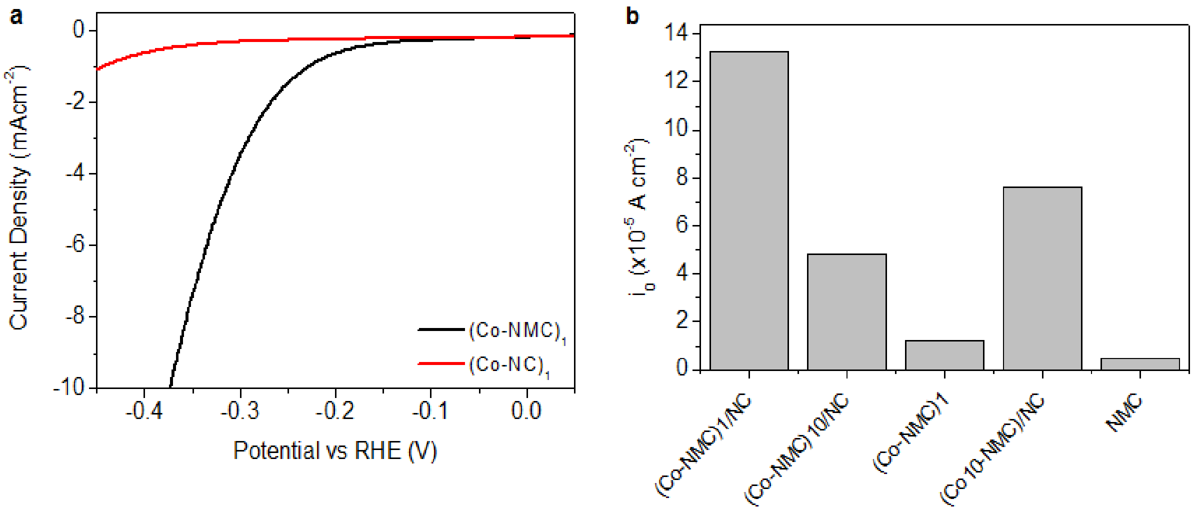

Figure S6. (a) HER polarization curves obtained for $(Co\text{-}NMC)_1$ and $(Co\text{-}NC)_1$ in 0.1 M KOH solution to study the effect of porous structure on the HER activity, (b) HER exchange current density for all synthesized electrocatalysts in 0.1 M KOH solution.

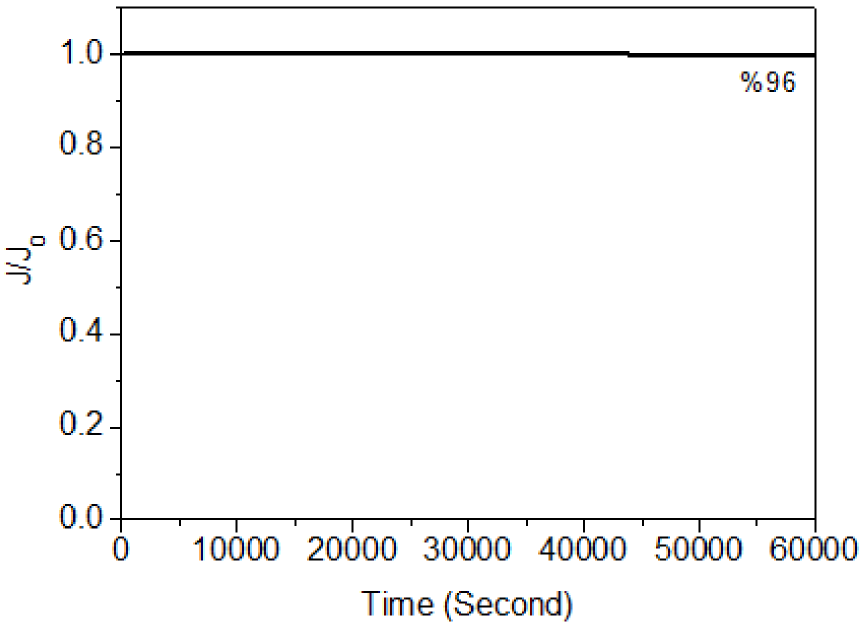

Figure S7. The chronoamperometric response of $(Co\text{-}NMC)_1/NC$ at -1.4 V after 60,000 seconds in 0.1 M KOH solution.

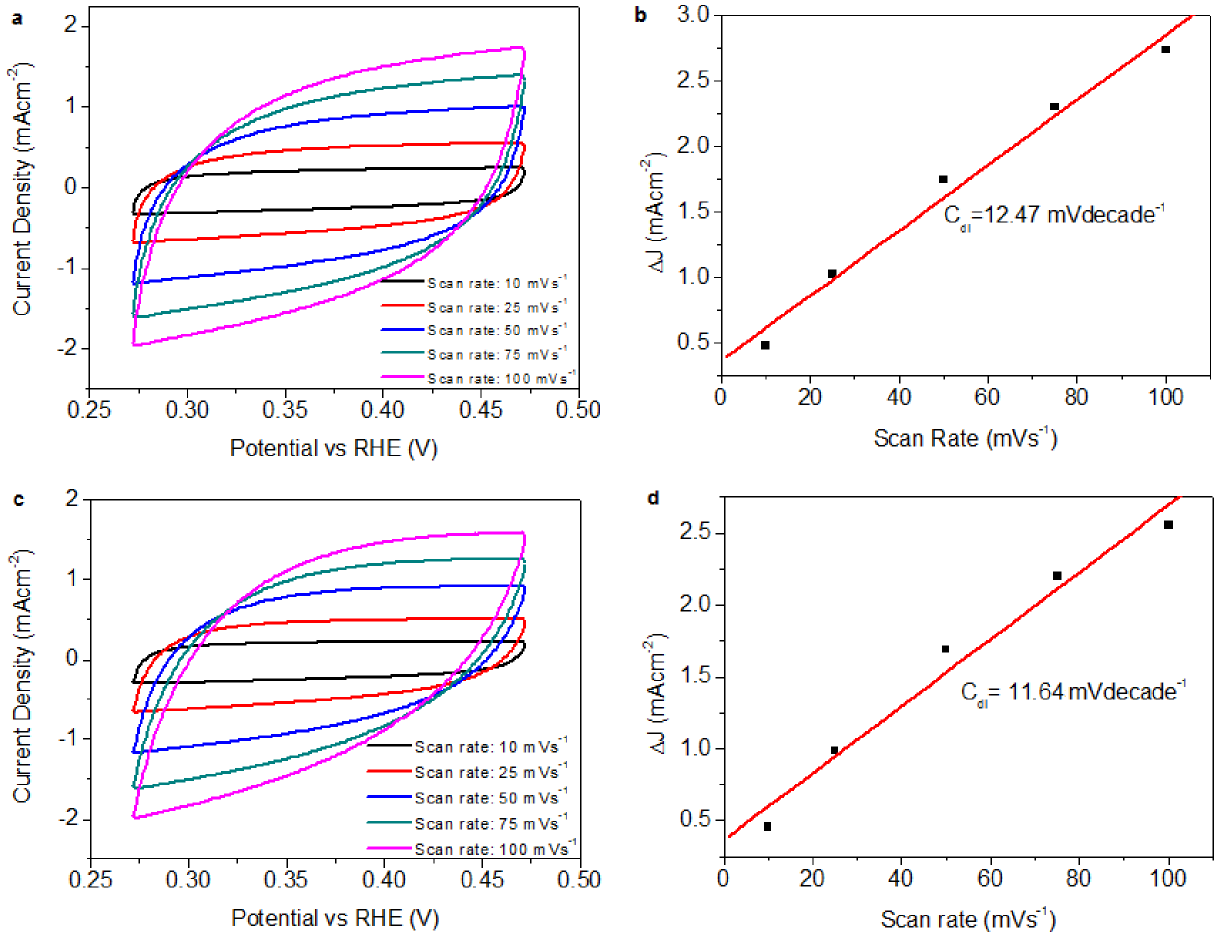

Figure S8. (a) CV curves, (b) the corresponding differences in the current density of $(Co\text{-}NMC)_1$/NC; (c) CV curves, (d) the corresponding differences in the current density of $(Co\text{-}NMC)_1$ at 0.375 V plotted against scan rate.

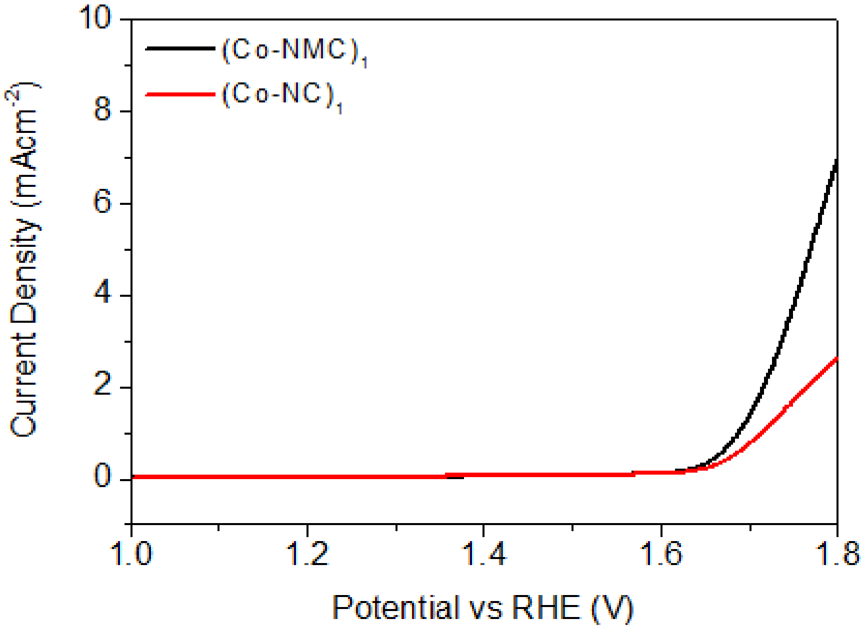

Figure S9. OER polarization curves obtained for (Co-NMC)$_1$ and (Co-NC)$_1$ in 0.1 M KOH solution to study the effect of porous structure on the OER activity.

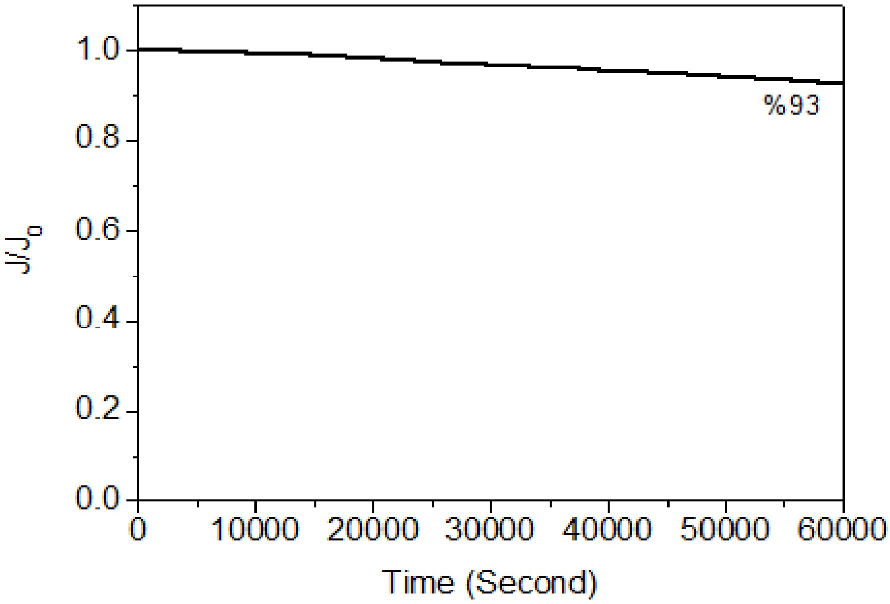

Figure S10. The chronoamperometric response of (Co-NMC)$_1$/NC at +0.8 V after 60,000 seconds in 0.1 M KOH solution.

Chapter 5

5. Pulsed laser deposition of porous N-carbon supported cobalt (oxide) thin films for highly efficient oxygen evolution

5.1. Introduction

Identifying efficient non-precious metal electrocatalysts for oxygen evolution reaction (OER) remains a great challenge. Inexpensive and durable “noble metal-free” electrocatalysts such as non-precious metal, metal composites and metal-free nanostructures, as well as their hybrids, have received much attention. Despite recent progress in developing non-precious metal- based hybrid materials, new OER electrocatalysts with low overpotentials and long-term stability are still needed. To overcome these challenges, new synthesis techniques are required to ensure effective control and tunability of morphology, structure and composition of multi-component materials. Herein, we demonstrate the novel preparation of highly porous N-carbon film supported cobalt (oxide) nanoparticles via two-step pulsed laser deposition under a reactive background gas at room temperature. New materials exhibit highly efficient and durable OER electrocatalytic activity in strongly alkaline electrolytes.

The highlights of this work include:

1. Porous N-carbon supported cobalt (oxide) thin films ($Co(Ox)_{50}$@PNC) have been developed via a two-step pulsed laser deposition technique which is versatile in the tuning of properties of deposited materials over a wide range.

2. By controlling deposition parameters (e.g. background gas type and pressure), porous structure, chemical composition and conductivity of electrodes are tuned, and their effect on catalytic activity has been investigated for the first time. This method may pave the way for the feasible design of N-carbon supported cobalt (oxide) thin films and their electrocatalysis application.

3. This work shows that the superior performance of $Co(Ox)_{50}$@PNC originates from the porous structure and high conductivity of N-carbon support as well as high Co^{2+}/Co^{3+} ratio and the synergetic effect of the cobalt (oxide) nanoparticles and the N-carbon framework.

4. This work shows that the superior performance of $Co(Ox)_{50}$@PNC originates from the porous structure and high conductivity of N-carbon support as well as the high Co^{2+}/Co^{3+}

ratio and the synergetic effect of the cobalt (oxide) nanoparticles and the N-carbon framework.

5.2. Research Outcome

This section is included in the thesis as it appears as a journal paper published by **Bita Bayatsarmadi**, Yao Zheng, Carlo Spartaco Casari, Valeria Russo, and Shi-Zhang Qiao, “Pulsed laser deposition of porous N-carbon supported cobalt (oxide) thin films for highly efficient oxygen evolution”, ***Chemical Communications***, 2016, 52, 11947-11950.

Statement of Authorship

Title of Paper	Pulsed laser deposition of porous N-carbon supported cobalt (oxide) thin films for highly efficient oxygen evolution
Publication Status	☑ Published ☐ Accepted for Publication ☐ Submitted for Publication ☐ Unpublished and Unsubmitted work written in manuscript style
Publication Details	B. Bayatsarmadi, Y. Zheng, C.S. Casari*, V. Russo and S.Z. Qiao*, "Pulsed laser deposition of porous N-carbon supported cobalt (oxide) thin films for highly efficient oxygen evolution", ***Chemical Communications***, 2016, 52, 11947-11950, [IF: 6.567]

Principal Author

Name of Principal Author (Candidate)	Bita Bayatsarmadi		
Contribution to the Paper	Research plan, material synthesis, most of the material characterisations, performance assessments and manuscript drafting.		
Overall percentage (%)	80%		
Certification:	This paper reports on original research I conducted during the period of my Higher Degree by Research candidature and is not subject to any obligations or contractual agreements with a third party that would constrain its inclusion in this thesis. I am the primary author of this paper.		
Signature		Date	18/11/2016

Co-Author Contributions

By signing the Statement of Authorship, each author certifies that:

i. the candidate's stated contribution to the publication is accurate (as detailed above);

ii. permission is granted for the candidate in include the publication in the thesis; and

iii. the sum of all co-author contributions is equal to 100% less the candidate's stated contribution.

Name of Co-Author	Dr. Yao Zheng		
Contribution to the Paper	Discussion of research plan, manuscript review and assessment.		
Signature		Date	21/11/2016

Name of Co-Author	Prof. Carlo Spartaco Casari		
Contribution to the Paper	Discussion of research plan, manuscript review and assessment.		
Signature		Date	18/11/2016

Name of Co-Author	Dr. Valeria Russo		
Contribution to the Paper	Discussion of material characterisation and manuscript review.		
Signature		Date	18/11/2016

Name of Co-Author	Prof. Shi-Zhang Qiao		
Contribution to the Paper	Supervised development of the work, organisation of the research, manuscript review and assessment.		
Signature		Date	18/11/2016

ChemComm

COMMUNICATION

Cite this: *Chem. Commun.*, 2016, **52**, 11947

Received 8th June 2016,
Accepted 6th September 2016

DOI: 10.1039/c6cc04776a

www.rsc.org/chemcomm

Pulsed laser deposition of porous N-carbon supported cobalt (oxide) thin films for highly efficient oxygen evolution†

Bita Bayatsarmadi,[a] Yao Zheng,[a] Carlo Spartaco Casari,*[b] Valeria Russo[b] and Shi-Zhang Qiao*[a]

Identification of efficient non-precious metal catalysts for the oxygen evolution reaction (OER) remains a great challenge. Here we report robust cobalt (oxide) nanoparticles deposited on a porous nitrogen-doped carbon (N-carbon) film prepared by pulsed laser deposition under a reactive background gas, which exhibit highly efficient OER performance with a low overpotential and high stability.

The global energy crisis has prompted intense research into the development of various types of sustainable energy conversion and storage systems.[1] Splitting of water is widely considered to be a critical step toward efficient renewable energy production, storage and usage. One of the major hurdles in making water electrolysis commercially more viable is the low efficiency of the anodic oxygen evolution reaction (OER) and the high cost of conventional OER catalysts such as IrO_2 and RuO_2.[2] Inexpensive and durable ''noble metal-free'' electrocatalysts have received much attention recently.[3] Among different non-precious metals, cobalt-based materials are promising OER catalysts; however, the easy accumulation and low conductivity of pure cobalt oxides decrease the available active sites and limit charge transport during the oxidation process.[4] On the other hand, various carbon-based materials possess unique advantages due to their tunable molecular structures, abundance, and strong tolerance to acid/alkaline environments. The interplay between carbon and cobalt oxide nanoparticles can modify the overall physicochemical and electronic structures, which makes the resultant composites highly competitive to traditional cobalt-based electrocatalysts.[5]

Despite recent progress in the development of non-precious metal (specifically cobalt) based hybrid materials, new OER electrocatalysts with low overpotentials and long-term stability are still needed. To overcome these challenges, synthesis techniques are required, which can ensure high control and tunability of morphology, structure and composition of multi-component materials. Physical vapour deposition (PVD) techniques allow high purity and control in the fabrication of coatings and thin films. In this context, pulsed laser deposition (PLD) is particularly versatile in the tuning of properties of deposited materials.[6] The control of the ablation process of target materials permits the tuning of the growth mode and properties of the deposited films over a wide range.[7]

Herein, we demonstrate highly porous N-carbon film supported cobalt (oxide) nanoparticles prepared by two-step pulsed laser deposition under a reactive background gas at room temperature as a highly efficient and durable OER electrocatalyst in strongly alkaline electrolytes. A detailed physicochemical characterization of this material further confirms that its superior performance originates from the porous structure and high conductivity of N-carbon and the synergetic effect of the cobalt (oxide) nanoparticles and the N-carbon films.

The two step fabrication process of cobalt (oxide) nanoparticles deposited on porous N-carbon films (denoted as $Co(Ox)_P$@PNC; subscript P is the background gas pressure in Pa) is illustrated in Fig. 1a. In the first step, porous N-carbon (PNC) films were deposited on substrates (silicon and copper foil) by PLD with a pulse energy of 200 mJ (λ = 532 nm, pulse duration = 9 ns) at room temperature using a highly pure graphite target under reactive N_2 gas flow. Laser pulses ablate the target ejecting material in a plasma plume in the presence of a background gas within the pressure range of 10 to 100 Pa to tune the morphology, structure and composition of the deposited film. The X-ray photoelectron spectroscopy (XPS) survey indicates that the chemical composition of PNC films consists of C, O and N (Fig. 1b). By controlling deposition parameters (*e.g.* background gas pressure, target-to-substrate distance and deposition time), thin films with various porous structures and specific surface area were formed (Fig. S1, ESI†). Such porous structures are favourable for the deposition of metal nanoparticles in the second step, as the latter could easily go through and stay on the surface or side walls of the porous carbon network.

---

[a] *School of Chemical Engineering, University of Adelaide, Adelaide, SA 5005, Australia. E-mail: s.qiao@adelaide.edu.au*

[b] *Department of Energy, Politecnico di Milano, via Ponzio 34/3, 20133 Milano, Italy. E-mail: carlo.casari@polimi.it*

† Electronic supplementary information (ESI) available. See DOI: 10.1039/c6cc04776a

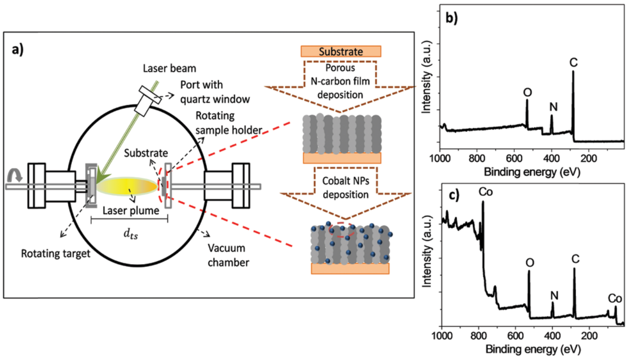

Fig. 1 (a) Schematic illustration of the two step synthesis process of cobalt (oxide) nanoparticles deposited on porous N-carbon film ($Co(Ox)_P$@PNC) and the XPS survey of (b) first step product (PNC) and (c) final product ($Co(Ox)_P$@PNC).

Following this, cobalt nanoparticles were deposited on PNC films (operating as the substrate) using an ultra-pure cobalt target with a nitrogen background gas pressure of 50 Pa to form $Co(Ox)_{50}$@PNC. As shown in Fig. 1c, the XPS survey of $Co(Ox)_{50}$@PNC confirms the successful incorporation of cobalt species into the N-carbon framework (see the Experimental section for details). The cobalt deposition time was calculated based on the desired amount of cobalt in the final product (*e.g.* 10 at%) using quartz crystal microbalance (QCM) measurements.

The morphology and nanostructures of the synthesized materials were investigated using scanning electron microscopy (SEM) and transmission electron microscopy (TEM). The SEM top view image of the PNC films (Fig. 2a) shows complete coverage of the surface by a porous carbon film formed by fine N-carbon nanoparticles deposited at low kinetic energy.[8] The SEM cross-sectional image (inset of Fig. 2a) demonstrates a highly porous thin film with a thickness of about 210 nm. As shown in Fig. S2 (ESI†), the surface morphology of deposited N-carbon films is more spongy with the increasing background gas pressure from 10 to 100 Pa during the deposition process. The cross-sectional SEM images (insets of Fig. S2, ESI†) show that the films formed at lower gas pressures (*i.e.* 10 and 30 Pa) are more compact while the films formed at higher pressures (*i.e.* 50 and 100 Pa) are more porous. Notably, Fig. S2d (ESI†) (film deposited at 100 Pa) exhibits an irregular and highly disordered structure.

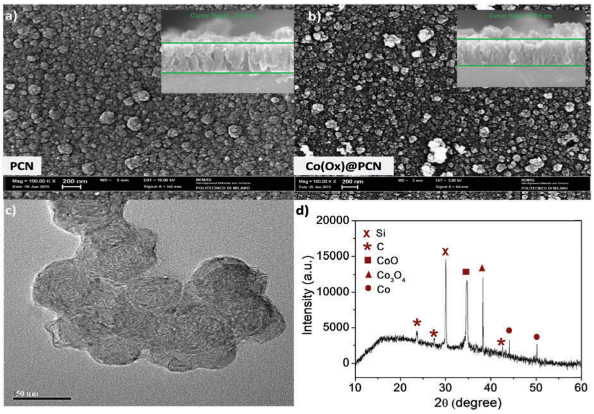

Fig. 2 Top view SEM image and (insets) cross-sectional image of (a) PNC film deposited at 50 Pa and (b) $Co(Ox)_{50}$@PNC at 50 Pa, (c) TEM image of $Co(Ox)_{50}$@PNC and (d) XRD pattern of $Co(Ox)_{50}$@PNC.

From these results, the PNC film deposited at 50 Pa represents the optimal condition for the deposition of low density N-carbon foam which is favourable as a substrate for cobalt (oxide) deposition. Hence, the deposition parameters were carefully tuned to ensure that the subsequent deposition of cobalt did not damage or alter the morphology of the porous N-carbon support layer, as shown in Fig. 2b, where it is clearly seen that there is no change on the surface and cross-section of the film compared to that of PNC. The magnified TEM image (Fig. 2c) shows that the $Co(Ox)_{50}$@PNC films are the aggregation and assembly of nanoparticles in a cauliflower-like fashion with an average diameter of about 50 nm. Note that there is no sign of the presence of large bulk cobalt species homogenous ablation of the cobalt target.

Fig. S3 (ESI†) displays the HR-TEM images, which confirm the $Co(Ox)_P$@PNC films with cobalt deposition at different background gas pressures ranging from 1 to 50 Pa. It is clearly seen that the cobalt nanoparticles form compact clusters at lower gas pressures (*e.g.* 1 and 10 Pa), while porous structured cobalt nanocrystals are embedded within the N-carbon framework at a gas pressure of 50 Pa, which could be more favourable for catalytic activity toward the OER.

The X-ray diffraction (XRD) pattern of the synthesized material corresponds well to what is expected for nanocrystalline $Co(Ox)_{50}$@PNC (Fig. 2d), which shows the existence of Co^0 and cobalt oxides including CoO and Co_3O_4.[9] The XRD pattern also exhibits a peak at *ca.* 24° and 27.5° which is attributed to the (002) facets of graphitic carbon and the stacking peak of pi-conjugated layers for graphitic materials.[10] A weak peak at 42.5° confirms the presence of the (100) plane of disordered amorphous carbon.

Fig. 3a represents the typical Raman spectrum of $Co(Ox)_{50}$@PNC, demonstrating a sharp peak at 675 cm^{-1} assigned to cobalt oxide[11] (the other sharp peak at 521 cm^{-1} is a silicon signal coming from the substrate) and a distinct large peak with a shoulder in the range of 1300–1600 cm^{-1} (G–D region). The shape of this large peak indicates that carbon is mostly in its amorphous form.[12] In order to identify the G and D peak properties (position, width and relative intensities), the Raman spectra were then analysed by fitting a Lorentzian to the D peak and a Breit–Wigner–Fano (BWF) line shape to the G peak. The best deconvolution of the peak at the G–D region (inset of Fig. 3a) shows two prominent broad G(1575 cm^{-1}) and D(1345 cm^{-1}) bands, which represent the presence of sp^2 carbon and the degree of structural disorder of carbon materials, respectively.[12] Notably, the substitution of carbon atoms by other species (*i.e.* nitrogen) is reasonably accompanied by the introduction of defects into the carbon network, which can reflect on the D band to G band intensity ratio (I_D/I_G).[13] Typical values of about 0.5 for the I_D/I_G ratio (Fig. S4, ESI†) together with the G position at about 1575 cm^{-1} are compatible with amorphous sp^2 carbon.[14] Fig. 3b displays the Raman spectra of $Co(Ox)_{50}$@PNC at three different excitation wavelengths (*i.e.* 266, 325 and 514 nm) in order to

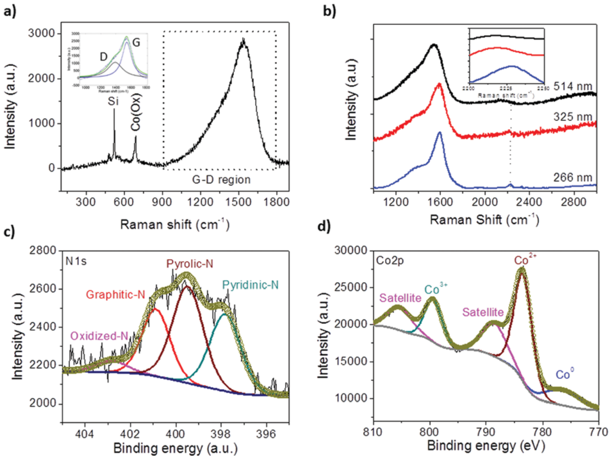

Fig. 3 (a) Raman spectrum of $Co(Ox)_{50}$@PNC film (inset of a) Deconvoluted peaks of the G–D region, (b) Raman spectra of $Co(Ox)_{50}$@PNC film for different laser type (wavelength range) (inset of b) enlarged view of Raman shift ranging 2200–2250 cm^{-1}, (c) high-resolution N1s spectrum and (d) high-resolution Co2p spectrum of $Co_{50}(Ox)$@PNC film.

confirm the C–N formation. A distinct peak at about 2200 cm^{-1}, which can be attributed to sp^1 bonded C–N groups, is clearly visible for the 266 nm excitation, whilst it is barely detectable at 325 and 514 nm excitations. The enhancement of the peak assigned to C–N groups during UV excitation occurs due to their π–π^* band gap which is only resonant for UV excitation.[15] As shown in Fig. S5 (ESI†), the absence of the C–N peak at about 2200 cm^{-1} for $Co(Ox)_{50}$@PC confirms the introduction of nitrogen by ablation under a reactive (nitrogen) atmosphere. By studying the cobalt oxide Raman peaks (Fig. S6, ESI†), it is clearly seen that the Raman active peak assigned to cobalt oxide slightly shifts and becomes weaker in samples deposited in lower nitrogen gas pressures. This might be attributed to the presence of cobalt (oxide) nanostructures with a different degree of structural order. Hence, the deposition of small cobalt nanoclusters may result in a better interconnection of cobalt with the C–N species with an improved electrical conductivity.[16] Moreover, the lower cobalt (oxide) peak intensity at $Co(Ox)_{50}$@PNC compared to that of $Co(Ox)_{50}$@PC indicates that cobalt oxides are partially surrounded by some graphitic carbon layers, which is favourable for electrocatalyst stability.[17]

As shown in Fig. 3c, the N1s XPS spectrum comprises three main peaks located at about 397.8, 399.6 and 400.9 eV, which correspond to pyridinic, pyrrolic and graphitic nitrogen, respectively. Additionally, the wide peak present at about 402.7 eV is assigned to oxidized-nitrogen species.[18] It should be noted that the presence of graphitic nitrogen species confirms the substitution of some carbon atoms by nitrogen atoms in the structure of $Co(Ox)_{50}$@PNC, which is believed to participate as the active sites.[19] Moreover, the existence of pyridinic and pyrrolic nitrogen is beneficial in improving the conductivity of the carbon framework due to the contribution of their p-conjugated system with a pair of p-electrons.[20] This successful incorporation of cobalt into the N-carbon framework was further revealed by the Co 2p XPS spectrum (Fig. 3d). The best deconvolution of the Co 2p profile was achieved under the assumption of five peaks, indicating the existence of Co^0, Co^{2+}, Co^{3+} and their shake-up satellites. It should be noted that peaks with binding energies of 782.2 and 796.9 eV correspond to oxygen-coordinated metals (CoO and Co_3O_4) and the peak at 778.2 eV is attributed to Co^0.[21] The integral data show that the ratio of Co^{2+}/Co^{3+} is 2.64 and Co^0 occupies 11.8% in $Co(Ox)_{50}$@PNC (Table S1, ESI†). By comparing the binding energies of the peaks assigned to pure cobalt oxides (~780.1 and 791.9 eV), the close assembly and strong interaction between oxygen-coordinated cobalt species and carbon is confirmed, which results in the impaired electron density of Co atoms in $Co(Ox)_{50}$@PNC films.[22]

The OER electrocatalytic activity of the synthesised electrocatalysts was evaluated in a standard three-electrode system in an N_2-saturated 1.0 M KOH solution (Fig. S7, ESI†). The OER performances of the prepared materials were tested using linear sweep voltammetry (LSV; Fig. 4a). Remarkably, the $Co(Ox)_{50}$@PNC film can afford a current density of 10 mA cm^{-2} at a small overpotential of 349 mV, which is smaller than those of $Co(Ox)_{50}$@PC (387 mV), commercial IrO_2/C (462 mV), and metal-free PNC (maximum achieved current density of 7.5 mA cm^{-2} at 576 mV). It is also comparable to the best reported carbon supported Co-based OER catalysts.[23] The OER kinetics of the above catalysts were studied by plotting their Tafel curves (Fig. 4b). The resulting Tafel slopes are found to be 75.3, 84.1 and 103.8 mV dec^{-1} for $Co(Ox)_{50}$@PNC, $Co(Ox)_{50}$@PC and PNC respectively, implying the critical role of cobalt (oxide) and nitrogen species in the OER activity of these materials.[24] Moreover, fast electron transport in OER at $Co(Ox)_{50}$@PNC is confirmed by the smallest semicircular diameter (R_{ct} = 4 Ω) of electrochemical impedance spectroscopy (EIS) at 0.7 V *vs.* Ag/AgCl (Fig. S8, ESI†), which is in good agreement with the

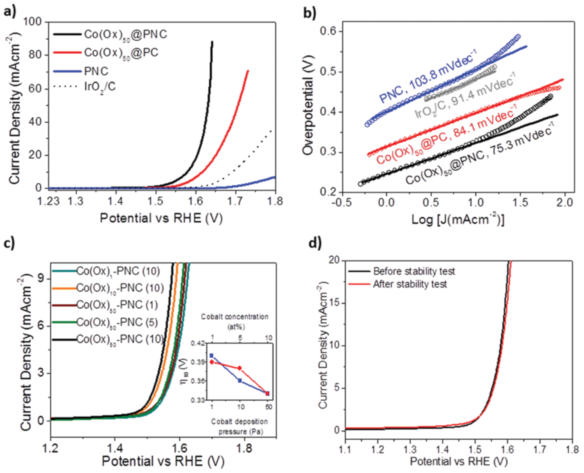

Fig. 4 (a) OER polarization curve of $Co(Ox)_{50}$@PNC, $Co(Ox)_{50}$@PC, metal-free PNC and benchmarked IrO_2/C samples in 1.0 M KOH solution and (b) corresponding OER Tafel plots of $Co(Ox)_{50}$@PNC, $Co(Ox)_{50}$@PC, metal-free PNC and IrO_2/c, (c) OER polarization curves and (inset of c) overpotential plots to reach a current density of 10 mA cm^{-2} for $Co(Ox)_P$@PNC films at different cobalt deposition pressures (blue line) and different cobalt concentrations at a background gas pressure of 50 Pa (red line) in 1.0 M KOH and (d) OER polarization curves of $Co(Ox)_{50}$@PNC before and after the stability test.

Tafel slope, implying faster electrode reaction kinetics. As shown in Fig. 4c, the overpotential (η_{10} at a current density of 10 mA cm^{-2}) decreases for samples fabricated at greater background gas pressures during the cobalt deposition process. This might be attributed to the formation of crystalline cobalt (oxide) at higher pressures (as confirmed *via* HRTEM images, Fig. S3, ESI†) which could possibly increase the interaction of cobalt species with the N-carbon structure. Moreover, a rise in the cobalt concentration (*i.e.* 1, 5 and 10 at%) results in a decrease in the overpotential, which could be due to presence of a greater number of accessible cobalt (oxide) active sites towards oxygen evolution. It is reported that the electrochemically active surface area (EASA) is directly proportional to the amount of active sites, which can be evaluated by the electrochemical double-layer capacitance (C_{dl}).[25] The C_{dl} results confirm the highest number of active sites and enhanced catalytic activity of Co(Ox)$_{50}$@PNC towards OER (Fig. S9, ESI†).

The stability of catalysts toward OER is also important for application of these catalysts in actual devices. Thus, a 24 h chronoamperometric test (Fig. S10, ESI†) of Co(Ox)$_{50}$@PNC was conducted, which exhibited only an 8 mV increase in the overpotential required to achieve a catalytic current density of 10 mA cm^{-2} (Fig. 4d). This excellent stability also demonstrates the potential of using Co(Ox)$_{50}$@PNC films as an efficient and stable OER catalyst.

The above discussions indicate that the remarkable OER catalytic activity of Co(Ox)$_{50}$@PNC arises from its tuned Co^{2+} content, when compared to its nitrogen-free counterpart (Fig. 3d, Fig. S11 and Table S1, ESI†). This can be attributed to the strong interaction and synergetic effect of cobalt (oxide) nanoparticles with N-carbon films and highly improved conductivity and charge transfer capability, which are favourable toward OER activity and stability. Moreover, the porous structure of the N-carbon film support increases the surface area, mass-transport capability and catalytic activity in comparison with that of compact films as evaluated by C_{dl}, which is supposed to be proportional to the surface area in the case of pure N-carbon supports (Fig. S12, ESI†).[26] Last but not the least, the direct growth of active materials on the conductive Cu-foil can greatly enhance the electron transport and adhesion between porous films and substrates, promoting the structural stability for long-term usage.[27]

In conclusion, Co(Ox)$_{50}$@PNC films were successfully developed *via* a two-step pulsed laser deposition technique. The synthesised material behaves as an efficient OER electrocatalyst and has superior activity in 1.0 M KOH electrolyte. The excellent catalytic activity of Co(Ox)$_{50}$@PNC films could be attributed to the surrounding N-carbon framework, and it was found that a higher ratio of Co^{2+}/Co^{3+} yields better catalytic activity towards the OER. The transport of reactants and products involved in electrochemical reactions was also facilitated by the porous structure of the N-carbon support. Together with the combined mutual effects of each structural component, this Co(Ox)$_{50}$@PNC OER catalyst outperforms most of the reported earth-abundant OER catalysts in activity and stability.

This work was financially supported by the Australian Research Council (ARC) through the Discovery Project programs (DP130104459, DP140104062, DP160104866).

Notes and references

1 S. Chu and A. Majumdar, *Nature*, 2012, **488**, 294.
2 J. L. Fillol, Z. Codolà, I. Garcia-Bosch, L. Gómez, J. J. Pla and M. Costas, *Nat. Chem.*, 2011, **3**, 807.
3 (*a*) J. Lai, S. Li, F. Wu, M. Saqib, R. Luque and G. Xu, *Energy Environ. Sci.*, 2016, **9**, 1210; (*b*) Y. Sun, Q. Wu and G. Shi, *Energy Environ. Sci.*, 2011, **4**, 1113; (*c*) Y. Zhang, B. Cui, O. Derr, Z. Yao, Z. Qin, X. Deng, J. Li and H. Lin, *Nanoscale*, 2014, **6**, 3376.
4 X. Zou, A. Goswami and T. Asefa, *J. Am. Chem. Soc.*, 2013, **135**, 17242.
5 (*a*) D. Kong, H. Wang, Z. Lu and Y. Cui, *J. Am. Chem. Soc.*, 2014, **136**, 4897; (*b*) M. Shen, C. Ruan, Y. Chen, C. Jiang, K. Ai and L. Lu, *ACS Appl. Mater. Interfaces*, 2015, **7**, 1207.
6 (*a*) C. S. Casari and A. Li Bassi, *in Oxide Nanostructures*, Pan Stanford Publishing, 2014, p. 99, DOI: 10.1201/b15633-3; (*b*) P. Gondoni, P. Mazzolini, V. Russo, A. Petrozza, A. K. Srivastava, A. Li Bassi and C. S. Casari, *Sol. Energy Mater. Sol. Cells*, 2014, **128**, 248.
7 D. Cattaneo, S. Foglio, C. S. Casari, A. Li Bassi, M. Passoni and C. E. Bottani, *Surf. Sci.*, 2007, **601**, 1892.
8 P. M. Ossi and A. Miotello, in *Carbon: The Future Material for Advanced Technology Applications*, ed. G. Messina and S. Santangelo, Springer Berlin Heidelberg, Berlin, Heidelberg, 2006, p. 359, DOI: 10.1007/11378235_18.
9 Y. Su, Y. Zhu, H. Jiang, J. Shen, X. Yang, W. Zou, J. Chen and C. Li, *Nanoscale*, 2014, **6**, 15080.
10 F. Dong, M. Ou, Y. Jiang, S. Guo and Z. Wu, *Ind. Eng. Chem. Res.*, 2014, **53**, 2318.
11 Y. Li, W. Qiu, F. Qin, H. Fang, V. G. Hadjiev, D. Litvinov and J. Bao, *J. Phys. Chem. C*, 2016, **120**, 4511.
12 A. Zani, D. Dellasega, V. Russo and M. Passoni, *Carbon*, 2013, **56**, 358.
13 K. Kobayashi, R. Kitaura, Y. Kumai, Y. Goto, S. Imagaki and H. Shinohara, *Carbon*, 2009, **47**, 722.
14 A. C. Ferrari and J. Robertson, *Phys. Rev. B: Condens. Matter Mater. Phys.*, 2000, **61**, 14095.
15 A. C. Ferrari, S. E. Rodil and J. Robertson, *Diamond Relat. Mater.*, 2003, **12**, 905.
16 D. Gallant, M. Pézolet and S. Simard, *J. Phys. Chem. B*, 2006, **110**, 6871.
17 H. Jin, J. Wang, D. Su, Z. Wei, Z. Pang and Y. Wang, *J. Am. Chem. Soc.*, 2015, **137**, 2688.
18 Z.-H. Sheng, L. Shao, J.-J. Chen, W.-J. Bao, F.-B. Wang and X.-H. Xia, *ACS Nano*, 2011, **5**, 4350.
19 G. Wu, C. M. Johnston, N. H. Mack, K. Artyushkova, M. Ferrandon, M. Nelson, J. S. Lezama-Pacheco, S. D. Conradson, K. L. More, D. J. Myers and P. Zelenay, *J. Mater. Chem.*, 2011, **21**, 11392.
20 B. Kumar, M. Asadi, D. Pisasale, S. Sinha-Ray, B. A. Rosen, R. Haasch, J. Abiade, A. L. Yarin and A. Salehi-Khojin, *Nat. Commun.*, 2013, **4**, 2819.
21 Y. Chen, S. Zhao and Z. Liu, *Phys. Chem. Chem. Phys.*, 2015, **17**, 14012.
22 N. Weidler, S. Paulus, J. Schuch, J. Klett, S. Hoch, P. Stenner, A. Maljusch, J. Brotz, C. Wittich, B. Kaiser and W. Jaegermann, *Phys. Chem. Chem. Phys.*, 2016, **18**, 10708.
23 (*a*) Y. Liang, Y. Li, H. Wang, J. Zhou, J. Wang, T. Regier and H. Dai, *Nat. Mater.*, 2011, **10**, 780; (*b*) S. Mao, Z. Wen, T. Huang, Y. Hou and J. Chen, *Energy Environ. Sci.*, 2014, **7**, 609; (*c*) A. J. Esswein, M. J. McMurdo, P. N. Ross, A. T. Bell and T. D. Tilley, *J. Phys. Chem. C*, 2009, **113**, 15068; (*d*) M.-R. Gao, Y.-F. Xu, J. Jiang, Y.-R. Zheng and S.-H. Yu, *J. Am. Chem. Soc.*, 2012, **134**, 2930; (*e*) J. Wu, Y. Xue, X. Yan, W. Yan, Q. Cheng and Y. Xie, *Nano Res.*, 2012, **5**, 521.
24 (*a*) Y. Hou, J. Li, Z. Wen, S. Cui, C. Yuan and J. Chen, *Nano Energy*, 2015, **12**, 1; (*b*) B. Bayatsarmadi, Y. Zheng, Y. Tang, M. Jaroniec and S.-Z. Qiao, *Small*, 2016, **12**, 3703.
25 C.-Z. Yuan, Y.-F. Jiang, Z. Wang, X. Xie, Z.-K. Yang, A. B. Yousaf and A.-W. Xu, *J. Mater. Chem. A*, 2016, **4**, 8155.
26 P. Simon and A. F. Burke, *Electrochem. Soc. Interface*, 2008, **17**, 38.
27 D. U. Lee, J.-Y. Choi, K. Feng, H. W. Park and Z. Chen, *Adv. Energy Mater.*, 2014, **4**, 1301389.

5.3. Supporting Information

This section is included in the thesis as supplementary information to section 5.2. It includes additional information which is not put in the main text of the published paper; however, it is freely accessible online as an electronic supplementary information.

Electronic Supplementary Material (ESI) for ChemComm.

Electronic Supporting information

Pulsed laser deposition of porous N-carbon supported cobalt (oxide) thin films for highly efficient oxygen evolution

B. Bayatsarmadi[a], Y. Zheng[a], C.S. Casari[b,*], V. Russo[b] and S.Z. Qiao[a,*]

[a] School of Chemical Engineering, University of Adelaide, Adelaide SA 5005 Australia. Email: s.qiao@adelaide.edu.au

[b] Department of Energy, Politecnico di Milano, via Ponzio 34/3, 20133 Milano, Italy. Email: carlo.casari@polimi.it

I. Experimental section

Material synthesis

Targets and substrate preparation

High purity (99.99%) pyrolytic graphite and an ultra-high purity cobalt target were used for deposition of carbon films and cobalt nanoparticles, respectively. Silicon wafer and copper foils (1 cm × 1 cm pieces) were used as the substrates for film deposition. All the substrates were cleaned by sonication in isopropanol for 20 minutes, rinsing in isopropanol and drying using N_2 flow before deposition.

Synthesis of porous nitrogen-doped carbon film

The porous nitrogen-doped carbon films were deposited at room temperature by reactive PLD using a Nd:YAG pulsed laser (λ = 532 nm, duration of 9 ns and repetition rate of 10 Hz), with a pulse energy of 200 mJ. The beam is directed on rotating graphite target with 45° angle of incidence. Laser pulses ablate the target ejecting material in a plasma plume. Ablated species are deposited on the substrates to form the carbon thin film. The ablation process is performed in the presence of a background gas to tune morphology, structure and composition of the deposited film. The distance between the target and the substrate and the laser spot size on the target were kept at 5 cm and 12.5 mm^2, respectively. The chamber was evacuated first to a base pressure (10^{-3} Pa) using a primary scroll pump and a turbo-molecular pump. The chamber was then fed with nitrogen gas (99.99% purity) within the pressure range of 10-100 Pa to introduce nitrogen to the carbon framework. Ablation in a reactive atmosphere (high purity N2 gas) was performed to incorporate nitrogen into the carbon framework and create C-N moieties to enhance the electrical conductivity. Porous carbon films (without nitrogen) in Argon flow were also prepared using the same PLD conditions for comparison. Based on desired morphology, the deposition times (i.e. number of laser pulses) were varied to control the film thickness (Figure S1).

Mass loading measurements were obtained using a quartz crystal microbalance (QCM) and keeping other deposition conditions (i.e. chamber pressure, pulse energy, target to substrate distance (QCM in the case of mass loading measurements)) constant.

Synthesis of cobalt (oxide) nanoparticles deposited on porous nitrogen-doped carbon film

A high purity Cobalt target was used for the deposition of cobalt (oxide) nanoparticles onto nitrogen-doped carbon films deposited on silicon and copper foil substrates. All the deposition conditions were similar to before. Cobalt (oxide) nanoparticles were deposited at three different background gas pressures (1, 10 and 50 Pa) and deposition times were calculated based on a desired cobalt mass percentage of 10 %at. All the calculations were done based on the mass loadings recorded from the quartz crystal microbalance (QCM) at constant PLD conditions (both carbon and cobalt deposition mass loading).

For comparative studies and to obtain some insight into the electrocatalytic activity of Co(Ox)@PNC films, a series of control samples were prepared at a nitrogen background gas pressure of 1 and 10 Pa (to form Co(Ox)$_1$@PNC and Co(Ox)$_{10}$@PNC and under an Argon background gas pressure of 50 Pa to form Co(Ox)$_{50}$@PC films. All other deposition conditions were kept the same. To study the effect of cobalt atomic concentration at optimized cobalt deposition pressure, Co(Ox)$_{50}$@PNC films with cobalt concentration of 1 , 5 and 10 at % were prepared. All other deposition conditions were kept the same.

Chemical characterization

The morphology of synthesized samples was characterized by a high resolution transmission electron microscope (TEM, JEM-2100) operating at 200 kV and a scanning electron microscope (SEM, ZEISS Supra40) operating at 10 kV. Elemental mapping was conducted using an EDAX detector attached to the JEM-2100. Raman spectra were collected on Renishaw micro-Raman with 514.5 nm and 325 nm excitation wavelengths and LabRAM (Horiba Ltd) with a 266 nm laser line. X-ray diffraction (XRD) patterns (10-80° in 2θ) were collected on a powder X-ray diffractometer at 40 kV and 15 mA using Co-Kα radiation (Miniflx-600, Rigaku). The X-ray photoelectron spectroscopy (XPS) analysis was conducted on an Axis Ultra spectrometer (Kratos Analytical Ltd.) with monochromated AlKα radiation (1486.6 eV) at ca. 510^{-9} Pa.

Electrochemical characterization

All electrochemical tests were performed in a three-electrode glass cell on a 760 workstation (Pine Research Instruments, US). The as-synthesized hybrid films were directly used as the working electrodes, platinum wire as the counter electrode and a standard Ag/AgCl/KCl (4 M) electrode as the reference electrode. A flow of N_2 was maintained over the electrolyte (1 M KOH) during the OER electrochemical measurements to eliminate dissolved oxygen. All potentials were referenced to a reversible hydrogen electrode (RHE) using the equation below:

$$E_{RHE} = E_{Ag/AgCl} + (0.059 \times pH + 0.205)$$

Cyclic voltammogram (CVs) plots were recorded at a scan rate of 100 mV s^{-1}, and linear sweep voltammograms (LSVs) at 5 mV s^{-1}, to minimize the capacitive current. The working electrodes were scanned several times to achieve stabilization before data collection occurred. The internal resistance of the electrochemical cell was 5 Ω and all CV and LSV data were corrected for this iR contribution within the cell.

The Tafel slope was calculated according to the Tafel equation as follows:

$$\eta = b\log j + a,$$

where η is overpotential (V), j is the current density (mA cm^{-2}), and b is the Tafel slope (mV dec^{-1}).

Electrode stability was tested using chronoamperometric response which was conducted at +0.8V (vs. Ag/AgCl) for the OER electrodes. LSVs plots were obtained before and after stability testing for comparison.

The electrical double layer capacitances (C_{dl}, μF cm^{-2}) of working electrodes were obtained from double-layer charging-discharging plots using CVs in a small potential range of -0.875 to -0.825 V (vs Ag/AgCl) at scan rates ranging from 10 to 100 mVs^{-1}. The plots of the current density (mA cm^{-2}) at -0.85V (vs. Ag/AgCl) against the scan rate are nearly linear and the slopes are C_{dl} (μF cm^{-2}).

II. Supporting figures

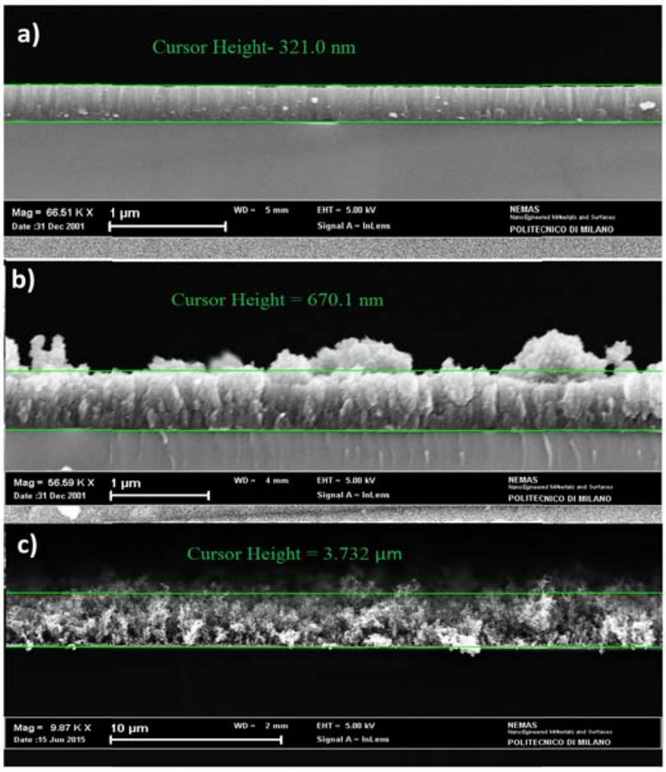

Figure S1. Cross sectional SEM image of PNC films prepared with a constant deposition time of 120 seconds and different background gas (N_2) pressures (a) 30 Pa, (b) 50 Pa and (c) 100 Pa.

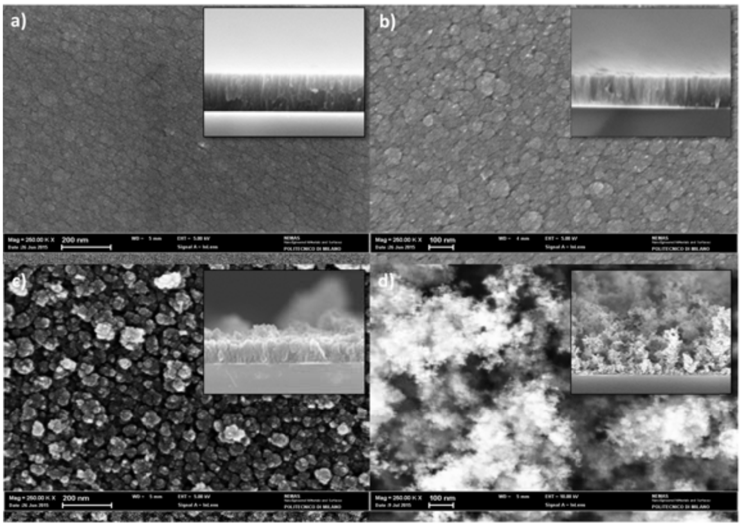

Figure S2. Top view SEM image and (insets) cross-sectional image of PNC films deposited at different background gas pressures; (a) 10 Pa, (b) 30 Pa, (c) 50 Pa and (d) 100 Pa.

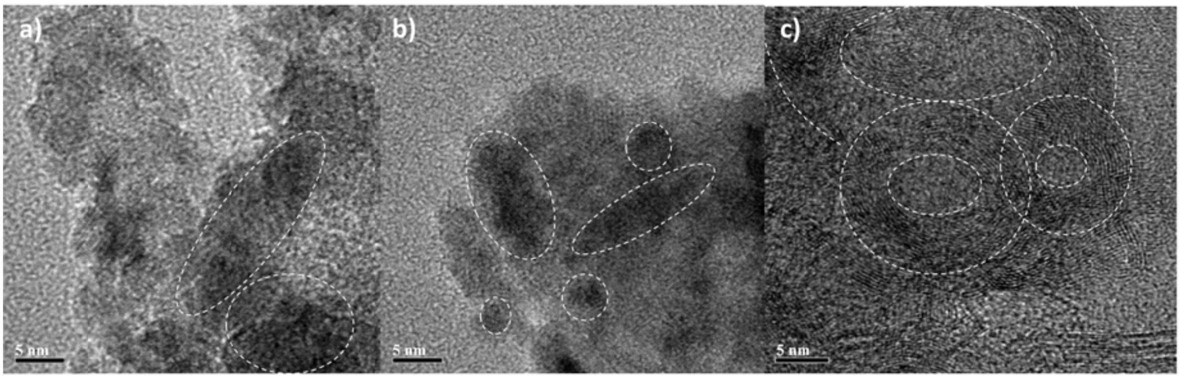

Figure S3. HRTEM image of $Co(Ox)_p$@PNC films prepared at different background gas pressures (for cobalt deposition); (a) 1 Pa, (b) 10 Pa and (c) 50 Pa.

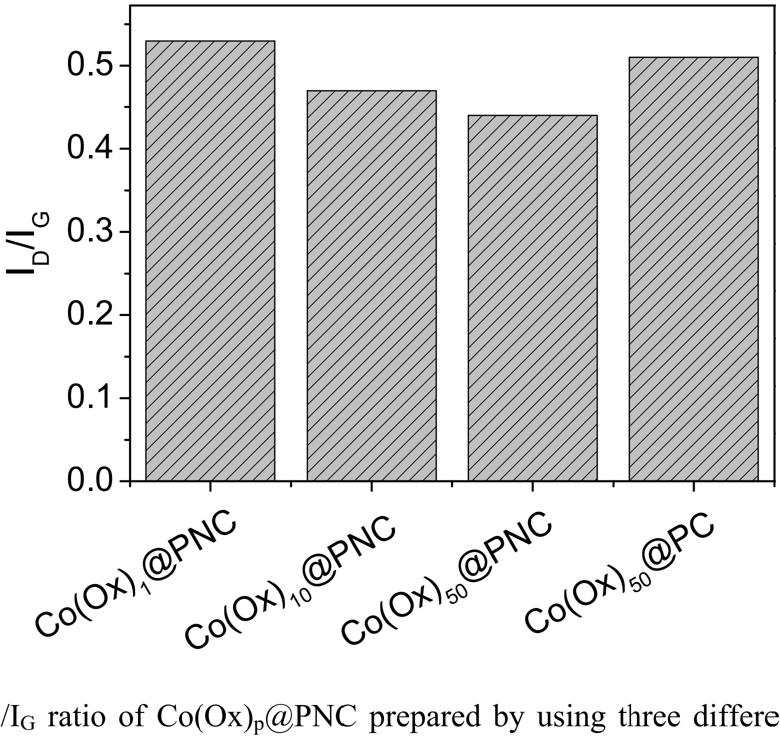

Figure S4. I_D/I_G ratio of $Co(Ox)_p$@PNC prepared by using three different background gas pressures (for cobalt deposition, i.e. 1, 10 and 50 Pa) and $Co(Ox)_{50}$@PC.

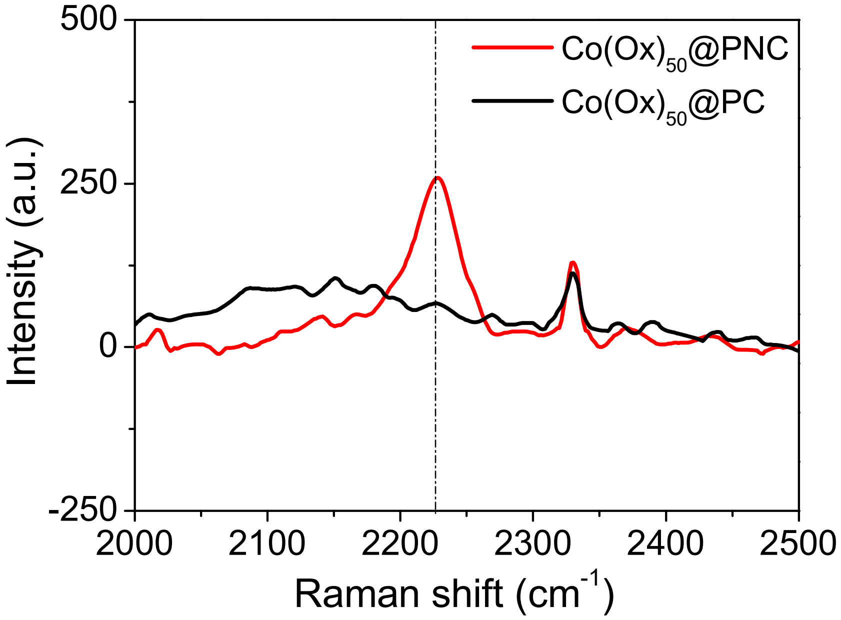

Figure S5. Enlarged view of Raman spectra (C-N peak) of Co(Ox)$_{50}$@PNC (red line) and Co(Ox)$_{50}$@PC (black line) films in UV range (wavelength=266 nm). The peak at 2330 cm^{-1} present in both samples originates from adsorbed N_2 gas molecules.

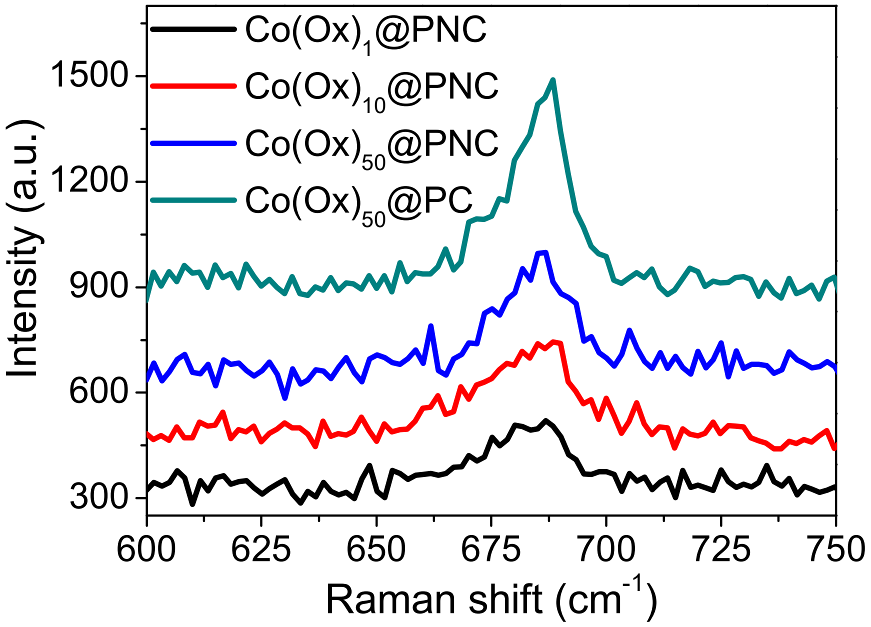

Figure S6. Raman spectra of Co(Ox)$_P$@PNC prepared by using three different background gas pressures for cobalt deposition (i.e. 1, 10 and 50 Pa) and Co(Ox)$_{50}$@PC.

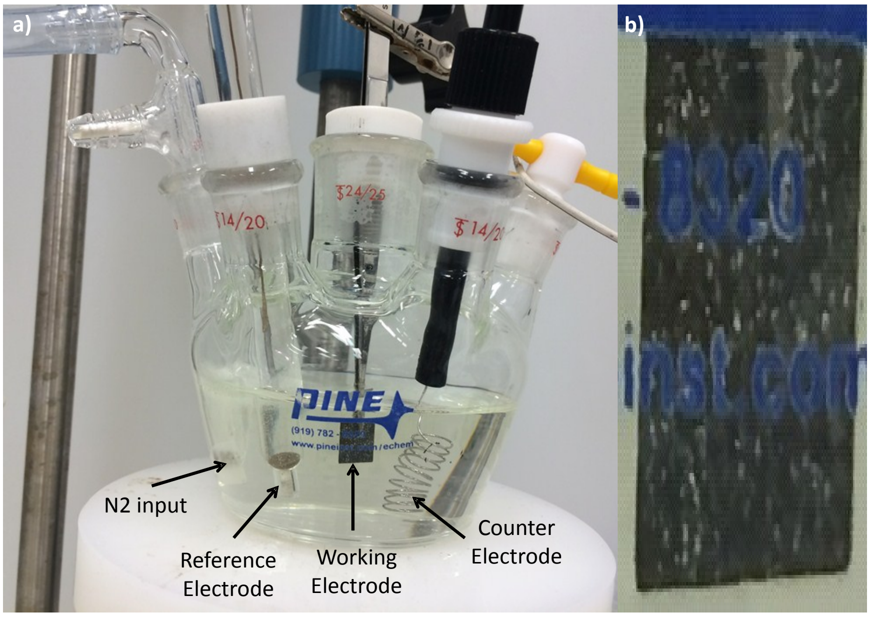

Figure S7. (a) Photographs of the applied electrochemical cell. The reference electrode is a standard Ag/AgCl in 4M KCl; the counter electrode is Platinum wire; N_2 was purged during measurements to eliminate dissolved O_2; working electrodes are the as-prepared films, (b) enlarged view of the working electrode during electrochemical tests.

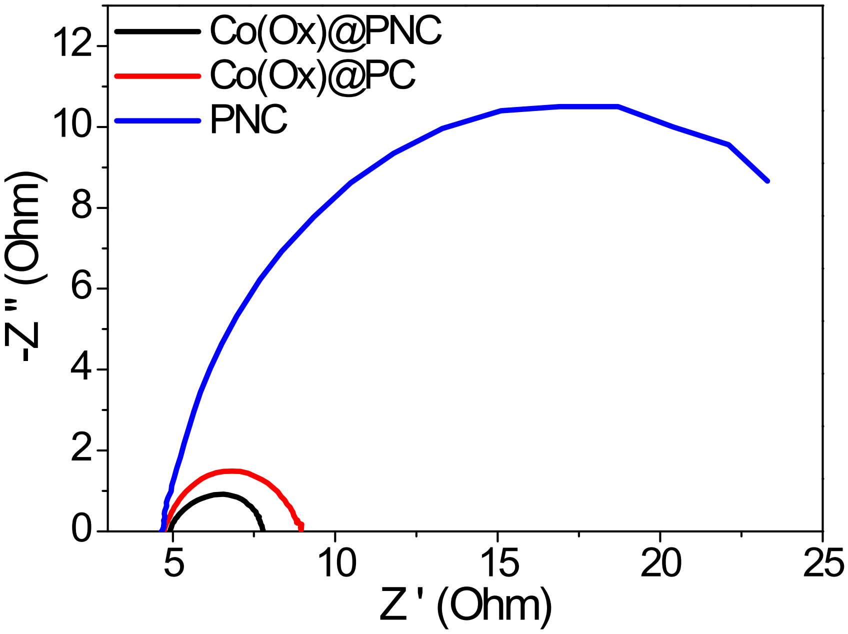

Figure S8- Electrochemical impedance spectra at +0.7 V vs Ag/AgCl of metal-free PNC, Co(Ox)@PC, Co(Ox)@PNC in 1.0 M KOH solution.

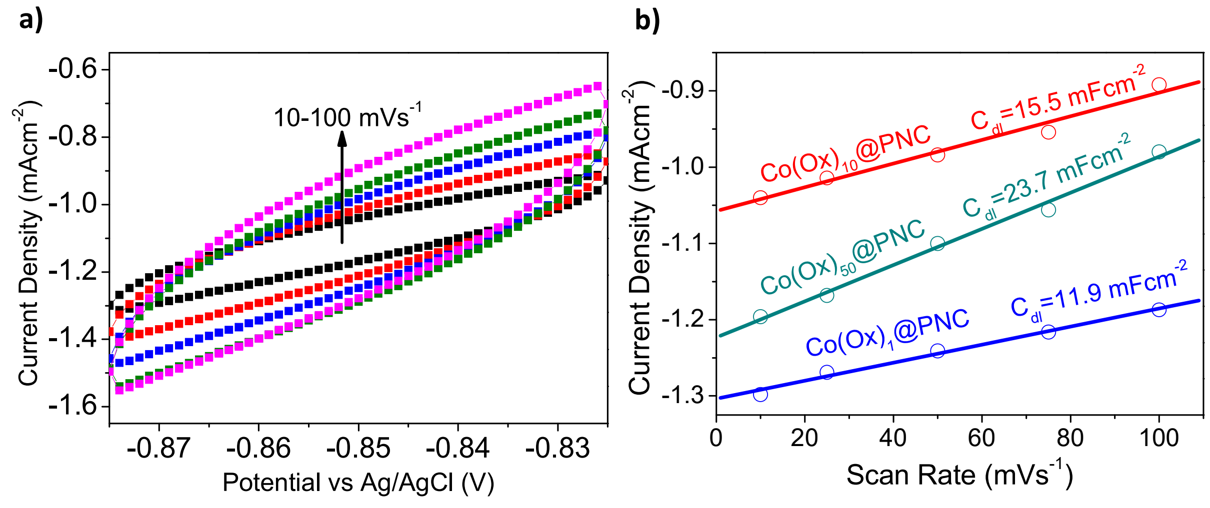

Figure S9- a) Cyclic voltammograms (CVs) of Co(Ox)@PNC at background gas pressure of 50 Pa measured at different scan rates from 10 to 100 mV s^{-1} and b) Plots of the current density at -0.85 V vs. the scan rate for Co(Ox)@PNC deposited at three background gas pressure (i.e. 1, 10 and 50 Pa).

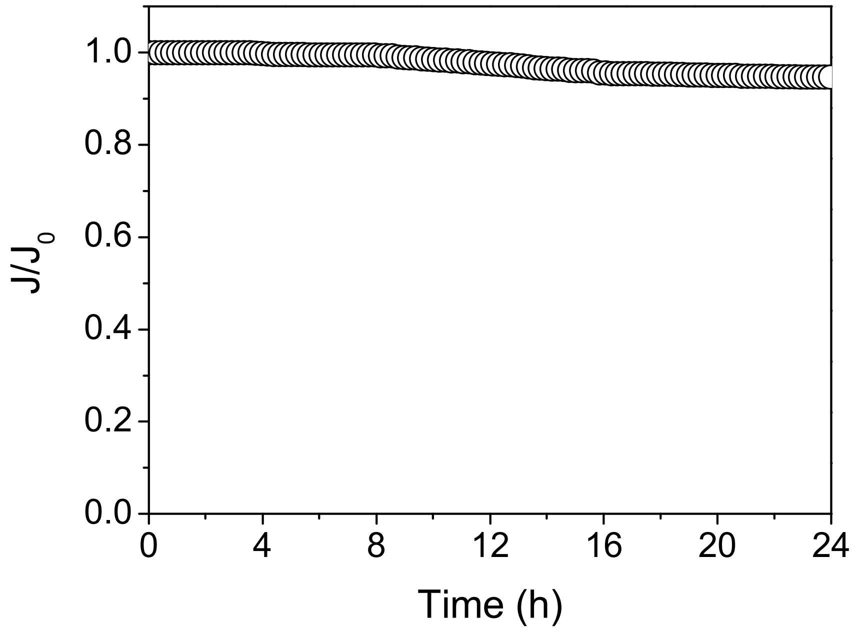

Figure S10- The chronoamperometric response of Co(Ox)$_{50}$@PNC at +0.8 V after 24 h in 1.0 M KOH solution.

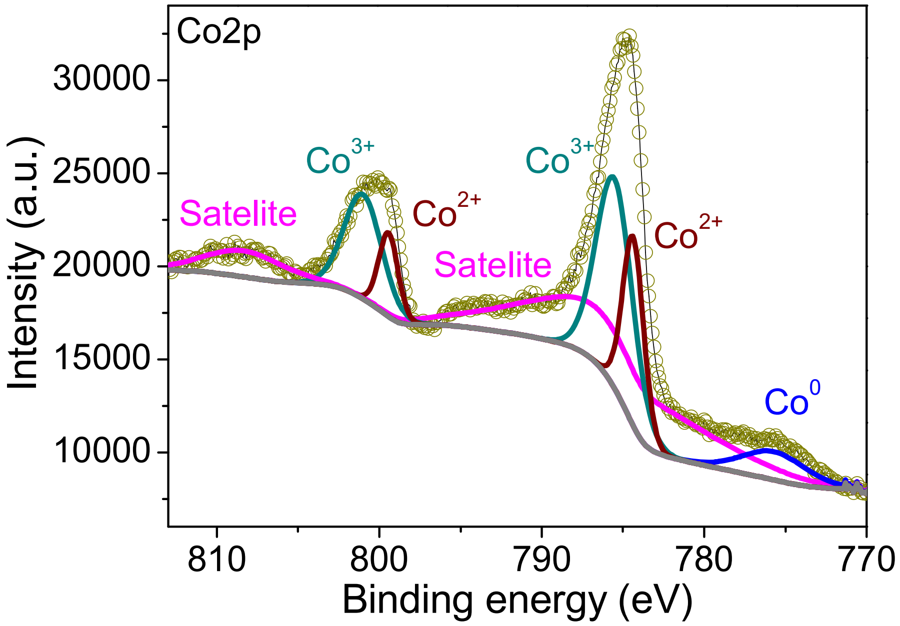

Figure S11- High resolution Co2p spectrum of Co(Ox)@PC.

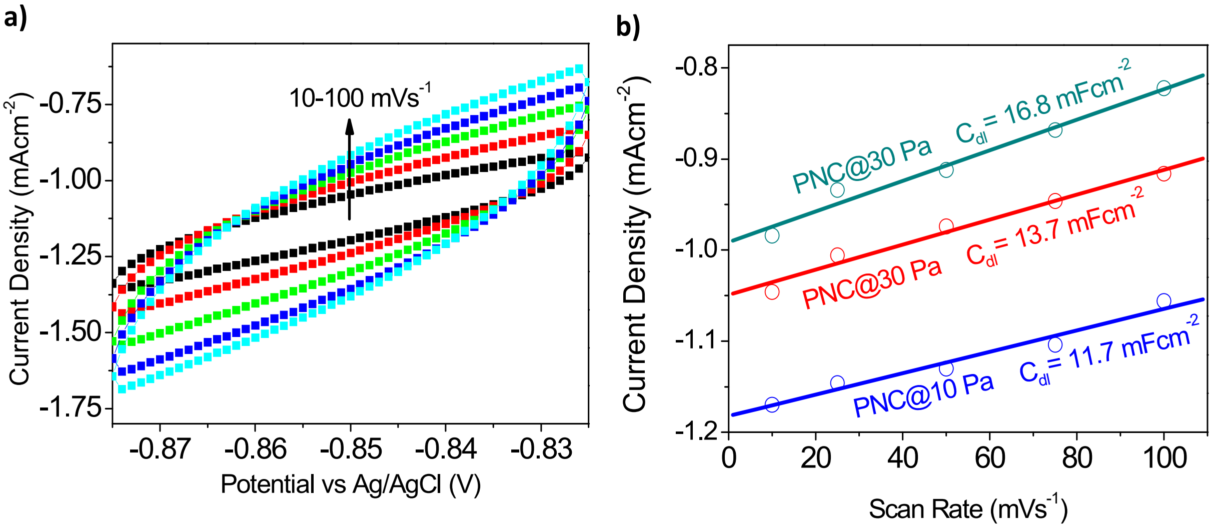

Figure S12- a) Cyclic voltammograms (CVs) of PNC at background gas pressure of 50 Pa measured at different scan rates from 10 to 100 mV s^{-1} and b) Plots of the current density at -0.85 V vs. the scan rate for PNC deposited at three background gas pressure (i.e. 10, 30 and 50 Pa).

Table S1- Cobalt species contents (obtained from Co2p XPS analysis) for the synthesized electrodes.

Sample	**%Co^{0}**	**%Co^{2+}**	**%Co^{3+}**	**Co^{2+}/Co^{3+}**
Co(Ox)@PNC	11.8	64.0	24.2	2.64
Co(Ox)@PC	12.6	28.7	58.7	0.49

Chapter 6

6. Highly Active binary Nickel-Cobalt/Nanocarbon thin films as Efficient Water Splitting electrodes

6.1. Introduction

Replacement of high cost and scarce precious metal catalysts with cost-effective alternatives for completely splitting water at low voltage has attracted wide attention in both industrial and scientific catalysis research. Inexpensive and durable “noble metal-free” electrocatalysts such as non-precious metal-based hybrids have been selected as effective components for either HER or OER. However, pairing the two electrode reactions for practical use is difficult due to the activity and stability issues at different pH ranges. Therefore, developing a bifunctional electrocatalyst with high activity towards both OER and HER in the same electrolyte becomes important yet challenging. To overcome these challenges, new synthesis techniques are required to ensure effective control and tunability of morphology, structure, and composition of multi-component materials. Herein, we demonstrate the novel preparation of a porous carbon film coated by Nickel-Cobalt nanoparticles via a two-step Pulsed laser deposition at room temperature in which nitrogen dopants are incorporated into the carbon framework by ablation under reactive and highly pure nitrogen gas. New developed materials exhibit highly efficient and durable electrocatalytic activity toward both HER and OER in strong alkaline electrolytes.

The highlights of this work include:

1. Nitrogen-doped carbon supported binary nickel-cobalt nanoparticles (Ni_xCo_{1-x}/NC) have been developed via a two-step pulsed laser deposition technique which is versatile in the tuning of properties of deposited materials over a wide range.

2. This work shows that the superior performance of Ni_xCo_{1-x}/NC originates from the porous structure and high conductivity of N-carbon support as well as the formation of interfacial covalent M−N−C and M−O−C bonds which can provide additional active centres in the synthesized hybrids for HER and OER, respectively.

3. The outstanding catalytic performance of developed composites was strongly correlated to the homogeneous distribution of nickel-cobalt active sites and synergetic coupling interaction with the porous N-carbon framework.

4. These findings provide evidence that Ni_xCo_{1-x}/NC electrocatalyst outperforms most of the earth-abundant material-based catalysts with a high current density and excellent stability, therefore shedding new light on the molecular design of next generation electrocatalysts for water splitting.

6.2. Research Outcome

This section is included in the thesis as it appears as a journal paper published by **Bita Bayatsarmadi**, Yao Zheng, Valeria Russo, Lei Ge, Carlo Spartaco Casari, and Shi-Zhang Qiao, “Highly Active binary NickelCobalt/Nanocarbon thin films as Efficient Water Splitting electrodes”, ***Nanoscale***, 2016, 8, 18507-18515.

Statement of Authorship

Title of Paper	Highly Active binary Nickel-Cobalt/Nanocarbon thin films as Efficient Water Splitting electrodes
Publication Status	☑ Published ☐ Accepted for Publication ☐ Submitted for Publication ☐ Unpublished and Unsubmitted work written in manuscript style
Publication Details	B. Bayatsarmadi, Y. Zheng, V. Russo, L. Ge, C.S. Casari, and S.Z. Qiao, "Highly Active binary Nickel-Cobalt/Nanocarbon thin films as Efficient Water Splitting electrodes", ***Nanoscale***, 2016, 8, 18507-18515, [IF: 7.394].

Principal Author

Name of Principal Author (Candidate)	Bita Bayatsarmadi		
Contribution to the Paper	Research plan, material synthesis, most of the material characterisations, performance assessments and manuscript drafting.		
Overall percentage (%)	80%		
Certification:	This paper reports on original research I conducted during the period of my Higher Degree by Research candidature and is not subject to any obligations or contractual agreements with a third party that would constrain its inclusion in this thesis. I am the primary author of this paper.		
Signature		Date	18/11/2016

Co-Author Contributions

By signing the Statement of Authorship, each author certifies that:

i. the candidate's stated contribution to the publication is accurate (as detailed above);
ii. permission is granted for the candidate in include the publication in the thesis; and
iii. the sum of all co-author contributions is equal to 100% less the candidate's stated contribution.

Name of Co-Author	Dr. Yao Zheng		
Contribution to the Paper	Discussion of research plan, manuscript review and assessment.		
Signature		Date	21/11/2016

Name of Co-Author	Dr. Valeria Russo		
Contribution to the Paper	Discussion of material characterisation and manuscript review.		
Signature		Date	18/11/2016

Name of Co-Author	Dr. Lei Ge		
Contribution to the Paper	Assistance with part of material characterisations.		
Signature		Date	18/11/2016

Name of Co-Author	Prof. Carlo Spartaco Casari		
Contribution to the Paper	Discussion of research plan, manuscript review and assessment.		
Signature		Date	18/11/2016

Name of Co-Author	Prof. Shi-Zhang Qiao		
Contribution to the Paper	Supervised development of the work, organisation of the research, manuscript review and assessment.		
Signature		Date	18/11/2016

Nanoscale

PAPER

View Article Online
View Journal | View Issue

Cite this: *Nanoscale*, 2016, **8**, 18507

Highly active nickel–cobalt/nanocarbon thin films as efficient water splitting electrodes†

Bita Bayatsarmadi,[a] Yao Zheng,[a] Valeria Russo,[b] Lei Ge,[c] Carlo Spartaco Casari*[b] and Shi-Zhang Qiao*[a]

Received 2nd September 2016,
Accepted 3rd October 2016

DOI: 10.1039/c6nr06961d

www.rsc.org/nanoscale

Developing low cost, highly active and stable electrocatalysts for both the hydrogen evolution reaction (HER) and the oxygen evolution reaction (OER) using the same electrolyte has remained a major challenge. Herein, we report a novel and robust material comprised of nickel–cobalt nanoparticles coated on a porous nitrogen-doped carbon (NC) thin film synthesized *via* a two-step pulsed laser deposition technique. The optimized sample ($Ni_{0.5}Co_{0.5}/NC$) achieved the lowest overpotentials of 176 mV and 300 mV at a current density of 10 mA cm^{-2} for HER and OER, respectively. The optimized OER activity might be attributed to the available metal oxide nanoparticles with an effective electronic structure configuration and enhanced mass/charge transport capability. At the same time, the porous nitrogen doped carbon incorporated with cobalt and nickel species can serve as an excellent HER catalyst. As a result, the newly developed electrocatalysts manifest high current densities and strong electrochemical stability in overall water splitting, outperforming most of the previously reported non-precious metal-based catalysts.

Introduction

In combatting global warming, the development of renewable energy systems, and in particular energy storage, is vital in order to reduce society's dependence on the finite fossil fuels. Hence, it is essential to develop efficient, low-cost and safe energy storage devices for powering vehicles and electronic devices.[1,2] Electrochemical water splitting represents one of the most important methods for renewable energy storage by generating hydrogen fuel.[3–5] In electrocatalytic water splitting, both water reduction and oxidation reactions are constrained by sluggish kinetics. Currently, the state-of-the-art catalysts used to split water are noble metal-based catalysts including Pt/C and IrO_2/C for the hydrogen evolution reaction (HER) and the oxygen evolution reaction (OER), respectively. These materials, however, are expensive, scarce and suffer low stability.[6,7] Thus, inexpensive and durable non-noble metal electrocatalysts, such as non-precious metals,[8] metal composites[9] and metal-free nanostructures,[10] as well as their hybrids,[11] have received much attention recently. First row transition metal-based materials have had particular interest and have been intensively investigated as potential candidates for electrocatalytic water splitting.

Recent developments demonstrate that the catalytic activity of non-precious metal-based catalysts can be substantially tuned by doping or fabrication of binary metallic mixtures.[12,13] Several strategies have been reported to further improve the catalytic activity of the aforementioned catalysts such as: creating porosity within the structure, immobilizing nanoparticles on carbon supports to increase the surface area and available active sites and making multi-metallic catalysts due to the synergistic interactions between different metals.[14–16] This enhancement may involve morphology changes and/or chemical changes with the possibility of creating bimetallic active sites with carbon bridging.

On the other hand, catalysts in large scale applications need to deliver high current density with low overpotential and high stability and durability.[17] Currently, most of the reported transition metal-based catalysts are powders which need to be coated on a conductive substrate (*e.g.* glassy carbon electrodes) with the help of polymeric binders (*e.g.* Nafion). This may result in a decrease in the contact area between the electrolyte and catalytic active sites and poor stability (*i.e.* peeling off from the substrate) causing loss in electrocatalytic performance.[18] Pulsed laser deposition (PLD) is a versatile synthesis technique to finely control the structure and properties of synthesized materials. PLD provides several advantages including deposition of thin films with either a porous/hierarchical structure or a smooth surface in which their chemical compo-

---

[a] *School of Chemical Engineering, University of Adelaide, Adelaide, SA 5005, Australia. E-mail: s.qiao@adelaide.edu.au*
[b] *Department of Energy, Politecnico di Milano, via Ponzio 34/3, 20133 Milano, Italy. E-mail: carlo.casari@polimi.it*
[c] *School of Chemical Engineering, University of Queensland, Brisbane, QLD 4072, Australia*

† Electronic supplementary information (ESI) available. See DOI: 10.1039/c6nr06961d

sition is quite close to that of the target, even for multicomponent targets as shown in the case of nanostructured doped oxides for energy applications.[19–21] In addition, PLD can be used to fabricate transition-metal based nanoparticles supported on surfaces[22,23] including conductive supports to be directly utilized as an electrode for both HER and OER reactions.[24]

However, pairing the two electrode reactions for practical use is difficult due to the activity and stability issues at different pH ranges. Therefore, developing a bifunctional electrocatalyst with high activity towards both OER and HER in the same electrolyte becomes important yet challenging.

Herein, we report a porous carbon film coated with nickel–cobalt nanoparticles *via* a two-step PLD process at room temperature in which nitrogen dopants are incorporated into the carbon framework by ablation under reactive and highly pure nitrogen gas (designated as Ni_xCo_{1-x}/NC). The obtained hybrids directly served as a binder- and conductive-agent-free electrode and exhibited good electrocatalytic performances toward both HER and OER. The sample with an optimized Ni–Co molar ratio ($Ni_{0.5}Co_{0.5}$/NC) achieved the lowest overpotentials of 176 mV and 300 mV at a current density of 10 mA cm^{-2} toward the HER and OER, respectively. This electrode was also applied as a bifunctional electrocatalyst for a two-electrode water splitting cell which could achieve a current density of 10 mA cm^{-2} at a low voltage of 1.75 V, which is lower than that of individual metallic electrodes (Ni/NC and Co/NC). Our results show great promise in developing new families of non-precious metal-based bifunctional electrocatalysts using controlled conversion of homogeneous metal complexes into solid-state carbon catalysts.

Experimental

Material synthesis

Targets and substrate preparation. High purity (99.99%) graphite, an ultra-high purity nickel foil (2.5 mm thick) and a cobalt target were used for deposition of nickel–cobalt/N-carbon. Silicon wafer and copper foils (1 cm × 1 cm pieces) were used as substrates for film deposition. All the substrates were cleaned by sonication in isopropanol for 20 minutes, rinsing with isopropanol and drying using a nitrogen gas flow before deposition.

Synthesis of N-doped carbon films. The porous nitrogen-doped carbon films were deposited at room temperature by reactive PLD using a Nd:YAG pulsed laser (λ = 532 nm, duration of 9 ns and a repetition rate of 10 Hz) with a pulse energy of 200 mJ. The beam was directed onto a rotating graphite target with a 45° angle of incidence. Laser pulses ablated the target ejecting material in a plasma plume. Ablated species were deposited on the substrates to form the carbon thin film. The ablation process was performed in the presence of nitrogen as a background gas to tune the morphology, structure and composition of the deposited film. The distances between the target and the substrates and the laser spot size on the target were kept at 5 cm and 12.5 mm^2, respectively. The chamber was first evacuated to a base pressure (10^{-3} Pa) using a primary scroll pump and a turbomolecular pump. Then, the chamber was fed with nitrogen gas (99.99% purity) at 50 Pa to introduce nitrogen into the carbon framework. The deposition time (*i.e.* number of laser pulses) was set to 120 seconds to form a film with a thickness of 250 nm. Mass loading measurements were performed using a quartz crystal microbalance (QCM) and keeping other deposition conditions (*i.e.* chamber pressure, pulse energy, target to substrate (QCM in the case of mass loading measurements)) constant.

Synthesis of nickel–cobalt/N-carbon films. High purity cobalt targets decorated with different nickel strips (Fig. S1†) were used as bimetallic targets for deposition of Ni_xCo_{1-x} on the N-carbon films from the previous step (used as a substrate). All deposition conditions were kept similar to conditions mentioned previously. Ni_xCo_{1-x} were deposited at a background gas pressure of 50 Pa and deposition times were calculated based on a desired cobalt mass percentage (10 at %). All calculations have been done based on mass loading records from a quartz crystal microbalance (QCM) under constant PLD conditions (both carbon and cobalt deposition mass loadings).

Chemical characterization

The morphology of the synthesized samples was characterized by using a scanning electron microscope (SEM, ZEISS Supra40) operating at 10 kV. Elemental mapping was conducted using an energy dispersive spectroscopy (EDS) detector attached onto a ZEISS Supra40 and EDS spectra collected from the EDS detector attached to the JEM-2100. Raman spectra were collected on a LabRAM (Horiba Ltd) with a 532 nm laser line. X-ray diffraction (XRD) patterns (10–60° in 2θ) were collected on an X-ray diffractometer at 40 kV and 15 mA using Co-Kα radiation (Miniflex-600, Rigaku). X-ray photoelectron spectroscopy (XPS) analysis was conducted on an Axis Ultra spectrometer (Kratos Analytical Ltd.) with monochromated AlKα radiation (1486.6 eV) at *ca.* 5×10^{-9} Pa.

Electrochemical characterization

All electrochemical measurements were performed in a three-electrode glass cell on a 760 workstation (Pine Research Instruments, US). The as-synthesized hybrid films were directly used as working electrodes, platinum wire as the counter electrode and Ag/AgCl/KCl (4 M) as the reference electrode. A flow of N_2 was maintained over the electrolyte (1.0 M KOH) during the OER and HER electrochemical measurements to eliminate dissolved oxygen. All potentials were referenced to a reversible hydrogen electrode (RHE) using the equation below:

$$E_{\mathrm{RHE}} = E_{\mathrm{Ag/AgCl}} + (0.059 \times \mathrm{pH} + 0.205).$$

Linear sweep voltammograms (LSVs) were recorded at 5 mV s^{-1} to minimize the capacitive current. The working electrodes were scanned several times until stabilization before data collection commenced. The internal resistance of the electrochemical cell was 5 Ω and all cyclic voltammetry (CV) and linear sweep voltammetry (LSV) data were corrected for the iR contribution within the cell.

The Tafel slope was calculated according to the Tafel equation as follows:

$$\eta = b \log j + a,$$

where η is the overpotential (V); j is the current density (mA cm^{-2}); b is the Tafel slope (mV dec^{-1}).

Electrode durability was tested using a chronoamperometric response which was conducted at −1.5 V (*vs.* Ag/AgCl) for HER and +0.8 V (*vs.* Ag/AgCl) for OER electrodes.

The electrical double layer capacitances (C_{dl}, μF cm^{-2}) of the working electrodes were obtained from double-layer charging–discharging plots using CV in a small potential range of −0.8 to −0.75 V (*vs.* Ag/AgCl) and at scan rates ranging from 10 to 100 mV s^{-1}. The plots of current density (mA cm^{-2}) at −0.775 V (*vs.* Ag/AgCl) against the scan rate are nearly linear and the slopes are C_{dl} (μF cm^{-2}).

The water splitting system was fabricated using a two-electrode cell configuration by integrating the $Ni_{0.5}Co_{0.5}$/NC bifunctional catalyst as the anode and the cathode in 1.0 M KOH. Polarization curves were obtained using LSV with a scan rate of 5 mV s^{-1}. Long-term durability tests were performed at a constant potential of 1.6 V. Ni/NC||Ni/NC, Co/NC||Co/NC and Pt/C||IrO_2/C two electrode water splitting cells were also studied to draw comparisons. All data for the two electrode electrolyzer were recorded without iR compensation.

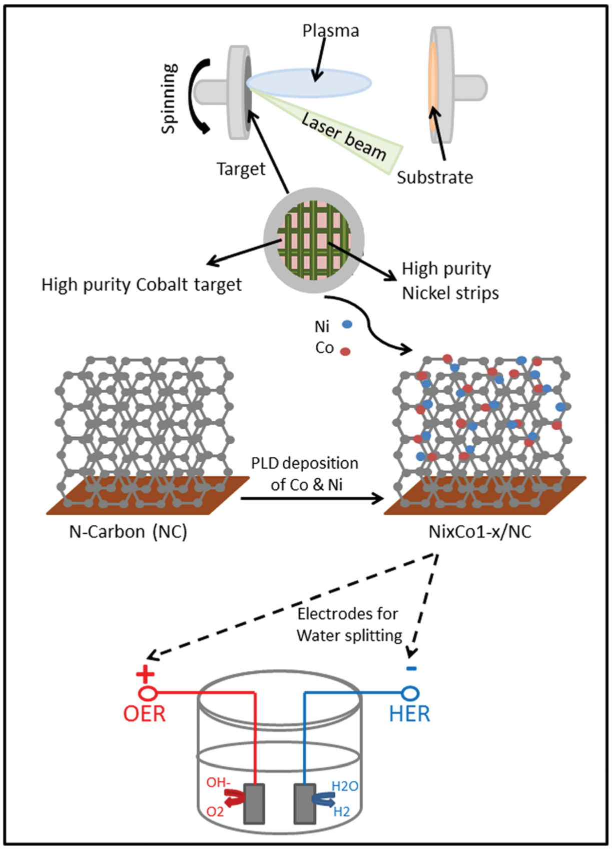

Fig. 1 Schematic illustration of the synthesis procedure of Ni_xCo_{1-x}/NC catalytic electrodes and their utilization in a water splitting system.

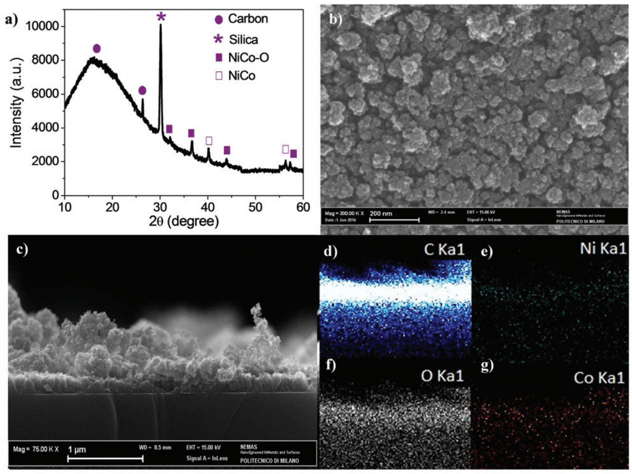

Fig. 2 (a) XRD spectrum, (b) the top view SEM image, and (c) the low-magnification cross-sectional SEM image (d–g). The corresponding SEM-EDS elemental mappings of C, O, Ni and Co of the Ni_xCo_{1-x}/NC film.

Results and discussion

The fabrication process of nitrogen doped carbon supported binary nickel–cobalt nanoparticles (Ni_xCo_{1-x}/NC; x denotes the molar ratio) is illustrated in Fig. 1. Porous structured nitrogen-doped carbon films were prepared on silicon wafers and copper foils as a substrate by a Pulsed laser deposition (PLD) technique under a reactive background gas at room temperature (Fig. S1a†). This procedure is modified from our previous report.[25] The resultant N-carbon film features unique advantages due to its porous structure and represents a favorable support with unique properties such as high electrical conductivity and enhanced electron transfer. Next, binary Ni_xCo_{1-x} nanoparticles were deposited on the N-carbon film using designed bimetallic targets (Fig. S1b†) and reactive PLD (λ = 532 nm with a pulse energy of 200 mJ) as described in the Experimental section. Laser pulses ablated the spinning target ejecting material in a plasma plume. Ablated cobalt and nickel species were deposited on the substrates (N-carbon) to form binary Ni_xCo_{1-x}/NC. The Ni/Co ratio was controlled by the number of nickel strips used at the designed target. The final products were directly utilized as electrodes for water splitting in a concentrated alkaline electrolyte (1.0 M). To obtain some insights into the electrocatalytic activity relationship of binary Ni_xCo_{1-x}/NC, individual Ni/NC and Co/NC were prepared using the same method for comparison.

X-ray diffraction (XRD) was initially used to investigate the crystalline nature of the Ni_xCo_{1-x}/NC as shown in Fig. 2a. The

XRD pattern demonstrates a broad peak centered around 19° and a diffraction peak at 26.3°, which suggests the availability of both amorphous and crystalline states of carbon, respectively. The broad peak corresponds to the disordered amorphous carbon[26] and the latter is attributed to the inter-plane (002) reflection of graphitic carbon which is related to the graphite-like stacking of the conjugated aromatic units[27,28] with an interlayer distance of 0.38 nm which is larger than that of graphite (0.34 nm) and similar to reported data.[29,30] Moreover, diffraction peaks located at about 32°, 37°, 40°, 45°, 57° and 59° could be indexed to a well-crystallized Ni–Co alloy which is bonded with either available O or N–C species.[31,32] There are no additional diffraction peaks in the pattern attributed to individual Co and Ni, indicating the high phase purity of binary Ni–Co formed (Fig. S2†).

The morphological and structural features of Ni_xCo_{1-x}/NC were examined by scanning electron microscopy (SEM) and transmission electron microscopy (TEM). As shown in Fig. 2b, the relatively uniform structure and high porosity of the nanoporous N-carbon (acting as a substrate) was maintained after the deposition of binary Ni–Co species by tuning the deposition parameters to prevent any morphological changes (Fig. S3†). The TEM image (Fig. S4a†) shows that the cauliflower-like nanoparticles are aggregated and assembled on the deposited films and there is no sign for the presence of large bulk metal species which confirms the homogeneous ablation of the bimetallic target. Fig. 2c shows the low magnification SEM cross-sectional image of the Ni_xCo_{1-x}/NC film followed by SEM energy dispersive X-ray spectroscopy (SEM-EDS) elemental mapping (Fig. 2d–g). The cross-sectional SEM image indicates the assembly of nanoparticles forming a thin film with a thickness of about 250 nm and a porous columnar nanostructure. The corresponding elemental mapping shows the presence of Ni, Co, C, and O in the thin film, verifying the uniform dispersion of these four elements. There is also no sign of ablated single species (Ni or Co) which can be clearly seen from the boundaries of the thin film from the corresponding elemental mapping images. It should be noted that nitrogen species are not detected due to the relatively small amount and the low spatial resolution of EDS elemental mapping. Thus, a high-resolution transmission electron microscopy-EDS (TEM-EDS) spectrum was collected to confirm the presence of nitrogen species in the developed materials (Fig. S4b†).

Further, the surface chemistry of binary Ni_xCo_{1-x}/NC and individual Ni/NC and Co/NC electrodes was investigated by X-ray photoelectron spectroscopy (XPS). The XPS survey spectra (Fig. 3a) demonstrate the presence of C, N and O at all the prepared electrodes. Moreover, they confirm the presence of both Ni and Co species at Ni_xCo_{1-x}/NC while there is only Ni present in Ni/NC and Co present in Co/NC films. The molar ratio of Co and Ni in Ni_xCo_{1-x}/NC has been investigated by XPS and is summarized in Table S1.† The high-resolution Ni 2p spectra of Ni_xCo_{1-x}/NC and Ni/NC are presented in Fig. 3b. For Ni/NC, two characteristic peaks at 856.3 eV and 873.1 eV, as well as the two satellite peaks at 861.8 and 880.7 eV, correspond well to Ni–O species.[33] Another peak at 852.7 eV might be attributed to the Ni bonded with available C–N species.[34] The Ni 2p XPS spectrum of Ni_xCo_{1-x}/NC represents all the five mentioned peaks with small shifts of about ±1 eV which could be assigned to the formation of Co–Ni alloys. Similarly, for Co elements in Co/NC, the $Co2p_{3/2}$ and $Co2p_{1/2}$ peaks at 781.3 and 795.5 eV as well as the two satellite peaks can be correlated to the presence of oxidized Co species (Fig. 3c).[35] There is also a peak assigned to metallic cobalt available at 778.2 eV which could be bonded with C–N species.[36] From the Co 2p XPS spectrum of Ni_xCo_{1-x}/NC, the formation of the Co–Ni alloy is further confirmed due to a small shift of 1 eV for all five available peaks.[37] The nitrogen bonding configuration of the Ni_xCo_{1-x}/NC film is further studied (Fig. S5†), in which four main components of the N 1s spectrum located at about 398.2, 399.4, 400.5 and 401.8 eV correspond to pyridinic, pyrrolic, graphitic and oxidized nitrogen, respectively.[38,39] The existence of pyridinic and pyrrolic nitrogen is beneficial to the improvement of conductivity due to the contribution of their p-conjugated system with a pair of p-electrons in the carbon framework. Moreover, pyridinic nitrogen is a good candidate for bonding with available ionic bimetallic species due to its electron donating properties to create a highly active center ($M–N_x$ centers) in the catalyst's structure which could be confirmed by a small shift of binding energy at a higher level.[40,41] The existence of the graphitic nitrogen species reveals substitution of some carbons with nitrogen atoms in films which is believed to provide the active sites.[42]

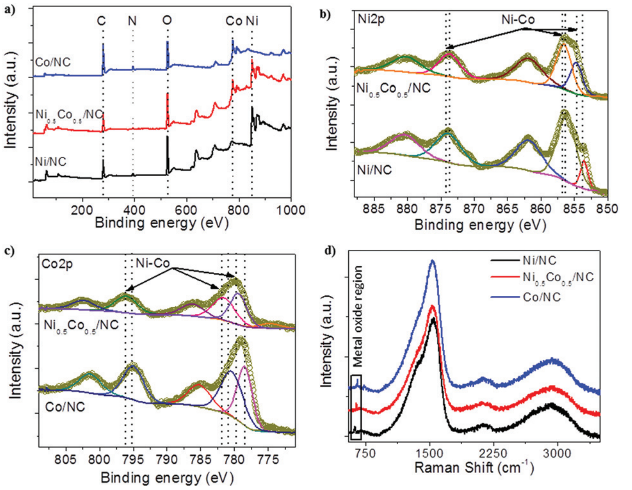

Fig. 3 (a) XPS survey of Ni/NC, $Ni_{0.5}Co_{0.5}$/NC and Co/NC films, (b) high-resolution Ni 2p spectra of Ni/NC and $Ni_{0.5}Co_{0.5}$/NC, (c) high-resolution Co 2p spectra of Co/NC and $Ni_{0.5}Co_{0.5}$/NC and (d) the Raman spectra of Ni/NC, $Ni_{0.5}Co_{0.5}$/NC and Co/NC films.

Raman spectroscopy is able to provide structural information on carbon-based composite materials. Fig. 3d shows the Raman spectra of the binary Ni_xCo_{1-x}/NC, exhibiting the typical fingerprint of amorphous carbon. In fact, the G and D modes, which are attributed to C–C stretching in the hexagonal plane of the sp^2 carbon and to the reduced size crystal domains and structural disorder, respectively, create a broad peak where the G band is the main contribution merged with the D mode constituting a shoulder with an I_D/I_G intensity ratio of about 0.61 (Fig. S6 and Table S2†).[43,44] The weak band at about 2200 cm^{-1} is characteristic of the presence of a small fraction of sp-hybridized carbon[45–47] which might enhance the catalytic activity and selectivity of deposited materials due to high electron density coupled by restricted rotation of the C–C bond.[48] The large band in the 2400–3200 cm^{-1} spectral region is the typical 2nd order Raman signal of amorphous carbon films. In addition, there is a weak peak at about 550–650 cm^{-1} assigned to the available metal oxides.[49,50] In comparison to the individual Ni/NC and Co/NC, small shifts are observed in the vibrational bands and metal oxide active peaks of Ni_xCo_{1-x}/NC (Fig. S7 and Table S2†). The small shifts of the vibrational bands and metal oxide active peaks in binary Ni_xCo_{1-x}/NC indicate strong interaction/mixing between Co and Ni species as well as between the formed binary component and porous carbon nanosheets, which would be favorable for charge transport during electrochemical reactions.

The effective operation of electrocatalysts in concentrated electrolytes is a critical figure of merit for practical applications.[51] Thus, with an average mass loading of 0.1 mg cm^{-2} across all electrodes for both HER and OER, the electrocatalytic activity of Ni_xCo_{1-x}/NC (where x = 0.2, 0.3, 0.4, 0.5 and 0.7; measured by XPS), control samples (including Ni/NC and Co/NC), unsupported binary $Ni_{0.5}Co_{0.5}$, and benchmark samples (Pt/C or IrO_2/C) was evaluated in 1.0 M KOH solution using a typical three-electrode system. Since the as-measured reaction currents cannot directly reflect the intrinsic behavior of catalysts due to the effect of ohmic resistance, an iR correction was applied to all of the initial data for further analysis. Fig. 4a shows HER linear sweep voltammetry (LSV) curves with a scan rate of 5 mV s^{-1}. For Ni_xCo_{1-x}/NC, an optimal HER catalytic activity is obtained when x = 0.5 with the lowest onset potential (η_0 defined as the potential to reach 1 mA cm^{-2}) of 0.048 V and achieves the largest current density of 100 mA cm^{-2} at an overpotential of 0.363 V. Increasing or decreasing the Ni doping ratio (from x = 0.5) led to lower activities of the Ni_xCo_{1-x}/NC hybrid catalysts. Thus, the operating potentials to drive a cathodic current density of 10 mA cm^{-2} (η_{10}) for $Ni_{0.5}Co_{0.5}$/NC and control samples were compared, which is related to the catalytic activity (Fig. 4b). As expected, Pt/C exhibits excellent activity with negligible overpotential (0.069 V) to deliver a current density of 10 mA cm^{-2}. Moreover, $Ni_{0.5}Co_{0.5}$/NC also shows a lower η_{10} of 0.176 V than other samples such as unsupported $Ni_{0.5}$ $Co_{0.5}$ (0.282 V), Ni/NC (0.406 V) and Co/NC (0.378 V). The overpotential of $Ni_{0.5}Co_{0.5}$/NC suggests its superior catalytic activity towards HER compared to other synthesized samples in this work and most earth-abundant, non-noble-metal HER catalysts in alkaline media (Table S3†).

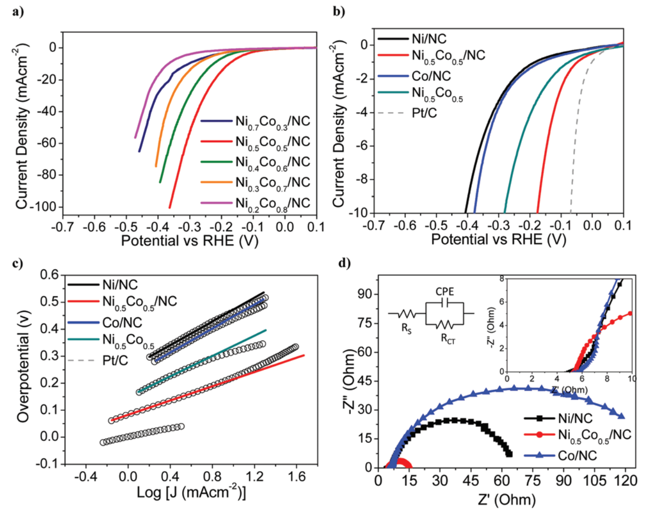

Fig. 4 (a) HER polarization curves of binary Ni_xCo_{1-x}/NC, (b) HER polarization curves and (c) the corresponding HER Tafel plots of Ni/NC, $Ni_{0.5}Co_{0.5}$/NC, Co/NC, unsupported $Ni_{0.5}$ $Co_{0.5}$ and commercial Pt/C in 1.0 M KOH, (d) Nyquist plots of Ni/NC, Co/NC and $Ni_{0.5}Co_{0.5}$/NC at a potential of −1.5 V (*vs.* Ag/AgCl) at 1.0 M KOH.

The HER kinetics of the prepared electrodes were studied by analyzing the Tafel plots which were recorded with the linear portions at low overpotential fitted to the Tafel equation (Fig. 4c and S8†). A Tafel slope of 132.1 mV dec^{-1} for $Ni_{0.5}Co_{0.5}$/NC is larger than Pt/C (80.2 mV dec^{-1}), but is smaller than those of Ni/NC (218.8 mV dec^{-1}), Co/NC (221.9 mV dec^{-1}) and unsupported $Ni_{0.5}Co_{0.5}$ (189.3 mV dec^{-1}), further confirming the favorable catalytic kinetic of $Ni_{0.5}Co_{0.5}$/NC for HER. On the basis of the Tafel analysis, the exchange current density of the $Ni_{0.5}Co_{0.5}$/NC catalyst was estimated to be 23.7 × 10^{-5} A cm^{-2}. This value is much higher than that reported for other non-precious metal-based catalysts.[52,53]

Electrochemical impedance spectroscopy (EIS) tests were conducted to investigate the electrode kinetics under HER at an applied potential of −1.5 V (*vs.* Ag/AgCl) in 1.0 M alkaline solution. The semicircles in the Nyquist plot are attributed to the charge-transfer resistance (R_{CT}) and solution resistance (R_S), which are related to the electrocatalytic kinetics and a lower value corresponds to a faster reaction rate. Therefore, the EIS analysis confirmed a faster HER kinetic process on $Ni_{0.5}Co_{0.5}$/NC (R_{CT} = 10 Ω) than its individual components (Ni/NC and Co/NC) and other Ni_xCo_{1-x}/NC films which is consistent with its lower overpotential (Fig. 4d and S9†).[54]

Since electrode durability in concentrated alkaline solution is very critical to evaluate catalytic performance, a long-term (60 000 seconds) chronoamperometric test was also performed at a constant potential of −1.5 V (*vs.* Ag/AgCl) for the $Ni_{0.5}$ $Co_{0.5}$/NC electrode in a 1.0 M KOH electrolyte. As shown in Fig. S10a,† 89% of the electrode activity is retained after long-term stability testing which can be attributed to the metal species embedded in the N-carbon framework. This superior durability of the newly developed material was also confirmed by the LSVs before and after the stability test. The result shows only a slight negative shift of the HER polarization curve (about 19 mV shift of the overpotential at 10 mA cm^{-2}) (Fig. S10b†), suggesting a good prognosis for these hybrid materials as efficient HER electrocatalysts.

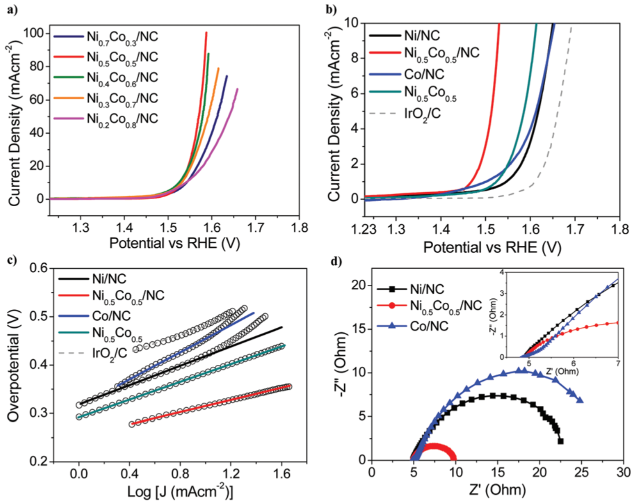

Fig. 5 (a) OER polarization curves of binary Ni_xCo_{1-x}/NC, (b) OER polarization curves and (c) the corresponding OER Tafel plots of Ni/NC, $Ni_{0.5}Co_{0.5}$/NC, Co/NC, unsupported $Ni_{0.5}Co_{0.5}$ and commercial IrO_2/C in 1.0 M KOH, (d) Nyquist plots of Ni/NC, Co/NC and $Ni_{0.5}Co_{0.5}$/NC at a potential of +0.8 V (*vs.* Ag/AgCl) at 1.0 M KOH.

The catalytic ability of Ni_xCo_{1-x}/NC to OER was also assessed in 1.0 M KOH solution. In typical LSV plots, the anodic current of all samples simultaneously increases as the potential becomes more positive, which is commonly observed for OER catalysts in alkaline media.[55] As shown in Fig. 5a and b, $Ni_{0.5}Co_{0.5}$/NC exhibited the lowest onset potential (η_0) of 1.467 V (*vs.* RHE) and manifested a current density of 100 mA cm^{-2} at an overpotential as low as 0.358 V, indicative of the lowest energy input for driving OER among other binary counterparts, individual components (Ni/NC and Co/NC) and benchmark IrO_2/C. $Ni_{0.5}Co_{0.5}$/NC also shows a lower overpotential (0.300 V) to deliver a current density of 10 mA cm^{-2} when compared with other samples such as IrO_2/C (0.463 V), Ni/NC (0.420 V), Co/NC (0.430 V) and unsupported $Ni_{0.5}Co_{0.5}$ (0.380 V). Remarkably, the OER current of $Ni_{0.5}Co_{0.5}$/NC exceeds that of IrO_2/C throughout the whole potential range, indicating that it has much better catalytic activity compared to this benchmark.

Tafel slopes and exchange current densities of all prepared electrodes were obtained from Tafel plots and the results are summarized in Fig. 5c, S11 and Table S4.† As can be seen, the Tafel slopes for all the binary electrodes (Ni_xCo_{1-x}/NC) were around 62–80 mV dec^{-1}, which is in good agreement with the literature.[56,57] $Ni_{0.5}Co_{0.5}$/NC confirms a higher OER activity compared to IrO_2/C (91.4 mV dec^{-1}), individual components (100.0 mV dec^{-1} and 136.2 mV dec^{-1} for Ni/NC and Co/NC, respectively) and unsupported $Ni_{0.5}Co_{0.5}$ (91.6 mV dec^{-1}). The exchange current densities were calculated to be 9.8×10^{-5}, 2.6×10^{-5}, 8.7×10^{-6} and 6.5×10^{-5} A cm^{-2} for $Ni_{0.5}Co_{0.5}$/NC, Ni/NC, Co/NC and unsupported $Ni_{0.5}Co_{0.5}$, respectively, implying the superior OER catalytic performance of $Ni_{0.5}Co_{0.5}$/NC.

As shown in Fig. 5d, the Nyquist plot of $Ni_{0.5}Co_{0.5}$/NC demonstrates a semicircle which is an indication of the charge transfer residence of the electrode. The calculated resistance of $Ni_{0.5}Co_{0.5}$/NC (4.9 Ω) is significantly less than that of individual Ni/NC (>15 Ω) and Co/NC (>20 Ω) electrodes which might be attributed to the higher OER activity. Additionally, the long-term stability test shows a seldom attenuation in the current density at 0.8 V *versus* Ag/AgCl (Fig. S12a†). The LSV data collected before and after durability tests show a slight negative shift of the OER polarization curve (about 14 mV shift of the overpotential at 10 mA cm^{-2}), which might be due to the activation and phase conversion of the catalyst during long time electrochemical tests (Fig. S12b†).

As for the role of the Ni ion in the electrocatalytic activity of the prepared electrodes, the difference of HER and OER metrics (relative potential at $E = -5$ mA cm^{-2} from the HER polarization curve and relative potential at $E = 10$ mA cm^{-2} from the OER polarization curve; $\Delta E_{\text{Overall}} = E_{j=-5} - E_{j=10}$) obtained using single Ni/NC, Co/NC and binary Ni_xCo_{1-x}/NC catalysts as a water-splitting electrode was compared (Fig. S13†). The smaller the ΔE is, the closer the catalyst is to an ideal bifunctional water-splitting electrode. Remarkably, binary $Ni_{0.5}Co_{0.5}$/NC can yield a smaller ΔE (1.705 V) than single Ni/NC and Co/NC (2.057 and 2.032 V, respectively) which clearly indicates some enhancement effect when part of the Co is replaced by Ni. Moreover, our previous studies indicated that the high HER and OER catalytic activity of non-precious metal doped N-carbon might originate from the formation of interfacial covalent M–N–C and M–O–C bonds which can provide additional active centers in the synthesized hybrids.[58,59] Bond formation between inorganic nanocatalysts and the underlying carbon support could change the chemical bonding environment for carbon, oxygen, and metal atoms in the hybrid material, resulting in an enhanced catalytic activity. Overall, the larger ΔE of 1.974 V for unsupported $Ni_{0.5}Co_{0.5}$ further confirms the highly improved conductivity and charge transfer capability of N-carbon supported binary composites which are favorable for high HER and OER activity and stability.

Furthermore, the porous structure of the prepared electrodes can enhance the catalyst contact area and the mass transport of the electrolytes. As a consequence, favorable mass and charge transport can allow high utilization efficiency of active species for catalysis. It is reported that the electrochemically active surface area (EASA) is directly proportional to a number of active sites which can be evaluated by the electrochemical double-layer capacitance (C_{dl}).[60] Fig. S14(a–d) and S15(a–d)† show the representative cyclic voltammograms of binary Ni_xCo_{1-x}/NC and individual Ni/NC and Co/NC electrodes at different scan rates in a potential region of −0.8 to −0.75 V (ΔE = 50 mV). The CV exhibits a typical rectangular feature of an electrical double layer capacitor. In this potential region, charge transfer electrode reactions were considered to be negligible and the current is solely from electrical double layer charging and discharging. The plot of current against the potential scan rate has a linear relationship (Fig. S14e and S15e†) and its slope is the double layer capacitance. The correlation of C_{dl} with the HER and OER overpotential to reach a current density

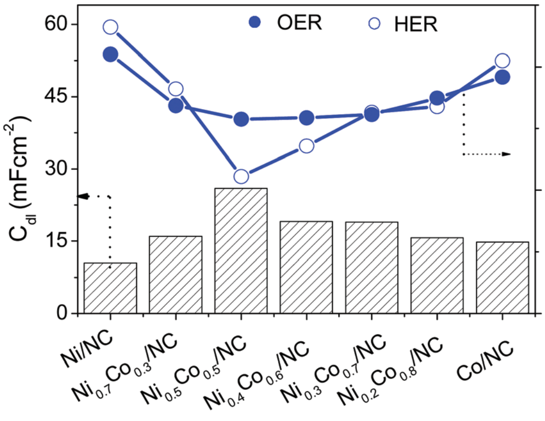

Fig. 6 Roughness factor and the HER/OER overpotential to reach a current density of 10 mA cm^{-2} plots of binary Ni$_x$Co$_{1-x}$/NC and individual Ni/NC and Co/NC.

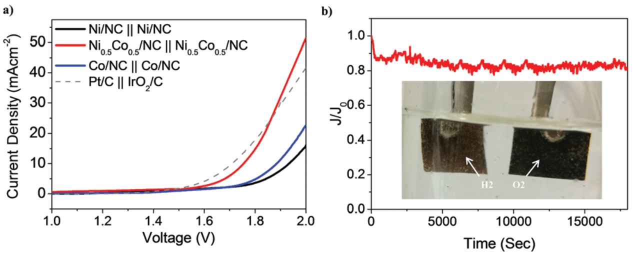

Fig. 7 (a) LSV plots of water splitting at Ni/NC||Ni/NC, Ni$_{0.5}$Co$_{0.5}$/NC||Ni$_{0.5}$Co$_{0.5}$/NC, Co/NC||Co/NC and Pt/C||IrO$_2$/C as cathode and anode electrodes and (b) the chronoamperometric response of the Ni$_{0.5}$Co$_{0.5}$/NC||Ni$_{0.5}$Co$_{0.5}$/NC cell working for splitting water at a voltage of 1.5 V for 18 000 seconds.

of 10 mA cm^{-2} for various electrodes is presented in Fig. 6. It is clearly seen that the Ni$_{0.5}$Co$_{0.5}$/NC has the highest C_{dl} and lowest HER/OER overpotential, demonstrating its improved catalytic activity and facilitated reaction kinetics compared to the other prepared electrodes. Further, the direct growth of active materials on conductive copper foils can greatly enhance the electron transport and adhesion between electrocatalytically active species on substrates, promote the structural stability for long-term usage and avoid utilization of polymeric binders and extra conductive additives, consequently reducing the dead volume and undesirable interface in the electrodes.[61–63] The enhancement in electrocatalytic activity of Ni$_{0.5}$Co$_{0.5}$/NC has long been noticed. Ni substitution is believed to improve Co/NC activity by either enlarging its active surface area (geometric effect) and/or by increasing its conductivity (electronic effect).[52]

Next, a proof-of-concept experiment was conducted to demonstrate the possibility of utilizing bifunctional Ni$_{0.5}$Co$_{0.5}$/NC for full water splitting using a two-electrode setup (Ni$_{0.5}$Co$_{0.5}$/NC||Ni$_{0.5}$Co$_{0.5}$/NC) in 1.0 M KOH. Other electrolyzers were prepared as controls using Pt/C as the cathode and IrO$_2$/C as the anode (Pt/C||IrO$_2$) and cells using single Ni/NC and Co/NC, both as bifunctional electrodes (Ni/NC||Ni/NC and Co/NC||Co/NC) for comparison. As shown in Fig. 7a, Ni$_{0.5}$Co$_{0.5}$/NC needs 1.75 V to afford a 10 mA cm^{-2} water-splitting current. Although this voltage is larger than that for Pt/C||IrO$_2$/C (1.71 V), it is smaller than those of individual Ni/NC||Ni/NC and Co/NC||Co/NC (1.93 and 1.88 V, respectively). The bifunctional activity of Ni$_{0.5}$Co$_{0.5}$/NC is also much lower than that of NiCo$_2$O$_4$NA/CC (1.98 V) and other reported commercial electrolyzers (1.8 V to 2.0 V).[64,65] Additionally, the practical operation of the catalyst is examined by electrolysis at a fixed potential of 1.6 V over an extended period. As observed in Fig. 7b, the cell exhibits considerable stability over nearly five hours. This exceptional durability shows promise for practical applications of this catalyst over long term operation.

Conclusions

In summary, nickel–cobalt nanoparticles supported on porous nitrogen doped carbon thin films (Ni$_x$Co$_{1-x}$/NC) were fabricated *via* a two-step pulsed laser deposition technique under reaction with a background gas (N$_2$ gas) at room temperature. The binary Ni$_{0.5}$Co$_{0.5}$/NC composite not only demonstrated efficient electrocatalytic activity and durability for HER but also offered impressive catalytic performance for OER in alkaline medium. The outstanding catalytic performance of the developed composites was strongly correlated to the homogeneous distribution of nickel–cobalt active sites and synergetic coupling interaction with the porous N-carbon framework. This earth-abundant composite could undoubtedly hold great promise for other practical applications in energy storage and conversion systems.

Acknowledgements

This work is financially supported by the Australian Research Council (ARC) through the Discovery Project programs (DP130104459, DP140104062, DP160104866). The authors acknowledge A. Facibeni for performing SEM images of the samples.

Notes and references

1 A. S. Arico, P. Bruce, B. Scrosati, J.-M. Tarascon and W. van Schalkwijk, *Nat. Mater.*, 2005, **4**, 366.
2 Y. Li, M. Gong, Y. Liang, J. Feng, J.-E. Kim, H. Wang, G. Hong, B. Zhang and H. Dai, *Nat. Commun.*, 2013, **4**, 1805.
3 Z. Peng, D. Jia, A. M. Al-Enizi, A. A. Elzatahry and G. Zheng, *Adv. Energy Mater.*, 2015, **5**, 1402031.
4 Y. Wang, T. Zhou, K. Jiang, P. Da, Z. Peng, J. Tang, B. Kong, W.-B. Cai, Z. Yang and G. Zheng, *Adv. Energy Mater.*, 2014, **4**, 1400696.

5 J. Luo, J.-H. Im, M. T. Mayer, M. Schreier, M. K. Nazeeruddin, N.-G. Park, S. D. Tilley, H. J. Fan and M. Grätzel, *Science*, 2014, **345**, 1593.

6 Y. Zheng, Y. Jiao, L. H. Li, T. Xing, Y. Chen, M. Jaroniec and S. Z. Qiao, *ACS Nano*, 2014, **8**, 5290.

7 T. Y. Ma, J. Ran, S. Dai, M. Jaroniec and S. Z. Qiao, *Angew. Chem., Int. Ed.*, 2015, **54**, 4646.

8 H. Xu, R. Q. Zhang, A. M. C. Ng, A. B. Djurišić, H. T. Chan, W. K. Chan and S. Y. Tong, *J. Phys. Chem. C*, 2011, **115**, 19710.

9 J. Shi, J. Hu, Y. Luo, X. Sun and A. M. Asiri, *Catal. Sci. Technol.*, 2015, **5**, 4954.

10 J. Lai, S. Li, F. Wu, M. Saqib, R. Luque and G. Xu, *Energy Environ. Sci.*, 2016, **9**, 1210.

11 W. Zhou, J. Zhou, Y. Zhou, J. Lu, K. Zhou, L. Yang, Z. Tang, L. Li and S. Chen, *Chem. Mater.*, 2015, **27**, 2026.

12 L. Trotochaud, J. K. Ranney, K. N. Williams and S. W. Boettcher, *J. Am. Chem. Soc.*, 2012, **134**, 17253.

13 M. W. Louie and A. T. Bell, *J. Am. Chem. Soc.*, 2013, **135**, 12329.

14 P. D. Tran, S. Y. Chiam, P. P. Boix, Y. Ren, S. S. Pramana, J. Fize, V. Artero and J. Barber, *Energy Environ. Sci.*, 2013, **6**, 2452.

15 Y.-P. Zhu, Y.-P. Liu, T.-Z. Ren and Z.-Y. Yuan, *Adv. Funct. Mater.*, 2015, **25**, 7337.

16 J. Qi, W. Zhang, R. Xiang, K. Liu, H.-Y. Wang, M. Chen, Y. Han and R. Cao, *Adv. Sci.*, 2015, **2**, 1500199.

17 M. Carmo, D. L. Fritz, J. Mergel and D. Stolten, *Int. J. Hydrogen Energy*, 2013, **38**, 4901.

18 J. Ji, L. L. Zhang, H. Ji, Y. Li, X. Zhao, X. Bai, X. Fan, F. Zhang and R. S. Ruoff, *ACS Nano*, 2013, **7**, 6237.

19 P. Mazzolini, P. Gondoni, V. Russo, D. Chrastina, C. S. Casari and A. Li Bassi, *J. Phys. Chem. C*, 2015, **119**, 6988.

20 R. Matarrese, I. Nova, A. Li Bassi, C. S. Casari and V. Russo, *Chem. Eng. Trans.*, 2014, **41**, 313.

21 P. Gondoni, P. Mazzolini, V. Russo, A. Petrozza, A. K. Srivastava, A. Li Bassi and C. S. Casari, *Sol. Energy Mater. Sol. Cells*, 2014, **128**, 248.

22 C. S. Casari, S. Foglio, M. Passoni, F. Siviero, C. E. Bottani and A. Li Bassi, *Phys. Rev. B: Condens. Matter*, 2011, **84**, 155441.

23 D. Cattaneo, S. Foglio, C. S. Casari, A. Li Bassi, M. Passoni and C. E. Bottani, *Surf. Sci.*, 2007, **601**, 1892.

24 H. Kim, in *Pulsed Laser Deposition of Thin Films*, John Wiley & Sons, Inc., 2006, ch. 11, pp. 239–260, DOI: 10.1002/9780470052129.

25 B. Bayatsarmadi, Y. Zheng, C. S. Casari, V. Russo and S. Z. Qiao, *Chem. Commun.*, 2016, **52**, 11947–11950.

26 P. L. Walker, J. F. Rakszawski and A. F. Amington, *ASTM Bull.*, 1955, **208**, 52.

27 W. Yang, T.-P. Fellinger and M. Antonietti, *J. Am. Chem. Soc.*, 2011, **133**, 206.

28 T.-P. Fellinger, F. Hasché, P. Strasser and M. Antonietti, *J. Am. Chem. Soc.*, 2012, **134**, 4072.

29 R. Liu, D. Wu, X. Feng and K. Müllen, *Angew. Chem., Int. Ed.*, 2010, **122**, 2619.

30 B. S. Girgis, Y. M. Temerk, M. M. Gadelrab and I. D. Abdullah, *Carbon Sci.*, 2007, **8**, 95.

31 G. Zhang and X. W. Lou, *Adv. Mater.*, 2013, **25**, 976.

32 Y. He, L. Xu, Y. Zhai, A. Li and X. Chen, *Chem. Commun.*, 2015, **51**, 14768.

33 M. Caffio, B. Cortigiani, G. Rovida, A. Atrei and C. Giovanardi, *J. Phys. Chem. B*, 2004, **108**, 9919.

34 J. Deng, P. Ren, D. Deng and X. Bao, *Angew. Chem., Int. Ed.*, 2015, **54**, 2100.

35 J. Yang, H. Liu, W. N. Martens and R. L. Frost, *J. Phys. Chem. C*, 2010, **114**, 111.

36 H. Fei, J. Dong, M. J. Arellano-Jimenez, G. Ye, N. Dong Kim, E. L. G. Samuel, Z. Peng, Z. Zhu, F. Qin, J. Bao, M. J. Yacaman, P. M. Ajayan, D. Chen and J. M. Tour, *Nat. Commun.*, 2015, **6**, 9668.

37 A. Lu, Y. Chen, H. Li, A. Dowd, M. B. Cortie, Q. Xie, H. Guo, Q. Qi and D.-L. Peng, *Int. J. Hydrogen Energy*, 2014, **39**, 18919.

38 O.-H. Kim, Y.-H. Cho, D. Y. Chung, M. J. Kim, J. M. Yoo, J. E. Park, H. Choe and Y.-E. Sung, *Sci. Rep.*, 2015, **5**, 8376.

39 Z.-H. Sheng, L. Shao, J.-J. Chen, W.-J. Bao, F.-B. Wang and X.-H. Xia, *ACS Nano*, 2011, **5**, 4350.

40 Y. Liang, Y. Li, H. Wang and H. Dai, *J. Am. Chem. Soc.*, 2013, **135**, 2013.

41 T. Palaniselvam, B. P. Biswal, R. Banerjee and S. Kurungot, *Chem. – Eur. J.*, 2013, **19**, 9335.

42 G. Wu, C. M. Johnston, N. H. Mack, K. Artyushkova, M. Ferrandon, M. Nelson, J. S. Lezama-Pacheco, S. D. Conradson, K. L. More, D. J. Myers and P. Zelenay, *J. Mater. Chem.*, 2011, **21**, 11392.

43 A. C. Ferrari and J. Robertson, *Phys. Rev. B: Condens. Matter*, 2000, **61**, 14095.

44 A. C. Ferrari and J. Robertson, *Phys. Rev. B: Condens. Matter*, 2001, **64**, 075414.

45 C. S. Casari, C. S. Giannuzzi and V. Russo, *Carbon*, 2016, **104**, 190.

46 C. S. Casari, M. Tommasini, R. R. Tykwinski and A. Milani, *Nanoscale*, 2016, **8**, 4414.

47 L. Ravagnan, F. Siviero, C. Lenardi, P. Piseri, E. Barborini, P. Milani, C. S. Casari, A. Li Bassi and C. E. Bottani, *Phys. Rev. Lett.*, 2002, **89**, 285506.

48 S. Bailey and F. King, in *Fine Chemicals through Heterogeneous Catalysis*, ed. H. v. B. R. A. Sheldon, John Wiley & Sons, 2008, ch. 8, p. 636.

49 Y. Li, W. Qiu, F. Qin, H. Fang, V. G. Hadjiev, D. Litvinov and J. Bao, *J. Phys. Chem. C*, 2016, **120**, 4511.

50 A. Jena, N. Munichandraiah and S. A. Shivashankar, *J. Power Sources*, 2013, **237**, 156.

51 C. C. L. McCrory, S. Jung, J. C. Peters and T. F. Jaramillo, *J. Am. Chem. Soc.*, 2013, **135**, 16977.

52 Y. Li, P. Hasin and Y. Wu, *Adv. Mater.*, 2010, **22**, 1926.

53 T.-W. Lin, C.-J. Liu and C.-S. Dai, *Appl. Catal., B*, 2014, **154–155**, 213.

54 J. Xie, H. Zhang, S. Li, R. Wang, X. Sun, M. Zhou, J. Zhou, X. W. Lou and Y. Xie, *Adv. Mater.*, 2013, **25**, 5807.

55 T. Takashima, K. Hashimoto and R. Nakamura, *J. Am. Chem. Soc.*, 2012, **134**, 18153.

56 B. Chi, J. Li, Y. Han and Y. Chen, *Int. J. Hydrogen Energy*, 2004, **29**, 605.

57 E. B. Castro, S. G. Real and L. F. Pinheiro Dick, *Int. J. Hydrogen Energy*, 2004, **29**, 255.

58 B. Bayatsarmadi, Y. Zheng, Y. Tang, M. Jaroniec and S.-Z. Qiao, *Small*, 2016, **12**, 3703.

59 T. Y. Ma, S. Dai, M. Jaroniec and S. Z. Qiao, *J. Am. Chem. Soc.*, 2014, **136**, 13925.

60 C.-Z. Yuan, Y.-F. Jiang, Z. Wang, X. Xie, Z.-K. Yang, A. B. Yousaf and A.-W. Xu, *J. Mater. Chem. A*, 2016, **4**, 8155.

61 X. Liu, Z. Chang, L. Luo, T. Xu, X. Lei, J. Liu and X. Sun, *Chem. Mater.*, 2014, **26**, 1889.

62 D. U. Lee, J.-Y. Choi, K. Feng, H. W. Park and Z. Chen, *Adv. Energy Mater.*, 2014, **4**, 1301389.

63 X. Liu, Z. Chang, L. Luo, T. Xu, X. Lei, J. Liu and X. Sun, *ChemInform*, 2014, **26**, 1889.

64 D. Liu, Q. Lu, Y. Luo, X. Sun and A. M. Asiri, *Nanoscale*, 2015, **7**, 15122.

65 K. Zeng and D. Zhang, *Prog. Energy Combust. Sci.*, 2010, **36**, 307.

6.3. Supporting Information

This section is included in the thesis as supplementary information to section 6.2. It includes additional information which is not put in the main text of the published paper; however, it is freely accessible online as electronic supplementary information.

Electronic Supporting information

Highly Active Nickel-Cobalt/Nanocarbon Thin Films as Efficient Water Splitting Electrodes

B. Bayatsarmadi[a], Y. Zheng[a], V. Russo[b], Lei Ge[c], C.S. Casari[b,*] and S.Z. Qiao[a,*]

[a] School of Chemical Engineering, University of Adelaide, Adelaide SA 5005 Australia.
Email: s.qiao@adelaide.edu.au

[b] Department of Energy, Politecnico di Milano, via Ponzio 34/3, 20133 Milano, Italy.
carlo.casari@polimi.it

[c] School of Chemical Engineering, University of Queensland, Brisbane, QLD 4072, Australia

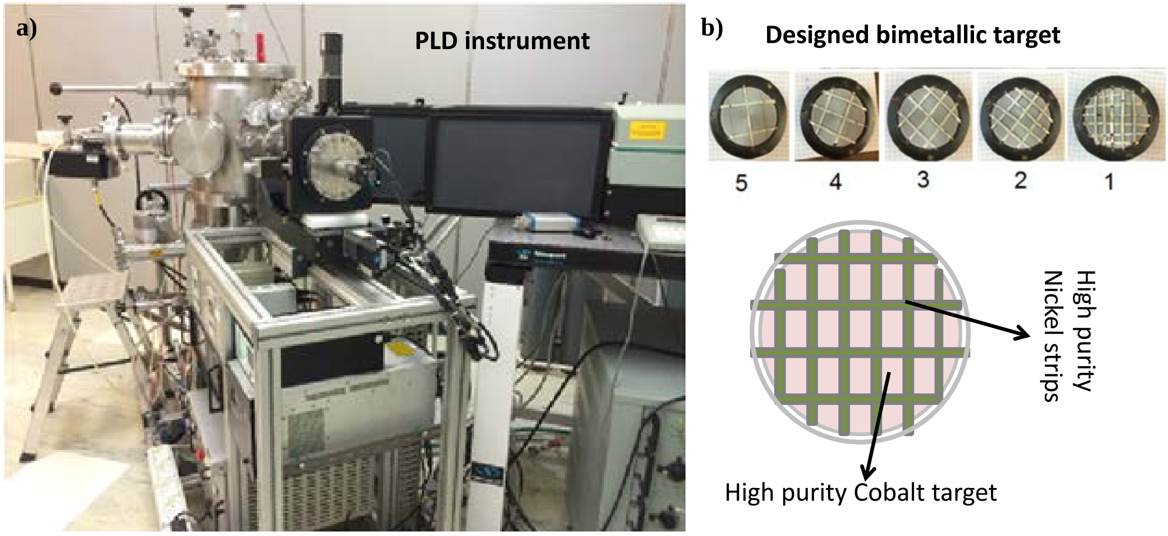

Fig. S1 (a) Optical image of the Pulsed laser deposition instrument and (b) Five designed bimetallic targets to induce deposition of deferent compositions of Ni_xCo_{1-x} species.

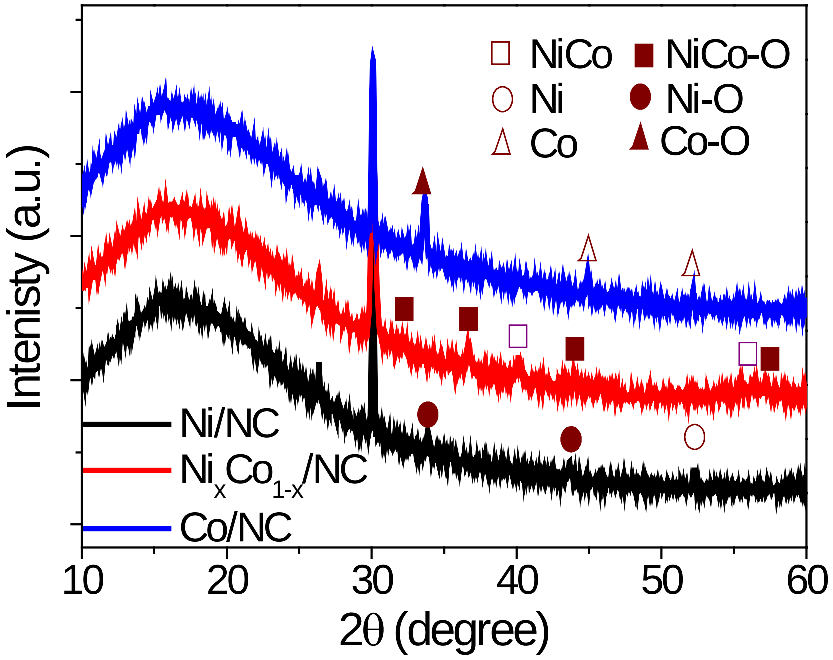

Fig. S2 XRD spectra of Ni/NC, Ni_xCo_{1-x}/NC and Co/NC.

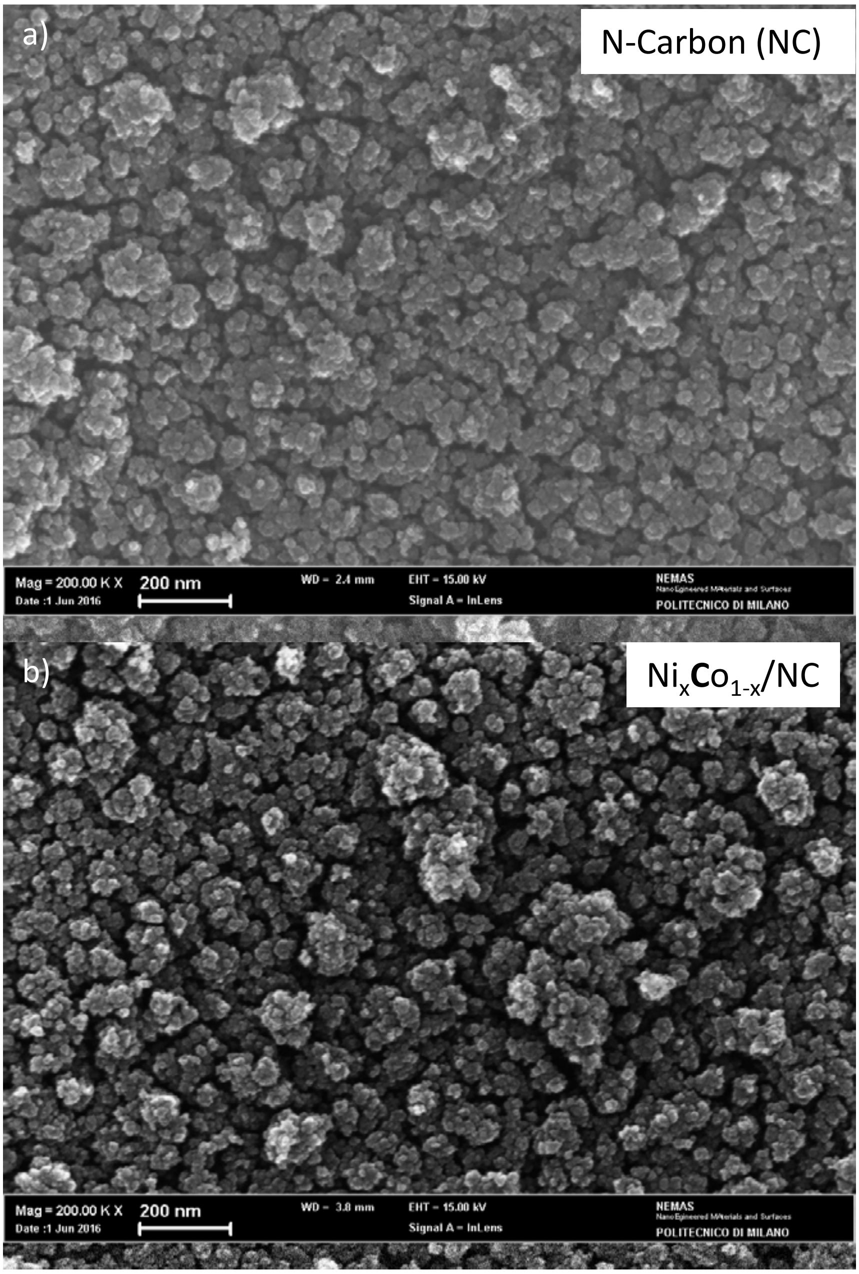

Fig. S3 SEM top-view of N-carbon and Ni_xCo_{1-x}/NC films.

.

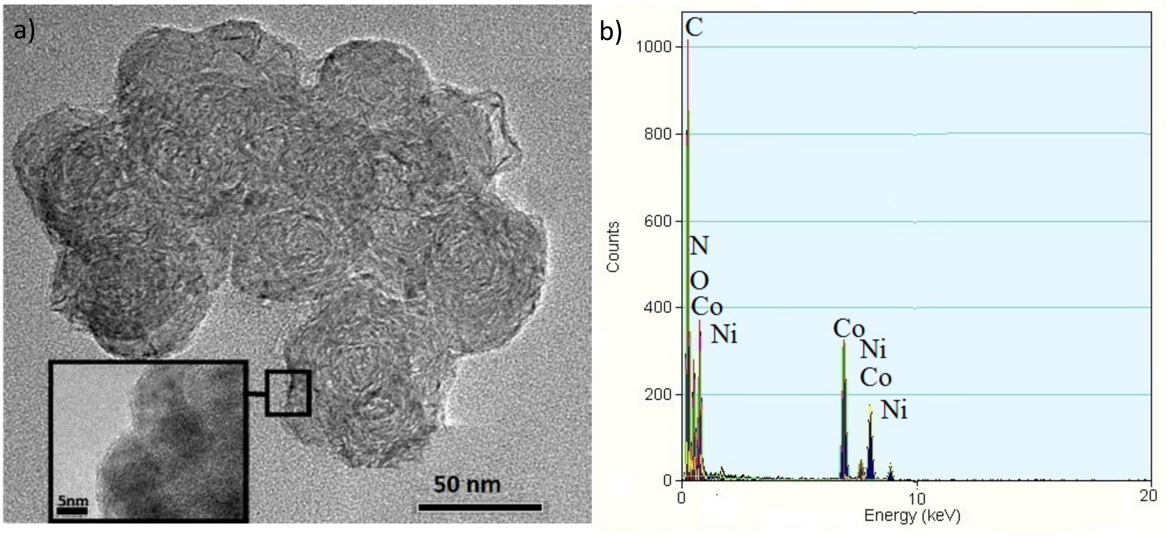

Fig. S4 (a) TEM image (inset of a) HR-TEM image and (b) TEM-EDS spectrum of Ni_xCo_{1-x}/NC film.

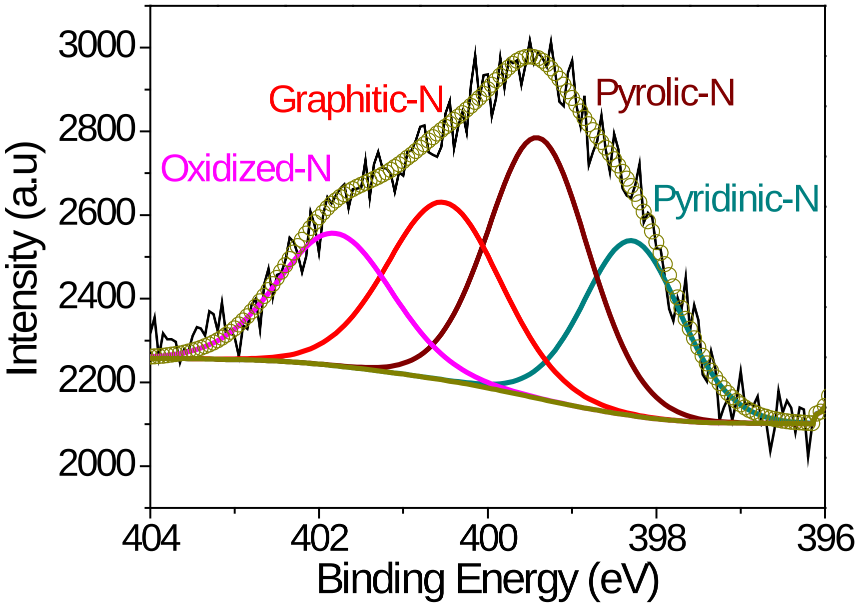

Fig. S5 High-resolution N1s spectrum of Ni_xCo_{1-x}/NC film.

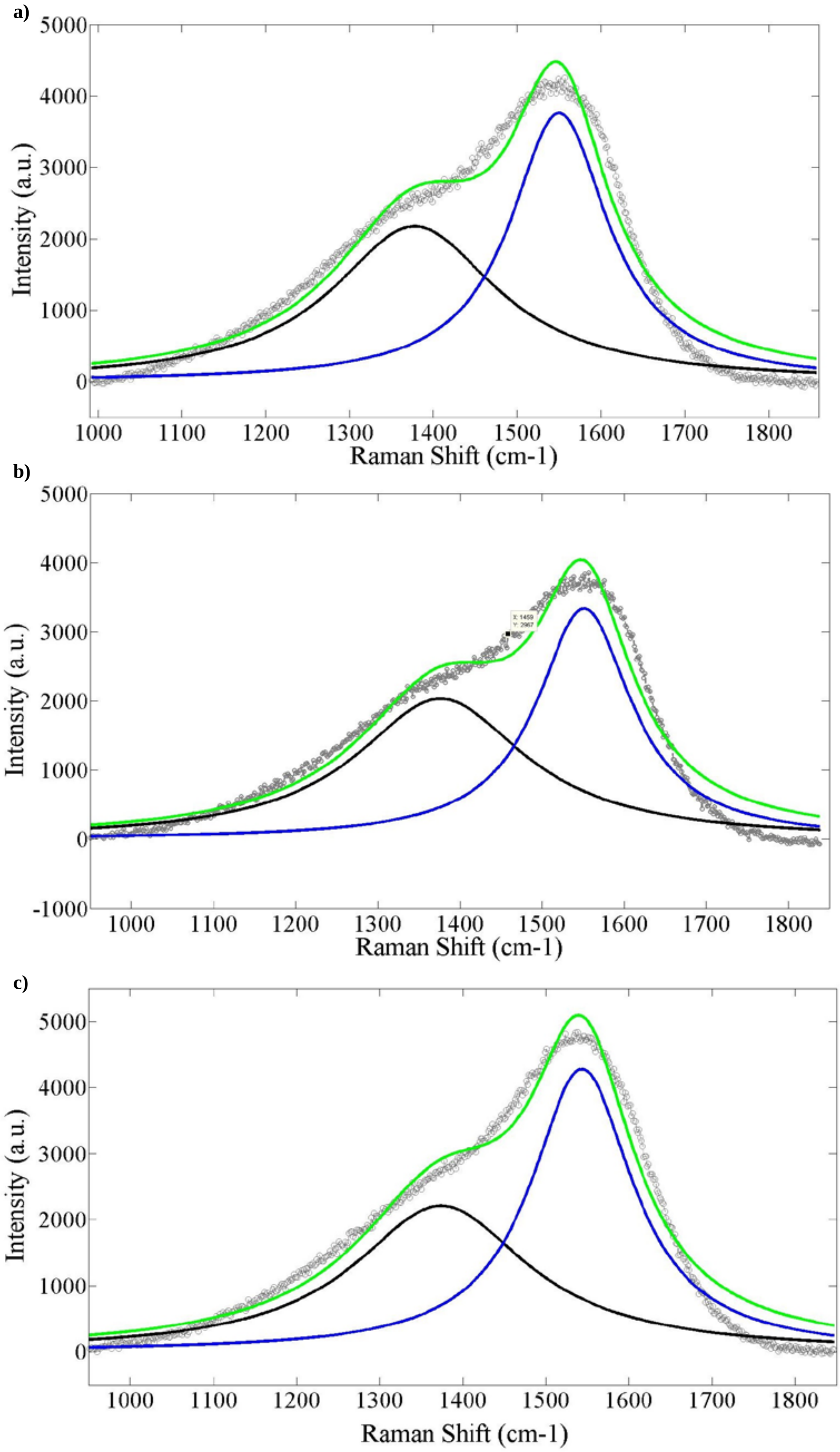

Fig. S6 Deconvoluted peaks of the D-G region in the Raman spectra of (a) Ni/NC, (b) $Ni_{0.5}Co_{0.5}$/NC and (c) Co/NC.

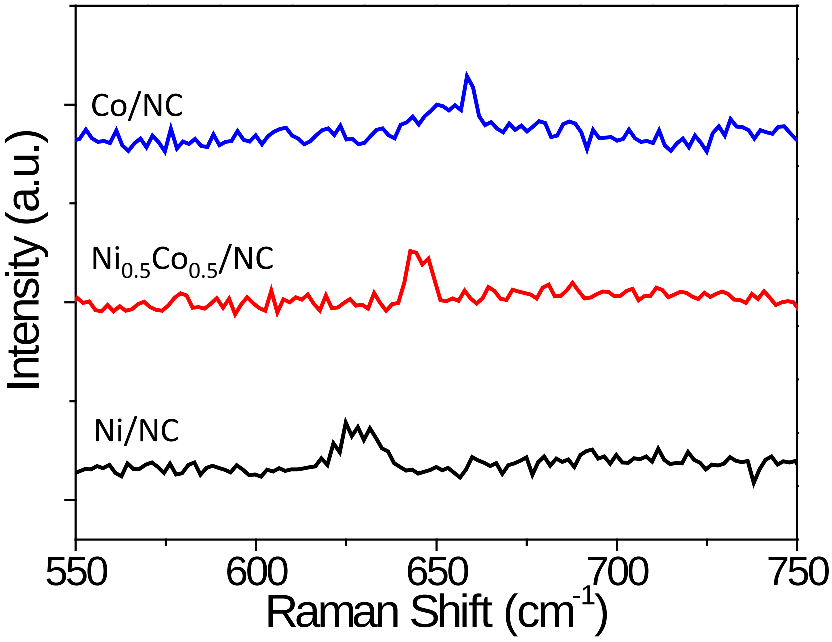

Fig. S7 Raman spectra (metal oxide region) of Ni/NC, $Ni_{0.5}Co_{0.5}$/NC and Co/NC.

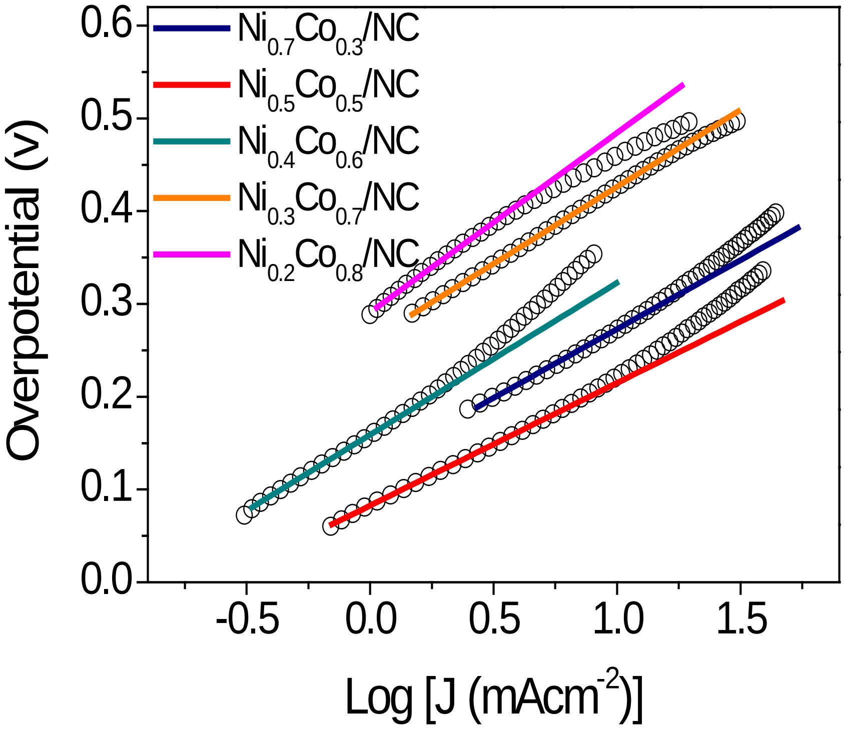

Fig. S8 HER Tafel plots of $Ni_{0.7}Co_{0.3}$/NC, $Ni_{0.5}Co_{0.5}$/NC, $N_{0.4}Co_{0.6}$/NC, $Ni_{0.3}Co_{0.7}$/NC and $Ni_{0.2}Co_{0.8}$/NC in 1.0 M KOH solution.

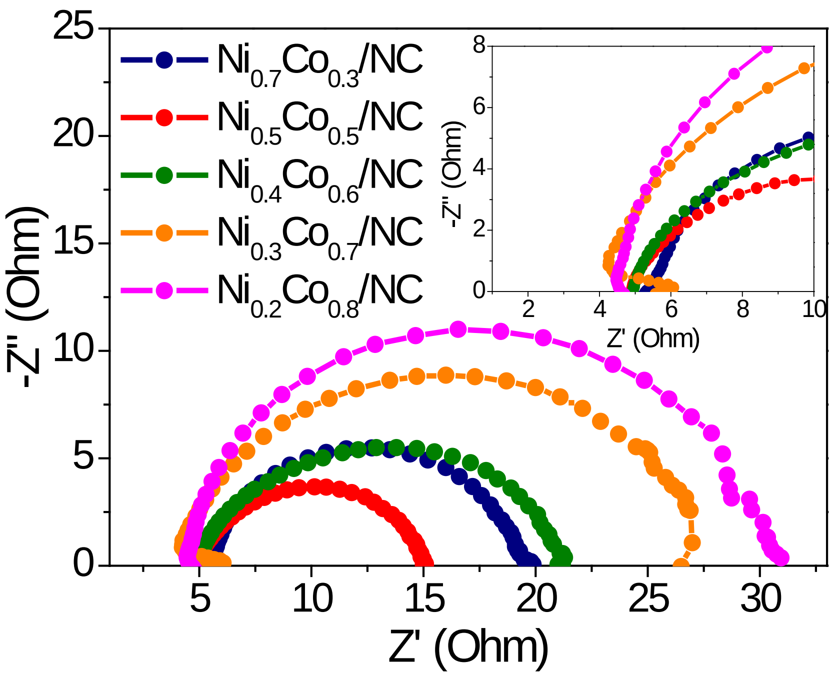

Fig. S9 Nyquist plots of binary Ni$_x$Co$_{1-x}$/NC at a potential of -1.5 V (vs. Ag/AgCl).

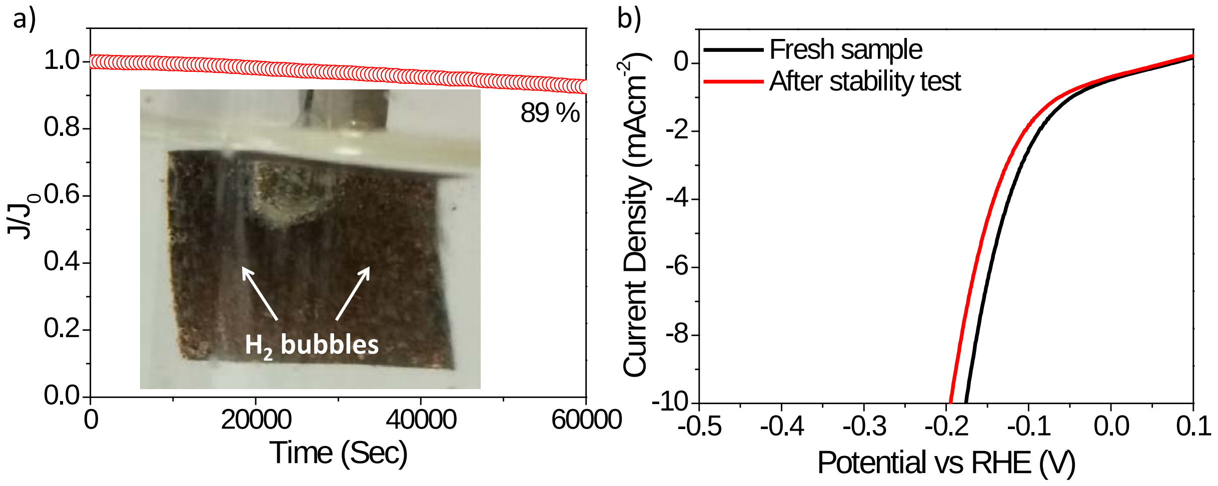

Fig. S10 Chronoamperometric response of Ni $_{0.5}$Co$_{0.5}$/NC under a constant voltage of -1.5 V (vs. Ag/AgCl) at 1.0M KOH (inset) enlarged view of the working electrode during electrochemical tests.

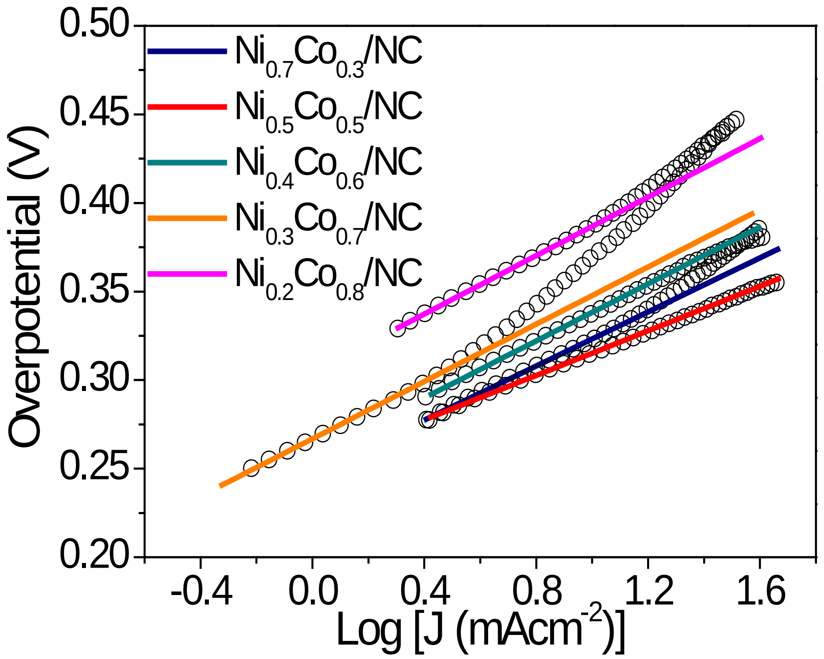

Fig. S11 OER Tafel plots of Ni$_{0.7}$Co$_{0.3}$/NC, Ni$_{0.5}$Co$_{0.5}$/NC, N $_{0.4}$Co$_{0.6}$/NC, Ni$_{0.3}$Co$_{0.7}$/NC and Ni$_{0.2}$Co$_{0.8}$/NC in 1.0 M KOH solution.

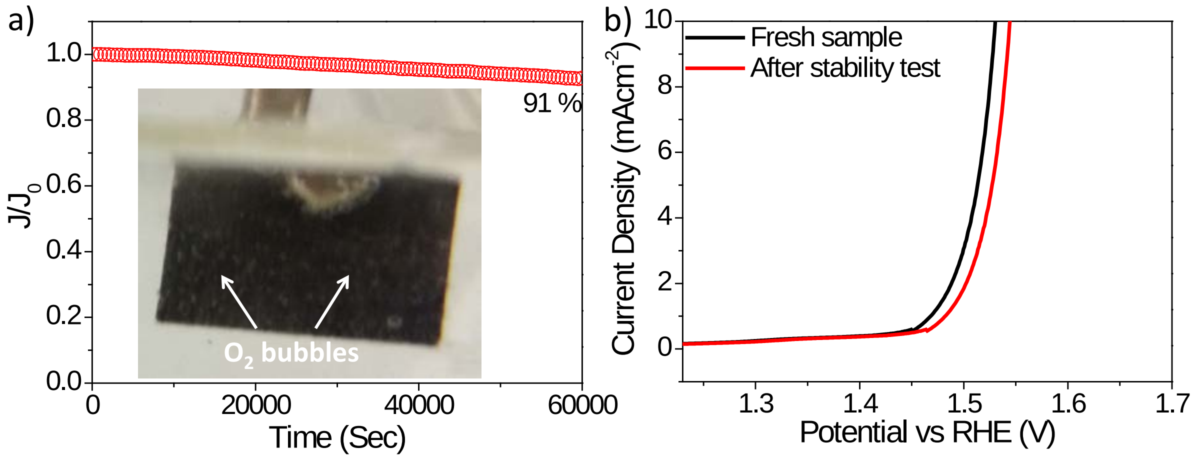

Fig. S12 Chronoamperometric response of Ni$_{0.5}$Co$_{0.5}$/NC under a constant voltage of +0.8 V (vs Ag/AgCl) in 1.0M KOH (inset) enlarged view of the working electrode during electrochemical tests.

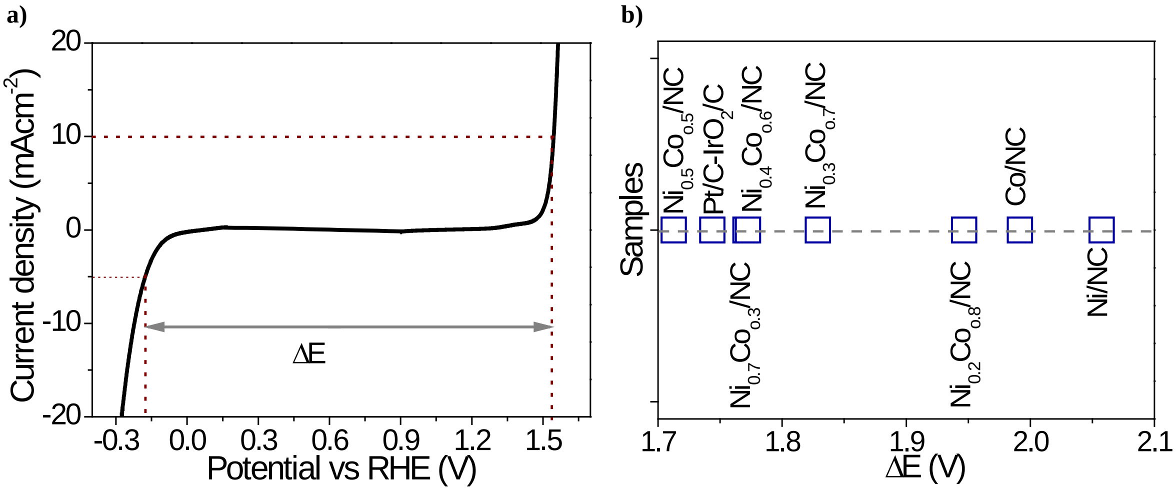

Fig. S13 (a) Full range OER and HER LSV of $Ni_{0.5}Co_{0.5}$/NC and (b) comparison of overall water splitting ability of the synthesized electrocatalysts.

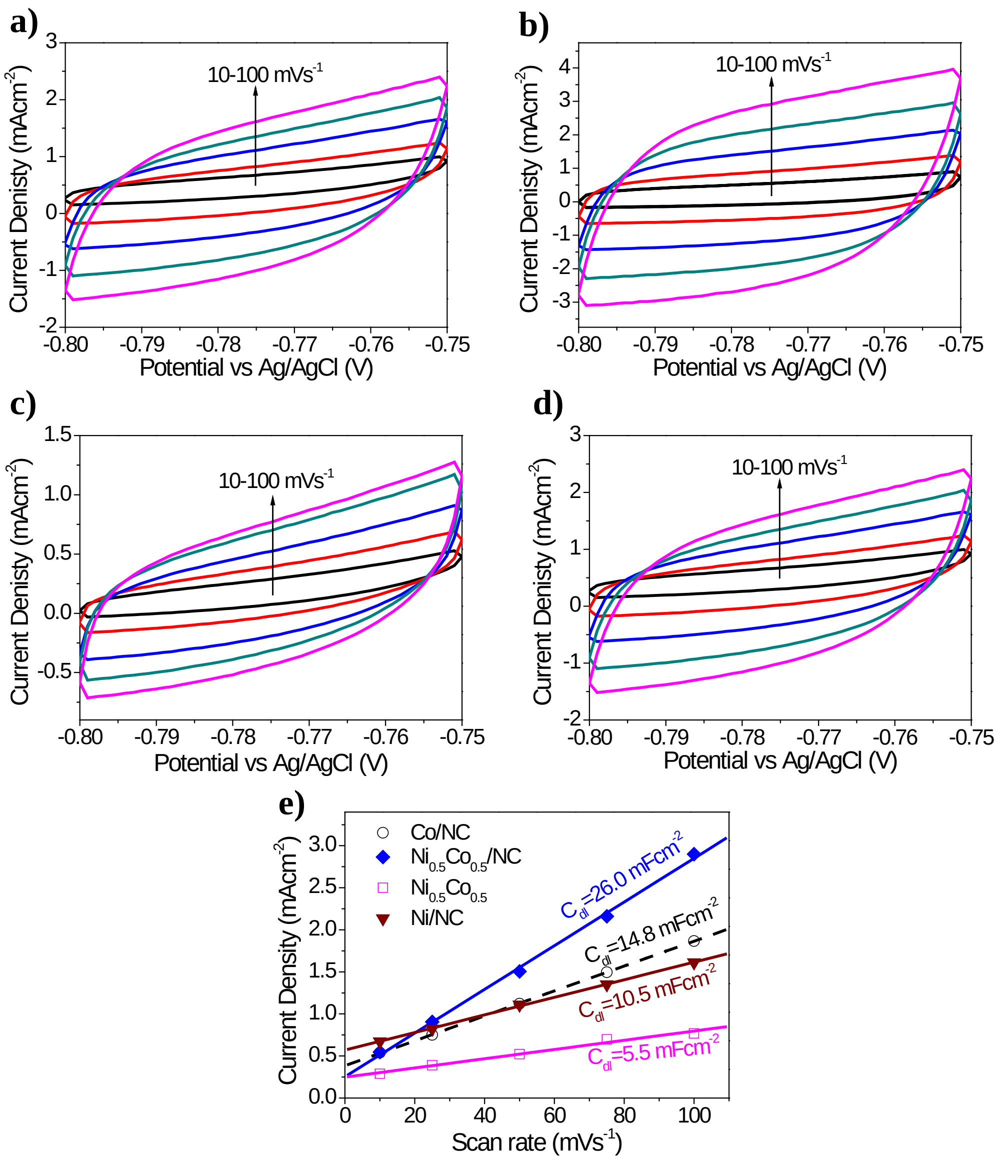

Fig. S14 Cyclic voltammograms (CVs) for (a) Ni/NC, (b) Ni$_{0.5}$Co$_{0.5}$/NC, (c) carbon-free Ni$_{0.5}$Co$_{0.5}$ and (d) Co/NC measured at different scan rates from 10 to 100 mV s^{-1} and (e) corresponding plots of the current density at -0.775 V vs. the scan rate.

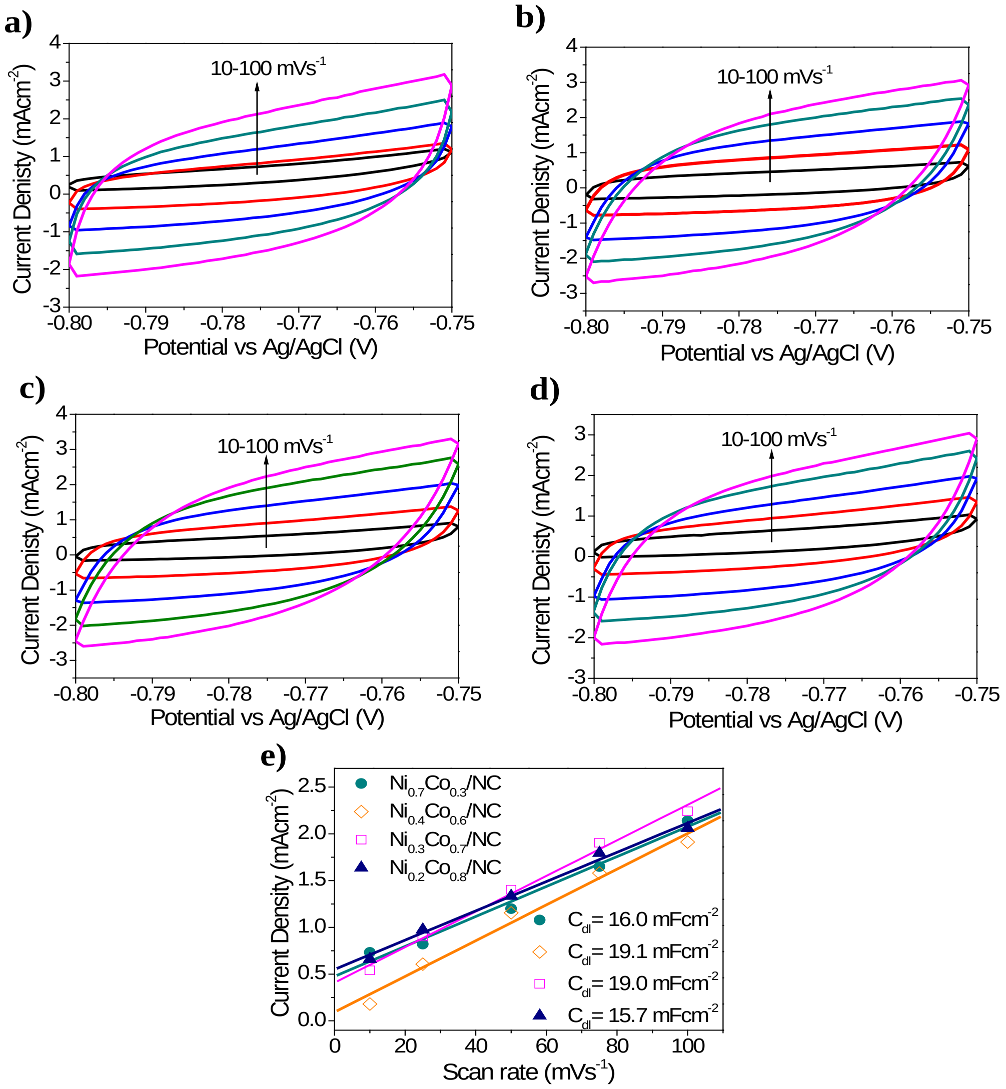

Fig. S15 Cyclic voltammograms (CVs) for (a) $Ni_{0.7}Co_{0.3}$/NC, (b) $Ni_{0.4}Co_{0.6}$/NC, (c) $Ni_{0.3}Co_{0.7}$/NC and (d) $Ni_{0.2}Co_{0.8}$/NC measured at different scan rates from 10 to 100 mV s^{-1} and (e) corresponding plots of the current density at -0.775 V vs. the scan rate.

Table S1 Chemical composition details obtained from XPS analysis for all synthesized electrodes

Sample	C	O	N	Ni	Co	% Ni	% Co
Ni/NC	52.56	34.12	3.67	9.65	0	100	0
$Ni_{0.7}Co_{0.3}$/NC	54.72	33.49	2.77	6.18	2.84	69	31
$Ni_{0.5}Co_{0.5}$/NC	49.63	35.58	3.36	5.47	5.96	48	52
$Ni_{0.4}Co_{0.6}$/NC	49.33	36.31	3.04	4.14	7.18	38	62
$Ni_{0.3}Co_{0.7}$/NC	49.85	35.02	2.4	4.13	8.60	32	68
$Ni_{0.2}Co_{0.8}$/NC	48.09	37.76	1.9	9.61	2.64	78	22
Co/NC	52.07	34.33	3.91	0	9.69	0	100

Table S2 Peak positions of Raman spectra for Ni/NC, $Ni_{0.5}Co_{0.5}$/NC and Co/NC.

Sample	D band position (cm^{-1})	G band position (cm^{-1})	I_D/I_G
Ni/NC	1373	1543	0.52
$Ni_{0.5}$ $Co_{0.5}$/NC	1376	1551	0.61
Co/NC	1377	1549	0.58

Table S3 Summary of recently reported HER electrocatalysts in 1.0 M KOH.

Samples	**η_0 (V)**	**η_{10} (V)**	**Tafel Slope**	**Reference**
Ni/NC	0.184	0.406	218.8	This work
$Ni_{0.7}Co_{0.3}$/NC	0.110	0.303	148.7	This work
$Ni_{0.5}Co_{0.5}$/NC	**0.048**	**0.176**	**132.1**	**This work**
$Ni_{0.4}Co_{0.6}$/NC	0.088	0.225	163.6	This work
$Ni_{0.3}Co_{0.7}$/NC	0.116	0.276	165.8	This work
$Ni_{0.2}Co_{0.8}$/NC	0.161	0.367	193.2	This work
Co/NC	0.163	0.378	221.9	This work
Ni0.5Co0.5	0.077	0.282	189.3	This work
Ni_3S_2/MWCNTs	>0.200	0.480	167	Ref 1
Co@NRCNT	160	370	80	Ref 2
NiO/Ni-CNT	90	~100	82	Ref 3
Co@N-C	125	200	100	Ref 4
Ni_2P	95	230	87	Ref 5

Table S4 Summary of recently reported OER electrocatalysts in 1.0 M KOH.

Samples	**η_0 (V)**	**η_{10} (V)**	**Tafel Slope**	**Reference**
Ni/NC	1.547	1.650	100.0	This work
$Ni_{0.7}Co_{0.3}$/NC	1.470	1.567	76.3	This work
$Ni_{0.5}$ $Co_{0.5}$/NC	**1.468**	**1.530**	**62.9**	**This work**
$Ni_{0.4}Co_{0.6}$/NC	1.472	1.558	80.4	This work
$Ni_{0.3}Co_{0.7}$/NC	1.473	1.572	80.9	This work
$Ni_{0.2}Co_{0.8}$/NC	1.477	1.579	82.6	This work
Co/NC	1.524	1.614	136.2	This work
$Ni_{0.5}$ $Co_{0.5}$	1.502	1.623	91.6	This work
$Co_{1-x}Fe_xS$@N-MC	1.570	1.640	159	Ref 6
N-graphene-$NiCo_2O_4$	1.540	1.664	156.0	Ref 7
$NiCo_2O_4$ NNs on FTO	1.595	1.795	292.0	Ref 8
$NiCo_2O_4$ nanowire	1.520	1.550	63.1	Ref 9
Ni-Co_2-O	>1.500	1.592	64.4	Ref 10
Co_3O_4-NrmGO	1.509	1.540	67.0	Ref 11
N-CG-CoO	1.514	1.570	71.0	Ref 12
Co_3O_4/MWCNT	1.585	1.840	65.0	Ref 13

References

1. T.-W. Lin, C.-J. Liu and C.-S. Dai, *Appl. Catal., B: Environ.*, 2014, **154–155**, 213.
2. X. Zou, X. Huang, A. Goswami, R. Silva, B. R. Sathe, E. Mikmeková and T. Asefa, *Angew. Chem. Int. Ed.*, 2014, **126**, 4461.
3. M. Gong, W. Zhou, M.-C. Tsai, J. Zhou, M. Guan, M.-C. Lin, B. Zhang, Y. Hu, D.-Y. Wang, J. Yang, S. J. Pennycook, B.-J. Hwang and H. Dai, *Nat. Commun.*, 2014, **5**, 4695.
4. J. Wang, D. Gao, G. Wang, S. Miao, H. Wu, J. Li and X. Bao, *J. Mater. Chem. A*, 2014, **2**, 20067.
5. L. Feng, H. Vrubel, M. Bensimon and X. Hu, *Phys. Chem. Chem. Phys.*, 2014, **16**, 5917.
6. M. Shen, C. Ruan, Y. Chen, C. Jiang, K. Ai and L. Lu, *ACS Appl. Mater. Interfaces*, 2015, **7**, 1207.
7. S. Chen and S.-Z. Qiao, *ACS Nano*, 2013, **7**, 10190.
8. H. Shi and G. Zhao, *J. Phys. Chem. C*, 2014, **118**, 25939.
9. R. Chen, H.-Y. Wang, J. Miao, H. Yang and B. Liu, *Nano Energy*, 2015, **11**, 333.
10. C. Zhu, D. Wen, S. Leubner, M. Oschatz, W. Liu, M. Holzschuh, F. Simon, S. Kaskel and A. Eychmuller, *Chem. Commun.*, 2015, **51**, 7851.
11. Y. Liang, Y. Li, H. Wang, J. Zhou, J. Wang, T. Regier and H. Dai, *Nat. Mater.*, 2011, **10**, 780.
12. S. Mao, Z. Wen, T. Huang, Y. Hou and J. Chen, *Energy & Environ. Sci.*, 2014, **7**, 609.
13. X. Lu and C. Zhao, *J. Mater. Chem. A*, 2013, **1**, 12053.

Chapter 7

7. Conclusion and Recommendation

7.1. Conclusion

This thesis is devoted to developing novel low-cost, active and durable carbon-based electrocatalysts as the substation for noble metal materials in the key electrocatalytic processes (e.g. ORR, OER and HER) in the renewable fuel cells, metal-air batteries and water electrolysers. Based on the research in this thesis, the following conclusions can be drawn:

- The electrocatalytic activity of synthesized materials can be effectively improved by tunning the porous structure, chemical composition and doping heteroatoms (e.g. nitrogen). For example, the superior electrocatalytic activity of N-doped mesoporous carbon spheres (NMCs) as compared to MCs without nitrogen doping could be attributed to the enhanced graphitization degree and the incorporation of nitrogen atoms into the carbon lattice, which favour the reactivity of the neighbouring carbon atoms via alteration of the electronic structure. Moreover, the best performance of the optimized sample (NMC5-900) for catalyzing ORR would be the result of a balanced graphitization degree and active species retained at moderate heating temperature, the presence of highly active C-N species, good conductivity, well-structured mesoporosity, large pore size, sufficient surface area, and high pore volume, which make it a promising catalyst for ORR in alkaline solutions.
- A unique coupling of Cobalt and Nitrogen co-doped porous carbon spheres with in situ grown N-carbon nanosheets as a composite results in a highly active bifunctional electrocatalyst, which successfully combines the desired merits such as highly active Co-N_x species, good conductivity, porous structure with very good mass transport, and sufficiently large surface area with accessible catalytically active sites. These excellent characteristics assure its excellent HER and OER catalytic activity as judged on the basis of the favourable onset potentials, small Tafel slopes and good stability, which make it a promising bifunctional electrocatalyst for both HER and OER.
- The electrocatalytic activity can be optimized by tunning the chemical composition and nanostructure of the electrocatalysts through the deposition of Cobalt (oxide) nanoparticles on porous N-carbon thin films via two-step pulsed laser deposition technique. The synthesized material with the optimized synthesis parameters (background gas, target to substrate distance, deposition time and pressure, etc.) behaves as an efficient OER electrocatalyst and has superior activity in concentrated

alkaline solution such as 1.0M KOH electrolyte. The excellent catalytic activity of $Co(Ox)_{50}$@PNC films could be attributed to the surrounding N-carbon framework, and it was found that a higher ratio of Co^{2+}/Co^{3+} yields better catalytic activity towards the OER. The transport of reactants and products involved in electrochemical reactions was also facilitated by the porous structure of the N-carbon support. Together with the combined mutual effects of each structural component, this $Co(Ox)_{50}$@PNC OER catalyst outperforms most of the reported earth-abundant OER catalysts in activity and stability.

- Bimetallic Nickel–Cobalt nanoparticles supported on porous nitrogen doped carbon thin films (Ni_xCo_{1-x}/NC) demonstrated not only efficient electrocatalytic activity and durability for HER but also offered impressive catalytic performance for OER in alkaline medium. The outstanding catalytic performance of the developed composites was strongly correlated to the homogeneous distribution of Nickel–Cobalt active sites and synergetic coupling interaction with the porous N-carbon framework. This earth-abundant composite could undoubtedly hold a great promise for other practical applications in energy storage and conversion systems.

7.2. Recommendation

Although all the objectives of this thesis listed in Chapter 1 have been addressed, there are still some challenges which require further work in the future.

- Despite that the catalytic activity of studied electrocatalysts is good and close to that of noble metals-based counterparts (e.g. Pt/C, RuO_2 and IrO_2), it is still challenging to fabricate non-precious metal-based materials commercially competitive to that of available in large scale applications. Thus, further research required in order to develop new metal compounds and their derivatives such as metalphosphides, metal carbides and their hybrids due to their good stability and resistance under harsh electrochemical environments.
- Moreover, fundamental studies of bifunctional electrocatalysis are required due to the growing interests on the development of new energy conversion devices such as flow batteries, water splitting systems and fuel cells. Progress in this area can only be achieved by coupling theoretical calculations and understanding of reaction pathways with experimental validation which may open new avenues for the development of

commercially feasible catalysts for broader applications ranging from energy conversion reactions to heterogeneous catalysis and photocatalysis.

- Further, synthesis of non-precious metal doped on carbon-based supports specifically in atomic form still presents significant conceptual challenges, where most methods used involve multi-step approaches and work successfully only on specific cases. For instance, this type of material must not be considered to be superior to the conventional nanostructured catalysts since the single atom metal sites might limit their application in catalytic processes which require multi-metal active sites. In addition, the control in functionality, size, shape and structure is worth further exploring in order to achieve new or enhanced properties and prevent aggregation of the small cluster and atomic dopant in the case of high metal loading due to a high level of single metals surface energy.

We believe that further exploration in this area will contribute to resolving the real-world energy issues and promote green energy production.